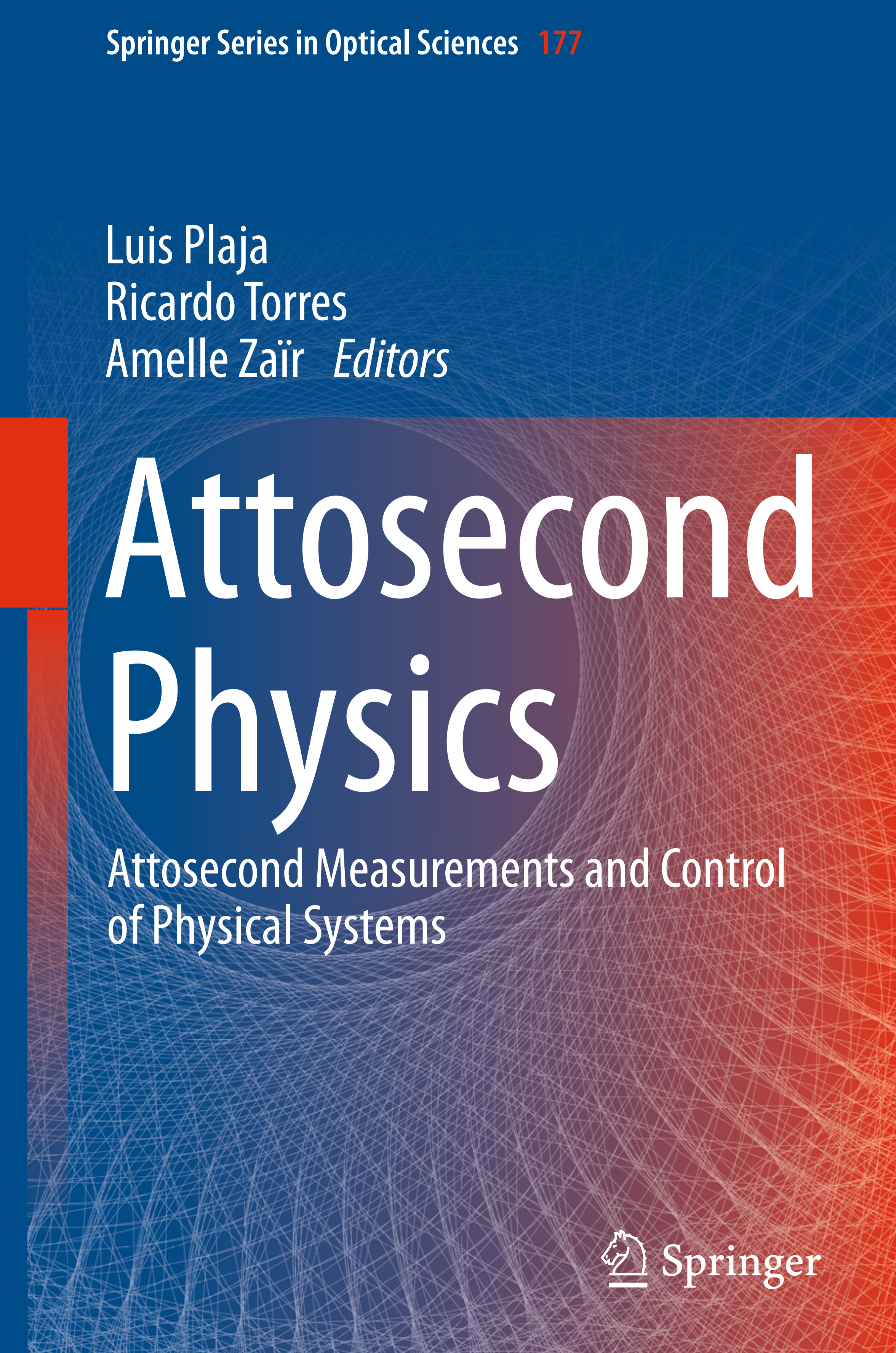

Springer Series in Optical Sciences 177

Luis Plaja
Ricardo Torres
Amelle Zaïr *Editors*

# Attosecond Physics

## Attosecond Measurements and Control of Physical Systems

Springer

# Springer Series in Optical Sciences

## Volume 177

For further volumes:
http://www.springer.com/series/624

# Springer Series in Optical Sciences

The Springer Series in Optical Sciences, under the leadership of Editor-in-Chief William T. Rhodes, Georgia Institute of Technology, USA, provides an expanding selection of research monographs in all major areas of optics: lasers and quantum optics, ultrafast phenomena, optical spectroscopy techniques, optoelectronics, quantum information, information optics, applied laser technology, industrial applications, and other topics of contemporary interest.

With this broad coverage of topics, the series is of use to all research scientists and engineers who need up-to-date reference books.

The editors encourage prospective authors to correspond with them in advance of submitting a manuscript. Submission of manuscripts should be made to the Editor-in-Chief or one of the Editors. See also www.springer.com/series/624.

*Editor-in-Chief*
William T. Rhodes
School of Electrical and Computer Engineering
Georgia Institute of Technology
Atlanta, GA 30332-0250, USA
bill.rhodes@ece.gatech.edu

*Editorial Board*
Ali Adibi
School of Electrical and Computer Engineering
Georgia Institute of Technology
Atlanta, GA 30332-0250, USA
adibi@ee.gatech.edu

Toshimitsu Asakura
Faculty of Engineering
Hokkai-Gakuen University
1-1, Minami-26, Nishi 11, Chuo-ku
Sapporo, Hokkaido 064-0926, Japan
asakura@eli.hokkai-s-u.ac.jp

Theodor W. Hänsch
Max-Planck-Institut für Quantenoptik
Hans-Kopfermann-Straße 1
85748 Garching, Germany
t.w.haensch@physik.uni-muenchen.de

Takeshi Kamiya
National Institution for Academic Degrees
Ministry of Education, Culture, Sports
Science and Technology
3-29-1 Otsuka, Bunkyo-ku
Tokyo 112-0012, Japan
kamiyatk@niad.ac.jp

Ferenc Krausz
Ludwig-Maximilians-Universität München
Lehrstuhl für Experimentelle Physik
Am Coulombwall 1
85748 Garching, Germany
Max-Planck-Institut für Quantenoptik
Hans-Kopfermann-Straße 1
85748 Garching, Germany
ferenc.krausz@mpq.mpg.de

Bo A.J. Monemar
Department of Physics and Measurement Technology,
Materials Science Division
Linköping University
58183 Linköping, Sweden
bom@ifm.liu.se

Herbert Venghaus
Fraunhofer Institut für Nachrichtentechnik
Heinrich-Hertz-Institut
Einsteinufer 37
10587 Berlin, Germany
venghaus@hhi.de

Horst Weber
Optisches Institut
Technische Universität Berlin
Straße des 17. Juni 135
10623 Berlin, Germany
weber@physik.tu-berlin.de

Harald Weinfurter
Sektion Physik
Ludwig-Maximilians-Universität München
Schellingstraße 4/III
80799 München, Germany
harald.weinfurter@physik.uni-muenchen.de

Luis Plaja • Ricardo Torres • Amelle Zaïr
Editors

# Attosecond Physics

## Attosecond Measurements and Control of Physical Systems

Springer

*Editors*
Luis Plaja
Física Aplicada
Universidad de Salamanca
Salamanca, Spain

Ricardo Torres
Centro de Láseres Pulsados
Salamanca, Spain

Amelle Zaïr
Department of Physics
Quantum Optics & Laser Science Group
Imperial College London
London, UK

ISSN 0342-4111 ISSN 1556-1534 (electronic)
Springer Series in Optical Sciences
ISBN 978-3-642-37622-1 ISBN 978-3-642-37623-8 (eBook)
DOI 10.1007/978-3-642-37623-8
Springer Heidelberg New York Dordrecht London

Library of Congress Control Number: 2013946017

© Springer-Verlag Berlin Heidelberg 2013
This work is subject to copyright. All rights are reserved by the Publisher, whether the whole or part of the material is concerned, specifically the rights of translation, reprinting, reuse of illustrations, recitation, broadcasting, reproduction on microfilms or in any other physical way, and transmission or information storage and retrieval, electronic adaptation, computer software, or by similar or dissimilar methodology now known or hereafter developed. Exempted from this legal reservation are brief excerpts in connection with reviews or scholarly analysis or material supplied specifically for the purpose of being entered and executed on a computer system, for exclusive use by the purchaser of the work. Duplication of this publication or parts thereof is permitted only under the provisions of the Copyright Law of the Publisher's location, in its current version, and permission for use must always be obtained from Springer. Permissions for use may be obtained through RightsLink at the Copyright Clearance Center. Violations are liable to prosecution under the respective Copyright Law.
The use of general descriptive names, registered names, trademarks, service marks, etc. in this publication does not imply, even in the absence of a specific statement, that such names are exempt from the relevant protective laws and regulations and therefore free for general use.
While the advice and information in this book are believed to be true and accurate at the date of publication, neither the authors nor the editors nor the publisher can accept any legal responsibility for any errors or omissions that may be made. The publisher makes no warranty, express or implied, with respect to the material contained herein.

Printed on acid-free paper

Springer is part of Springer Science+Business Media (www.springer.com)

# Preface

Attosecond science is the art of controlling and measuring phenomena that occur in the timescale of $10^{-18}$ seconds. Very much in the same way as the invention of the microscope revealed a thitherto unobserved world to the scientists of the 17th century, attosecond technology is opening up a vast field for discovery to the scientists of the present day. If the aim of a microscope is to magnify the image of small objects in order to observe their tiniest features, the goal of attosecond technology is to take *movies* of ultrafast phenomena in slow motion, in order to reveal its dynamics in the shortest time intervals.

The atomic unit of time is 24 attoseconds; therefore to speak about attosecond science is tantamount to time-resolved electron dynamics in its natural timescale. The properties of matter, in whichever state, are largely determined by its electronic structure. Likewise, any change of these properties, through a chemical reaction or as a response to an external field, is ultimately driven by the electron dynamics. Therefore, it is not difficult to realize that the implications of controlling this dynamics are enormous for many areas of science, from atomic physics to materials science or biochemistry. As the 20th century was the era of the study and control of the *structure* of matter, we can affirm that the 21st will see the dominance of the *dynamics* of matter at its most fundamental level.

The advancement of ultrafast science has been closely connected with the development of lasers. When the first visible laser was demonstrated in 1960, very few could anticipate the huge impact that this little device would have in the history of science. The ultrafast revolution started with the invention of Q-switching for the generation of nanosecond pulses soon after the discovery of the laser itself. The development of the mode-locking technique, together with the finding of laser materials with a broad gain bandwidth, led to the generation of the first sub-picosecond pulses in 1974. These lasers have already originated a whole new branch of chemistry, dubbed femtochemistry.

The following step down in timescale required another breakthrough in laser technology: the invention of Chirped Pulse Amplification or CPA. This technique has allowed the generation of terawatt ($10^{12}$ Watts) laser pulses with table-top systems, and it has spread out dramatically the research in ultraintense laser-matter interactions. As it turns out, the concept of *ultraintense* is intimately linked to that of *ultrashort*. The best example is seen in the process of high-order harmonic generation, where a high intensity laser field is capable of rivalling the Coulomb field experienced by the electrons in an atom, and drives the electron motion back and forth, generating high energy photons in the process. As the oscillation period of a near-infrared laser field is of the order of femtoseconds, the controlled motion of the electrons, and the radiation emitted subsequently occurs in a sub-femtosecond timescale. Currently, high-harmonic generation and related processes like above-threshold ionization and non-sequential double ionization, made possible by high-intensity lasers, are the gateway to the attosecond world.

We can distinguish two main areas of activity in the current endeavours of attosecond science: the development of attosecond light sources, and the measurement and control of attosecond phenomena. In the first, the ultimate goal is to achieve a source of fully-controlled high-energy isolated few-attosecond pulses which may then be used for ultrafast pump and probe experiments, non-linear XUV spectroscopy, etc. The first part of this book reviews the present status of these efforts, including the not less challenging task of fully characterizing the ultrashort pulses.

The second main area of activity in attosecond science, covered in the second part of this book, is exploring and demonstrating different methods to measure and control the dynamics of electrons in atoms, molecules and solids, either in pump and probe schemes using XUV attosecond and IR femtosecond pulses, or directly driving the electron motion with an intense IR laser field. Some of these techniques have already produced spectacular results.

Attosecond science is a young discipline and it is bound to undergo a dramatic development in the next few years. Research in the field is very active as it can be verified from the remarkable increase in the number of publications with the keyword *attosecond*, from barely 20 in the year 2000 to more than 250 in 2012. Some anticipated breakthroughs are the arrival of free-electron lasers at the attosecond regime, the generation of microjoule-energy keV attosecond pulses from relativistic laser-plasma interactions, the sub-cycle shaping of light waveforms, and the introduction of attosecond time resolution into well-established techniques of microscopy and electron diffraction, to name a few.

We hope this book will serve as a guide to newcomers to the field as well as a reference for the most experienced but, specially, we hope it will inspire a new generation of scientists to accomplish the just started conquest of the attosecond world.

Salamanca, London

Luis Plaja
Ricardo Torres
Amelle Zaïr

# Contents

## Part I Fundamentals

## Part II Generation, Control and Characterization of Attosecond Pulses

**Part III Attosecond Measurements and Control of Physical Systems**

**Part IV Future Trends**

# Contributors

**Pierre Agostini** Department of Physics, The Ohio State University, Columbus, OH, USA

**T. Balciunas** Photonics Institute, Vienna University of Technology, Vienna, Austria

**A. Baltuska** Photonics Institute, Vienna University of Technology, Vienna, Austria

**Andreas Becker** JILA and Department of Physics, University of Colorado, Boulder, CO, USA

**J.B. Bertrand** Joint Attosecond Science Laboratory, National Research Council of Canada and University of Ottawa, Ottawa, Ontario, Canada

**J. Caillat** Laboratoire de Chimie Physique-Matière et Rayonnement (LCPMR), UPMC Université Paris 6, UMR 7614, Paris Cedex 05, France

**F. Calegari** Department of Physics, Politecnico di Milano, Institute of Photonics and Nanotechnologies (CNR-IFN), National Research Council of Italy, Milan, Italy

**Claudio Cirelli** Physics Department, Institute for Quantum Electronics, ETH Zürich, Zurich, Switzerland

**P.B. Corkum** Joint Attosecond Science Laboratory, University of Ottawa and National Research Council of Canada, Ottawa, Canada

**Marcus Dahlström** Atomic Physics, Stockholm University, Stockholm, Sweden

**Anthony D. DiChiara** Department of Physics, The Ohio State University, Columbus, OH, USA

**Louis F. DiMauro** Department of Physics, The Ohio State University, Columbus, OH, USA

**Z. Diveki** Service des Photons, Atomes et Molécules, CEA-Saclay, IRAMIS, Gif-sur-Yvette, France

**N. Dudovich** Department of Physics of Complex Systems, Weizmann Institute of Science, Rehovot, Israel

**Petrissa Eckle** Physics Department, Institute for Quantum Electronics, ETH Zürich, Zurich, Switzerland

**G. Fan** Photonics Institute, Vienna University of Technology, Vienna, Austria

**Thomas Fordell** Centre for Metrology and Accreditation (MIKES), Espoo, Finland

**Mette B. Gaarde** Department of Physics and Astronomy, Louisiana State University, Baton Rouge, LA, USA

**Shambhu Ghmire** SLAC National Accelerator Laboratory, PULSE Institute, Menlo Park, CA, USA

**Mathieu Gisselbrecht** Synchrotron Radiation Research, Lund University, Lund, Sweden

**R. Guichard** Laboratoire de Chimie Physique-Matière et Rayonnement (LCPMR), UPMC Université Paris 6, UMR 7614, Paris Cedex 05, France

**S. Haessler** Photonics Institute, Vienna University of Technology, Vienna, Austria

**Feng He** Key Laboratory for Laser Plasmas (Ministry of Education) and Department of Physics and Astronomy, SJTU, Shanghai, People's Republic of China

**Ulrich Heinzmann** Faculty of Physics (Molecular and Surface Physics), University of Bielefeld, Bielefeld, Germany

**J. Itatani** Institute for Solid State Physics, The University of Tokyo, Kashiwa, Chiba, Japan

**M.Y. Ivanov** Department of Physics, Imperial Colledge London, London, UK

**Agnieszka Jaroń-Becker** JILA and Department of Physics, University of Colorado, Boulder, CO, USA

**Per Johnsson** Atomic Physics, Lund University, Lund, Sweden

**Ursula Keller** Physics Department, Institute for Quantum Electronics, ETH Zürich, Zurich, Switzerland

**J.C. Kieffer** Institut National de la Recherche Scientifique INRS-EMT, Varennes, Quebec, Canada

**Kathrin Klünder** Atomic Physics, Lund University, Lund, Sweden

**Ferenc Krausz** Max Planck Institute of Quantum Optics, Garching, Germany

**Anne L'Huillier** Atomic Physics, Lund University, Lund, Sweden

**Pengfei Lan** Extreme Photonics Research Group, RIKEN Center for Advanced Photonics (RAP), Wako, Saitama, Japan

**J. Levesque** Centre for Operational Research and Analysis, Defence R & D Canada, Department of National Defence, Ottawa, Canada

**F. Légaré** Institut National de la Recherche Scientifique INRS-EMT, Varennes, Quebec, Canada

**M. Lucchini** ETH Zurich, Physics Department, Institute of Quantum Electronics Ultrafast Laser Physics, HPT E11, Zurich, Switzerland

**Y. Mairesse** CELIA, UMR5107, Université de Bordeaux, CNRS, CEA, Talence, France

**A. Maquet** Laboratoire de Chimie Physique-Matière et Rayonnement (LCPMR), UPMC Université Paris 6, UMR 7614, Paris Cedex 05, France

**Johan Mauritsson** Atomic Physics, Lund University, Lund, Sweden

**Katsumi Midorikawa** Extreme Photonics Research Group, RIKEN Center for Advanced Photonics (RAP), Wako, Saitama, Japan

**A.V. Mitrofanov** Photonics Institute, Vienna University of Technology, Vienna, Austria

**H. Niikura** Department of Applied Physics, Waseda University, Shinjyuku, Tokyo, Japan

**M. Nisoli** Department of Physics, Politecnico di Milano, Institute of Photonics and Nanotechnologies (CNR-IFN), National Research Council of Italy, Milan, Italy

**J.A. Pérez-Hernández** Centro de Láseres Pulsados CLPU, Salamanca, Spain

**Adrian N. Pfeiffer** Physics Department, Institute for Quantum Electronics, ETH Zürich, Zurich, Switzerland; Chemical Sciences Division, Lawrence Berkeley National Laboratory, Berkeley, CA, USA

**Antonio Picón** JILA and Department of Physics, University of Colorado, Boulder, CO, USA

**David A. Reis** SLAC National Accelerator Laboratory, PULSE Institute, Menlo Park, CA, USA; Departments of Photon Science and Applied Physics, Stanford University, Stanford, CA, USA

**L. Roso** Centro de Láseres Pulsados CLPU, Salamanca, Spain

**T. Ruchon** Service des Photons, Atomes et Molécules, CEA-Saclay, IRAMIS, Gif-sur-Yvette, France

**Camilo Ruiz** Centro de Laseres Pulsados CLPU, Edificion M3, Parque Cientifico, C/ Adaja s/n, Villamajor, Spain

**P. Salières** Service des Photons, Atomes et Molécules, CEA-Saclay, IRAMIS, Gif-sur-Yvette, France

**G. Sansone** Department of Physics, Politecnico di Milano, Institute of Photonics and Nanotechnologies (CNR-IFN), National Research Council of Italy, Milan, Italy

**Kenneth J. Schafer** Department of Physics and Astronomy, Louisiana State University, Baton Rouge, LA, USA

**B.E. Schmidt** Institut National de la Recherche Scientifique INRS-EMT, Varennes, Quebec, Canada

**E.E. Serebryannikov** M.V. Lomonosov Moscow State University, Moscow, Russia

**A.D. Shiner** Ciena Canada Ltd., Kanata, Ontario, Canada

**Mathias Smolarski** Physics Department, Institute for Quantum Electronics, ETH Zürich, Zurich, Switzerland

**S. Stagira** Department of Physics, Politecnico di Milano, Institute of Photonics and Nanotechnologies (CNR-IFN), National Research Council of Italy, Milan, Italy

**Marko Swoboda** B CUBE—Center for Molecular Bioengineering, TU Dresden, Dresden, Germany

**R. Taïeb** Laboratoire de Chimie Physique-Matière et Rayonnement (LCPMR), UPMC Université Paris 6, UMR 7614, Paris Cedex 05, France

**Eiji J. Takahashi** Extreme Photonics Research Group, RIKEN Center for Advanced Photonics (RAP), Wako, Saitama, Japan

**Norio Takemoto** Department of Chemical Physics, Weizmann Institute of Science, Rehovot, Israel

**A.J. Verhoef** Photonics Institute, Vienna University of Technology, Vienna, Austria

**D.M. Villeneuve** Joint Attosecond Science Laboratory, National Research Council of Canada and University of Ottawa, Ottawa, Ontario, Canada

**C. Vozzi** Department of Physics, Politecnico di Milano, Institute of Photonics and Nanotechnologies (CNR-IFN), National Research Council of Italy, Milan, Italy

**H.J. Wörner** Laboratorium für Physikalische Chemie, Eidgenössische Technische Hochschule Zürich, Zürich, Switzerland

**A.M. Zheltikov** M.V. Lomonosov Moscow State University, Moscow, Russia; Department of Physics, Texas A&M University, College Station, TX, USA

# Part I
# Fundamentals

# Chapter 1
# Attosecond Science

**P.B. Corkum**

**Abstract** Attosecond technology builds on, and contributes to, important historic directions in science. For this reason, the science has the depth to yield important discoveries for a long time. Unfortunately the title “attosecond” science biases us to think mostly about dynamics but many of the most important applications of “attosecond technology” may not be related to dynamics at all. This broad set of applications point to the future impact of the technology.

It is a pleasure to introduce this new publication with some thoughts of the past and future of attosecond science. During the last decade we have engineered a radical advance in Quantum Electronics. As Fig. 1.1 shows, the duration of the shortest pulse that we can create has decreased by more than one order-of-magnitude after about a decade in which there had been little advance. We have achieved this by moving to shorter wavelength as also illustrated in Fig. 1.1. Therefore, you will see that we developed not only the shortest pulses but also the shortest wavelength sources available with laser-based methods. In fact, as you read this new volume you will see that there are four scientific traditions from which attosecond physics grows and these traditions open four complimentary ways for attosecond science to influence the world’s scientific agenda.

We can understand one tradition by thinking of attosecond science as the current frontier of ultrafast science—a 50 year old sub-field of laser science, with even deeper roots. For 50 years, ultrafast science has been a major direction of research. It has retained its freshness because time is a natural frontier of all of the physical sciences. As we pursue time to shorter and shorter intervals, we inevitably find unexplored science, opening new processes for inspection. From the perspective of where we sit today, we are a very long way from any natural boundary. Therefore, for the foreseeable future we can expect technology to drive the production of even shorter pulses, motivated by the demand to study ever faster phenomena.

---

P.B. Corkum (✉)
Joint Attosecond Science Laboratory, University of Ottawa and National Research Council of Canada, 100 Sussex Drive, Ottawa K1A 0R6, Canada
e-mail: Paul.Corkum@nrc-cnrc.gc.ca

L. Plaja et al. (eds.), *Attosecond Physics*, Springer Series in Optical Sciences 177,
DOI 10.1007/978-3-642-37623-8_1,

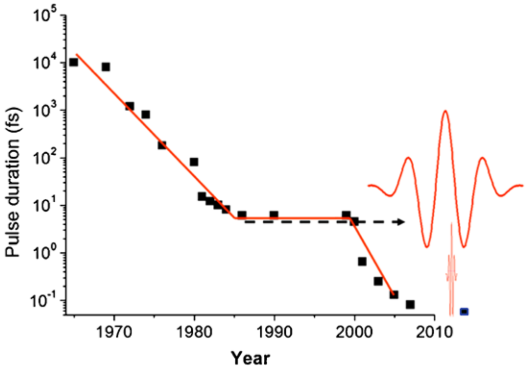

**Fig. 1.1** The shortest pulse that could be generated as a function of time since mode locking was developed

So attosecond science inherits the benefits of 50 years of research into concepts and approaches for fast measurement. As attosecond researchers, it is our task to improve, adapt and apply those methods. From our current perspective, just 10 years into the "attosecond age", there remains a lot of work to do. Because the sources are still not intense enough, we cannot directly apply attosecond pump-attosecond probe spectroscopy—to say nothing of the more powerful femtosecond methods such as 2-D spectroscopy [1]. However, we have also added something new. We have learned to use a low frequency (visible in our case) pulse as either the pump [2, 3] or probe [4] or both [5]. With a low frequency pump or probe, time resolution can arise through the many photon nature of the absorption [5] or through a coherent interaction [4]. With this mixed approach, we have made major advances. For example, using the "attosecond streak camera" [6, 7], we can time resolve the appearance of electrons from different bands in materials after attosecond pulse illumination [4]. We can also time resolve cascading recombination in atomic media (to mention but two of the recent advances [8]). This mixed approach may find natural applications in ultrafast terahertz spectroscopy.

Nonlinear optics is the second tradition from which attosecond science springs. Nonlinear optics is also a 50 year old sub-field of optical science. In fact, all ultrafast measurements are *of necessity* nonlinear. Since nonlinear optics is so fundamental to time resolved measurements, we should expect the development of non-perturbative nonlinear optics to open new measurement paradigms. In fact, this expectation is true. It allows attosecond pulses to be measured as they are being formed [9, 10]. Furthermore, non-perturbative nonlinear optics allows us to excite and observe unexpected phenomena. For example, we can time resolve tunnelling [11] or excite attosecond bound-state electronic wave packets in atoms [5, 12] or molecules [2] launched by tunnelling. We can image molecular orbital wavefunctions [13, 14], something that chemists are taught is conceptually impossible. New time-resolved spectroscopes are being developed that exploits this new nonlinearity [15–17].

The form of non-perturbative nonlinear optics that has led to attosecond pulse generation has a clear physical model—the "recollision" model [18, 19]. The success of the model is based on the control that a short, intense pulse can exert on an ionizing electron. The classical intuition that this model encourages has been very helpful. It suggests that control can go much deeper—to weakly bound electrons and perhaps even more strongly bound electrons. The better we control laser fields, the better we will control these electrons and through electrons, matter.

"Recollision" emphasizes a third tradition on which attosecond science can draw—one of the oldest fields of physics—collision physics. It is through collisions that science first learned about the structure of matter, from the structure of the atom, to the structure of the nucleus, to the structure of the proton. Therefore, through recollision, optics gains systematic access to this kind of structural information with spatial resolution appropriate to the collision energy range in which recollision operates. This includes atomic and molecular structure [20–22] and it will eventually include nuclear structure [23].

But it is not all a one-way street. Attosecond science offers two important tools to collision physics that were previously lacking. First, it offers the opportunity to time-resolve collision events [24, 25], something that was not systematically available previously. This may be particularly helpful for ultrafast studies of the dynamics in the atomic nucleus [23]. Secondly, since collisions can be timed with respect to optical pulses, collision physics gains access to the powerful pump-probe methods of optics. A pump pulse might initiate dynamics to be studied by delayed collisions or it might control the system—aligning or orienting molecules, for example, to simplify scattering.

The collision-inspired aspect of attosecond science offers us a very powerful dream. It should be possible to simultaneously make spatial and temporal measurements with spatial resolution on the interatomic (or even nuclear) scale and time resolution on the valence electron time scale [25, 26] or even, ultimately on the nuclear time scale.

Finally, the mathematics of short pulse formation and the technology of their generation require that attosecond pulses lie in the XUV or soft X-ray spectral region. This is the spectral region that synchrotrons opened for study about 30 years ago. Thus we can benefit from the 30 years of synchrotron experience. Using atomic specific resonances, and other related X-ray methods, we will be able to probe molecules or solids.

Of these grand traditions, attosecond science is not the only radically new "game-in-town". Just as femtosecond technology has given birth to attosecond technology, so also synchrotrons have given birth to free-electron lasers [27]. While each of these technical advances is important, when viewed together, it is clear that we are experiencing a historic advance in photonics technology whose ramifications we are only beginning to explore. One major task we have for the next decade is to step outside of our own field and identify those areas of science where we can have a major impact. There are many sub-fields to explore.

I would like to take this opportunity to very briefly highlight one specific new direction that work in my laboratory is opening—polar molecules [28–30], although there is no attosecond dynamics involved—in fact no dynamics at all except for the dynamics we impose by recollision. However, as I have argued, our tools can be applied much more broadly than to only study dynamics. If we can provide new insight into polar molecules—a class of molecules that are very important to chemistry—that is an equally important accomplishment.

**The Issue** Chemistry is highly directional. When reagents approach, they experience local fields that modify the collision and therefore the reaction. When at least one of the reagents is a polar molecule, then the reaction proceeds differently depending on the direction of approach of the reagents. This is the field of stereo chemistry. Can we offer new insight into polar molecules?

A re-collision electron is a natural and highly sensitive tool to study these local fields:

- It is charged.
- It is launched by directional tunnelling and it ends with a re-collision from the same direction.
- It can report on the recollision electron characteristics through the attosecond photons that it emits.
- We have powerful tools for measuring both the amplitude and the phase of the electron or the associated photons, allowing us to compare different sides of the molecule.

From these studies we will gain a detailed understanding of an electron tunnelling from each side of a molecule and also the local field structure around the molecule.

**The Technology** It is now feasible to orient polar molecules in a robust manner. Those interested in the approach are referred elsewhere [29, 30].

In oriented polar molecules, on alternate half-cycles of the laser field, the electron tunnels from one side of the molecule or the other. The subsequent motion of this electron wave packet is initially likewise restricted to one side for both the short trajectory electrons and the long trajectory electrons. Thus, both the ATI electrons and the attosecond pulse that they launch encode the natural asymmetry of the orbital, the Stark shift and the local electronic environment through which the electron departs. It is this asymmetry that is also responsible for stereo chemistry.

If the driving pulse were to gate an isolated attosecond pulse, then, as we change the carrier-envelope phase (CEP), we would change the re-collision direction and, in fact, the whole time structure of the attosecond pulse. The latter is the case, because the frequency dependent transition moment that describes recombination is different in both amplitude and phase for an electron recolliding from opposite directions [28].

If the driving pulse has multiple cycles, then the interference between subsequent attosecond pulses in the train create even harmonics as illustrated in Fig. 1.2 as the weak spectral lines between the stronger high harmonics (taken from [28]).

While these are early experiments we will soon be able to bring the full array of attosecond tools to bear on polar molecules.

## References

1. J.D. Hybl, A.A. Ferro, D.M. Jonas, J. Chem. Phys. **115**, 6606 (2001)
2. M. Uiberacker et al., Nature **446**, 627–632 (2007)

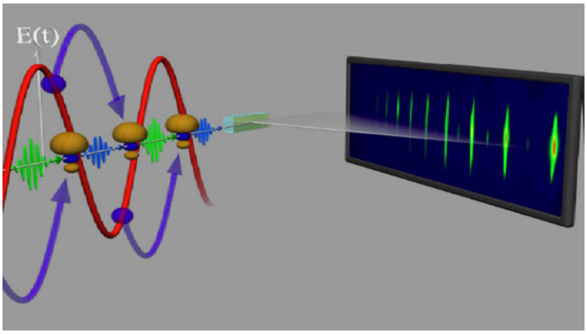

**Fig. 1.2** Illustration of high harmonic generation from CO molecules (taken from [28]). The asymmetry of CO leads to even harmonics as seen in the experimental spectrum that stretches from H15 *on the right* to H29 *on the left* are oriented

3. O. Smirnova et al., Nature **460**, 972–977 (2009)
4. A.L. Cavalieri et al., Nature **449**, 1029–1032 (2007)
5. A. Fleischer et al., Phys. Rev. Lett. **107**, 113003 (2011)
6. J. Itatani et al., Phys. Rev. Lett. **88**, 173903 (2002)
7. E. Constant et al., Phys. Rev. A **56**, 3870 (1997)
8. M. Drescher et al., Nature **419**, 803 (2002)
9. N. Dudovich et al., Nat. Phys. **2**, 781 (2006)
10. K.T. Kim et al., Nat. Phys. (2013). doi:10.1038/nphys2525
11. D. Shafir et al., Nature **485**, 343–346 (2012)
12. E. Goulielmakis et al., Nature **466**, 739–743 (2010)
13. J. Itatani et al., Nature **432**, 867 (2004)
14. C. Vozzi et al., Nat. Phys. **7**, 822–826 (2011)
15. W. Li et al., Science **322**, 1207–1211 (2008)
16. H.J. Wörner et al., Nature **466**, 604–607 (2010)
17. H.J. Wörner et al., Science **334**, 208 (2011)
18. P.B. Corkum, Phys. Rev. Lett. **71**, 1994 (1993)
19. M. Lewenstein et al., Phys. Rev. A **49**, 2117 (1994)
20. T. Zuo, A.D. Bandrauk, P.B. Corkum, Chem. Phys. Lett. **259**, 313 (1996)
21. M. Meckel et al., Science **320**, 1478 (2008)
22. C.I. Blaga et al., Nature **483**, 194 (2012)
23. N. Milosevic, P.B. Corkum, T. Brabec, Phys. Rev. Lett. **92**, 013002 (2004)
24. D. Zeidler et al., Phys. Rev. Lett. **95**, 203003 (2005)
25. H. Niikura et al., Nature **421**, 826 (2003)
26. S. Baker et al., Science **312**, 424 (2006)
27. P. Emma et al., Nat. Photonics **4**, 641–647 (2010)
28. E. Frumker et al., Phys. Rev. Lett. **109**, 233904 (2012)
29. M. Spanner et al., Phys. Rev. Lett. **109**, 113001 (2012)
30. E. Frumker et al., Phys. Rev. Lett. **109**, 113901 (2012)

# Part II

# Generation, Control and Characterization of Attosecond Pulses

# Chapter 2
# Theory of Attosecond Pulse Generation

**Mette B. Gaarde and Kenneth J. Schafer**

**Abstract** This chapter will discuss the theoretical aspects of producing attosecond pulses via the process of high harmonic generation driven by an intense infrared laser pulse. We will discuss the generation of attosecond pulses both at the single atom and at the macroscopic level, including a discussion of phase matching. Our goal is to broaden the understanding of attosecond pulse generation beyond the single atom level, where one thinks about the emission in terms of the laser-atom interaction alone, to include macroscopic aspects of this process.

## 2.1 Introduction

The rapidly growing field of attosecond science lies at the interface between ultrafast atomic physics and extreme non-linear optics. Attosecond pulses are the shortest bursts of light ever produced [1, 2], and allow for probing the dynamics of bound electrons on their natural time scales, the attosecond ($10^{-18}$ s) [3–7]. The production of a pulse with a duration of 100 as is a formidable scientific and technological task. Since light pulses must contain at least one optical cycle, and the period of 30 eV radiation is 138 as, it requires generating extreme ultraviolet (XUV) radiation spanning a bandwidth of about 20 eV. In addition, the amplitude and phase of the light must be tightly controlled to avoid temporal dispersion of the pulse. The process of high harmonic generation (HHG) driven by an intense, ultrafast laser pulse [8, 9] provides such a source and in this chapter we will discuss in detail the production of attosecond pulses via HHG. The attosecond pulses generated via this process result from an intricate balance between microscopic quantum mechanical effects at the level of the individual atom interacting with the laser pulse, and macroscopic phase matching of the driving pulse and the generated XUV radiation in the rapidly ionizing gas. This determines not only the yield but also the spatial and temporal coherence properties of the XUV radiation [10–12].

---

M.B. Gaarde (✉) · K.J. Schafer
Department of Physics and Astronomy, Louisiana State University, Baton Rouge,
LA 70803-4001, USA
e-mail: gaarde@phys.lsu.edu

K.J. Schafer
e-mail: schafer@phys.lsu.edu

L. Plaja et al. (eds.), *Attosecond Physics*, Springer Series in Optical Sciences 177,
DOI 10.1007/978-3-642-37623-8_2,

The full theoretical description of these strong field laser-matter interaction processes is the subject of this chapter. We will describe in detail how to perform "complete" calculations of attosecond pulse generation, by simultaneous solution of the time-dependent Schrödinger equation (TDSE) to describe the microscopic laser-atom interaction, and the Maxwell wave equation (MWE) to describe the macroscopic propagation and phase matching of the radiation. The theoretical methods described in this chapter have been well-validated by comparison to experiments as described in the references throughout. However, experimental results will be only minimally discussed in this chapter. Likewise, we will not discuss in any detail *specific* methods of producing attosecond pulses (isolated, or in trains). For more details we refer to Chaps. 3–6 in this book, or to review articles such as [13, 14].

In the remainder of this introductory section, we will discuss the conceptual understanding of the strong-field generation of high order harmonics and attosecond pulses by an atom provided by the semi-classical model [15, 16]. Then we go on to describing the single atom calculations in Sect. 2.2 and the macroscopic calculations, including phase matching, in Sect. 2.3.

In the semi-classical model the atom is presumed to have just one active electron which initially tunnel ionizes due to the strong field, next is accelerated as a free particle in the laser field, and upon returning to the ion core recombines to the ground state and gives up the energy gained from the laser field in the form of a high energy photon. If the driving laser pulse lasts several optical cycles the half-cycle periodicity of the process (corresponding to the emission of a periodic train of XUV pulses) means that only odd harmonics of the laser frequency will be emitted [1, 8–10, 17, 18], whereas a few-cycle pulse can give rise to a continuous emission spectrum resulting from a single recollision event [2, 3, 19–21].

Figure 2.1 illustrates the perspective of the semi-classical model. We show the results of classical trajectory calculations for an electron in an oscillating electric field of the form $E_0 \sin(\omega t)$ ($\omega$ is the IR laser frequency, and $T$ its optical period). The trajectory followed by an electron released into the continuum will depend on its time of release (ionization). For release times between zero and $T/4$ the electron never returns to the core (not shown in the figure), whereas for release times between $T/4$ and $T/2$ the electron will return to the core at different times with different kinetic energies, see Fig. 2.1(a). The return kinetic energies determines the range of photon energies which can be produced, up to the cutoff energy of $I_p + 3.2U_p$ [22], where the ponderomotive energy $U_p$ is the average quiver energy of an electron in the field, and $I_p$ is the ionization potential. For each energy below the cutoff energy there are two quantum paths that give rise to the same return kinetic energy; the long path where the electron is released early and returns to the core late, and the short path where the electron is released later and returns earlier [10, 23].

There is a natural attosecond time scale in the harmonic generation process since the emission of the high frequency radiation happens only during a fraction of the laser optical cycle. Figure 2.1(b) illustrates how one would synthesize attosecond pulses by selecting a broad range of photon energies from the harmonic spectrum. Because of the relationship between emission time and emission energy, this corresponds to a sub-cycle temporal gate during which XUV radiation will be emitted.

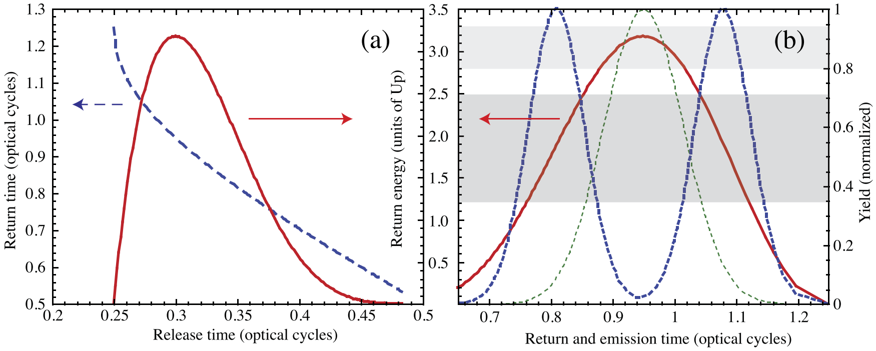

**Fig. 2.1** Classical calculations of electron trajectories in an oscillating electric field. In (**a**) we show return time (*left axis*) and return kinetic energy (*right axis*) as a function of release time, in (**b**) *the solid line* shows the return energy as a function of the return time, and *the dashed thick* (*thin*) *line* shows a schematic time profile of the attosecond pulses synthesized from the range of XUV energies selected by the *dark* (*light*) *grey*, *shaded area*

The simplest conceptual approach to attosecond pulse generation involves spectrally selecting photon energies around the harmonic cutoff energy (green shaded area) which are all emitted around the same time. The duration of the resulting attosecond pulse will be largely determined by the available bandwidth. If the driving pulse duration is short enough (less than two optical cycles) and its carrier envelope phase is chosen correctly this can give rise to an isolated few-hundred attosecond pulse. This has been successfully demonstrated in a number of experiments over the past decade [3, 19, 21].

Even shorter attosecond pulses can be produced by selecting a broader range of frequencies (blue shaded area in Fig. 2.1(b). At the single atom level this gives rise to two irregularly spaced attosecond bursts per half-cycle, corresponding to the return time of the short and long trajectories [10]. This is often the spectral range selected in experiments performed with multi-cycle driving pulses, resulting in a train of attosecond pulses.

Figure 2.2 shows the radiation spectrum and time profile of an argon atom exposed to an 800 nm laser pulse, calculated by numerical integration of the TDSE as described in more detail in Sect. 2.2.1. The results illustrate and confirm the conceptual understanding of the semi-classical model: The harmonic spectrum in Fig. 2.2(a) extends to a cutoff energy around the 30th harmonic (46 eV, corresponding to $I_p + 3.2U_p$ at a peak intensity of $1.6 \times 10^{14}$ W/cm$^2$), and the time profile of a range of harmonics from the plateau region (shaded area) consists of two attosecond bursts per half-cycle as illustrated in Fig. 2.2(b). The bursts corresponding to the “short” and “long” quantum paths are shown in different colors for clarity. In Fig. 2.2(c) we show a time-frequency analysis of the full time-dependent dipole radiation, see [24] for details. The semi-classical prediction for the return time and energy of the short and long trajectories is indicated in solid line and is in excellent agreement with the full quantum result.

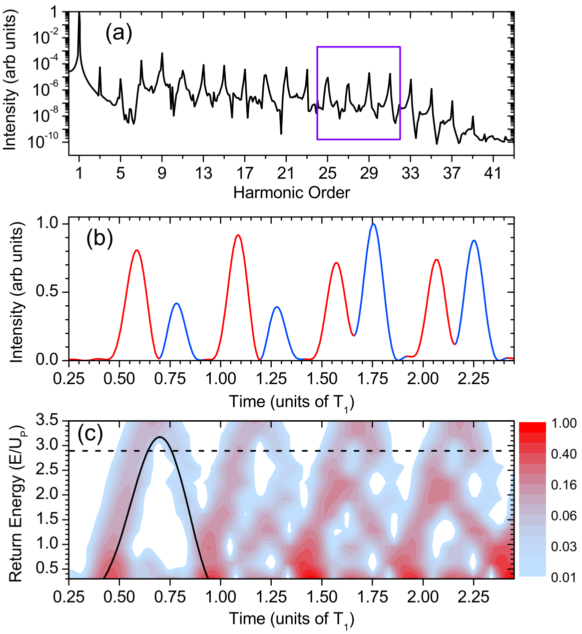

**Fig. 2.2** Time-resolved harmonic emission: (**a**) The single atom harmonic spectrum from an argon atom exposed to an 800 nm, $1.6 \times 10^{14}$ W/cm$^2$ laser pulse with a flat top time profile. (**b**) The time profile of the boxed part of the spectrum in (**a**). (**c**) Time-frequency analysis of the full time-dependent dipole radiation. *The solid black line* shows the semi-classical prediction for the return energy of the two shortest trajectories. *The dotted horizontal line* indicates the central frequency of the range of harmonics used to construct the pulse train shown in (**b**). Reprinted from [38]

There are several more interesting observations one can make from Fig. 2.2: (i) The time-frequency analysis in part (c) clearly shows that trajectories with return times longer than one cycle also contribute to the emission profile, and in fact often seem to dominate over the long-trajectory contribution. (ii) The individual attosecond pulses are chirped, with the highest XUV energies emitted later (earlier) than the lowest XUV energies for the short (long) trajectory. This is also apparent from Fig. 2.1(b) which shows that the return time increases (decreases) as the return energy increases for the short (long) trajectory. This *atto-chirp* of the individual attosecond pulses in an attosecond pulse train (APT) is approximately linear [25, 26] and must be compensated in order to make the shortest possible attosecond pulses. This can be done either via post-generation compression in a second medium [27, 28], or via group velocity dispersion during the generation process itself [29].

Finally, Fig. 2.2(b) clearly shows that the single atom emission, even after spectral filtering, bears little resemblance to a useable attosecond pulse, or attosecond pulse train. The XUV emission must therefore be additionally filtered through, for instance, phase matching, spatial gating or polarization gating in order to be a useful attosecond light source.

## 2.2 Single Atom Response

We start by describing the treatment of attosecond pulse generation, and more generally high harmonic generation, by a single atom interacting with an intense infrared laser field, linearly polarized along the $z$ axis. In this and the following sections we will work in the single active electron (SAE) approximation, in which the laser-atom interaction is described via the response of one active electron only. Our goal is to calculate the radiation spectrum of the atom caused by the laser pulse. At the macroscopic level this is given by the power spectrum of the generated electric field, $|\tilde{E}(\omega)|^2$, which we don't have access to at the single atom level. However, the source term of the generated radiation (in the wave equation) is proportional to the dipole spectrum $|\tilde{d}(\omega)|^2$ which can be calculated as the Fourier transform of the time-dependent single-atom dipole moment (using atomic units):

$$d(t) = -\langle \psi(t) | z | \psi(t) \rangle, \tag{2.1}$$

where $\psi(t)$ is the time-dependent wave function. From the radiation spectrum one can then obtain the time profile of some part of the radiation spectrum by applying a spectral filter in the form of a window function centered on some frequency $\omega_{XUV}$ and inverse Fourier transforming:

$$d_{XUV}(t) = \int \tilde{d}(\omega) W(\omega - \omega_{XUV}) \exp(i\omega t) d\omega. \tag{2.2}$$

The window function mimics the action of an experimental spectral filter that selects only a range of XUV frequencies.

To calculate the time-dependent wave function of the active electron in the strong field, we must solve the TDSE which in the dipole approximation and the length gauge has the form (in atomic units):

$$i \frac{\partial}{\partial t} |\psi(t)\rangle = \big(H_0 + E_L(t) z\big) |\psi(t)\rangle, \tag{2.3}$$

where $H_0$ is the field-free ion-valence electron Hamiltonian and $E_L(t)$ is the time-dependent laser electric field. In this chapter we will concentrate on calculations in which the laser field is linearly polarized along the $z$-direction, the most favorable condition for producing HHG. Polarization gating as a means of generating isolated attosecond pulses, using a laser field with a time-dependent polarization, will be discussed in Chap. 4.

Below we will describe two approaches to solving this TDSE. The numerical, grid-based solution of the TDSE (referred to as the SAE-TDSE below) in which the laser and atomic potentials are treated on an equal footing (see [30] for details), and the solution to the TDSE within the strong field approximation (SFA) as presented by Lewenstein et al. in [31].

### *2.2.1 Numerical Solution of the TDSE*

We restrict our discussion of grid-based numerical solutions of the TDSE to linear polarization. In three dimensions the interaction in the length gauge for a laser linearly polarized along the $z$ direction is proportional to $r\cos(\theta) \propto rY_1^0$ which strongly suggests that we expand the time-dependent state vector in a mixed basis of discrete radial functions times spherical harmonics:

$$\big|\psi(\mathbf{r},t)\big\rangle \to \sum_{\ell=|m|}^{\ell_{\max}} \psi_\ell(r_j,t)|\ell,m\rangle, \tag{2.4}$$

where $\langle\theta,\phi|\ell,m\rangle = Y_\ell^m(\theta,\phi)$ and $r_j$ is the $j$th radial grid point. For linear polarization the $m_\ell$ quantum number is conserved.

For three dimensional SAE calculations we use a one-electron pseudopotential that has as its ground state the valence state that we are interested in. The pseudopotential is constructed starting from an all-electron potential calculated using an atomic structure code. The all-electron potential is then modified to include the correct long-range Coulomb attraction. The valence orbital of angular momentum $\ell$ is then used to construct the $\ell$-dependent potential for that value of the angular momentum [32]. The potentials take the form

$$V(\mathbf{r}) = \sum_\ell V_\ell(r)|\ell\rangle\langle\ell| - 1/r \tag{2.5}$$

where the short range potentials $V_\ell$ can depend on the angular momentum of the electron as well as the radial distance. This form of the potential, which is non local in space, allows for great flexibility in treating different atomic systems when spherical coordinates are used.

To calculate the time-dependent wave function we start from a well defined initial state that is an eigenstate of the *discrete* field-free Hamiltonian. For the time integration we use a short-time approximation to the full (time-ordered) evolution operator. The wave function is propagated from time $t_n$ to time $t_{n+1} = t_n + \delta t$ via

$$\big|\psi(t_{n+1})\big\rangle = e^{-iH_{\bar{n}}\delta t}\big|\psi(t_n)\big\rangle. \tag{2.6}$$

where the Hamiltonian is evaluated at the intermediate time $t_n + \delta t/2$.

The Hamiltonian in the length gauge consists of two pieces, $H_0$, the atomic Hamiltonian which is diagonal in the $\ell$ quantum number, and the interaction piece, $H_I$, which couples the $\ell$ channels. Because of this splitting of $r$ and $\ell$ couplings, it is most convenient to use a "split-operator" expansion of the full short-time propagator which is unitary and correct to $\mathcal{O}(\delta t)^3$:

$$\psi(t+\delta t) = e^{-i(H_0+H_I)\delta t}\psi(t) \approx e^{-iH_I\delta t/2}e^{-iH_0\delta t}e^{-iH_I\delta t/2}\psi(t) \tag{2.7}$$

The action of the exponentials on the time-dependent wave function can not be calculated directly due to the non-diagonal nature of the matrices representing $H_0$ and $H_I$. We therefore resort to approximations to the full exponentials which are themselves unitary and correct to the same order in $\delta t$ as the split-operator method. Among many alternatives, perhaps the simplest is the Crank-Nicholson form [33]

$$e^{-iH_0\delta t} \approx [1 + iH_0\delta t/2]^{-1}[1 - iH_0\delta t/2] + \mathcal{O}(\delta t)^3. \tag{2.8}$$

The application of this operator requires the solution of a sparse set of linear equations at every time step, which can be accomplished very fast.

From the time-dependent wave function we can calculate the time-dependent dipole using Eq. (2.1). In practice, it is very hard to calculate the dipole moment directly from the time dependent wave function because of the form of the matrix element, which heavily weights the behavior of the electron far from the ion core. This means that small errors in the wave function propagation near the boundary show up as large errors in the time-dependent dipole. It is better to start by calculating the acceleration of the electron using the Ehrenfest theorem

$$a(t) = \frac{d^2}{dt^2}\langle z \rangle = -\big\langle \big[H, [H, z]\big]\big\rangle, \tag{2.9}$$

where $H$ is the full Hamiltonian including the laser interaction. The dipole strength is related to the Fourier transform of the acceleration, $\tilde{\mathcal{A}}(\omega)$, by

$$\tilde{\mathcal{D}}(\omega) = \tilde{\mathcal{A}}(\omega)/\omega^2. \tag{2.10}$$

Intuitively we expect the acceleration to be dominated by contributions from regions near the ion core where the electron experiences a large force. This weighting of the region close to the ion core helps make the calculation more tractable. That said, individual calculations of the HHG spectrum for a specific set of laser parameters are almost impossible to converge. There are two reasons for this. The first one is physical and stems from the fact that the individual harmonics in the spectrum are calculated as a coherent sum over several quantum pathways that lead to the same final emission energy. These individual contributions are rapidly varying with laser intensity, which means that very small changes in the laser parameters or the details of the calculation can lead to large changes in individual harmonics. Fortunately, such convergence is hardly warranted. What is of physical relevance is the highly nonlinear intensity scaling of the harmonic's amplitude and phase, and these *trends* can be converged with moderate effort.

The second reason HHG calculations are difficult to converge is numerical, and stems from reflections of the ionized wave packets from the grid boundary. The proper damping of these reflections is crucial for calculating, for example, the characteristic high energy cutoff of the spectrum. Because of the broad spectrum of energies that make up the wave packets, it is not possible to design optimal absorbing boundaries for the grid. Instead we use a very soft ($\cos^{1/8}$) mask function spread over several hundred grid points [34].

### 2.2.2 Solution of the TDSE Within the Strong Field Approximation

The strong field approximation allows for a relatively simple evaluation of the time-dependent dipole moment in the high-intensity, long-wavelength limit where the ponderomotive energy $U_p$ is much larger than the ionization potential $I_p$ [31]. To obtain an expression for the dipole moment, Lewenstein and collaborators make three basic approximations, very similar in spirit to those of the semi-classical model: (i) the only bound state that contributes to the strong field process is the ground state, (ii) the depletion of the ground state can be neglected (it must be put in by hand separately to account for ionization), and (iii) when in the continuum the electron can be treated as a free particle [31].

For a linearly polarized driving field $E_1(t) = f(t)\sin(\omega_1 t + \phi)$, with a time-dependent envelope $f(t)$, a carrier frequency $\omega_1$ and a carrier envelope phase $\phi$, one gets a time-dependent dipole moment (in atomic units):

$$\begin{aligned} d(t) = 2Re\biggl\{ i \int_{-\infty}^{t} dt' \biggl( \frac{\pi}{\epsilon + i(t-t')/2} \biggr)^{3/2} \\ \times d^*\bigl[p_{st}\bigl(t',t\bigr) + A(t)\bigr] d\bigl[p_{st}\bigl(t',t\bigr) + A\bigl(t'\bigr)\bigr] \\ \times \exp\bigl[-iS_{st}\bigl(t',t\bigr)\bigr] E_1\bigl(t'\bigr) \biggr\}, \end{aligned} \tag{2.11}$$

where $\epsilon$ is a small positive regularization constant, $A(t)$ is the vector potential associated with the electric field $E_1(t)$, and $d(p)$ is the field free dipole transition matrix element. For hydrogen-like atoms, $d(p)$ is given by [31]:

$$d(p) = i\frac{2^{7/2}(2I_p)^{5/4}}{\pi} \frac{p}{(p^2 + 2I_p)^3}, \tag{2.12}$$

where $I_p$ is the ionization potential.

The stationary values of the momentum $p_{st}(t',t)$ and action integral along the trajectory $S_{st}(t',t)$ are given by:

$$p_{st}\bigl(t',t\bigr) = \frac{1}{t'-t} \int_{t'}^{t} A\bigl(t''\bigr) dt'' \tag{2.13}$$

$$S_{st}\bigl(t',t\bigr) = \bigl(t-t'\bigr)\bigl(I_p - p_{st}^2/2\bigr) + \frac{1}{2} \int_{t'}^{t} A^2\bigl(t''\bigr) dt''. \tag{2.14}$$

As first proposed by Lewenstein et al. [31], one can interpret $d(t)$ as a sum over all possible quantum paths characterized by an electron tunnel ionizing at time $t'$, and returning to the core at time $t$ with kinetic energy $(p_{st}(t',t) + A(t))^2/2$. For return energies below the classical maximum of $3.17U_p$, the stationary action quantum paths in the SFA are similar to the returning electron trajectories in the semi-classical model [23, 25, 35, 36]. The two quantum paths with travel time $\tau$ less than one cycle dominate the SFA dipole response at most intensities. For a detailed comparison of the single atom response calculated within the SFA and the SAE-TDSE discussed in the previous section we refer to [37]. For a detailed discussion of the properties of attosecond pulses calculated using the SFA we refer to [26].

### *2.2.3 Time-Dependent Ionization Probability*

High harmonic and attosecond pulse generation are ionization driven processes that are initiated when an electron is promoted from the ground state to the continuum.

The effects of ionization on attosecond pulse generation can therefore not be altogether ignored. In particular, ionization affects attosecond pulse generation at the macroscopic level because it gives rise to a space- and time-dependent variation of the refractive index through the creation of free electrons in the medium. This affects the propagation of the laser pulse and generally the phase matching of the attosecond pulses, see for instance [38, 39].

At the single atom level, though, ionization does not play a major role. This is because the range of laser intensities used for attosecond pulse generation is such that substantial ionization only happens over a multi-cycle time interval. Over an attosecond pulse train, ionization may thus make a difference in the amplitude of the attosecond pulses in the trailing part of the train compared to the rising end of the train.

For a macroscopic calculation one usually needs either the time-dependent ionization probability, $p_{ion}(t)$, or the intensity dependent ionization rates, $\gamma(t)$, or both. They are related in the following way:

$$p_{ion}(t) = 1 - \mathrm{e}^{-\int_{-\infty}^{t} \gamma(t')dt'} \tag{2.15}$$

The ionization probability and/or rate can be calculated in at least two different ways. In a numerical solution of the SAE-TDSE, one has direct access to the time-dependent ionization probability via projection onto the (field free) ground state, $p_{ion}(t) = 1 - |\langle\psi(t)|\psi_0\rangle|^2$. However, this quantity is only meaningful when the oscillating laser electric field has zero amplitude (twice per optical cycle). In our calculations we usually calculate the time-dependent ionization probability from the fraction of the wave function which is located *spatially* outside a small volume around the core, typically a sphere of radius 12–15 atomic units. For details see [38]. Ionization rates can also be calculated within the tunneling approximation, for instance as proposed by Ammosov, Delone, and Krainov (ADK) [40]. In this formulation the ionization rate can be calculated as a function of the cycle-averaged laser intensity, or as a function of the instantaneous (oscillating) intensity. ADK rates are well known to overestimate the ionization probability at high intensities and ideally should be corrected, for instance as proposed by Ilkov and collaborators [41].

## 2.3 Macroscopic Response

To calculate the realistic time profile of attosecond XUV pulses which can be generated in an experiment one needs the full time- and space dependent electric field of the XUV radiation that emerges from the macroscopic generating medium. This involves solving the coupled MWE and TDSE, keeping track of the evolution of the laser and XUV electric fields as they propagate through the medium. This is a rather formidable task as we will describe in more detail below. However, a lot of insight into the macroscopic response can be gained by considering simple phase matching requirements.

The generated XUV electric field results from the coherent sum of the radiation from all the atoms in the non-linear medium, which interferes constructively mostly in the forward direction. By constructive interference we mean that the radiation generated at a position $z_2$ some distance into the non-linear medium must be in phase with the radiation that was generated at an earlier position $z_1 < z_2$ and then propagated to position $z_2$. In the most general terms, phase matching is the matching of the phase front of the newly generated field to the phase front of the propagating field, which mathematically can be expressed as

$$\mathbf{k}_{source} = \mathbf{k}_\omega, \quad \text{or} \quad \Delta\mathbf{k}_\omega = \mathbf{k}_\omega - \mathbf{k}_{source} = 0, \tag{2.16}$$

where $\mathbf{k}_\omega$ is the wave vector of the propagating field with angular frequency $\omega$ and $\mathbf{k}_{source}$ is the wave vector of the newly generated field which depends on the phase variation of the source term (the non-linear polarization field), $\mathbf{k}_{source} = \boldsymbol{\nabla}\phi_{source}(r,z)$. $\Delta\mathbf{k}_\omega$ is the phase mismatch.

For efficient generation of attosecond pulses one needs to additionally consider that it is not enough to have efficient phase matching of just one harmonic, but rather that it is necessary to simultaneously phase match and phase lock the whole range of harmonic energies that constitute the spectrum of the attosecond pulse. In the following we will discuss the most important elements of phase matching of attosecond pulses.

**Phase Matching in the Absence of Ionization and Dispersion** There is a range of experimental conditions for which one can think of phase matching without considering effects of ionization. These include when the laser intensity is safely below saturation, when the atomic density is low (few tens of Torr pressure), and the medium is short compared to the ionization-induced dephasing length. Then the two biggest contributions to $\phi_{source}(r,z)$ are the geometrical phase variation $\phi_{focus}(r,z)$ due to the focused laser beam, and the intrinsic intensity dependent phase $\phi_{dip}(r,z)$ of the dipole radiation, which we will describe in more detail below [23, 42–44]. In such conditions, we can write the phase matching requirement as (using cylindrical coordinates):

$$\mathbf{k}_{dip}(r,z) + \frac{\omega}{\omega_1}\big(\mathbf{k}_{focus}(r,z) + \mathbf{k}_1\big) = \mathbf{k}_\omega \tag{2.17}$$

where $\omega_1$ and $\mathbf{k}_1$ are the central frequency and wave vector of the laser light. Balcou et al. suggested that the phase mismatch $\Delta k_\omega(r,z)$ could be approximated by [44]:

$$\Delta k_\omega(r,z) = \frac{\omega}{c} - \left|\mathbf{k}_{dip}(r,z) + \frac{\omega}{\omega_1}\big(\mathbf{k}_{focus}(r,z) + \mathbf{k}_1\big)\right|. \tag{2.18}$$

This corresponds to requiring that the length of the propagating XUV light wave vector, which is chosen to be $\omega/c$, equals the length of the newly generated XUV light wave vector (which has had the dipole and the focusing phase imposed on it). Equation (2.18) also assumes that the XUV field predominantly propagates in the forward direction, and ignores linear dispersion.

For a Gaussian beam, the geometric phase variation is given by

$$\phi_{focus}(r,z) = -\tan^{-1}\left(\frac{2z}{b}\right) + \frac{2k_1 r^2 z}{b^2 + 4z^2}, \tag{2.19}$$

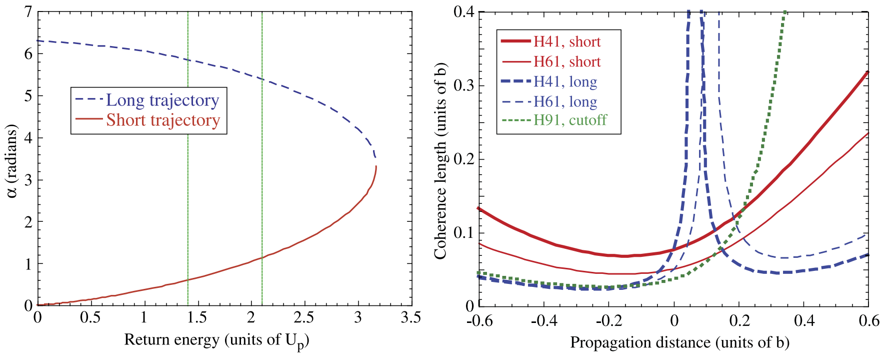

**Fig. 2.3** Quantum path contributions to the coherence length: (**a**) The phase coefficient $\alpha$ as a function of electron return energy, in units of $U_p/\omega_1$. (**b**) Coherence length for on-axis phase matching of the short (*solid lines*) and long (*dashed lines*) quantum path contributions to the 41st and 61st harmonics in neon generated at a peak intensity of $6.6 \times 10^{14}$ W/cm$^2$. Lengths are given in units of the confocal parameter $b$

where $b$ is the confocal parameter of the beam [45]. On axis ($r = 0$), this phase decreases monotonically from $\pi/2$ to $-\pi/2$, giving a negative contribution to the laser field wave vector.

The intrinsic phase, $\phi_{dip}(r, z)$, depends on $r$ and $z$ through its dependence on the laser field intensity, which can be understood within the quantum path description of the SFA and the semi-classical model [11, 23, 42]. The intrinsic phase is the phase accumulated by the electron wave packet during its acceleration by the laser field between time of release $t'$ and time of return $t$ and is given by the action integral:

$$\phi(t', t) = -\int_{t'}^{t} S(t'')dt'', \tag{2.20}$$

where $S(t'') = U_{kin}(t'') - U_{pot}(t'')$ is the classical action given by the difference between the kinetic and the potential energy. In the long pulse limit, the kinetic energy of the electron is proportional to $U_p \propto I/\omega_1^2$, with a proportionality constant $\alpha$ that depends on the time spent in the continuum. For a given electron trajectory $j$ we write the phase as $-\alpha_j U_p/\omega_1$ (in atomic units). The phase coefficient increases monotonically with the time spent in the continuum. A plot of $\alpha_j$ as a function of return energy for the two shortest electron trajectories is shown in Fig. 2.3(a), calculated for a monochromatic field as outlined in Eqs. (15)–(16) of [31].

Figure 2.3(a) shows that for each XUV energy in the plateau region, the different quantum path contributions to the dipole moment have different intensity dependent phases, each with a phase coefficient that changes with XUV energy. For a range of energies in the plateau region $\alpha_1$ (for the short trajectory) is small and $\alpha_2$ (long trajectory) is large, and for energies closer to the cutoff region the two phase coefficients become more similar.

The intensity dependent phase influences phase matching conditions through the spatial variation of the focused laser beam. Since the phase coefficient $\alpha$ is different for the two quantum path contributions to each harmonic, they will in general phase match differently [10, 46]. And since $\alpha$ varies with photon energy, different harmonics will experience slightly different phase matching conditions [25, 26, 29]. As a simple example, consider the phase matching condition in Eq. (2.18) along the axis of propagation only, for one quantum path contribution $j$ and one harmonic $\omega$:

$$\Delta k_\omega(z) = \alpha_j \frac{d(U_p/\omega_1)}{dz} + \frac{\omega}{\omega_1} \frac{2}{b(1+(2z/b)^2)}. \tag{2.21}$$

The second term (from the focused laser beam) is always positive so to achieve perfect phase matching on axis, we find the familiar result that we must place the non-linear medium after the laser focus ($z = 0$) where the intensity is decreasing with $z$, so that $dU_p/dz$ is negative.

This is illustrated in Fig. 2.3(b) for harmonic generation in neon driven by an 800 nm laser field with a peak intensity of $6.6 \times 10^{14}$ W/cm$^2$. We show the coherence length, defined as $L_{coh} = 2\pi/\Delta k_\omega$, for on-axis phase matching of the short and long quantum path contributions to the 41st and 61st harmonics. A long coherence length (small phase mismatch) corresponds to good phase matching. One can draw several interesting conclusions from this figure: (i) If the medium is placed close to $z = 0$ in Fig. 2.3(b), phase matching is much better for the long path contribution than for the short path contribution. In contrast, if the medium is placed close to $z = 0.5b$, phase matching prefers the short path contribution. Thus, phase matching can *separate the quantum path contributions* and thereby clean up the single atom pulse train which consists of two bursts per half-cycle as shown in Fig. 2.1. This was first proposed by Antoine and collaborators [10]. (ii) It is generally much easier to phase match a range of short trajectory harmonics (required to make an attosecond pulse) than it is to phase match a range of long trajectory harmonics. This is because, although the coherence length can be quite long for the long trajectory contribution, it changes rapidly in the medium, and is very sensitive to the harmonic order. In contrast, the short trajectory harmonics are much less sensitive both as a function of medium placement and as a function of harmonic order. This is in good agreement with experimental results in which APTs attributed to short trajectory harmonics have been readily detected whereas it has been much harder to isolate long trajectory harmonics, much less long trajectory APTs [1, 25, 47, 48]. (iii) Harmonics in the cutoff region, which are usually employed for the generation of single attosecond pulses, can also phase match quite well on axis, if the medium is placed after the center of the laser focus.

Equation (2.18) can more generally be used to consider phase matching both on axis and off axis by including the radial variation of the laser intensity and phase. For details we refer to the original work by Balcou et al. [44], or the more recent analysis by Chipperfield et al. [49]. A well known result of this type of analysis is that the contributions from the two different quantum paths are separated spatially because of phase matching, with the short path contribution giving rise to a mostly collimated XUV beam and the long path contribution giving rise to a mostly annular XUV beam. The two contributions can therefore be spatially separated in the far field by applying a spatial filter [1, 11, 46, 48]. Such a spatial filter thus represents another macroscopic temporal gate for cleaning up an APT so that it only consists of one (short trajectory) attosecond burst per half-cycle [1, 38].

**Phase Matching Including Dispersion and Ionization** When generating attosecond pulses at high photon energies, which generally also requires very high intensities, it is no longer justified to ignore effects of dispersion, in particular the dispersion caused by free electrons in the nonlinear medium [50–54]. Also, in long generating media such as gas cells or wave guides, dispersion and absorption from neutral atoms should not be ignored [29, 52, 55–58].

To first order, one can include the effects of dispersion in the phase mismatch equation (2.21) in the following way:

$$\Delta k_\omega(z) = \frac{\omega}{c}\Delta n_{at}(\omega) + \frac{\omega}{c}\Delta n_{el}(\omega) + \alpha_j \frac{dU_p/\omega_1}{dz} + \frac{\omega}{\omega_1}\frac{2}{b(1+(2z/b)^2)}, \quad (2.22)$$

where the difference in refractive index $\Delta n(\omega) = n(\omega) - n(\omega_1)$ is negative for the atomic contribution and positive for the free electron contribution.

One can even think about this phase matching equation in a time-dependent manner, especially if the dispersive terms dominate over the atomic and focusing terms (for instance for high photon energies and long generation geometries). During the laser pulse, the atomic/electron density will decrease/increase with time since $\Delta n_{at}(\omega)$ is proportional to $1 - P_{ion}(t)$ and $\Delta n_{el}(\omega)$ is proportional to $P_{ion}(t)$. Equation (2.22) then shows that there will be an optimal ionization fraction for a given phase matching configuration and a given range of photon energies, i.e. a given time during a pulse when phase matching will be optimized. Using phase matching as a temporal gate in this way has been explored by various groups as a means of shortening the XUV pulse duration [59–61].

More generally, the group of Murnane and Kapteyn have explored time-dependent one dimensional (1D) phase matching quite extensively in the context of generating XUV radiation inside capillaries, which are approximately 1D generation media. The phase mismatch in Eq. (2.22) then has an extra term due to the capillary mode. For an extensive review of phase matching and quasi phase matching in such a geometry see [61].

As a conclusion to this section on phase matching, let us note that although it is very useful to think about adiabatic phase matching requirements such as Eq. (2.22), the propagation of the laser field and the build-up of coherent XUV radiation in the macroscopic, ionizing medium is a process which is highly dynamical in both space and time. The space- and time-dependence of the freed electrons in the medium will cause the laser pulse to be spatio-temporally reshaped and acquire a shape in which the pulse is shorter and peaks earlier on axis, and has a longer tail off axis, see for instance [38, 39]. The resulting laser pulse can generate an isolated attosecond pulse via phase matching and farfield spatial filtering, even starting with an up to 10 fs long laser pulse [2, 62]. In the following section we outline a theoretical approach to describing these large-scale extremely non-linear dynamics and the XUV radiation that results from them.

### *2.3.1 Numerical Solution of the Propagation Equation*

We start from the MWE with source terms, written in the time domain as (using SI units):

$$\nabla^2 E(t) - \frac{1}{c^2}\frac{\partial^2}{\partial t^2}E(t) = \frac{1}{\epsilon_0 c^2}\frac{\partial^2}{\partial t^2}P(t). \tag{2.23}$$

$E(t)$ is the time-dependent electric field and $P(t)$ is the time-dependent polarization field representing for the moment all source terms for the driving and the generated field. Both $E(t)$ and $P(t)$ are functions of the cylindrical coordinates $r$ and $z$.

The solution of the full MWE (which is second order in both the longitudinal and the transverse directions) requires a very fine resolution in the propagation direction to account for both forward and backward propagating waves [63]. However, in the regime of interest for generation of harmonics and attosecond pulses, both the laser and the XUV radiation is strongly phase matched in the forward direction and one can in general safely ignore the backward propagating light. This is often done by transforming to a coordinate system that moves at the group velocity $v_g$ of the pulse, $z' = z, t' = t - z/v_g$ and applying the so-called slowly evolving wave approximation (SEWA) in which one assumes that the laser and XUV light changes slowly in the propagation direction compared to the wavelength (see [64]) for details. In contrast with the slowly varying envelope approximation, which also leads to a first order propagation equation in $z'$, the SEWA is valid for light pulses with durations as short as one optical cycle. Finally, after Fourier transforming with respect to $t'$ we get a frequency domain propagation equation:

$$\nabla_\perp^2 \tilde{E}(\omega) + \frac{2i\omega}{v_g}\frac{\partial \tilde{E}(\omega)}{\partial z'} + \left[\frac{\omega^2}{c^2} - \frac{\omega^2}{v_g^2}\right]\tilde{E}(\omega) = -\frac{\omega^2}{\epsilon_0 c^2}\tilde{P}(\omega). \tag{2.24}$$

The source term on the right hand side describes the response of the medium to the electric field and includes both linear and non-linear terms. The non-linear terms drive both the XUV generation through the dipole radiation and the non-linear effects of ionization on the laser field, whereas the linear terms describe absorption and dispersion of the laser and XUV radiation.

In the following we will describe two different approaches to solving Eq. (2.24), depending on whether we solve the SAE-TDSE as described in Sect. 2.2.1, or solve the TDSE using the SFA as described in Sect. 2.2.2.

#### 2.3.1.1 Source Terms Calculated Using the SAE-TDSE

It is particularly important to use an accurate description of the atomic response such as provided by the SAE-TDSE approach when one is interested in effects that have to do with atomic structure. Examples include the generation of XUV radiation near the ionization threshold [65] or the influence of the so-called Cooper minimum on the structure of the harmonic spectrum [66, 67]. In addition, this approach is absolutely necessary to address phenomena such as ultrafast transient absorption which requires one to describe absorption processes in a dynamical manner [7, 68, 69].

When we directly solve the SAE-TDSE the time-dependent dipole moment will contain information about the linear and non-linear response of the atom to the driving electric field. In particular, if the driving electric field includes XUV radiation, the dipole moment will also include terms that will lead to absorption and dispersion of the XUV radiation. The XUV radiation in the driving field could either be there to start with, if one is interested in harmonic or attosecond pulse generation performed in a IR+XUV two-color scheme [70–72], or it could result from build-up of the XUV radiation via HHG.

We solve Eq. (2.24) by space-marching through the ionizing non-linear medium, using a Crank-Nicholson scheme. We start with a driving electric field $E(r,t)$ which is a Gaussian beam in space, and a pulse with a finite extent in the time domain. In each plane $z$ in the propagation direction, we calculate the non-linear atomic response in the time-domain by solving the TDSE at each radial point $r$, using $E(r,t)$ as the driving field (see below). The time-dependent atomic response is used to calculate the frequency-dependent source terms in the wave equation, which are then used for marching to the next plane in $z$. We then calculate the new time-dependent driving field $E(r,t)$ at that $z$ as the inverse Fourier transform of $\tilde{E}(r,\omega)$, and so on. Note that $\tilde{E}(\omega)$ contains all the frequencies we are interested in, both the laser and the XUV frequencies. See [68] for more details.

The source term in Eq. (2.24) is a sum of two terms:

$$\tilde{P}(\omega) = \tilde{P}_{dip}(\omega) + \tilde{P}_{ion}(\omega). \tag{2.25}$$

The first term is given by the Fourier transform ($\widetilde{FT}$) of the time-dependent acceleration from Eq. (2.9) and the density of neutral atoms $N_a(t)$:

$$\tilde{P}_{dip}(\omega) = \widetilde{FT}\big[N_a(t)a(t)W(t)\big]/\omega^2. \tag{2.26}$$

The window function $W(t)$ serves the important numerical purpose of bringing the time-dependent source term to zero at the end of the time-axis in the calculation. It thereby also becomes a time-limit on the duration over which XUV radiation is absorbed in the calculation, which in turn gives rise to a minimum spectral bandwidth of absorption lines in the XUV spectrum. For details see [68]. The second term is due to the ionization of the medium and is calculated from the time-dependent current density $J(t) = \frac{\partial P_{ion}(t)}{\partial t}$ so that $-\frac{\omega^2}{\epsilon_0 c^2}\tilde{P}_{ion}(\omega) = \widetilde{FT}[\frac{1}{\epsilon_0 c^2}\frac{\partial J(t)}{\partial t}]$ [73]:

$$\frac{\partial J(t)}{\partial t} = \frac{e^2 N_e(t)}{m_e} E_1(t). \tag{2.27}$$

$N_e(t) = [1-[1-p_{ion}(t)]^2]N_a(t)$ is the time-dependent electron density for an atom with two $m=0$ electrons, and $p_{ion}(t)$ is the one-electron ionization probability calculated from the spatial distribution of the one-electron wave function as described in Sect. 2.2.3. $\tilde{P}_{ion}(\omega)$ gives rise to a spatial and temporal variation of the refractive index, which in turn causes defocusing and self-phase modulation and gives rise to

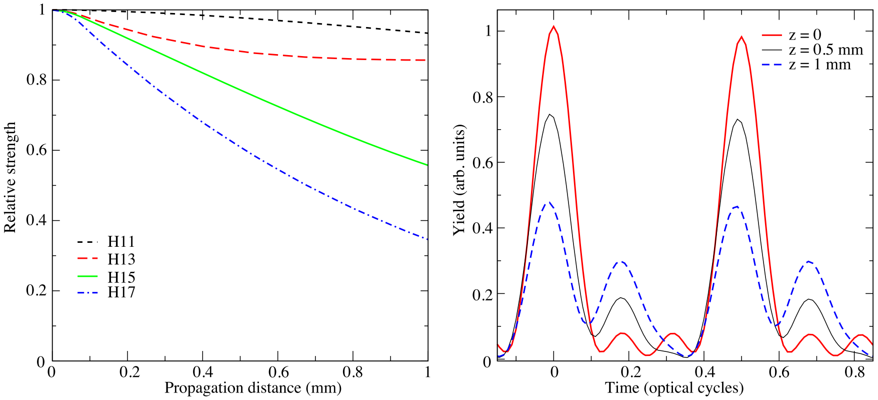

**Fig. 2.4** The effect of absorption on an APT. (**a**) shows the strength of harmonics 11 through 17 as a function of propagation distance through a 1 mm gas of helium atoms with a density of $1.5 \times 10^{18}$ cm$^{-3}$, (**b**) shows the time structure of the APT at the beginning, middle, and end of the gas jet

an additional phase mismatch in the propagation of the harmonics relative to the driving field. As we discussed above, this term can be very important for how the spatio-temporal shape of the laser electric field evolves during propagation through the non-linear medium, especially in situations where the laser intensity and/or the atomic density is high, or when the driving pulse is very short.

As a final comment on the source term, we have found that it is not numerically stable to include $\tilde{P}_{dip}(\omega)$ for frequencies around the driving laser frequency. Typically we substitute the SAE-TDSE response by $\epsilon_0\tilde{\chi}(\omega)\tilde{E}(\omega)$ for frequencies between zero and approximately $2\omega_1$.

Figure 2.4 illustrates the effect of propagation on the time structure of an attosecond pulse train in a 1 mm long helium gas with a pressure of 45 Torr. The driving pulse in this calculation consists of harmonics 11 through 17, which are initially in phase and have identical amplitudes. An IR field with a modest peak intensity of $10^{13}$ W/cm$^2$ is also present but is too weak to generate harmonics on its own. Figure 2.4(a) shows how the different harmonics are absorbed at different rates, with the 15th and 17th harmonic being substantially depleted by the end of the medium. Figure 2.4(b) shows how this changes the time structure of the attosecond pulse train from being a regular one-burst-per-half-cycle APT to having two bursts per half-cycle.

### 2.3.1.2 Source Terms Calculated Using the SFA

When using the SFA to provide the non-linear source terms for the propagation equation, it is necessary to separate the polarization field into its linear and non-linear components $\tilde{P}(\omega) = \epsilon_0\tilde{\chi}(\omega)\tilde{E}(\omega) + \tilde{P}_{NL}(\omega)$, where the linear susceptibility

$\tilde{\chi}(\omega)$ includes both linear dispersion and absorption through its real and imaginary parts. This is because the dipole moment calculated within the SFA only gives a good description of the *non-linear* response. The linear response has to be included via tabulated frequency dependent values of dispersion and absorption coefficients. To be consistent, we must also separate the propagation equations for the laser $\tilde{E}_1(\omega)$ and the generated XUV fields $\tilde{E}_h(\omega)$, so that the XUV fields are not ever included in the driving field (and thereby allowed to generate more XUV radiation through the SFA-TDSE solution). This treatment yields two propagation equations (now dropping primes on the $z$-coordinate):

$$\nabla_\perp^2 \tilde{E}_1(\omega) + \frac{2i\omega}{c}\frac{\partial \tilde{E}_1(\omega)}{\partial z} = -\frac{\omega^2}{\epsilon_0 c^2}\tilde{P}_{ion}(\omega) \tag{2.28}$$

$$\nabla_\perp^2 \tilde{E}_h(\omega) + \frac{2i\omega}{c}\frac{\partial \tilde{E}_h(\omega)}{\partial z} + \tilde{f}_{lin}(\omega)\tilde{E}_h(\omega) = -\frac{\omega^2}{\epsilon_0 c^2}\tilde{P}_{dip}(\omega). \tag{2.29}$$

The function $\tilde{f}_{lin}(\omega)$ includes the linear response and has the form:

$$\tilde{f}_{lin}(\omega) = i\frac{\omega}{c}\tilde{\alpha}(\omega) + \frac{\tilde{n}^2(\omega)\omega^2}{c^2} - \frac{\omega^2}{v_g^2}, \tag{2.30}$$

where $\tilde{\alpha}(\omega)$ and $\tilde{n}(\omega)$ are the absorption coefficient and refractive index, respectively, and can be found in the literature [74–76]. Both of these are proportional to the density of neutral atoms. The source term for the XUV fields, $\tilde{P}_{dip}(\omega)$, is calculated in analogy with the SAE-TDSE case:

$$\tilde{P}_{dip}(\omega) = \widetilde{FT}\big[N_a(t)d(t)W(t)\big], \tag{2.31}$$

where $d(t)$ is the time-dependent dipole moment evaluated using the SFA formalism. The driving field source term, $\tilde{P}_{ion}(\omega)$, is calculated as in Eq. (2.27), using intensity dependent ionization rates to calculate the electron density.

An SFA-based TDSE-MWE solver has been employed by a number of groups and has been generally very successful in reproducing many different types of experimental results on the production of attosecond pulses, see for instance [42, 54, 62, 77–81]. An SFA-MWE calculation can provide an excellent qualitative understanding of many attosecond pulse generation experiments and in some cases also quantitative comparisons. However, it cannot be used for experiments in which sub-cycle or multi-frequency absorption is important (such as recently investigated in [69]) as shown in Fig. 2.4, and more generally where close-to-threshold XUV frequencies dominate [29, 65]. It is also questionable how well an SFA-based calculation could work for attosecond pulses generated by mid-infrared (MIR) wavelength lasers. SAE-TDSE based calculations have found that the MIR-driven dipole moment has surprisingly large contributions from quantum paths longer than one optical cycle, something which is not well reproduced by the SFA [24]. In such cases it becomes necessary to perform first principles calculations of the attosecond pulse generation and absorption process, such as presented by the SAE-TDSE based MWE solver described above.

## 2.4 Summary and Outlook

In this chapter we have described in detail how to perform calculations of attosecond pulse generation in atomic gases, both at the microscopic, quantum level, and at the macroscopic level. The coupled solutions of the TDSE-MWE have been validated in a number of theory-experiment comparisons and are flexible enough to describe a number of different generation scenarios in terms of different driving fields, different experimental geometries, and different levels of sophistication in the model for the atomic response. A fruitful extension of this formalism, based on a single active electron description, would be the ability to fully understand and model attosecond transient absorption. This work is currently in progress [68, 82].

Finally, a grand-challenge level problem in the theory of attosecond physics is to move beyond atomic systems and potentially even beyond the single active electron approximation, both at the single-emitter level and at the macroscopic level. A number of groups are working on this problem. The macroscopic harmonic generation signal from a gas of molecules has been calculated within the SAE approximation by coupling an MWE solver to either a grid-based TDSE solution [83], or the so-called quantitative rescattering theory TDSE solution [84]. Recently, a few groups have attempted to calculate harmonic generation from systems with more than one active electron, and have in particular included electron correlations [85–89]. Macroscopic effects for HHG in multielectron systems, or in high-density systems such as crystals or nano-structures, have yet to be explored. Within current computational resources, such effects can only be explored using model descriptions of either the quantum or macroscopic response.

## References

1. P.M. Paul, E.S. Toma, P. Breger, G. Mullot, F. Augé, P. Balcou, H.G. Muller, P. Agostini, Science **292**, 1689 (2001)
2. M. Hentschel, R. Kienberger, C. Spielmann, G.A. Reider, N. Milosevic, T. Brabec, P. Corkum, U. Heinzmann, M. Drescher, F. Krausz, Nature **414**, 509 (2001)
3. R. Kienberger, E. Goulielmakis, M. Uiberacker, A. Baltuska, V. Yakovlev, F. Bammer, A. Scrinzi, T. Westerwalbesloh, U. Kleineberg, U. Heinzmann, M. Drescher, F. Krausz, Nature **427**, 817 (2004)
4. T. Remetter, P. Johnsson, J. Mauritsson, K. Varjú, F.L.Y. Ni, E. Gustafsson, M. Kling, J. Khan, R. López-Martens, K.J. Schafer, M.J.J. Vrakking, A. L'Huillier, Nat. Phys. **2**, 323 (2006)
5. M. Uiberacker, T. Uphues, M. Schultze, A.J. Verhoef, V. Yakovlev, M.F. Kling, J. Rauschenberger, N.M. Kabachnik, H. Schroder, M. Lezius, K.L. Kompa, H.G. Muller, M.J.J. Vrakking, S. Hendel, U. Kleineberg, U. Heinzmann, M.D.F. Krausz, Nature **446**, 627 (2007)
6. J. Mauritsson, P. Johnsson, E. Gustafsson, M. Swoboda, T. Ruchon, A. L'Huillier, K.J. Schafer, Phys. Rev. Lett. **100**, 073003 (2008)
7. E. Goulielmakis, Z.H. Loh, A.A. Wirth, R. Santra, N. Rohringer, V. Yakovlev, S. Zherebtsov, T. Pfeifer, A. Azzeer, M. Kling, S.R. Leone, F. Krausz, Nature **466**, 739 (2010)
8. A. McPherson, G. Gibson, H. Jara, U. Johann, T.S. Luk, I.A. Mclntyre, K. Boyer, C.K. Rhodes, J. Opt. Soc. Am. B **4**, 595 (1987)
9. M. Ferray, A. L'Huillier, X.F. Li, L.A. Lomreé, G. Mainfray, C. Manus, J. Phys. B **21**, L31 (1988)

10. P. Antoine, A. L'Huillier, M. Lewenstein, Phys. Rev. Lett. **77**, 1234 (1996)
11. M.B. Gaarde, F. Salin, E. Constant, P. Balcou, K.J. Schafer, K.C. Kulander, A. L'Huillier, Phys. Rev. A **59**, 1367 (1999)
12. E. Seres, J. Seres, F. Krausz, C. Spielmann, Phys. Rev. Lett. **92**, 163002 (2004)
13. P. Agostini, L.F. DiMauro, Rep. Prog. Phys. **67**, 813 (2004)
14. P.B. Corkum, F. Krausz, Nat. Phys. **3**, 381 (2007)
15. K.J. Schafer, B. Yang, L.F. DiMauro, K.C. Kulander, Phys. Rev. Lett. **70**, 1599 (1993)
16. P.B. Corkum, Phys. Rev. Lett. **71**, 1994 (1993)
17. S. Harris, J.J. Macklin, T.W. Hänsch, Opt. Commun. **100**, 487 (1993)
18. G. Farkas, C. Tóth, Phys. Lett. A **168**, 447 (1992)
19. I.P. Christov, M.M. Murnane, H.C. Kapteyn, Phys. Rev. Lett. **78**, 1251 (1997)
20. M. Drescher, M. Hentschel, R. Kienberger, G. Tempea, C. Spielmann, G.A. Reider, P.B. Corkum, F. Krausz, Science **291**, 1923 (2001)
21. J. Seres, E. Seres, A.J. Verhoef, G. Tempea, C. Streli, P. Wobrauschek, V. Yakovlev, A. Scrinzi, C. Spielmann, F. Krausz, Nature **433**, 596 (2005)
22. J.L. Krause, K.J. Schafer, K.C. Kulander, Phys. Rev. Lett. **68**, 3535 (1992)
23. M. Lewenstein, P. Salières, A. L'Huillier, Phys. Rev. A **52**, 4747 (1995)
24. J. Tate, T. Auguste, H.G. Muller, P. Salières, P. Agostini, L.F. DiMauro, Phys. Rev. Lett. **98**, 013901 (2007)
25. Y. Mairesse, A. de Bohan, L.J. Frasinski, H. Merdjo, L.C. Dinu, P. Monticourt, P. Breger, M. Kovačev, R. Taíeb, B. Carré, H.G. Muller, P. Agostini, P. Salières, Science **302**, 1540 (2003)
26. K. Varjú, Y. Mairesse, B. Carré, M.B. Gaarde, P. Johnsson, S. Kazamias, R. Lopez-Martens, J. Mauritsson, K.J. Schafer, P. Balcou, A. L'Huillier, P. Salières, J. Mod. Opt. **52**, 379 (2005)
27. R. López-Martens, K. Varjú, P. Johnsson, J. Mauritsson, Y. Mairesse, P. Salières, M.B. Gaarde, K.J. Schafer, A. Persson, S. Svanberg, C.G. Wahlström, A. L'Huillier, Phys. Rev. Lett. **94**, 033001 (2005)
28. D.H. Ko, K.T. Kim, J. Park, J.H. Lee, C.H. Nam, New J. Phys. **12**, 063008 (2010)
29. T. Ruchon, C.P. Hauri, K. Varjú, E. Mansten, M. Swoboda, R. López-Martens, A. L'Huillier, New J. Phys. **10**, 025027 (2008)
30. K.J. Schafer, in *Strong Field Laser Physics*, ed. by T. Brabec (Springer, New York, 2008), p. 111
31. M. Lewenstein, P. Balcou, M.Y. Ivanov, A. L'Huillier, P.B. Corkum, Phys. Rev. A **49**, 2117 (1994)
32. K.C. Kulander, T.N. Rescigno, Comput. Phys. Commun. **63**, 523 (1991)
33. J.L. Krause, K.J. Schafer, J. Phys. Chem. A **103**, 10118 (1999)
34. J.L. Krause, K.J. Schafer, K.C. Kulander, Phys. Rev. A **45**, 4998 (1992)
35. P. Salières, B. Carré, L.L. Déroff, F. Grasbon, G.G. Paulus, H. Walther, R. Kopold, W. Becker, D.B. Milošević, A. Sanpera, M. Lewenstein, Science **292**, 902 (2001)
36. N. Dudovich, O. Smirnova, J. Levesque, Y. Mairesse, M.Y. Ivanov, D.M. Villeneuve, P.B. Corkum, Nat. Phys. **2**, 781 (2006)
37. M.B. Gaarde, K.J. Schafer, Phys. Rev. A **65**, 031406(R) (2002)
38. M.B. Gaarde, J.L. Tate, K.J. Schafer, J. Phys. B **41**, 132001 (2008)
39. V. Tosa, K. Kim, C. Nam, Phys. Rev. A **79**, 043828 (2009)
40. M.V. Ammosov, N.B. Delone, V.P. Krainov, Sov. Phys. JETP **64**, 1191 (1986)
41. F.A. Ilkov, J.E. Decker, S.L. Chin, J. Phys. B **25**, 4005 (1992)
42. P. Salières, A. L'Huillier, M. Lewenstein, Phys. Rev. Lett. **74**, 3776 (1995)
43. A. L'Huillier, T. Auguste, P. Balcou, B. Carré, P. Monot, P. Salières, C. Altucci, M.B. Gaarde, J. Larsson, E. Mevel, T. Starczewski, S. Sveanberg, C.G. Wahlström, R. Zerne, K.S. Budil, T. Ditmire, M.D. Perry, J. Nonlinear Opt. Phys. Mater. **4**, 647 (1995)
44. P. Balcou, P. Salières, A. L'Huillier, M. Lewenstein, Phys. Rev. A **55**, 3204 (1997)
45. P.W. Milonni, J.H. Eberly, *Lasers* (Wiley, New York, 1988)
46. M. Bellini, C. Lyngå, A. Tozzi, M.B. Gaarde, T.W. Hänsch, A. L'Huillier, C.G. Wahlström, Phys. Rev. Lett. **81**, 297 (1998)

47. G. Sansone, E. Benedetti, J.P. Caumes, S. Stagira, C. Vozzi, S.D. Silvestri, M. Nisoli, Phys. Rev. A **73**, 053408 (2006)
48. A. Zair, M. Holler, A. Guandalini, F. Schapper, J. Biegert, L. Gallmann, U. Keller, A.S. Wyatt, A. Monmayrant, I.A. Walmsley, E. Cormier, T. Auguste, J.P. Caumes, P. Salieres, Phys. Rev. Lett. **100**, 143902 (2008)
49. L. Chipperfield, P. Knight, J. Tisch, J. Marangos, Opt. Commun. **264**, 494 (2006)
50. G. Tempea, M. Geissler, M. Schnürer, T. Brabec, Phys. Rev. Lett. **84**, 4329 (2000)
51. M. Geissler, G. Tempea, T. Brabec, Phys. Rev. A **62**, 033817 (2000)
52. E.A. Gibson, A. Paul, N. Wagner, R. Tobey, D. Gaudiosi, S. Backus, I.P. Christov, A. Aquila, E.M. Gullikson, D.T. Attwood, M.M. Murnane, H.C. Kapteyn, Science **302**, 95 (2003)
53. E. Seres, J. Seres, C. Spielmann, Appl. Phys. Lett. **89**, 181919 (2006)
54. V.S. Yakovlev, M. Ivanov, F. Krausz, Opt. Express **15**, 15351 (2007)
55. I. Christov, H. Kapteyn, M. Murnane, Opt. Express **7**, 362 (2000)
56. A. Paul, R.A. Bartels, R. Tobey, H. Green, S. Weiman, I.P. Christov, M.M. Murnane, H.C. Kapteyn, S. Backus, Nature **421**, 51 (2003)
57. E. Constant, D. Garzella, P. Breger, E. Mével, C. Dorrer, C.L. Blanc, F. Salin, P. Agostini, Phys. Rev. Lett. **82**, 1668 (1999)
58. J.F. Hergott, M. Kovacev, H. Merdji, C. Hubert, Y. Mairesse, E. Jean, P. Breger, P. Agostini, B. Carré, P. Salières, Phys. Rev. A **66**, 021801 (2002)
59. A.S. Sandhu, E.E. Gagnon, A. Paul, I. Thomann, A. Lytle, T. Keep, M.M. Murnane, H.C. Kapteyn, I.P. Christov, Phys. Rev. A **74**, 061803 (2006)
60. M.J. Abel, T. Pfeifer, P.M. Nagel, W. Boutu, M.J. Bell, C.P. Steiner, D.M. Neumark, S.R. Leone, Chem. Phys. **366**, 9 (2009)
61. T. Popmintchev, M.C. Chang, P. Arpin, M.M. Murnane, H.C. Kapteyn, Nat. Photonics **4**, 822 (2010)
62. M.B. Gaarde, K.J. Schafer, Opt. Lett. **31**, 3188 (2006)
63. E. Lorin, S. Chelkowski, A.D. Bandrauk, Comput. Phys. Commun. **177**, 908 (2007)
64. T. Brabec, F. Krausz, Rev. Mod. Phys. **72**, 545 (2000)
65. D.C. Yost, T.R. Schibli, J. Ye, J.L. Tate, J. Hostetter, M.B. Gaarde, K.J. Schafer, Nat. Phys. **5**, 815 (2009)
66. H.J. Wörner, H. Niikura, J.B. Bertrand, P.B. Corkum, D.M. Villeneuve, Phys. Rev. Lett. **102**, 103901 (2009)
67. J.P. Farrell, L.S. Spector, B.K. McFarland, P.H. Bucksbaum, M. Gühr, M.B. Gaarde, K.J. Schafer, Phys. Rev. A **83**, 023420 (2011)
68. M.B. Gaarde, C. Buth, J.L. Tate, K.J. Schafer, Phys. Rev. A **83**, 013419 (2011)
69. M. Holler, F. Schapper, L. Gallmann, U. Keller, Phys. Rev. Lett. **106**, 123601 (2011)
70. K.J. Schafer, M.B. Gaarde, A. Heinrich, J. Biegert, U. Keller, Phys. Rev. Lett. **92**, 023003 (2004)
71. J. Biegert, A. Heinrich, C.P. Hauri, W. Kornelis, P. Schlup, M. Anscombe, K.J. Schafer, M.B. Gaarde, U. Keller, Laser Phys. **15**, 899 (2005)
72. G. Gademann, F. Kelkensberg, W.K. Siu, P. Johnsson, K.J. Schafer, M.B. Gaarde, M.J.J. Vrakking, New J. Phys. **13**, 033002 (2011)
73. S.C. Rae, K. Burnett, Phys. Rev. A **46**, 1084 (1992)
74. A. L'Huillier, X.F. Li, L.A. Lompré, J. Opt. Soc. Am. B, Opt. Phys. **7**, 527 (1990)
75. B. Henke, E. Gullikson, J. Davis, At. Data Nucl. Data Tables **54**, 181 (1993)
76. C.T. Chantler, J. Phys. Chem. Ref. Data **24**, 71–591 (1995)
77. E. Priori, G. Cerullo, M. Nisoli, S. Stagira, S.D. Silvestri, P. Villoresi, L. Poletto, P. Ceccherini, C. Altucci, R. Bruzzese, C. de Lisio, Phys. Rev. A **61**, 063801 (2000)
78. C. Altucci, V. Tosa, R. Velotta, Phys. Rev. A **75**, 061401R (2007)
79. J. Seres, V.S. Yakovlev, E. Seres, C. Streli, P. Wobrauschek, C. Spielmann, F. Krausz, Nat. Phys. **3**, 878 (2007)
80. Z. Chang, Phys. Rev. A **76**, 051403R (2007)
81. S. Gilbertson, S.D. Khan, Y. Wu, M. Chini, Z. Chang, Phys. Rev. Lett. **105**, 093902 (2010)
82. S. Chen, K.J. Schafer, M.B. Gaarde, Opt. Lett. **37**, 2211 (2012)

83. E. Lorin, S. Chelkowski, A.D. Bandrauk, New J. Phys. **10**, 025033 (2008)
84. C. Jin, A.H. Le, C.D. Lin, Phys. Rev. A **83**, 023411 (2011)
85. D.A. Telnov, S.I. Chu, Phys. Rev. A **80**, 043412 (2009)
86. J.M.N. Djiokap, A.F. Starace, Phys. Rev. A **84**, 013404 (2011)
87. A.D. Shiner, B.E. Schmidt, C. Trallero-Herrero, H.J. Woerner, S. Patchkovskii, P.B. Corkum, J.C. Kieffer, F. Legare, D.M. Villeneuve, Nat. Phys. **7**, 464 (2011)
88. E.P. Fowe, A.D. Bandrauk, Phys. Rev. A **84**, 035402 (2011)
89. D.S. Tchitchekova, H. Lu, S. Chelkowski, A.D. Bandrauk, J. Phys. B **44**, 065601 (2011)

# Chapter 3
# Perspectives for the Generation of Intense Isolated Attosecond Pulses at Ultra-high Laser Intensities

**J.A. Pérez-Hernández and L. Roso**

**Abstract** Attosecond pulses result from the Fourier synthesis of the higher frequency part of the harmonic spectra, emitted by atoms, ions and molecules interacting with strong lasers. Therefore, their characteristics (central wavelength, width and dispersion) depend on the particular relation of the spectral phase and amplitudes between successive high harmonics. In this chapter we will expose the particular features of the harmonic spectrum generated with intensities well above saturation where the harmonic spectra is expected to be degraded by the fast ionization of the atoms. However, we shall see how for the case of laser pulses with non-adiabatic turn-on interacting with a single atom, the harmonic efficiency is recovered for sufficiently high intensities. Our study combines classical analysis and full quantum description via numerical integration of 3-Dimensional Time Dependent Schrödinger Equation. Results presented here reveals that non-adiabatic pulses with intensities well above the saturation threshold open the door for a new pathway for XUV coherent light generation through high-order harmonic generation providing a potential tool to obtain intense isolated attosecond pulses.

## 3.1 Introduction

Nowadays trains of intense attosecond pulses are routinely produced. However, the generation of isolated attosecond pulses remains a key challenge and this relies on our capacity to control a broad range of parameters, some of them not easy to set. In this chapter we shall show a tentative approach which raises the possibility to synthesize intense isolated attosecond pulses beyond the conventional procedure. Our starting point is a detailed description of the underlying electron dynamics during the fast turn-on of different laser pulses. For this goal, different approaches will be carried out. On the one hand, classical analysis reveal that under specific conditions,

---

J.A. Pérez-Hernández · L. Roso (✉)
Centro de Láseres Pulsados CLPU, 37008 Salamanca, Spain
e-mail: roso@usal.es

J.A. Pérez-Hernández
e-mail: joseap@usal.es

L. Plaja et al. (eds.), *Attosecond Physics*, Springer Series in Optical Sciences 177,
DOI 10.1007/978-3-642-37623-8_3,

a new kind of trajectories emerges in the turn-on which recombine efficiently in less than one optical cycle. These trajectories are different from the conventional, so-called "long" and "short". In the following, we will refer to these as Non Adiabatic Turn-on (NAT) trajectories.

On the other hand, a single-atom numerical simulations based on the exact integration of the 3 Dimensional Time Dependent Schrödinger Equation (3D TDSE) confirms that this new kind of trajectories are responsible for the unexpected growth of the harmonic yield when the laser intensity is increased up to two order of magnitude beyond the saturation limit. This fact contradicts the general belief of a progressive degradation of the harmonic efficiency due to the effect of the barrier suppression, based on the experience with pulses with smoother turn-on.

Additionally, at this high intensity regime, a complete depletion of the neutral atom population occurs on the leading edge of the driving laser pulse. As we will expose later, these two facts: the increase of the harmonic yield at high intensity together with the fast depopulation of the ground state, provide a potential method to synthesize intense and narrow isolated attosecond pulses.

## 3.2 Attosecond Pulses Production via High-Order Harmonic Generation

In the early nineties Farkas and Tóth, in a pioneering theoretical work, suggest the possibility to synthesize pulses of near to attosecond duration based on the multiple harmonic generation in gases [1]. In this paper, they also remark:

> *"…the described idea and technique seems to be realizable in all nonlinear processes, where high harmonic generation takes place, … ".*

These predictions have been gradually confirmed by a large number of experiments carried out later [2–7]. In light of these facts, nowadays, high-order harmonic generation (HHG) constitutes the most adequate way to generate attosecond pulses. For this reason, a great part of this chapter is focused on the study of the HHG as a source of attosecond pulses.

HHG process was observed in the eighties by McPherson et al. [8] and Ferray et al. [9] when an intense infrared laser pulse was focused into a jet of rare gas, generating a comb of odd harmonics, whose amplitudes approximately equal over a large spectral range, forming a "plateau", followed by an abrupt decrease, the "cutoff" region. These results also confirmed that HHG is clearly a non perturbative non linear process.

### *3.2.1 Trajectory Analysis*

According to the three step model [10, 11] HHG process can be accurately understood studying the trajectory that the electron describes when it is ionized by the laser field. In this context, the electron can be assumed as a classical free particle located at the ion's coordinate, with zero initial velocity. Then, the liberated electron is driven by the Lorentz force. The electric field of the laser drives the electron away from the atomic core. But at a later time, when the sing of the laser field reverses, the electron returns to the core. When this occurs, it can recombine to its initial ground state. The excess of kinetic energy that it has acquired during this process is released in the form of radiation. In this context the electron displacement from the core can be calculated integrating the Newton-Lorentz equation,

$$\frac{d^2\mathbf{r}(t)}{dt^2} = -\mathbf{E}(t), \tag{3.1}$$

where $\mathbf{E}(t)$ represents the driving laser pulse (the dipolar approximation is assumed) and atomic units (a.u.) are used ($q_e = m_e = \hbar = 1$). Additionally, in our calculations we will consider a linearly polarized laser field along the $z$ axis that propagates in $x$ direction. Assuming these conditions Eq. (3.1) turns into a scalar equation where $\mathbf{E}(t) \rightarrow E(t)$ and $d^2\mathbf{r}(t)/dt^2 \rightarrow d^2z(t)/dt^2$.

Figure 3.1(a) shows the rescattering kinetic energy as a function of the ionization time (grey circles) and as a function of the recombination time (black triangles) for a field with constant envelope. As it is shown, the most energetic trajectories correspond to electrons ionized near the field maxima, that recollide with the core at approximately $3/4$ of a cycle later. In the following, we will refer to these as Schafer-Corkum (SC) trajectories, since they were proposed by Schafer et al. [10] and Corkum [11] to explain the plateau's cut-off law. The first two sets of SC trajectories are labelled SC-long and SC-short in Fig. 3.1. Part b of the figure shows the same trajectory analysis for a NAT pulse. In this particular case, we have chosen an ultrashort pulse (1.5 cycles FWHM) whose analytic form is given by

$$E(t) = E_0 \sin^2\left(\frac{\omega t}{6}\right) \sin(\omega t + \phi), \tag{3.2}$$

where $E_0$ is the laser field amplitude, and $\phi$ is the carrier-envelope phase, CEP (in the following $\phi = 0$, unless otherwise is specified).

By a simple inspection of Fig. 3.1(b) it is easy to discern two different classes of trajectories. The first class originates from electrons ionized at the last part of the turn-on, that follow trajectories with similar characteristics as the SC type, i.e., with the most energetic recombinations corresponding to electrons ionized near the field maxima. The second class of trajectories, labeled as NAT, correspond to the electrons ionized in the initial part of the turn on. These ones follow the opposite trend: the most energetic rescatterings originated from electrons ionized almost a quarter cycle before the first field maximum. The emergence of these trajectories is related with the fast turn-on of the laser pulse.

For pulses with a smooth turn-on, the harmonic yield is degraded when the saturation intensity is rebased [12, 13]. This fact is related to the decay in efficiency of the radiation generated by SC type trajectories. This decay is caused by the fast

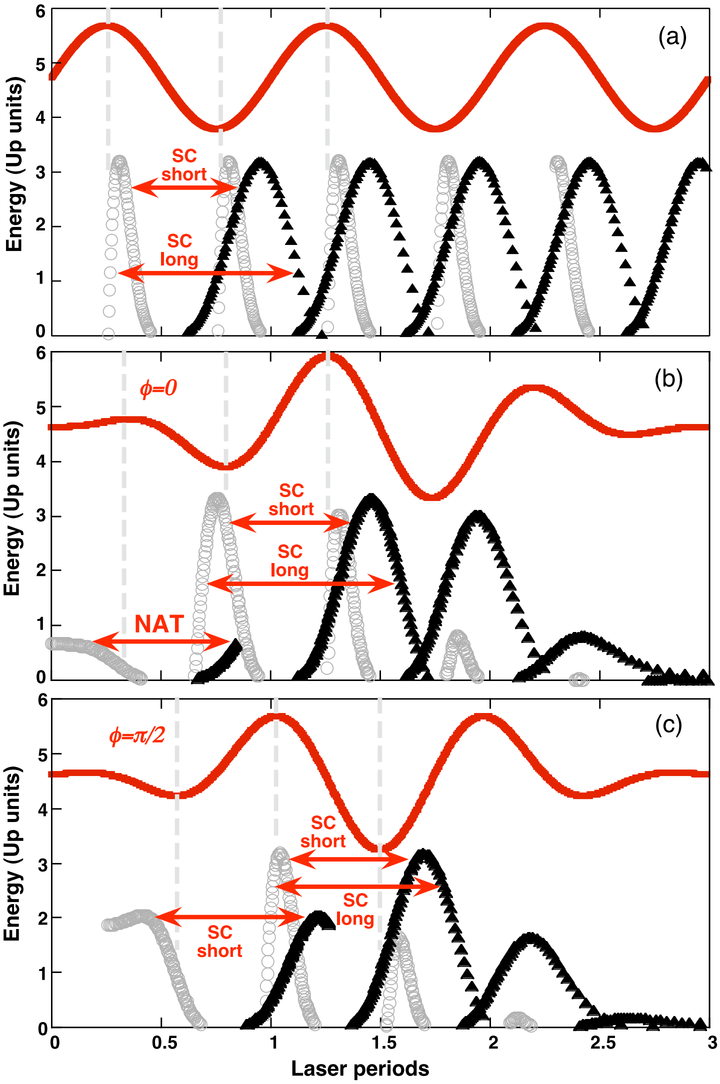

**Fig. 3.1** Rescattering (first rescatering) energies of electrons as a function of the ionization time (*grey circles*) and recombination time (*black triangles*), for three different driving laser pulses: (**a**) constant envelop, and (**b**) and (**c**) as described in Eq. (3.1) with (**b**) $\phi = 0$ and (**c**) $\phi = \pi/2$. The driving field used in each case is shown as a sketch in *solid lines*. Note that for the case $\phi = 0$, a new set of trajectories emerges in the turn-on, labeled as NAT

ionization of the ground state during the time that the electron spends in the continuum. As a consequence, at the instant of rescattering, the ground state is practically empty and the dipole amplitude is relatively small. These two facts lead to a considerable decrease of the HHG efficiency produced by SC types trajectories. We will also demonstrate that NAT trajectories are particularly resistant to the effects of saturation and, therefore, play a fundamental role in harmonic generation with ultraintense fields [15].

### *3.2.2 Behavior of the Harmonic Yield: Valley Structure*

In the following, we will quantitatively describe of the effect the NAT trajectories have in the harmonic yield. An evaluation of the relative contributions to the harmonic spectrum of the different trajectories can be estimated by the absolute value of the complex dipole amplitude (assuming constant transition matrix elements)

$$\left|d(t)\right| \propto \left|a_0^*(t)\right|\left|a_{\mathbf{v}}(t)\right| \tag{3.3}$$

where $a_0(t)$ is the probability amplitude of the ground state and $a_{\mathbf{v}}(t)$ is the probability amplitude of the free electron state with velocity $\mathbf{v}$, at the time of rescattering $t$. These values are extracted from the results of the exact numerical integration of the 3D TDSE: $|a_0(t)|$ is found projecting of the total wavefunction on the ground state, and $|a_{\mathbf{v}}(t)|$ is estimated computing the ground-state depletion during a small time-window around the corresponding ionization time $t_0$, i.e., the initial time of the trajectory associated to the rescattering at time $t$. Specifically

$$|a_{\mathbf{v}}|^2 \simeq \frac{d}{dt}|a_0|^2\Big|_{t_0}\Delta t \tag{3.4}$$

with $\Delta t$ being a small time interval, whose particular value is not important for the relative comparison between different trajectories, as long as it is kept unchanged. The values of the ionization and recombination times ($t_0$ and $t$) for a particular trajectory are extracted from the classical analysis shown in Fig. 3.1. This allows us to associate each pair $(t_0, t)$ to a well-defined NAT or SC trajectory. In order to compare the harmonic efficiency for different laser intensities, we will focus on the yield at a fixed energy, $W_0$.

Then, for each laser intensity, we use the data in Fig. 3.1 to determine the ionization time $t_0$, and the recombination time $t$, corresponding to the electronic trajectories with recombination kinetic energy $W_0 - I_p$. We take $W_0 = 73$ eV, corresponding to the cut-off energy of the harmonic spectrum in hydrogen at the threshold intensity for saturation (see Fig. 3.3(a)). The results for the estimations of the harmonic efficiencies at $W_0$ using different laser intensities are shown in Fig. 3.2(a), for the short pulse considered in Fig. 3.1(b). SC curves in Fig. 3.2(a) show a descendent behavior with increasing field amplitude, which is related to the degradation of the harmonic generation by these type of trajectories. The underlying reason of this behavior can be found in the following analysis of the dipole amplitudes written in Eq. (3.3).

As it is discussed in [15] the decrease in the efficiency of the harmonics radiated by SC type trajectories is connected with the fast ionization of the ground state for intensities above saturation and, consequently, with the decrease of $|a_0|$. In addition,

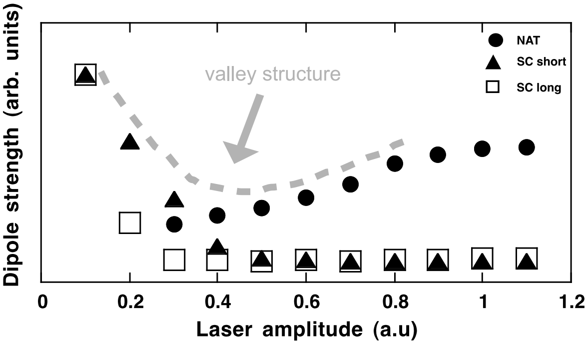

**Fig. 3.2** Different contributions to the harmonic yield at the fixed energy $W_0 = 73$ eV (see also Fig. 3.3(a)), for the sets of trajectories plotted in Fig. 3.1(b). Contributions of NAT trajectories are shown as *black circles*, long SC trajectories as *open squares* and short SC as *black triangles*. *The grey dashed line* is a sketch of the resulting valley structure for the total radiation yield (sum of the two contributions: $|a_0(t)|$ and $|a_{\mathbf{v}}|$). The laser amplitudes, $E_0$, are given in atomic units, corresponding to intensities $E_0^2 \times 3.5 \times 10^{16}$ W/cm$^2$

the depletion of the ground state increases also the population of electrons in the continuum, i.e. $|a_v|$ increases when $|a_0|$ decreases. However, the product of both amplitudes has a net decrease and the efficiency of the dipole transition falls as it is shown in [15].

In contrast, for the case of NAT trajectories, the behavior is the opposite: since they are originated during the first part of the turn-on, the ionization is moderate, even in the case of laser field amplitudes one order of magnitude above saturation (i.e., laser intensities two orders of magnitude above saturation). At rescattering, therefore, there is still a considerable population in the ground state, and the product of probability amplitudes does not vanish. Therefore, the dipole amplitude is found to increase gradually with the laser field. As a consequence, the global behavior of the harmonic yield with the laser amplitude (Fig. 3.2(a)) describes the form of a valley: First, a decrease related with the degradation of the efficiency of the SC trajectories, followed by an increase as the efficiency of the NAT trajectories becomes the relevant contribution to the dipole spectrum. NAT trajectories will eventually be degraded for ultraintense fields well above the atomic unit ($3.5 \times 10^{16}$ W/cm$^2$), however for these intensities one should expect also a decay caused by the breaking of the dipole approximation and the associated drift of the electronic trajectories away from the ion due to the interaction with the magnetic field [14].

### *3.2.3 Harmonic Spectrum and Attosecond Pulses*

In Fig. 3.3(a) it is shown the resulting spectra for intensities corresponding to threshold of saturation ($I \leq 3.51 \times 10^{14}$ W/cm$^2$), saturation ($I \simeq 5.6 \times 10^{15}$ W/cm$^2$) and deep saturation ($I = 3.5 \times 10^{16}$ W/cm$^2$) regimes, extracted from the exact integration of the 3D TDSE for a hydrogen atom. As it is well known, below the saturation

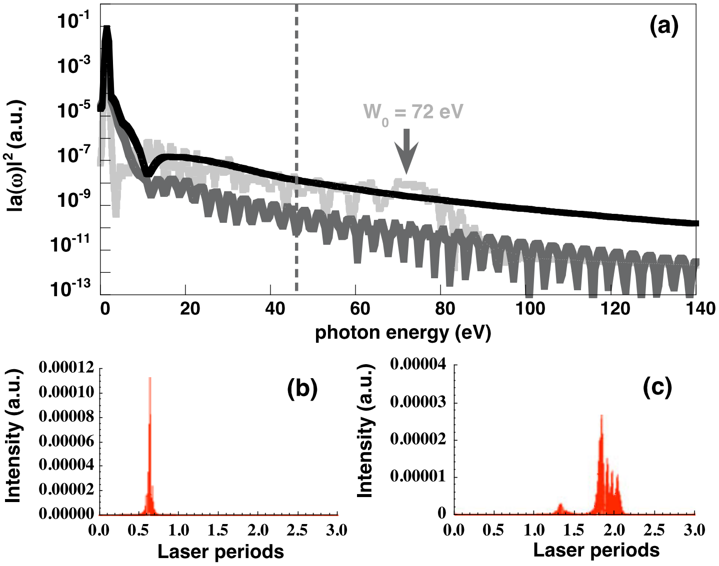

**Fig. 3.3** (**a**) Single-atom spectrum obtained from the exact integration of the 3D TDSE corresponding to the hydrogen atom for the laser pulse described in Eq. (3.2) with $\phi = 0$ (Fig. 3.1(b)), for different values of the field intensity corresponding also to harmonic : threshold of saturation ($I = 3.5 \times 10^{14}$ W/cm$^2$, *light grey line*), saturation ($I = 5.6 \times 10^{15}$ W/cm$^2$, *dark grey line*) and deep saturation ($I = 3.5 \times 10^{16}$ W/cm$^2$, *black line*). $W_0$ corresponds to the cut-off energy of the harmonic spectrum in hydrogen at the threshold intensity for saturation. (**b**) Isolated attosecond pulse generated from the harmonic spectrum for the case of deep saturation regime corresponding to the spectrum in *black* of (**a**). (**c**) Subfemtosecond temporal structure obtained by filtering in the spectrum of threshold of saturation regime plotted in *light grey* in (**a**). In both cases we filter harmonics below the 31st (*vertical dashed line*) which corresponds to 46 eV photon energy

threshold the harmonic yield increases with the laser intensity and the harmonic plateau extends accordingly to the cut-off law $I_p + 3.17U_p$. Above the saturation threshold, the harmonic yield gradually decreases until a minimum corresponding to the bottom of the valley structure sketched in Fig. 3.2. After that, according to our simulations, for higher intensities the harmonic yield increases as a consequence of the emergence of the contribution of the NAT-type trajectories to the radiation spectrum. As it can be seen in Fig. 3.3(a), for field intensities at the threshold of saturation (solid light grey) and deep saturation regime (solid black line), the harmonic yield in both cases is comparable since they correspond to opposite sides of the valley in Fig. 3.2. This unexpected growth of the harmonic efficiency constitutes the main contribution of our approach, which is clearly explained in [15], and contradicts the general believe about the degradation of the efficiency at hight intensity regime. Furthermore, as we will see later, this fact will have important consequences in the intensity of the potential attosecond pulses that could be synthesized at these high laser intensities.

The 3D TDSE spectrum of Fig. 3.3(a) for the deep saturation case (solid black line) reveals important details. A characteristic is the absence of modulations in the harmonic plateau. This is related to the fact that for a given energy there is a single NAT trajectory, and therefore a single rescattering event generates the high-frequency radiation. Figure 3.3(b) shows a narrow (about FWHM $\simeq 50$) isolated attosecond pulse generated by the spectrum corresponding to the deep saturation case (spectrum plotted in black in the Fig. 3.3(a)). The attosecond pulse is obtained filtering the harmonics below the 31 th, which corresponds to a photon energy of 46 eV (generated by a 800 nm fundamental field). Figure 3.3(c) shows the sub-femtosecond temporal structure resulting for the case of saturation threshold. One observes that, this temporal structure is noisier and wider than the deep saturation case, in spite of being filtered using the same window (harmonics below 31st). Note also that the attosecond plotted in Fig. 3.3(b) is almost one order of magnitude more intense than the one in the case of threshold saturation plotted in Fig. 3.3(c). This is also a potential advantage in comparison with the standard procedure to obtain attosecond pulses, which consist in filtering the harmonics near the cut-off where their efficiency is significantly lower, and which is proportional to the intensity of attosecond pulse resulting to filter in this zone. The full spectrum of the deep saturation case is plotted below, in Fig. 3.5(a) in dotted light grey. As it can be observed the extension of the harmonic plateau is no longer given by the cut-off law, reflecting that the most efficient contributions correspond to trajectories different from the SC type. Note that, while there is no clear spectral cut-off, the extension can be well estimated by the maximum rescattering energy of the NAT-type trajectories, which is approximately $I_p + 0.5U_p$. It is accurately confirmed by the wavelet-transformation analysis which we will perform later.

In order to analyze in the full quantum context the effect of the NAT trajectories in the harmonic emission, we have performed the time frequency-analysis of the dipole acceleration extracted from the exact integration of the 3D TDSE. The wavelet analysis provides for the information of the times and efficiencies at which a certain wavelength is radiated [16]. Figure 3.4 shows the wavelet analysis for the three intensity values plotted in the Fig. 3.3(a), corresponding to the NAT-type pulse plotted in Fig. 3.1(b). We also have superimposed over the wavelet results the rescattering energies computed from the classical trajectories labelled in Fig. 3.1(b). By inspection of the three plots of Fig. 3.4 it is easy to see that in the case of threshold of saturation (Fig. 3.4(a)) SC short and long trajectories are responsible of the harmonic generation. When the intensity increases beyond the saturation limit, the efficiency of the harmonic emission produced by long and short SC trajectories is degraded (Fig. 3.4(b)). Note that, at this intensity regime, NAT trajectories turn out important. Figure 3.4(c) shows the deep saturation case where only NAT trajectories survive since the atom is completely depleted, except approximately during the first half period of the driving pulse. For this reason, SC short and long trajectories are not involved in the harmonic generation at this intensity regime. In light of these results, in deep saturation regime, only NAT trajectories are responsible of the harmonic radiation. This is the cause of the absence of modulations in the harmonic spectrum of the deep saturation case plotted in Fig. 3.3(a), and consequently, it is connected to the fact that the attosecond obtained from the deep saturation spectrum is noise-less and narrow.

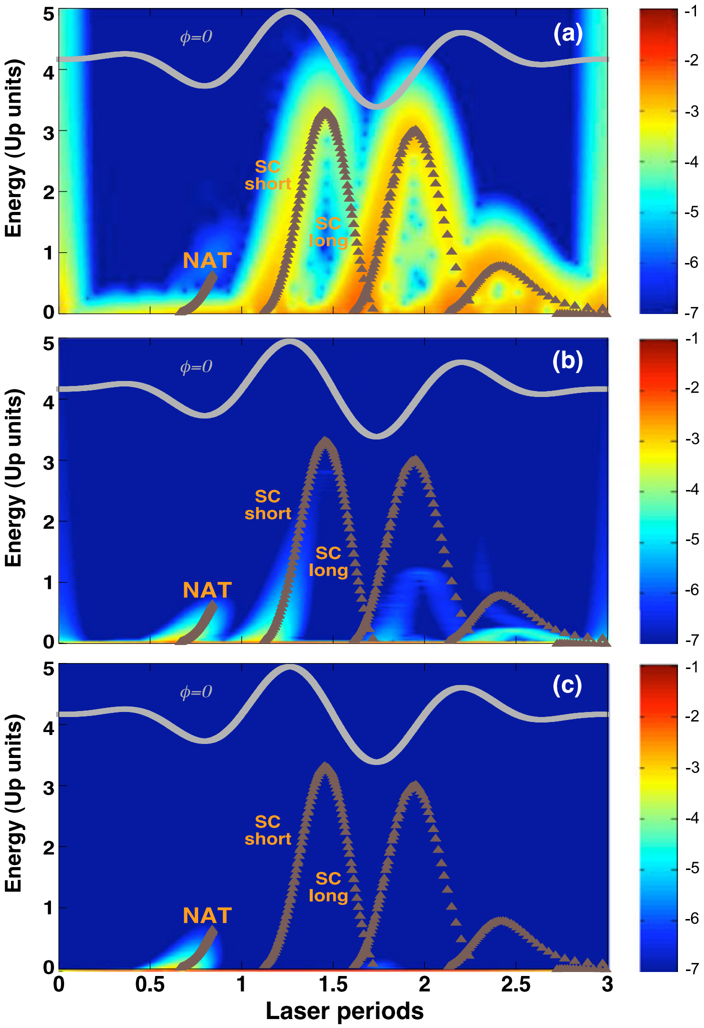

**Fig. 3.4** Wavelet-transformation analysis of dipole acceleration extracted from the numerical resolution of 3D TDSE, and (superimposed) classical rescattering energies of electrons as a function of the recombination time (*brown triangles*) for laser pulse described in Eq. (3.2) with $\phi = 0$ for the three laser intensities used in Fig. 3.3 (in (**a**) $E_0 = 0.1$ a.u., in (**b**) $E_0 = 0.4$ a.u. and in (**c**) $E_0 = 1.0$ a.u.). The driving laser pulse is plotted in *solid grey lines*. Note that the scale of the efficiencies (plotted in *the colour bars*) is the same in all cases

We also point out that the interaction of NAT pulses with matter is strongly dependent on the carrier-envelope phase (CEP), $\phi$ in Eq. (3.2). Figure 3.1(c) shows the energy diagram for the driving laser pulse given by Eq. (3.2), but with $\phi = \pi/2$. In this case, the only relevant trajectories for harmonic generation are of the SC type which are not effective at high intensity due to the atom being practically empty.

NAT trajectories are not useful, as the electron excursion is too short to acquire energy relevant for HHG. These results are confirmed by our 3D TDSE calculations which, for this case, show an strongly decrease in the harmonic yield when the intensity is increased above saturation. This strong dependence with the CEP makes the experimental viability of this technique more difficult.

## 3.3 Ionization Gating

According to our interpretation, the increase of the yields at ultrahigh intensities is a consequence of the non-adiabatic character of the pulse turn-on. Therefore one should expect that pulses with different shapes and lengths but with similar turn-on will give very similar harmonic spectrum, as the full ionization of the ground state occurs practically during the first stage of the interaction. To confirm this point, we have performed exact 3D TDSE calculations of a pulse with the same turn-on as in Eq. (3.2), followed by two cycles of constant amplitude as it is plotted in Fig. 3.5(a).

As it is shown in Fig. 3.5(a), for intensities in the deep saturation regime, it is found that the spectrum generated with the longer pulse, plotted in solid blue line in Fig. 3.5(a), overlaps the corresponding spectrum for the shorter pulse plotted in dotted light grey in the same plot. Note that the ground state depletion is quite similar (practically both are overlapped) as it is plotted in Fig. 3.5(a), and this fast depletion occurs in the turn-on of the pulse when the barrier suppression intensity (horizontal dashed lines in Fig. 3.5(a)) is rebased. Therefore, is confirmed that actual shape of the pulse is irrelevant, as long as the turn on coincides. This constitutes the basis of the method known as ionization gating, used to generate isolated attosecond pulses as already pointed out in [17–19] and more recently in [20].

In Fig. 3.6 are shown the corresponding attosecond pulses synthesized using three filters in different zones along the both spectrums plotted in Fig. 3.5(b). All filters have the same wide (15 eV). As it can be see in this figure, the attosecond obtained using the same filter in both spectra have identical intensity. Note that the temporal wide is practically the same in all of them ($\sim$ 50 attosecond). On the contrary, the intensity is quite different depending on where the filtering is done. The attosecond synthesized using the filter 3 situated in harmonic 800th (plots (e) and (f) of Fig. 3.6) are six order of magnitude lower intense than attosecond obtained using the filter 1 (plots (a) and (b)), situated in harmonic 100 th. This is another advantage to use NAT-type pulses, the potentiality to obtain attosecond pulses in the first part of the plateau, where the harmonic efficiency is high, and consequently, the attosecond pulse synthesized in this zone will also quite intense.

Finally, we would like to point out that the results presented here correspond to a single atom, the macroscopic response is not included. To include propagation effects via TDSE for the parameters used in this work is, at present, an impossible goal. Only propagation codes based on approximated models such as Strong Field Approximation (SFA) are computationally viable. But according to our test with 3D TDSE, the SFA model do not describe with sufficient accuracy the HHG process at the intensity regimes presented here.

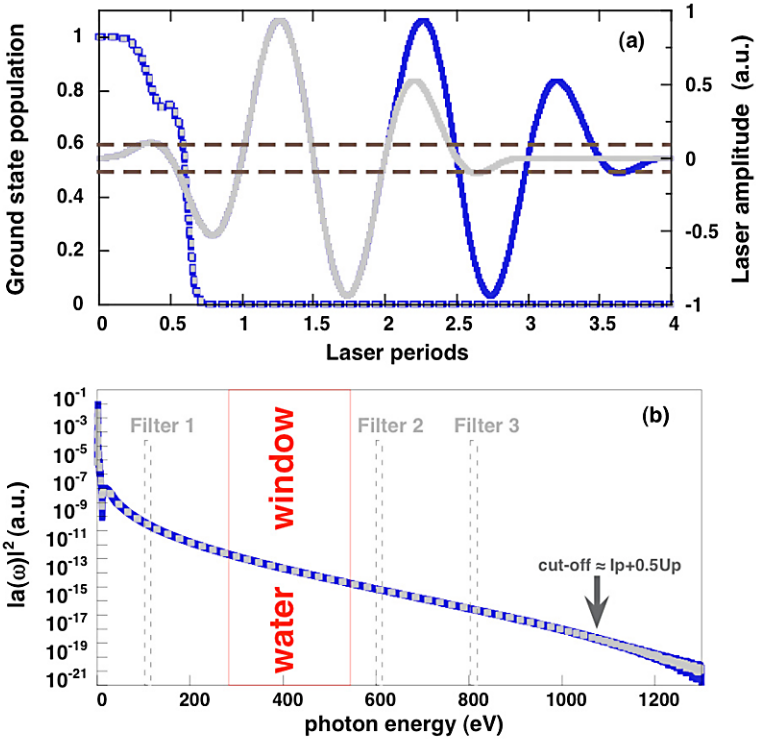

**Fig. 3.5** (**a**) NAT-type driving laser pulses with the same turn-on and different length. In solid grey is plotted the pulse described by Eq. (3.2) with $\phi = 0$. In *solid blue* is plotted a pulse with the same turn-on as in Eq. (3.2) with $\phi = 0$, followed by two cycles of constant amplitude. *The dotted grey lines* represents the ground state population corresponding to the pulse in *solid grey* and *the dotted blue lines* represents the ground state population related to the pulse in *solid blue*. *Horizontal brown dashed lines* represents the estimated value of the barrier suppression for hydrogen. In (**b**) are plotted harmonic spectrums generated by each one of driving laser pulses plotted in (**a**). *Dotted grey* represents the spectrum generated by the driving laser pulse in *solid grey* in (**a**). Spectrum in solid blue correspond to the pulse plotted in *solid blue* in (**a**). *Vertical dashed rectangles* represent three different filters along the plateau, each one has a window of 15 eV

## 3.4 Summary

In this chapter we have reviewed the potential advantages of generating harmonics at ultra high laser intensities beyond the tunnel regime, considering NAT-type pulses as a method to obtain intense isolated attosecond pulses. A detailed study of the physics underlying in the turn-on of the ultra-intense laser pulses has been carried out. This study reveals the existence of a new type of trajectories which emerges during the turn-on of the driving laser pulse. Although, the rescattering energy of these trajectories is much lower than the conventional SC short and long, it turns important at ultra-high laser intensities. In addition, we have found that the harmonic spectrum generated by NAT-type pulses at intensities well above saturation

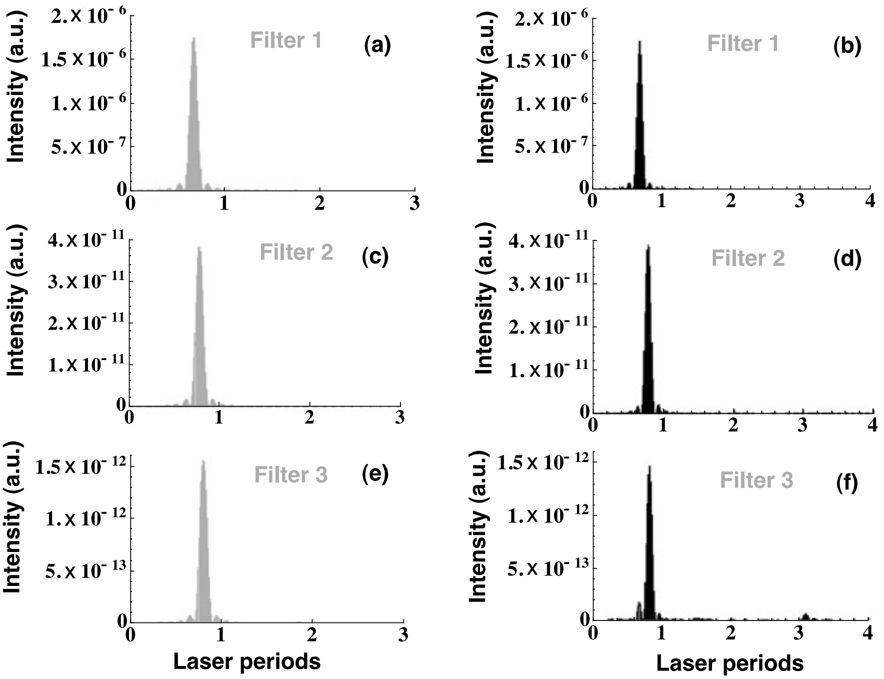

**Fig. 3.6** Plots (**a**), (**c**) and (**e**) in *grey*, represents the attosecond pulses synthesized from the spectrum in *dotted grey* in Fig. 3.5(b). Plots (**b**), (**d**) and (**f**) in *black*, represents the attosecond pulses corresponding to spectra in *solid blue* from Fig. 3.5(b). Attosecond pulses plotted in (**a**) and (**b**) are synthesized using the filter 1 in Fig. 3.5(b), which is situated in harmonic 100th of both spectra. Attoseconds plotted in (**c**) and (**d**) are obtained using the filter 2 fixed in the harmonic 600th of the Fig. 3.5(b). Attosecond pulses (**e**) and (**f**) are obtained using the filter 3 situated in the harmonic 800th in the spectrum of the same figure. The temporal width of each temporal structure is approximately 50 attosecond

presents peculiar characteristics such as, and unexpected high efficiency and absence of modulations in the totality of the plateau. According to our analysis, based on classical and quantum formalisms, we conclude that the NAT trajectories are responsible of the increasing of the harmonic efficiency at ultra-high laser intensities and the phase-locked structureless spectra is caused by total depletion of the atom in the first half cycle of the pulse. These two facts constitute ideal conditions to synthesize intense attosecond pulses from input pulses with arbitrary duration. We have obtained numerically isolated XUV pulses with durations around 50 attoseconds. Concerning to the potential experimental viability, one of the main impediments to this technique is that an optimal control of the CEP is required in an intense few cycle driving laser pulse. For this reason, we emphasize the interest of developing techniques to obtain CEP controlled ultraintense pulses with non-adiabatic turn-on, without any other constraints regarding the global pulse shape and length. Finally, we remark that the interest to use NAT-type driving pulses as a source of attosecond pulses lies in the fact that not only narrow, also quite intense attosecond pulses can be obtained, since the degradation of the harmonic efficiency at ultra-high laser intensity can be avoided. In light of this results, and in spite of the fact that the experimental feasibility, up to date, remains a challenge, we think that a research line focused on this technique deserves to be carried out.

**Acknowledgements** Authors acknowledge support from Spanish Ministerio de Ciencia e Innovación through the Consolider Program SAUUL (CSD2007-00013) and research project FIS2009-09522, from Junta de Castilla y León through the Program for Groups of Excellence (GR27) and from the EC's Seventh Framework Programme (LASERLAB-EUROPE, grant agreement no. 228334).

## References

1. Gy. Farkas, Cs. Toth, Phys. Lett. A **168**, 447–450 (1992)
2. P.M. Paul, E.S. Toma, P. Breger, G. Mullot, F. Augé, Ph. Balcou, H.G. Muller, P. Agostini, Science **292**, 1689 (2001)
3. M. Hentschel, R. Kienberger, Ch. Spielmann, G.A. Reider, N. Milosevic, T. Brabec, P. Corkum, U. Heinzmann, M. Drescher, F. Kraus, Nature **414**, 509 (2001)
4. M. Drescher, M. Hentschel, R. Kienberger, M. Uiberacker, V. Yakovlev, A. Scrinzi, Th. Westerwalbesloh, U. Kleineberg, U. Heinzmann, F. Krausz, Nature **419**, 803 (2002)
5. Y. Mairesse, A. de Bohan, L.J. Frasinski, H. Merdji, L.C. Dinu, P. Monchicourt, P. Breger, M. Kovacev, R. Taïeb, B. Carré, H.G. Muller, P. Agostini, P. Salières, Science **302**, 1540–1543 (2003)
6. P. Tzallas, D. Charalambidis, N.A. Papadogiannis, K. Witte, G.D. Tsakiris, Nature **426**, 267–271 (2003)
7. E. Goulielmakis, V.S. Yakovlev, A.L. Cavalieri, M. Uiberacker, V. Pervak, A. Apolonski, R. Kienberger, U. Kleineberg, F. Krausz, Science **10**, 769–775 (2007)
8. A. McPherson, G. Gibson, H. Jara, U. Johann, T.S. Luk, I.A. McIntyre, K. Boyer, C.K. Rhode, J. Opt. Soc. Am. B **21**, 595–601 (1987)
9. M. Ferray, A. L'Huillier, X.F. Li, L.A. Lompre, G. Mainfray, C. Manus, J. Phys. B, At. Mol. Opt. Phys. **21**, L31–L35 (1998)
10. K. Schafer, B. Yang, L.F. DiMauro, K.C. Kulander, Phys. Rev. Lett. **70**, 1599–1602 (1993)
11. P.B. Corkum, Phys. Rev. Lett. **71**, 1994–1997 (1993)
12. P. Moreno, L. Plaja, V. Malyshev, L. Roso, Phys. Rev. A **51**, 4746–4753 (1995)
13. V.V. Strelkov, A.F. Sterjantov, N.Y. Shubin, V.T. Platonenko, J. Phys. B, At. Mol. Opt. Phys. **39**, 577–589 (2006)
14. J. Vazquez de Aldana, L. Roso, Opt. Express **5**, 144–148 (1999)
15. J.A. Pérez-Hernández, L. Roso, A. Zaïr, L. Plaja, Opt. Express **19**, 19430–19439 (2011)
16. J.A. Pérez-Hernández, J. Ramos, L. Roso, L. Plaja, Laser Phys. **20**, 1044–1050 (2010)
17. K.T. Kim, C.M. Kim, M.G. Baik, G. Umesh, C.H. Nam, Phys. Rev. A **69**, 051805(R) (2004)
18. T. Sekikawa, A. Kosuge, T. Kanai, S. Watanabe, Nature **432**, 605–608 (2004)
19. M. Schnürer, Ch. Spielmann, P. Wobrauschek, C. Streli, N.H. Burnett, C. Kan, K. Ferencz, R. Koppitsch, Z. Cheng, T. Brabec, F. Krausz, Phys. Rev. Lett. **80**, 3236–3239 (1998)
20. F. Ferrari, F. Calegari, M. Lucchini, C. Vozzi, S. Stagira, G. Sansone, M. Nisoli, Nat. Photonics **4**, 875–879 (2010)

# Chapter 4
# Generation of Isolated Attosecond Pulses

**Eiji J. Takahashi, Pengfei Lan, and Katsumi Midorikawa**

**Abstract** Experiments on isolated attosecond pulse creation that have been performed in recent years and on their underlying physics are reviewed in detail. We present the various methods of generating isolated attosecond pulses, such as the use of a phase-stabilized few-cycle laser pulse, polarization gating, and two-color gating, as well as the prospects for other methods. An insight into the power scaling of isolated attosecond pulses is also included.

## 4.1 Introduction

High-order harmonic generation (HHG) has been recognized as one of the best methods of producing an ultrafast (less than femtosecond) coherent light source covering a wavelength range from the extreme ultraviolet (XUV) region to the soft X-ray region. At present, the shortest pulse duration of an isolated attosecond pulse (IAP) produced by HHG is 80 as [1] in the soft X-ray region. Recent years have witnessed the birth of a new research area called attosecond science [2]. The use of IAPs has led to the development of new applications, enabling us to track the motion of electrons inside atoms, molecules, and solids. This new field is expected to reveal new features of the interaction between electrons and photons.

In this chapter, we review the generation methods for IAPs that have been developed in recent years. Various methods of creating IAPs by HHG, such as the use of few-cycle pulses for driving lasers [3–6], polarization gating (PG) [7], the use of a synthesized electric fields consisting of two-color laser pulses [8, 9], double optical gating [10], and others [11–14] have been proposed. In order to utilize

---

E.J. Takahashi · P. Lan · K. Midorikawa (✉)
Extreme Photonics Research Group, RIKEN Center for Advanced Photonics (RAP),
2-1 Hirosawa, Wako, Saitama 351-0198, Japan
e-mail: kmidori@riken.jp

E.J. Takahashi
e-mail: ejtak@riken.jp

P. Lan
e-mail: pengfeilan@riken.jp

L. Plaja et al. (eds.), *Attosecond Physics*, Springer Series in Optical Sciences 177,
DOI 10.1007/978-3-642-37623-8_4,

IAPs, we have to select the best method of creating IAPs depending on their applications, the specifications of our own laser system, and other factors. This chapter might give a good precept for deciding which generation method for IAPs to use. First, we briefly explain the essential conditions of a driving laser field for creating IAPs.

## 4.2 Essential Conditions of a Driving Laser Field for Creating IAPs

The HHG process is well explained by the semi-classical three step model [15]. According to this model, an intense, nonresonant electric field tilts the atomic potential, suppressing the binding barrier in the first step. A bound electron can tunnel through the Coulomb potential, reaching a continuum with zero velocity. A free electron is accelerated by an oscillating laser field and moves on a classical trajectory. When the field reverses its direction, the electron returns to the nucleus, recombines with the parent ion, and emits a high-energy photon. The maximum photon (cutoff) energy is determined by the maximum energy of the recombining electron. Specifically, the harmonic cutoff is given by $E_{HHG} = I_p + 3.17U_p$, where $I_p$ is the ionization potential of the atom and $U_p$ is the ponderomotive energy. This generation process occurs during each half-cycle of the laser field. Therefore, when a multicycle laser field is used in generating high-order harmonics, the temporal structure of the harmonics has a pulse train formation. In order to create IAPs, it is necessary to confine the driving laser field to a few optical cycles.

A most straightforward method of confining HHG to one laser cycle becomes feasible with the availability of intense few-cycle ($\tau_0 < 5$ fs) laser pulses. Figure 4.1 shows features of HHG with a few-cycle laser field ($\tau_0 = 5$ fs). Here, the HHG spectrum was calculated using the single-atom response within the nonadiabatic strong field approximation, which is based on a previously reported model [16]. When the pumping pulses have a few-cycle electric field, the highest photon energy (near the cutoff energy region) of HHG can be confined to one half of the electric field at the central peak (Fig. 4.1(b)). As can be seen in Fig. 4.1(c), a continuous harmonic spectra in the cutoff region is obtained. By extracting the cutoff components of the high harmonics beam, it is possible to obtain an isolated light pulse with an attosecond temporal width (Fig. 4.1(d)).

Here, note the absolute phase (which is called the carrier-envelope phase; CEP, or $\phi_{CE}$) as well as the pulse duration of the pumping electric field. The electric field is generally described as

$$E(t) = E_0 \exp\left[-2\ln 2\left(\frac{t}{\tau_0}\right)^2\right]\cos(\omega_0 t + \phi_{CE}).$$

If $\phi_{CE}$ changes shot by shot, the structure of the electric field also changes with CEP. This effect leads to a multiburst HHG, which becomes attosecond pulse trains.

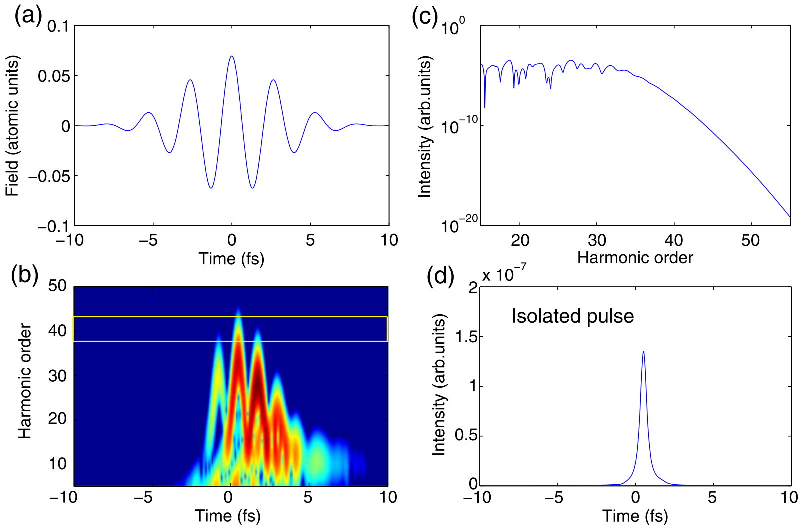

**Fig. 4.1** Overview of harmonic emission with a few-cycle ($\lambda = 800$ nm, $\tau_0 = 5$ fs, $1.5 \times 10^{14}$ W/cm$^2$) laser field. (**a**) Electric-field waveform with a pulse duration of 5 fs. (**b**) Temporal evolution of HHG as a function of field cycle. (**c**) Harmonic spectrum. (**d**) Schematic temporal intensity profile of the cutoff harmonic component (37th–45th)

Therefore, it is necessary to accurately stabilize and control CEP. From the theoretical point of view, the following conditions for generating IAPs are required: (1) confining HHG to one laser cycle, and (2) stabilizing CEP.

## 4.3 Few-Cycle Laser Field with CEP Stabilization

The first demonstration of IAP creation was performed using a CEP-stabilized few-cycle laser system [4]. IAPs were generated by gently focusing CEP-stabilized laser pulses onto a 2-mm-long neon gas target. This laser system delivered 5-fs, 0.5-mJ pulses with a carrier wavelength of 750 nm. The jitter of CEP was found to be less than 50 mrad (rms) owing to the excellent energy stability of the amplified pulses ($<1$ % rms). Baltuška et al. found that the cutoff components ($>120$ eV) of HHG are strongly influenced by CEP. Notably, with a change in CEP, the continuous spectral distribution of the cutoff radiation gradually transforms into discrete harmonic peaks, with the maximum modulation depth appearing for $\pm\pi/2$. The observed CEP dependence clearly shows the possibility of generating IAPs from a few-cycle laser field.

This most straightforward approach to creating IAPs is making further progress together with ultrashort laser technology. Goulielmakis et al. [1] have recently reported isolated sub-100-as pulses with $\sim$0.5 nJ of energy. They used phase-controlled sub-1.5-cycle (3.3 fs) laser pulses carried at a wavelength 720 nm to generate XUV harmonics up to photon energies of $\sim$110 eV in a Ne gas jet. For the

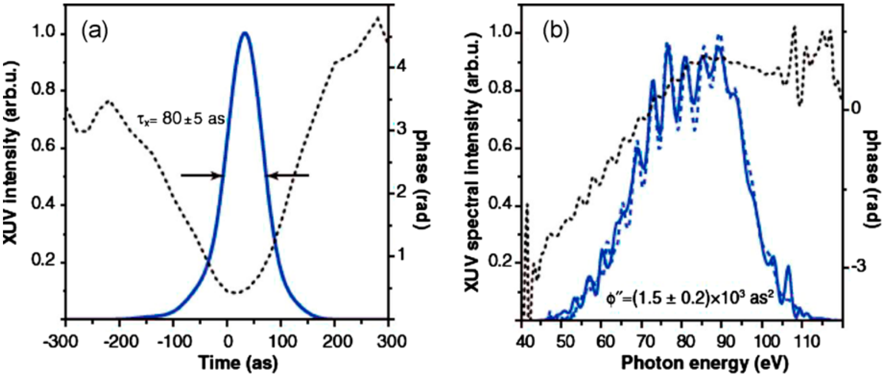

**Fig. 4.2** (**a**) Retrieved temporal intensity profile and spectral phase of an XUV pulse. *Arrows* indicate the temporal FWHM of the XUV pulse. (**b**) XUV spectra evaluated from a measurement of the XUV-generated photoelectron spectrum in the absence of the NIR streaking field (*dashed line*) and from ATR retrieval (*solid line*). *The dotted line* indicates the retrieved spectral phase. Cited from Ref. [1]

spectral filtering of the soft-X-ray supercontinuum, they used a Mo/Si multilayer mirror with a FWHM bandwidth of 30 eV centered at 75 eV. A 300-nm-thick Zr foil was used to suppress the second-order reflectivity peak and eliminate lower-energy XUV photons. Moreover, to fine-tune the frequency chirp of the generated attosecond pulses, Goulielmakis et al. also took advantage of the negative group delay dispersion (GDD) introduced in the 70–100 eV range by thin foils of Zr. To measure the temporal profile of the generated XUV supercontinuum, they irradiated the NIR field onto the Ne atoms ionized by the XUV pulse to implement the atomic transient recorder (ATR) technique. Figure 4.2 (a) shows the retrieved temporal intensity profile and phase of the XUV pulse. The pulse duration of 80 ± 5 as is close to its transform limit of 75 as, with a small positive chirp of $1.5 \pm 0.2 \times 10^3$ as$^2$ being responsible for the deviation. At present, this measured pulse duration is the shortest. Note that the possible pulse duration of IAPs by HHG is limited by not only the pulse duration of the pumping laser but also the acceptable bandwidth of an XUV multilayer mirror.

## 4.4 Polarization Gating and Interference Polarization Gating

According to the three-step model, in an elliptically polarized field, the ionized electron will be displaced in the direction of the minor axis of the polarization ellipse and make it more difficult to recombine with the parent ion. If the displacement exceeds a large amount, the electron cannot recombine with the ion and the HHG emission is suppressed [17]. Therefore, recombination probability and thus HHG efficiency depend sensitively on the ellipticity ($\varepsilon$) of the driving laser field. This effect enables us to control HHG by modulating the ellipticity of the driving laser pulse. In this section, we review such a scheme, called polarization gating (PG), for producing IAPs.

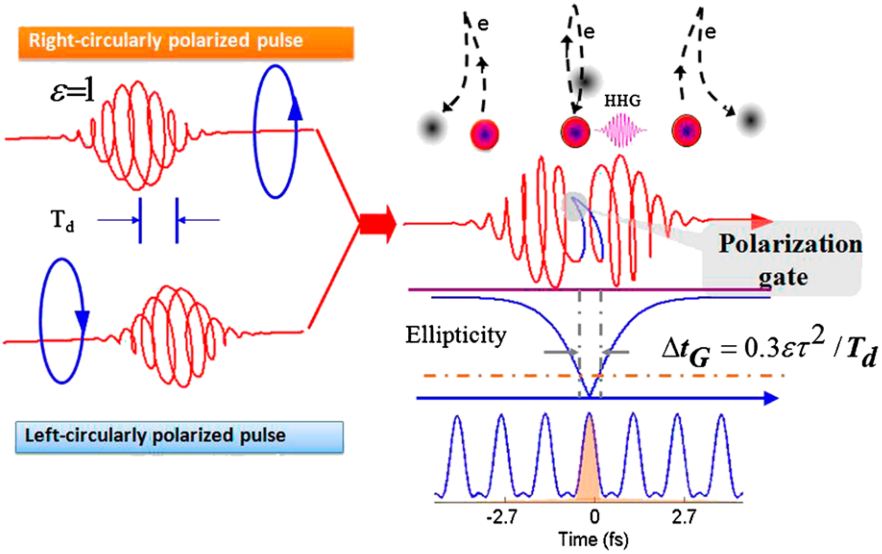

**Fig. 4.3** Principle of the PG scheme. Adapted from Ref. [19]

### *4.4.1 Conventional Polarization Gating*

The principle of conventional PG is shown in Fig. 4.3: By synthesizing a right-circularly polarized pulse and a delayed left-circularly polarized pulse, a laser pulse with a time-dependent ellipticity can be created. It is elliptically polarized, which prevents efficient HHG, at the leading and trail edges of the laser pulse and becomes linearly polarized at the pulse center, where HHG can be effectively produced. The polarization gate width is defined by the time interval for effectively producing HHG and it is approximately expressed by $\Delta t_G \simeq 0.3\varepsilon\tau^2/T_d$ where $\varepsilon$, $\tau$, and $T_d$ are the ellipticity, pulse duration and delay between driving pulses, respectively. If the gate width is less than half the optical cycle of the driving pulse, i.e., $\Delta\ t_G < 1.3$ fs, it will be able to generate only one attosecond pulse as the other cycles outside the PG will not produce attosecond pulses. Consequently, an IAP will be produced instead of an attosecond pulse train (see the shaded pulse in Fig. 4.3). The gate width can in principle be reduced to less than 1.3 fs by increasing the delay, no matter how long the pulse duration is. However, we need to emphasize that the delay between counter-rotating, elliptically polarized pulses should be less than $2\tau$, otherwise the driving pulses will be too far apart to create an effective PG. Actually, the delay is usually set approximately equal to the pulse duration in experiments. On the other hand, the ionization of the target medium is another important factor that limits the driving pulse duration. The green line in Fig. 4.4 shows the ionization probability of an Ar atom in the PG scheme [10]. The ADK model [18] is used for the calculation. As shown in Fig. 4.4, the neutral medium is completely depleted if the pulse duration is longer than 6.5 fs, which is the upper limit of the driving pulse.

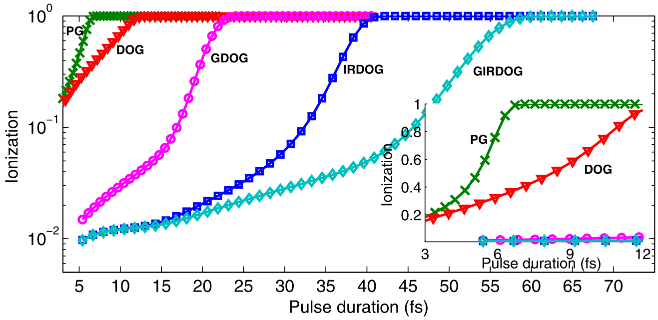

**Fig. 4.4** Ionization probability for the PG [10], DOG [10], GDOG [36], IRDOG [21] and GIRDOG [21] schemes, respectively. The target is Ar. To produce the same continuum high harmonics around 50 eV, the laser intensity is set to be $2.8 \times 10^{14}$ W/cm$^2$ for PG, DOG and GDOG and $1.0 \times 10^{14}$ W/cm$^2$ for IRDOG and GIRDOG, respectively. *The inset* shows the same result in the linear scale

The PG field with a time-dependent ellipticity can be constructed from a linearly polarized pulse by passing through two birefringent plates. The first plate splits the incoming linearly polarized pulse into two orthogonally polarized pulses, i.e., one ordinary and one extraordinary, which are separated in time, and the delay can be adjusted by varying the thickness of the plate. After the first plate, a quarter waveplate is placed with its optic axis along the initial polarization direction of the driving pulse. After passing through the quarter waveplate, the ordinary and extraordinary pulses are converted to left- and right-circularly polarized pulses, respectively, finally producing a PG pulse with a time-dependent ellipticity. Chang et al. [19] have produced a continuum of high harmonics covering 25 to 45 nm, indicating the generation of IAPs, with an 8-fs driving pulse. By taking advantage of a CEP-stabilized 5-fs driving pulse, Sansone et al. [7] have demonstrated a supercontinuum at approximetely 36 eV. The advantage of such a pulse over the 5-fs driving pulse alone is that a broadband supercontinuum can be produced through the plateau up to the cutoff regions. A temporal profile of the supercontinuum was also constructed by employing the FROG-CRAB technique.[1] The measurement indicates an IAP of 130 as, corresponding to less than 1.2 optical cycles.

### 4.4.2 Interference Polarization Gating

Another slightly complex but more efficient technique, called interference polarization gating (IPG), for producing PG is double-Michelson interferometry [20]. Figure 4.5(a) shows its basic setup: a linearly polarized pulse is firstly split to two pulses, which are then sent to the double Michelson interferometer. One of the beam passes through the first Michelson interferometer (first MI in Fig. 4.5(a)). A constructive interference maximum can be induced at the pulse center by adjusting

---

[1] For details of the characterization method, see Chap. 4 of [39].

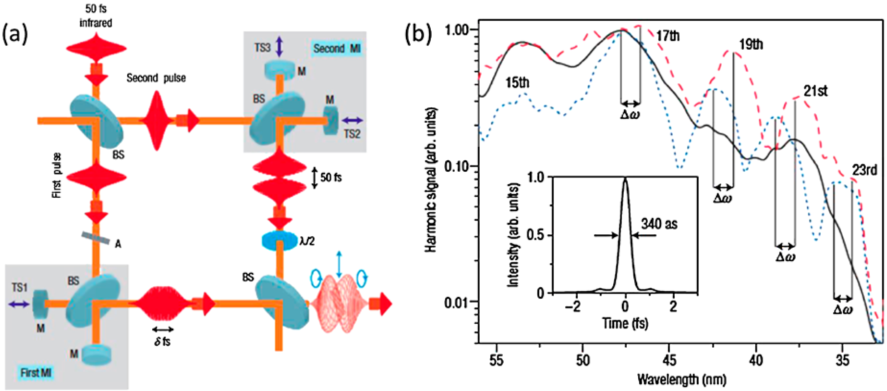

**Fig. 4.5** (**a**) Basic setup for producing a PG field with a double-Michelson interferometer. (**b**) High-harmonic spectrum recorded at different CEPs. Cited from Ref. [20]

the delay between the two arms of the interferometer. The other beam enters the second Michelson interferometer (second MI in Fig. 4.5(a)), where a proper delay is introduced to form a destructive interference minimum at the pulse center. After that, a half waveplate is introduced into the second beam, so that its polarization is adjusted to be perpendicular to the first beam. The synthesized pulse is linearly polarized at the pulse center and becomes elliptically polarized at the leading and trailing edges. This optimal technique requires fine adjustment of the double Michelson interferometer, thus complicating the experiment; however, it enables the independent manipulation of two fields and thus provides an effectively controllable PG field, making it possible to use a longer driving pulse. Tzallas et al. [20] have demonstrated the generation of supercontinuum high harmonics by the IPG technique. Figure 4.5(b) shows the spectrum of HHG from an Ar gas jet. As shown in this figure, by carefully tailoring the PG field, a supercontinuum covering from 35 to 55 nm can be produced even if a 50-fs driving pulse is used. As most high-peak-power ($\sim$ 100 TW) laser systems deliver pulses with a duration of $\geq$ 30 fs, the use of driving pulses with longer durations in IPG is an attractive technique for intense IAP generation. A drawback of the IPG technique is that, as shown in Fig. 4.5(b), the supercontinuum depends sensitively on the CEP of the driving pulse; therefore, a CEP-stabilized pulse is required for creating IAPs. However, even with start-of-the-art techniques, no high-peak-power laser system with CEP stabilization has been demonstrated yet.

## 4.5 Ionization Gating

According to the three-step model, the generation of high harmonics and IAPs can be manipulated by controlling the ionization, acceleration or recombination processes. The PG introduced in Sect. 4.4 is based on the manipulation of the recombination process. In this section, we introduce the ionization gating scheme for IAP generation by controlling the ionization process.

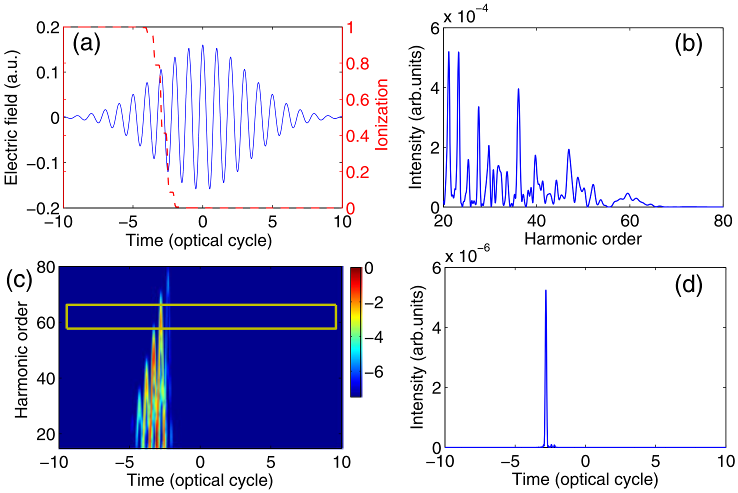

**Fig. 4.6** (**a**) Electric field of a multicycle (15 fs) laser pulse (*solid line*) and corresponding ionization probability of Ar (*dashed line*). The laser intensity is $8 \times 10^{14}$ W/cm$^2$ and the central wavelength is 800 nm. (**b**) High harmonic spectrum. (**c**) Time-frequency spectrogram of HHG. (**d**) Temporal profile of IAPs generated by selecting the cutoff around the 60th harmonic

### *4.5.1 Ionization Gating Induced by Single Atomic Response*

When atoms are exposed to an oversaturated laser field, as shown in Fig. 4.6(a), the electron is rapidly ionized within one optical cycle (from $-3T_0$ to $-2T_0$) and the neutral target is completely depleted at the leading edge of the laser pulse. Recall that ionization is the first step in HHG. At the trail edge of the driving pulse, there will be no HHG because of the suppression of ionization. Therefore, as shown in Fig. 4.6(c), in the oversaturated ionization case, HHG can be confined to the leading edge, producing a ionization gate, even though a multicycle pulse is used. On the other hand, at the leading edge, the laser intensity increases rapidly. Every subsequent half-cycle has a higher instantaneous intensity, such that, as shown in Fig. 4.6(c), in each half-cycle, a new spectral range of higher-order harmonics than the previous half-cycle can be generated. However, because HHG is suppressed from $-2.5T_0$ (see Fig. 4.6(c)), the highest-order harmonics of approximately the 60th order are generated only in the half-cycle from $-3$ to $-2.5T_0$ and they become continuous, as shown in Fig. 4.6(b). After filtering out the lower-order harmonics, an IAP can be produced in the leading edge of the driving pulse (see Fig. 4.6(d)).

Sekikawa et al. [22] have demonstrated the generation of IAPs by ionization gating. To increase the IAP energy, a blue laser, generated by frequency-doubling the Ti:Sapphire laser pulse, was focused onto Ar gas. When the blue laser becomes sufficiently intense to completely ionize the target gas, as shown in Fig. 4.7(c), supercontinuum harmonics at approximately 27.9 eV are obtained. The supercontinuum had an energy of about 2 nJ. By focusing the supercontinuum onto He using a Sc/Si multilayer spherical mirror, electrons could be ionized via a two-photon process, thus

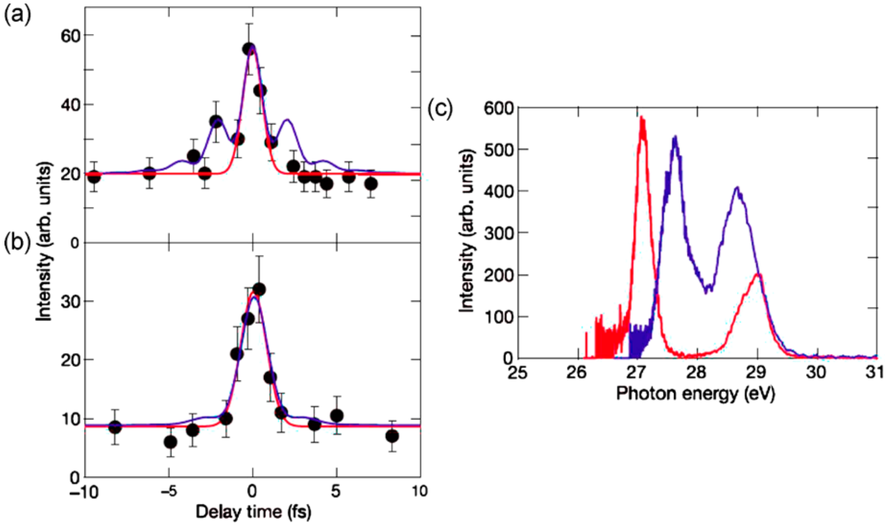

**Fig. 4.7** Autocorrelation traces of the supercontinuum generated using (**a**) 8.3- and (**b**) 12-fs blue pulses. *The lines in red* show the fitting results. *The lines in blue* show the calculated autocorrelation traces from the supercontinuum spectrum. (**c**) The spectra of the supercontinuum generated using 12- and 8.3-fs pulses are shown by *the blue and red lines*, respectively. Cited from Ref. [22]

enabling the characterization of the temporal profile of IAPs by the autocorrelation technique for the first time. Figures 4.7 (a) and (b) show the autocorrelation traces of the supercontinuum generated using 8.3- and 12-fs blue pulses, respectively.[2] The full widths at half maximum (FWHM) of the autocorrelation traces obtained from a least-squared fit to the Gaussian functions were $1.3 \pm 0.1$ and $1.8 \pm 0.1$ fs, resulting in pulse durations of $950 \pm 90$ as and $1.3 \pm 0.1$ fs, respectively.

Pfeifer et al. [23] have also demonstrated this ionization gating scheme using a Ti:Sapphire laser, where a broadband and a tunable supercontinuum were reported. Recently, Altucci et al. [24] have proposed and demonstrated a combination scheme based on PG and ionization gating . Supercontinuum was observed from 35 to 55 eV, which however depended on the CEP of the driving pulse. On the other hand, even though it has not been demonstrated experimentally, an alternative and more efficient ionization gating scheme by seeding XUV pulses to Ti:Sapphire driving pulses has been proposed in several theoretical works [25–27]. Owing to its higher photon energy, an electron can be more easily ionized by absorbing one XUV photon. Even a weak XUV pulse can result in a higher ionization rate than the Ti:Sapphire laser. Moreover, the ionization process can be confined within one optical cycle of the Ti:Sapphire laser using an ultrashort XUV pulse [27], thus creating a ionization gate. The advantage of this scheme utilizing the XUV pulse is that it can efficiently

---

[2] The optical cycle of the blue pulse is 1.3 fs, thus, 8.3 fs and 12-fs laser pulses are multicycle fields, with 6.4 and 9.2 optical cycles, respectively.

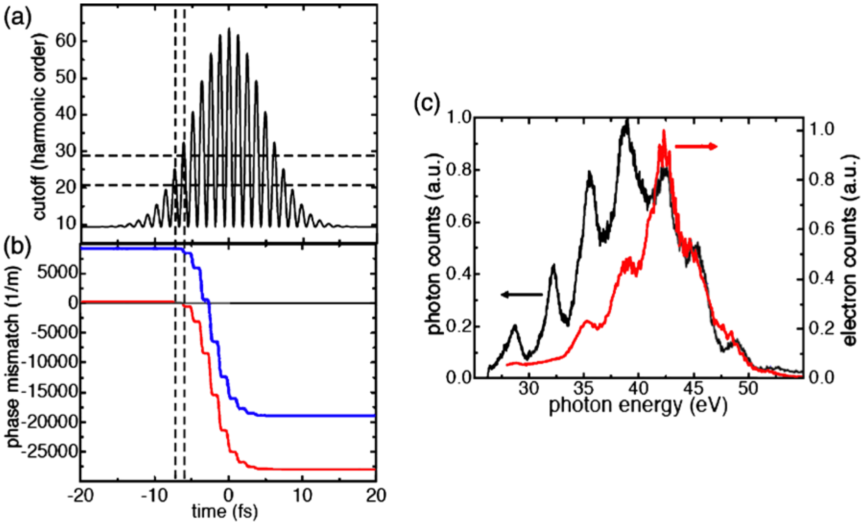

**Fig. 4.8** (**a**) High harmonic cutoff in different half-cycles. (**b**) Phase mismatch for the 25th harmonic in a straight fiber (*red line*) and the effect of employing a quasi-PM fiber (*blue*). (**c**) High-harmonic spectrum (*black line*) and corresponding photoelectron spectrum upshifted by the ionization potential without laser field (*red line*). Cited from Ref. [29]

boost ionization and thus significantly increase the efficiency of HHG. The simulation has shown that HHG intensity can be one or two orders of magnitude higher than that produced with a Ti:Sapphire field alone [25, 27]. This enhancement mechanism has also been demonstrated by using mixed gases [28].

## *4.5.2 Ionization Gating Induced by Macroscopic Effects*

Attosecond pulses are generated by a large number of ionizing atoms interacting with a focused laser pulse. This process consists of an interplay between the microscopic interaction and macroscopic effects due to ionization and phase matching (PM). In order to efficiently produce HHG and create IAPs, we must realize the PM conditions, which depend sensitively on the ionization-induced plasma of the gas medium. However, in the oversaturated ionization regime, ionization probability changes rapidly, thus significantly affecting the PM of HHG. On the basis of this idea, Thomann et al. [29] have recently demonstrated ionization gating induced by a dynamic PM mechanism. They firstly obtained a laser pulse of about 15 fs centered at 740 nm, and focused this laser onto a 150 μm diameter, 3.5 cm long hollow-core waveguide filled with Ar gas, in which high harmonics were generated. The phase mismatch between the driving laser and the high harmonics is shown in Fig. 4.8(b). We can see that the phase mismatch is initially small and that the high harmonics can be coherently built up. However, because of the rapid increase of the ionization rate, plasma density increases rapidly. The growing plasma contribution sweeps the phase mismatch through zero and then to large negative values, so that HHG is suppressed after the leading edge, resulting in the same ionization gating as that described in the previous subsection. By using this technique, supercontinuum harmonics covering from 25 to 55 eV have been produced (see Fig. 4.8(c)). In order to create IAPs, an Al filter was used to filter out lower-order harmonics. The FROG-CRAB technique was then used to characterize the temporal profile of IAPs. A Mo/Si multilayer mirror centered at 47 eV with a bandwidth of 13 eV was used to focus the supercontinuum onto Ne gas. Under the streak of the fundamental field, photoelectrons are ionized and then detected using a magnetic bottle time-of-flight spectrometer and a microchannel plate (MCP). The FROG-CRAB trace was constructed by recording a series of photoelectron spectra, from which the temporal profile of an isolated 210-as pulse was retrieved.

## 4.6 Two-Color Gating Method

As described in Sect. 4.2, the creation of IAPs generally requires highly sophisticated technology for the driving laser system, such as few-cycle pulses, CEP stabilization, and high intensity. In fact, the demonstration and measurement of IAPs have been realized using state-of-the-art few-cycle CEP-stabilized Ti:Sapphire laser systems (see Sect. 4.3). On the other hand, various methods of creating IAPs from multicycle laser fields, such as the use of a synthesized field consisting of the fundamental of a sub-10 fs laser and its second harmonic [8] and/or a MIR field [9], and the double optical gating (DOG) [10] technique that combines the PG and a two-color gating, have been proposed. HHG from multicycle laser fields has a major advantage for the energy scaling of IAPs using a high-power pump. In this section, we review a promising way to create IAPs using multicycle laser fields.

### *4.6.1 Two-Color Field Synthesis (800 nm + 400 nm, Parallel Polarization)*

In order to obtain IAPs, the temporal duration of the driving field must be shortened to a few optical cycles, within which either one-half or one cycle contributes to the generation of XUV radiation on the attosecond time scale. As one approach to creating IAPs, Oishi et al. [8] have examined the use of a two-color (TC) field consisting of a sub-10-fs fundamental ($\omega_0$) and its second-harmonic field ($2\omega_0$). This method is based on the interferometric electric field produced by two-color lasers ($\omega_0$: 800 nm + $2\omega_0$: 400 nm). The synthesized two-color electric field ($E_{mix}$) is generally expressed as

$$\begin{aligned} E_{mix}(t) = E_0 \exp\left[-2\ln 2\left(\frac{t}{\tau_0}\right)^2\right]\cos(\omega_0 t + \phi_{CE}) \\ + E_1 \exp\left[-2\ln 2\left(\frac{t-\delta t}{\tau_1}\right)^2\right]\cos(K\omega_0 t + \phi_{CE} + \phi_1), \end{aligned}$$

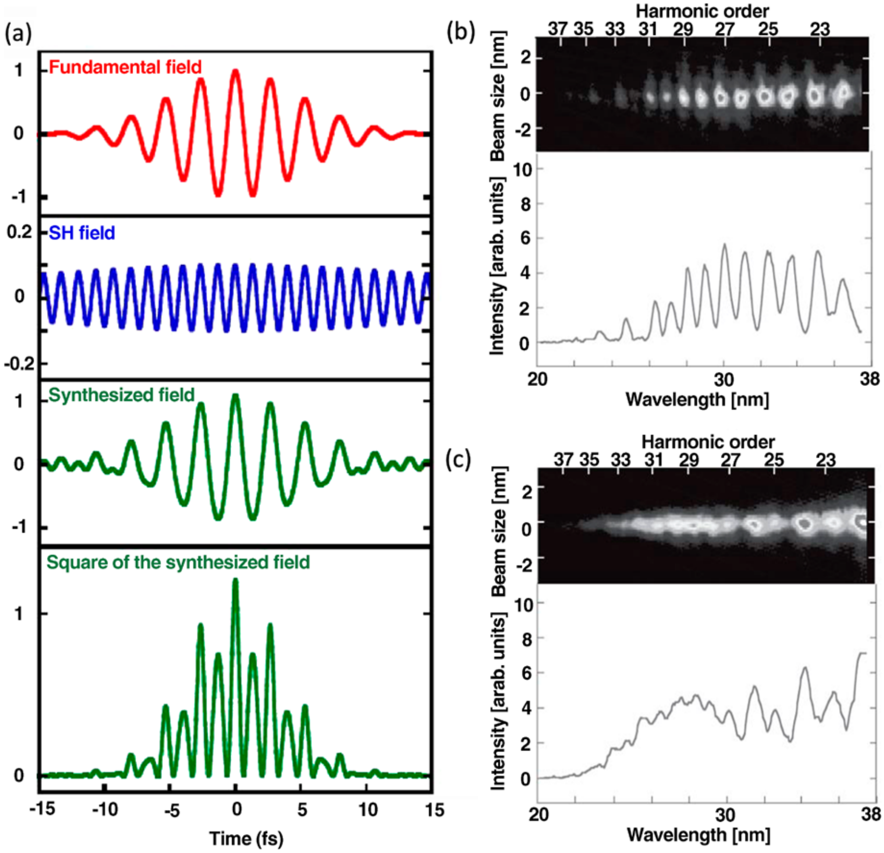

**Fig. 4.9** (**a**) Temporal profiles of fundamental, SH and synthesized TC electric fields and square of the TC electric field. $E_0$ and $E_1$ are 0.9 and 0.1, respectively. (**b**), (**c**) Typical spectral profiles with 20-fs and 9-fs two-color pulses (taken in a single shot), respectively. Adapted from Ref. [8]

where $K$ is the frequency ratio between the main field ($\omega_0$) and the supplementary laser field ($\omega_1 = K\omega_0$), the subscripts 0 and 1 denote the two laser field components, $E_{0,1}$ is the electric field amplitude, and $\tau_{0,1}$ and $\phi_1$ denote the pulse duration and phase, respectively. Here, these two pulses are parallel polarized, the lower-frequency component ($\omega_0$) acts as the main driving laser field, and the higher-frequency component ($K = 2$) modulates the main field. Figure 4.9(a) shows one example of the synthesized TC field. From the top to the bottom, the figure shows the fundamental field, second harmonic field, synthesized field, and square of the synthesized field, where $E_0$ and $E_1$ are set at 0.9 and 0.1, and $\tau_0$ and $\tau_1$ are 9 and 35 fs, respectively. All the other parameters ($\phi_{CE}$, $\phi_0$, and $\delta t$) are set to zero. As can be seen around the central peak of the synthesized field squared, the amplitude of the nearest neighbors on both sides is well suppressed by adding a small amount of the SH field (10 %) to the fundamental field. Therefore, efficient broadband XUV emission near the cutoff can be obtained even using relatively long driving pulses

($\sim$10 fs), and the SH pulse duration is allowed to be much longer than the fundamental pulse duration.

Figure 4.9(c) shows the typical observed continuum spectrum driven by TC fields (9 fs: 800 nm + 35 fs: 400 nm). Discrete components emerged at wavelengths longer than 33 nm, where the end of the discrete structure corresponds to the ionization potential plus three-times the ponderomotive energy gained by the second-highest driving field, as expected from the reshaped field in Fig. 4.9(a). The spectral bandwidth of the continuum structure is comparable to that of typical single attosecond pulses driven by few-cycle pulses. The pulse duration corresponding to the spectrum that was obtained would be 200 as. The harmonic energy within the spectrum limited by the Al filter was measured at 0.5 nJ, from which the generated energy in the gas cell was evaluated as 10 nJ. Note that these spectra were taken in a single-shot measurement. Most of the observed spectra have discrete structures (see Fig. 4.9(b)), and the continuum radiation shown in Fig. 4.9(c) appeared occasionally. This might be due to the unlocked CEP in this laser system. Moreover, when a TC field is composed of an 800-nm, 20-fs pulse and its SH, the continuum structure at the cutoff region disappears. This TC method with linearly polarized fundamental (800 nm) and second harmonic (400 nm) fields has a major advantage of simplifying the energy scaling of the IAPs; however, the pulse duration of the pump laser should be restricted to less than $\sim$ 10 fs with CEP stabilization. This technique has also been demonstrated experimentally by another group [33].

### *4.6.2 Double Optical Gating, Generalized Double Optical Gating*

The combination of TC gating (see Sect. 4.6.1) and PG (see Sect. 4.4) provides another gating scheme, such as a double optical gating (DOG), which enables us to create IAPs with a multicycle laser pulse. As explained in the previous subsection, the synthesis of the SH with the fundamental field breaks the inversion symmetry of the laser-atom interaction system. Therefore, both even and odd high harmonics are produced, i.e., the frequency interval becomes $\omega_0$. According to the Fourier transform theory, in the time domain, the synthesis of both odd and even harmonics results in a train of attosecond pulses with an equal interval of $2\pi/\omega_0 = T_0 = 2.7$ fs. In other words, in each optical cycle, only one attosecond pulse is produced, as shown in Fig. 4.10(b). In contrast, two attosecond pulses are produced in the one-color field (see Fig. 4.10(a)). As a result, for DOG, an IAP can be created even though the gate width increases to 2.7 fs, i.e., twice that of convectional PG. This condition enables us to use a longer driving pulse. On the other hand, as mentioned in Sect. 4.4, the ionization of the target medium is another important factor that limits the driving pulse duration. It can be seen from Fig. 4.4 that the DOG method can reduce the depletion of the neutral target. The duration of the longest pulses that can be used for creating IAPs with DOG is thus increased to 12 fs.

Mashiko et al. [10] have performed an experiment to demonstrate the DOG scheme. The main pulse was constructed by two counter-rotating circularly polar-

**Fig. 4.10** *Solid line*: driving fields for (**a**) PG and (**b**) DOG. *The filled curves* show the attosecond pulses. *The background color* shows the ellipticity of the driving field. Cited from Ref. [10]

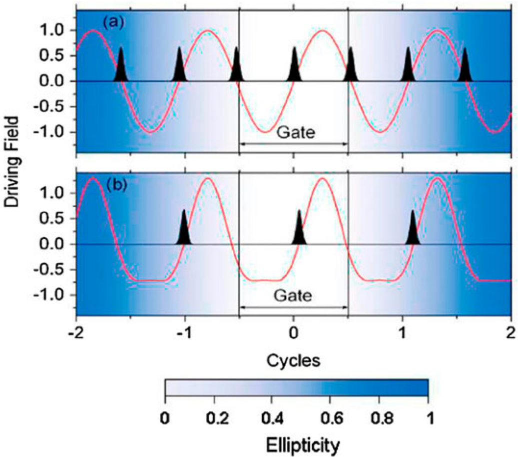

**Fig. 4.11** Harmonic spectrum images obtained by various gating methods. Cited from Ref. [10]

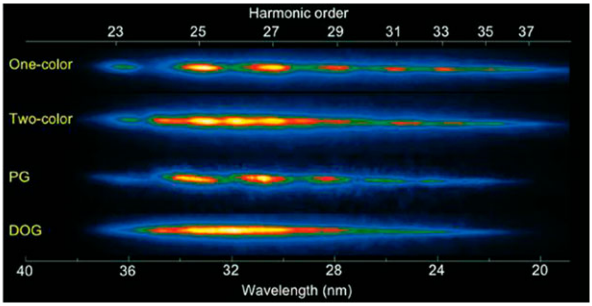

ized 9-fs laser pulses using the same method of conventional PG. Additionally, a linearly polarized SH pulse was synthesized using the main pulse. Figure 4.11 shows the harmonic spectra for one-color (linearly polarized fundamental field only), two-color (a SH is added to the fundamental field polarized in the same direction), and conventional PG and DOG methods. As expected, discrete odd harmonics are generated by the one-color field, whereas even harmonics appear with the two-color field, broadening the high harmonics. For the PG field, because the gating width is larger than 1.3 fs, discrete harmonics are produced. However, the harmonics merge with a supercontinuum in the DOG field. Also, note that the harmonic intensity is higher than that generated in the conventional PG case. Another advantage of DOG over the TC is that the supercontinuum appears through the plateau up to the cutoff region as opposed to the cutoff supercontinuum in the TC field shown in Fig. 4.9. In other words, the bandwidth of the supercontinuum generated by DOG is broader, which allows the creation of IAPs with a shorter duration. In addition, note that the time-dependent modulation of the ellipticity of DOG method enables us to significantly reduce the satellite attosecond pulses compared with that of the TC method. This is an important advantage, because in many pump-probe applications of IAPs, satellite attosecond pulses set the lower limit of the intensity of probe pulses. Strong satellite attosecond pulses may result in some misleading structures, which can make data analysis difficult.

The DOG concept has been generalized for the elliptically polarized field by Feng et al. group and called GDOG [36]. The difference of GDOG from DOG is that the main pulse is synthesized by two counter-rotating elliptically polarized pulses, e.g., $\varepsilon = 0.5$. As shown in Sect. 4.4, the gate width is $\Delta t_G \simeq 0.3\varepsilon\tau^2/T_d$. Generally, the delay $T_d$ is approximately equal to the driving pulse duration $\tau$, $\Delta\ t_G \approx 0.3\varepsilon\tau$. Because $\varepsilon < 1$ for an elliptically polarized field, a longer driving pulse can be used for the GDOG scheme to produce the same gate width. For instance, if $\varepsilon = 0.5$, the driving pulse duration of GDOG can be increased by a factor of 2 compared with that of DOG. To relax the required driving pulse duration, we also need to reduce the ionization of the target. As shown in Fig. 4.4, the ionization in the GDOG scheme is markedly reduced as compared with those of the PG and DOG methods. The upper limit of the driving pulse duration increases to 25 fs. Feng et al. have demonstrated the advantages of GDOG. The experimental setup is similar to that of conventional PG. However, to adjust the ellipticity of the driving pulse, a fused silica Brewster window was set between the birefringent plates. When the ellipticity is set to about 0.5, supercontinuum harmonics and an IAP of 260-as in duration are obtained from Ar gas using a 20-fs driving pulse. Moreover, from Ne gas, a 140-as IAP can be created even though the driving pulse duration is increased to 28 fs. Note that such a long driving pulse is much easier to create for most laboratories. Moreover, the energy can be much higher than those of few-cycle lasers, which is beneficial for producing high-power IAPs.

To produce high-power IAPs, not only the driving pulse duration requirement but also the stabilization of CEP need to be relaxed. This is because no high-peak-power laser system with CEP stabilization has been demonstrated yet. In their very recent work [30], Gilbertson et al. have repeated the GDOG experiment for different CEPs using a 9-fs driving pulse, which resulted in a narrower gating of 1 fs. Supercontinuum harmonics were observed from Ar, which were then focused onto a Kr gas jet. This converted the IAP photon burst into a replica photoelectron burst, which was recorded by a time-of-flight detector. Figure 4.12(a) shows the photoelectron spectrum for different CEPs. As can be observed, the spectrum is a continuum for all these CEPs but its intensity varies with CEP. The temporal profiles of the IAPs were constructed by the FROG-CRAB technique. Figures 4.12(b) and (c) show the temporal profiles for four different CEPs. Note that an IAP can be created for all these CEPs and its pulse duration is independent of the CEP. These results indicate that although the intensity changes with CEP, IAPs can be produced without CEP stabilization using the GDOG method if the gate width is sufficiently narrow. Gilbertson et al. have also successfully demonstrated this conclusion even using a 23-fs driving pulse. Therefore, a conventional CEP-unstabilized high-power laser can be used for creating IAPs. The output energy, however, is still very low, say, $\sim 170$ pJ [31], using a 2-mJ driving pulse. An important factor that limits its efficiency is the high ionization probability. As shown in Fig. 4.4, the ionization probability reaches more than 90 % when using a 23-fs driving pulse. Such a highly ionized gas medium leads to a high plasma density and a large phase mismatch, which prevents the efficient production of HHG and creation of IAPs.

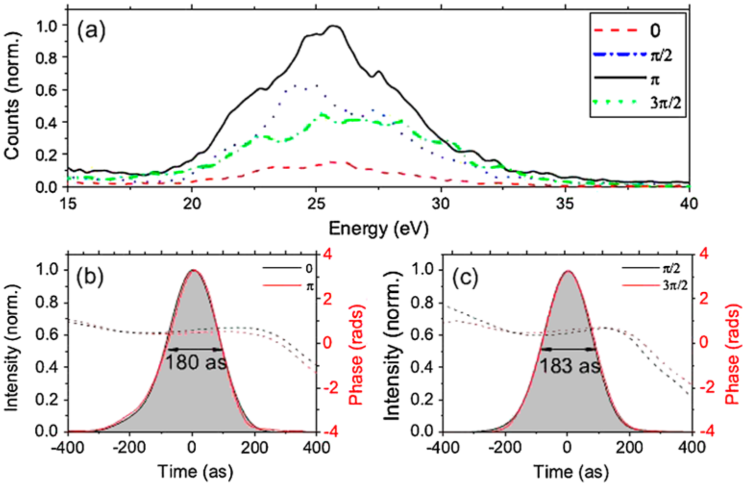

**Fig. 4.12** (**a**) Photoelectron spectrum produced by supercontinuum harmonics under a streaking fundamental field. (**b**) Temporal profiles and phases for an IAP obtained at CEP = 0 (*black line*) and $\pi$ (*red line*). (**c**) same as (**b**), but CEP = $\pi/2$ and $3\pi/2$. Cited from Ref. [30]

### *4.6.3 IR Two-Color Field Synthesis and IR Double Optical Gating*

The conventional TC gating method (800 nm + 400 nm, see Sect. 4.6.1) allows us to use multicycle laser fields to create IAPs. However, the pulse duration of the pump laser should be restricted to less than ∼ 10 fs with CEP stabilization [8]. Recently, Takahashi et al. [9] have proposed and demonstrated the generation of a continuum high-order harmonic spectrum by mixing multicycle (∼30 fs) TC laser fields. They utilized a TC IR driver source to markedly reduce the requirements for the pump laser system used for generating an IAP. A similar approach has been proposed theoretically by other groups [34, 35], who essentially assumed that a CEP-stabilized pulse is used for the driving field. As mentioned above, the requirement of CEP stabilization is one of the factors hindering the generation of an intense IAP by a TW-class high-power laser system. To meet this requirement for laser technology, they optimized and demonstrated, for the first time, the creation of an IAP with non-CEP-stabilized multicycle laser pulses.

This method is also based on the field synthesis produced by the TC (800 nm + MIR: $K < 1$). When the TC field is generated by an 800-nm, 30-fs pulse and a 1300-nm, 40-fs pulse, the field amplitude ($E_{mix}^2$) of the nearest neighbors on both sides of the central peak is markedly suppressed (see Fig. 4.13 ). Here, the intensity ratio ($\xi = E_1^2/E_0^2$) and phases ($\phi_{CE}, \phi_1$) are fixed at 0.15 and 0 rad, respectively. The intensity ratio between the central peak and the highest side peak is 0.8, which is almost the same as that of a 5-fs pulse at 800-nm (red line). They also considered the upper-limit pulse duration ($\tau_0$) of the main driving laser ($E_0$) to relax the requirements for the pulse duration. By optimizing the synthesized electric field ($E_{mix}$)

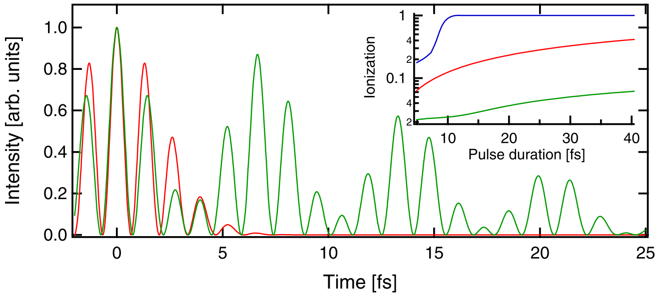

**Fig. 4.13** Field amplitude ($E_{mix}^2$) of an 800-nm, 5-fs pulse (*red line*) and TC field (*green line*). The TC field is generated by an 800-nm, 30-fs pulse mixed with a 1300-nm, 40-fs pulse. Intensity ratio ($\xi$) and phases ($\phi_{CE}$, $\phi_1$) are fixed at 0.15 and 0 rad, respectively. Inset, ADK ionization probabilities of an Ar atom calculated for the DOG (*blue line*), OC (*red line*), and TC (*green line*) methods as a function of the pulse duration of the main field. Cited from Ref. [9]

structure, the acceptable pulse duration for creating an IAP increases to 30-fs. In the TC field scheme, the cutoff formula of HHG is slightly modified as

$$E_{HHG} \simeq I_p + U_{p0}(3.17 + 2\sqrt{\xi}\omega_0/\omega_1) + 3.17U_{p1},$$

where $I_p$ is the binding energy of the electrons and

$$U_p\ [\mathrm{eV}] = 9.38 \times 10^{-14} I\ \left[\mathrm{W/cm^2}\right]\left(\lambda_0\ [\mu\mathrm{m}]\right)^2$$

is the electron quiver energy. Two new terms appear by adding the supplementary field in the two-color method. This equation indicates that the maximum cutoff energy can be increased by the supplementary IR field.

To efficiently generate IAPs, we must suppress the ground-state population depletion induced by the laser field. The inset of Fig. 4.13 shows the ADK ionization [18] probability of an argon gas calculated by the one-color (800 nm), DOG, and two-color methods as a function of the pulse duration of the main driving field. Here, for each method, the focused intensities are adjusted to obtain the same cutoff photon energy, which is approximately the 43rd harmonic order (18.6 nm). The peak intensities are determined as $2.8 \times 10^{14}$ W/cm$^2$ and $7 \times 10^{13}$ W/cm$^2$ for the DOG method, $2.45 \times 10^{14}$ W/cm$^2$ for the one-color method, and $1.15 \times 10^{14}$ W/cm$^2$ with $\xi = 0.15$ for the two-color method. Recently, a successful method of reducing the required pulse duration called the GDOG [36] method has been proposed (see Sect. 4.6.2). In the GDOG method, which uses 20-fs pulses, the ionization probability becomes the same as that of the DOG method, which uses 12-fs pulses. Although the GDOG method enables us to use a multicycle laser field to create IAPs, the target gas medium is fully ionized. On the other hand, we can reduce the intensity of the main field by mixing it with a supplementary IR field, which leads to a decrease in ionization probability. Obviously, our two-color method significantly reduces the ionization probability in the multicycle region. This is a major advantage for efficiently generating intense IAPs from neutral-medium conditions, because neutral media allow us to not only apply the most appropriate PM technique, but also employ an energy-scaling scheme.

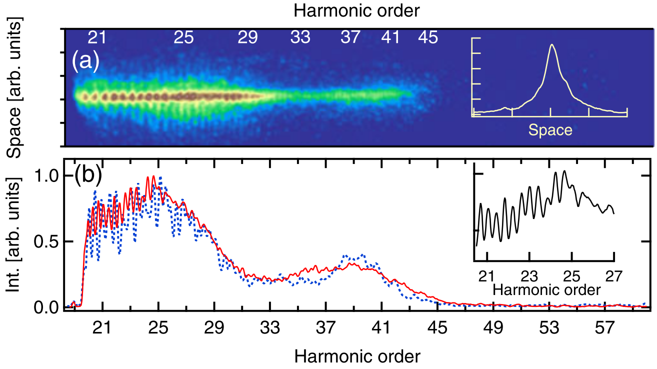

**Fig. 4.14** (**a**) 2D single-shot harmonic image driven by a TC field. (**b**) Single-shot 1D harmonic spectrum driven by a TC field. *The insets* in *the top and bottom panels* correspond to the spatial profile of cutoff harmonics (38th to 45th) and to the enlargement of the spectrum from the 21st to 27th harmonic order, respectively. Cited from Ref. [9]

Figure 4.14(a) shows a 2D single-shot harmonic spectrum imaged on a microchannel plate (MCP) generated by the two-color field (800 nm + 1300 nm). A dense harmonic spectrum appears in the lower-order region (see the inset of Fig. 4.14(b)). This dense harmonic spectrum can be considered as high-order sum and difference frequency generations (SFG, and DFG) [37]. Each harmonic component is assigned to SFG and/or DFG between 800 and 1300 nm. Since the resolution of the spectrometer is not sufficiently high to perfectly resolve each order in the dense spectrum, the modulation depth of the spectrum has a shallow structure. However, the dense components disappear as the harmonic order reaches the cutoff region, and a continuum harmonic spectrum can be clearly seen (33rd to 45th order). The inset of Fig. 4.14(a) shows the measured far-field spatial profile of the harmonic beam (38th to 45th order). In this TC scheme, Takahashi et al. obtained a high-quality beam with a Gaussian-like profile because laser intensity was fixed to less than the ionization threshold of the harmonic medium. When they changed the wavelength of the IR pulse from 1300 to 1400 nm while maintaining the focused intensity, the measured harmonic spectrum maintained its continuum structure (see the dotted line in Fig. 4.14(b)) as predicted on the basis of the concept. When extracting the cutoff region (38th to 45th order), the attosecond pulse duration becomes shorter than 500 as.

On the other hand, if the CEP changes shot by shot, the two-color electric field also changes. Therefore, it is generally necessary to stabilize and control the CEP of both the two-color components [38, 39]. In order to relax moderately the requirement for CEP stabilization, Tahahashi et al. also investigated the optimization of the mixed IR wavelength to suppress the multiburst HHG even if CEP changes. From the calculation, they indicate that the optimal wavelengths for suppressing the shoulder pulses range from 1280 to 1400 nm, where the multiple pulse burst is well suppressed, generating IAPs. In other words, the temporal profile of the attosecond pulse is not markedly affected by the CEP drift under the optimized-IR-wavelength condition. Actually, to evaluate the CEP effect, Takahashi et al. simultaneously measured the harmonic spectrum and the corresponding CEP for each laser shot using a nonlinear interferometer. Although the intensity of the cutoff region changed shot by shot, the continuum spectra were observed without CEP stabilization.

To further relax the requirement for the driving laser pulse, Lan and Takahashi et al. proposed to improve the IR-TC by combining it with PG. This optimized scheme is called IRDOG [21]. Similar to those in PG and DOG, the main pulse is constructed by two counter-rotating, elliptically polarized fundamental Ti:Sapphire laser pulses (800 nm). In addition, a weak IR control pulse at 1300 nm, which was optimized to relax the CEP dependence of IAPs as discussed above, is synthesized together with the main driving pulse. In such IR synthesis, as shown in Fig. 4.13, the time interval between the first and second maximum peaks increases to 6.7 fs, i.e., 5 times longer than that of the fundamental field alone. In this situation, attosecond pulses are generated every 6.7 fs instead of every 1.3 fs in the fundamental field alone. Consequently, IAPs can be produced as long as the gating width $\Delta t_G < 6.7$ fs rather than $< 1.3$ fs. This condition significantly relaxes the required driving pulse duration, which becomes 5 or 2.5 times longer than those of the conventional PG and DOG method, respectively. Similarly, IRDOG can be generalized to the elliptically polarized laser case (e.g., $\varepsilon = 0.5$), leading to the technique called GIRDOG, which allows us to further increase the driving pulse duration. Therefore, the upper limit of the driving pulse duration now has increased to 10 times longer than convectional PG, i.e., 60 fs, which is currently the longest pulse one can use for creating IAPs. Another great advantage of IRDOG and GIRDOG is that the ionization can be significantly suppressed. As shown in Fig. 4.4, the ionization probability is only 4 % if the driving pulse is 40 fs and is not completely depleted even for a 60-fs driving pulse. The low ionization allows us to easily realize the PM of HHG and achieve a high efficiency. Lan and Takahashi et al. have also simulated the CEP dependence of the high-harmonic spectrum and IAPs generated from Ar. It was shown that IAPs can be generated without CEP stabilization although their intensity varies with CEP. Therefore, the output energy of IAP can be scaled up by employing the well-established PM and energy-scaling method with a high-power CEP-unstabilized laser. Such a method will pave the way for creating intense IAPs using multicycle conventional driving laser pulses that are easily accessible for most ultrafast laser laboratories.

## 4.7 Other Methods

Aside from the above methods, there are many other methods proposed to produce more intense IAP, a broader supercontinuum and shorter IAPs as well as to relax the requirements for driving pulses. In this section, we briefly introduce several methods that have been proposed recently. One of them is based on the phase-matching effect [41–44], which can be called spatiotemporal gating. Because the macroscopic propagation effect plays an important role in HHG even though the ionization is far from saturated [41], by controlling the spatial shape of the fundamental beam and the geometry of the laser-gas interaction, the phase-matching of HHG may be realized under a specific condition, which can provide both a high efficiency and a strong temporal confinement. Several groups [41–44] have proposed and theoretically demonstrated this gating method to produce IAPs with a multi-cycle driving pulse.

On the other hand, aside from the TC gating, many other methods of shearing the temporal profile of driving pulses to create IAPs have been proposed. It includes the use of a three-color IR pulse [45], a specially chirped TC field [46], mid-IR modulated PG [47], and the synthesis of a THz or static field with a fundamental pulse [48]. However, these methods need a sophisticated and complex experimental setup compared with the TC gating introduced in Sect. 4.6.

Additionally, molecular HHG has attracted increasing attention in recent years. Since molecules have additional degrees of freedom and more complex structures, we can control HHG by aligning molecules. Lan et al. [49] and Hu et al. [50] have proposed to increase the harmonic cutoff and produce sub-100 IAP from stretched molecules. On the other hand, HHG from asymmetric molecules have also been investigated by several groups [51–53]. Similarly to TC gating, it was shown that both even and odd harmonics can be produced owing to the asymmetric structure of molecules [53]. Therefore, only one attosecond pulse is generated in every full cycle of the driving pulse, which enables us to create an IAP with a multi-cycle driving pulse. Another advantage over atomic HHG is that the production of IAPs from asymmetric molecules depends less sensitively on the CEP of the driving pulse [52]. With further development of the molecular alignment technique [54], it will become possible to experimentally create IAPs by molecular gating.

## 4.8 Summary—Generation of High-Power IAPs

As discussed above, various methods of generating an IAP have been proposed. For a breakthrough in *attosecond science* for XUV nonlinear optics and the next frontier, one of the most important issues is the development of high-power IAP sources. Progress in HHG techniques has resulted in the creation of IAPs and APTs. High-power APTs have been successfully generated as a result of research on harmonic energy scaling using a loosely focusing geometry [40, 55]. These APT sources have already been employed in an attosecond nonlinear optical experiment in the XUV region. Although IAPs have already achieved pulse durations as short as 80 attoseconds for tracing the motion of electrons inside atoms using a state-of-the-art Ti:Sapphire laser system, the output energy is still insufficient to induce nonlinear phenomena, because the pump pulse energy is typically limited to a few mJ owing to the requirements of sophisticated laser technology such as few-cycle pulses and CEP stabilization. In addition, a PM technique should be included in the generation conditions to efficiently create an IAP. At present, the maximum IAP yields are limited to a few nanojoules [6].

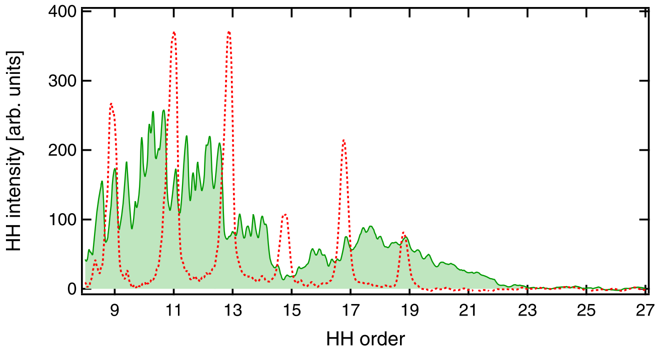

**Fig. 4.15** Harmonic spectra obtained with a one-color laser field of 800 nm (*dotted profile*) and TC laser field of 800 nm (9 mJ) + 1300 nm (1.5 mJ) (*filled profile*). Taken from [56]

Recently, Takahashi et al. have demonstrated one of the most promising methods of scaling the IAP energy. This scheme is based on TC-optimized IR laser field synthesis (see Sect. 4.6.3) and the energy-scaling method [40, 55] for HHG. As we previously explained in Sect. 4.6.3, the IR TC scheme for generating IAPs enables us to not only relax the requirements for the pump pulse duration (∼30 fs) but also reduce the ionization of the harmonic medium. These are major advantages for efficiently generating intense IAPs, because the use of neutral media allows us to use the PM technique. In the experiment, to increase both the interaction length and the acceptable pump energy, Takahashi et al. employed a loosely focused pumping geometry with $f = 4000$ mm. The target Xe gas was statically filled in the interaction cell of 10 cm length. Figure 4.15 shows a single-shot harmonic spectrum using the TC laser field (800 nm + 1300 nm). Although the spectrum in the cutoff region varied slightly with every laser shot because of the CEP of the two-color laser pulse was not stabilized, they were able to obtain the continuum spectrum with a high intensity. The total pulse energy of the continuum harmonic spectrum (18th–23rd) was evaluated to be ∼1 μJ. If the cutoff harmonic spectrum was extracted, IAPs of 600 as pulse duration would be obtained. By focusing this continuum spectrum, a XUV intensity of $> 10^{14}$ W/cm$^2$ could be obtained, which is sufficient for producing nonlinear effects in atoms and/or molecules.

## References

1. E. Goulielmakis et al., Science **320**, 1614 (2008)
2. F. Krausz, M. Ivanov, Rev. Mod. Phys. **81**, 163 (2009)
3. M. Hentschel et al., Nature (London) **414**, 509 (2001)
4. A. Baltuska et al., Nature **421**, 611 (2003)
5. R. Kienberger et al., Nature (London) **427**, 817 (2004)
6. F. Ferrari et al., Nat. Photonics **14**, 1 (2010)
7. G. Sansone et al., Science **314**, 443 (2006)
8. Y. Oishi et al., Opt. Express **16**, 7230 (2006)

9. E.J. Takahashi et al., Phys. Rev. Lett. **104**, 233901 (2010)
10. H. Mashiko et al., Phys. Rev. Lett. **100**, 103906 (2008)
11. Y. Zheng et al., Opt. Lett. **33**, 234 (2008)
12. T. Sekikawa et al., Nature (London) **432**, 605 (2004)
13. P. Tzallas et al., Nat. Phys. **3**, 846 (2007)
14. Q. Zhang et al., Opt. Express **23**, 9795 (2008)
15. P.B. Corkum, Phys. Rev. Lett. **71**, 1994 (1993)
16. P. Lan et al., Phys. Rev. A **79**, 043413 (2009)
17. P.B. Corkum et al., Opt. Lett. **19**, 1870 (1994)
18. M.V. Amosov et al., Ž. èksp. Teor. Fiz. **91**, 2008 (1986)
19. B. Shan et al., J. Mod. Opt. **52**, 277 (2005)
20. P. Tzallas et al., Nature **426**, 267 (2003)
21. P.F. Lan et al., Phys. Rev. A **83**, 063839 (2011)
22. T. Sekikawa et al., Nature **432**, 605 (2004)
23. T. Pfeifer et al., Opt. Express **15**, 17120 (2007)
24. C. Altucci et al., Opt. Lett. **35**, 2798 (2010)
25. A.D. Bandrauk, N.H. Shon, Phys. Rev. A **66**, 031401(R) (2002)
26. K.L. Ishikawa et al., Phys. Rev. A **75**, 021801(R) (2007)
27. P.F. Lan et al., Phys. Rev. A **76**, 043803 (2007)
28. E.J. Takahashi et al., Phys. Rev. Lett. **99**, 053904 (2007)
29. I. Thomann et al., Opt. Express **17**, 4611 (2009)
30. S. Gilbertson et al., Phys. Rev. Lett. **105**, 093902 (2010)
31. S. Gilbertson et al., Phys. Rev. A **81**, 043810 (2010)
32. H. Hasegawa et al., Phys. Rev. A **72**, 023407 (2005)
33. Y. Zheng et al., Opt. Lett. **33**, 234 (2008)
34. T. Pfeifer et al., Phys. Rev. Lett. **97**, 163901 (2006)
35. B. Kim et al., Opt. Express **16**, 10331 (2008)
36. X. Feng et al., Phys. Rev. Lett. **103**, 183901 (2009)
37. M.D. Perry et al., Phys. Rev. A **48**, 4051 (1993)
38. C. Vozzi et al., Phys. Rev. A **79**, 033842 (2009)
39. F. Calegari et al., Opt. Lett. **34**, 3125 (2009)
40. E. Takahashi et al., Phys. Rev. A **66**, 021802 (2002)
41. M.B. Gaarde, K.J. Schafer, Opt. Lett. **31**, 3188 (2006)
42. C.A. Haworth et al., Nat. Phys. **3**, 52 (2007)
43. V.V. Strelkov, E. Mevel, E. Constan, New J. Phys. **10**, 083040 (2008)
44. C. Liu et al., Opt. Lett. **35**, 2618 (2010)
45. H.C. Bandulet et al., Phys. Rev. A **81**, 013803 (2010)
46. P. Zou et al., Phys. Rev. A **81**, 033428 (2010)
47. W.Y. Hong et al., Opt. Express **18**, 11308 (2010)
48. W.Y. Hong et al., Opt. Express **17**, 5139 (2009)
49. P.F. Lan et al., Phys. Rev. A **74**, 063411 (2006)
50. S.X. Hu, L.A. Collins, J. Phys. B **39**, L185 (2006)
51. G.L. Kamta et al., J. Phys. B **38**, L339 (2005)
52. P.F. Lan et al., Opt. Lett. **32**, 1186 (2007)
53. P.F. Lan et al., Phys. Rev. A **76**, 021801(R) (2007)
54. A. Goban, S. Minemoto, H. Sakai, Phys. Rev. Lett. **101**, 013001 (2008)
55. E.J. Takahashi et al., Opt. Lett. **27**, 1920 (2002)
56. E.J. Takahashi et al., in *Abstracts of the 3rd International Conference on Attosecond Physics (ATTO3)*, University of Hokkaido, Sapporo, 6–8 July (2011)

# Chapter 5
# Attosecond Pulse Characterization

**F. Calegari, M. Lucchini, G. Sansone, S. Stagira, C. Vozzi, and M. Nisoli**

**Abstract** This chapter reviews several experimental methods to measure the temporal duration of sub-femtosecond pulses, either isolated or in the form of trains. Two classes of techniques, developed over the last few years, are presented in this chapter. The first is based on cross-correlation measurements between the extreme ultraviolet (XUV) pulse and the infrared (IR) driving pulse, the other is based on nonlinear effects induced by the attosecond XUV pulses.

## 5.1 Introduction

In the last decade the progress in attosecond science has been promoted by advances in laser technology and by the introduction of novel techniques for the measurement and application of attosecond pulses [1, 2]. Attosecond metrology is now a mature field; various methods for temporal characterization of sub-femtosecond pulses have been proposed and implemented, both in the case of trains and isolated pulses. So far two general schemes have been used. The first one is essentially a cross-correlation measurement between the extreme ultraviolet (XUV) pulse and a

---

F. Calegari · G. Sansone · S. Stagira · C. Vozzi · M. Nisoli (✉)
Department of Physics, Politecnico di Milano, Institute of Photonics and Nanotechnologies
(CNR-IFN), National Research Council of Italy, Piazza L. da Vinci 32, 20133 Milan, Italy
e-mail: mauro.nisoli@polimi.it

F. Calegari
e-mail: francesca.calegari@polimi.it

G. Sansone
e-mail: giuseppe.sansone@polimi.it

S. Stagira
e-mail: salvatore.stagira@polimi.it

C. Vozzi
e-mail: caterina.vozzi@polimi.it

M. Lucchini
ETH Zurich, Physics Department, Institute of Quantum Electronics Ultrafast Laser Physics,
HPT E11, Wolfgang-Pauli-Str. 16, 8093 Zurich, Switzerland
e-mail: mlucchini@phys.ethz.ch

L. Plaja et al. (eds.), *Attosecond Physics*, Springer Series in Optical Sciences 177,
DOI 10.1007/978-3-642-37623-8_5,

replica of the infrared (IR) driving pulse. This method has remarkable analogies with the streak-camera approach, used in the case of much longer pulses (hundreds of femtoseconds). The streak-camera approach, which will be described in Sect. 5.2, turned out to be an extremely useful method; indeed, many applications of isolated attosecond pulses reported so far have been based on this experimental technique. Novel cross-correlation schemes, as the Phase Retrieval by Omega Oscillation Filtering (PROOF), will be discussed in Sect. 5.3. The second class of measurements is based on the use of nonlinear effects and will be analyzed in Sect. 5.4.

## 5.2 Attosecond Streak-Camera Methods

A complete temporal characterization of attosecond pulses can be achieved by using a cross-correlation method. The basic idea of the measurement is the following: the attosecond pulse ionizes a gas, by single photon absorption, thus generating an attosecond electron pulse, which, far from any resonance, is a perfect replica of the optical pulse. The conversion of the XUV pulse into an electron wavepacket is obtained in the presence of a streaking IR pulse, whose electric field acts as an ultrafast phase modulator on the generated electron wavepacket. In this way a time-nonstationary filter [3], which is required to achieve the temporal characterization of the ultrashort pulse, is realized. The evolution of the photoelectron spectra as a function of the delay, $\tau$, between the attosecond and the IR pulses allows one to retrieve the temporal intensity profile and phase of the XUV pulses and the electric field of the IR pulse. This technique has been called Frequency Resolved Optical Gating for Complete Reconstruction of Attosecond Bursts (FROG CRAB) [4].

The first step of the measurement is ionization of an atom produced by an XUV pulse. The transition amplitude $a_{\mathbf{v}}$ from the ground state to a continuum state characterized by the momentum $\mathbf{v}$, can be obtained from first-order perturbation theory:

$$a_{\mathbf{v}} = -i \int_{-\infty}^{\infty} dt \mathbf{d}_{\mathbf{v}} \mathbf{E}_X(t) e^{i(W+I_p)t}, \tag{5.1}$$

where $\mathbf{E}_X(t)$ is the electric field of the XUV pulse; $\mathbf{d}_{\mathbf{v}}$ is the dipole transition matrix element from the ground state to the continuum state; $W = \mathbf{v}^2/2$ is the final kinetic energy of the electron (in atomic units) and $I_p$ is the atom ionization potential. From Eq. (5.1) it is possible to understand that, far from any resonance, the photoelectron spectrum is directly related to the attosecond field spectrum, both in amplitude and phase [5]. In order to obtain the temporal characteristics of the electron wavepacket, the photoelectron spectra have to be measured in the presence of a low-frequency laser field.

Considering a single atom in a classical electromagnetic field, the Schrödinger equation can be solved using the following approximations: (i) single active electron approximation: the atom is treated as a hydrogenlike system and multiple ionization is neglected; (ii) strong field approximation (SFA): the electron in the continuum is treated as a free particle moving in the electric field, i.e. the influence of the

Coulomb potential is completely neglected; (iii) only the ground state and the continuum are considered, the influence of the other bound states of the atom is completely neglected. By using these approximations it is possible to obtain a simple expression of the transition amplitude $a_{\mathbf{v}}$ [4, 6]:

$$a_{\mathbf{v}}(\tau) = -i \int_{-\infty}^{\infty} dt e^{i\phi(t)} \mathbf{d}_{\mathbf{p}(t)} \mathbf{E}_X(t-\tau) e^{i(W+I_p)t}, \tag{5.2}$$

where $\tau$ is the temporal delay between the XUV and low-frequency pulses, $\mathbf{p}(t) = \mathbf{v} + \mathbf{A}(t)$ is the instantaneous kinetic momentum, $\mathbf{A}(t)$ is the vector potential of the low-frequency field, $\mathbf{d}_{\mathbf{p}(t)}$ is the dipole transition matrix element from the ground state to the continuum with kinetic momentum $\mathbf{p}(t)$ and $\phi(t)$ is the temporal phase modulation imposed by the low-frequency field to the electron wavepacket, $\mathbf{d} \cdot \mathbf{E}_X(t)$, generated by the attosecond pulse in the continuum. Such phase modulation is given by

$$\phi(t) = -\int_{t}^{\infty} dt' \bigl[\mathbf{v} \cdot \mathbf{A}\bigl(t'\bigr) + \mathbf{A}^2\bigl(t'\bigr)/2\bigr]. \tag{5.3}$$

From (5.1) and (5.2) it is evident that the effect of the low-frequency field, usually in the infrared spectral region, on the electron wavepacket generated by the XUV pulse is to produce an ultrafast phase modulation $\phi(t)$. Assuming a linearly polarized IR field $\mathbf{E}_L(t) = \mathbf{E_0}(t)\cos(\omega_L t)$, long enough for the slowly varying envelope approximation to apply, the induced phase modulation can be written as the sum of three phase terms, $\phi(t) = \phi_1(t) + \phi_2(t) + \phi_3(t)$, given by the following expressions [4]:

$$\begin{aligned} \phi_1(t) &= -\int_{t}^{\infty} dt' U_p\bigl(t'\bigr), \\ \phi_2(t) &= (\sqrt{8WU_p}/\omega_L)\cos\theta\cos\omega_L t, \\ \phi_3(t) &= -(U_p/2\omega_L)\sin(2\omega_L t), \end{aligned} \tag{5.4}$$

where $U_p = E_0^2(t)/4\omega_L^2$ is the ponderomotive energy and $\theta$ is the angle between $\mathbf{v}$ and the IR polarization direction. The phase terms $\phi_2(t)$ and $\phi_3(t)$ oscillate at the IR field frequency and at its second harmonic frequency, respectively. Since $\phi_2(t)$ increases as $W^{1/2}$ and, in most cases, $U_p \ll W$, this phase term predominates over $\phi_1(t)$ and $\phi_3(t)$ for almost all observation angles except $\theta \approx \pi/2$. For a correct characterization of the electron wavepacket generated by the XUV pulses, the phase modulation imposed by the IR pulse must be fast enough. The bandwidth of the phase-modulator is given by the maximum value of $|\partial\phi/\partial t|$, which corresponds to the maximum energy shift of the photoelectron spectrum produced by the IR field [5], which we will call streaking field hereafter. For a correct XUV pulse reconstruction, such bandwidth should be a significant fraction of that of the attosecond field to be characterized.

It is possible to demonstrate that the photoelectron spectra $|a_{\mathbf{v}}(\tau)|^2$ as a function of the delay between the XUV and IR pulses contains all the information required for a complete reconstruction of the temporal characteristics of both the attosecond XUV pulse and the IR streaking pulse, and can be seen as a FROG trace. The frequency-resolved optical gating (FROG) is a well known technique used for complete temporal characterization of ultrashort light pulses [7]. In a FROG measurement the pulse to be characterized is divided into temporal slices by using a proper gate pulse. The FROG trace, $S(\omega,\tau)$, is given by the evolution of the spectra of these temporal slices, measured as a function of the delay $\tau$ between the pulse to be measured, with electric field $E(t)$, and the gate pulse, $G(t)$, which can be an amplitude or a pure phase gate:

$$S(\omega,\tau)=\left|\int_{-\infty}^{\infty} dt G(t)E(t-\tau)e^{i\omega t}\right|^2. \tag{5.5}$$

Comparing Eqs. (5.5) and (5.2) it is evident that the FROG CRAB trace $|a_{\mathbf{v}}(\tau)|^2$ can be considered as a FROG spectrogram of the electron wavepacket generated by the attosecond pulse, with a phase gate $G(t)=e^{i\phi(t)}$. In order to retrieve the temporal phase and intensity profile of the attosecond pulse it is possible to use various iterative algorithms, such as the principal component generalized projection algorithm (PCGPA) [8]. It is worth to point out that although the phase term $\phi(t)$ depends on the energy $W$, as shown by Eq. (5.4), the FROG algorithm neglects such a dependence, considering an energy-independent phase modulation. This assumption is usually referred to as the central momentum approximation (CMA) and it is well satisfied as long as the energy bandwidth does not exceed the central energy of the attosecond pulse. As a second approximation the dipole transition matrix element $\mathbf{d}_{\mathbf{p}}(t)$ is assumed constant, both in momentum (for the CMA) and in time. With such assumptions, the spectrogram obtained by acquiring the energy of the emitted electrons as a function of the delay between the XUV and IR pulses can be treated just like a conventional FROG trace.

Figure 5.1 shows the calculated evolution of the spectra of the photoelectrons generated by isolated transform-limited XUV pulses with different durations, as a function of the temporal delay between the XUV pulse and a 5-fs streaking pulse at 800 nm. The electrons are detected around $\theta=0^\circ$. When the XUV pulse duration is shorter than the optical period of the streaking field the photoelectron spectra follow the temporal evolution of the vector potential, $\mathbf{A}(t)$, of the streaking pulse. When the XUV pulse duration is comparable or longer than the optical cycle of the IR field, the photoelectron spectra show sidebands spaced by $\hbar\omega_L$ (where $\omega_L$ is the angular frequency of the IR pulse) in correspondence of the temporal overlap between the XUV and IR pulses. Such sidebands are due to quantum interferences between different portions of the ejected electron wave packet experiencing the same momentum shift by the IR field.

An important advantage of the FROG CRAB technique is its great versatility, that makes it possible to analyze not only isolated pulses, with a duration that can be longer or shorter than the period of the modulating electric field, but also trains of attosecond pulses or even intermediate configurations of arbitrary complexity [4]. It is also possible to exploit the dependence of $\phi(t)$ on the envelope of the modulating electric field to retrieve the global temporal structure in the case of trains of non

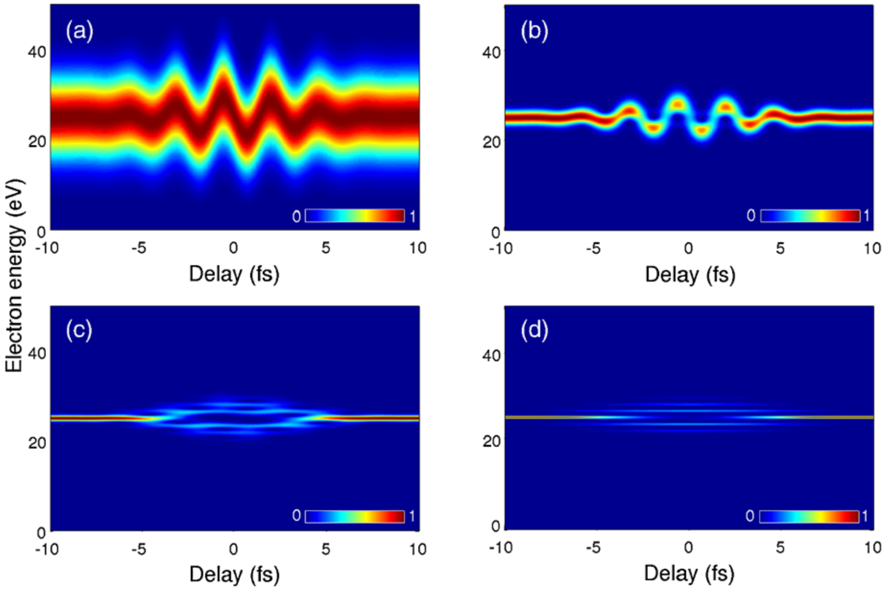

**Fig. 5.1** Evolution of the photoelectron spectra as a function of the delay between the XUV and IR pulses, calculated for isolated and transform-limited XUV pulses with duration of 130 as (**a**), 750 as (**b**), 1.5 fs (**c**) and 5 fs (**d**), assuming a 5-fs IR field with peak intensity $I = 1.5 \times 10^{15}$ W/cm$^2$. The photoelectrons average kinetic energy is 25 eV and the detection angle is kept fix around $\theta = 0°$

identical pulses. The FROG CRAB technique also presents other advantages, inherited from FROG: due to the high redundancy of information in the FROG CRAB trace, it is very robust against noise, and it is unlikely to properly converge if experimental flaws exist [9]. In addition, in the case of isolated attosecond pulses only one optical cycle of the gating IR field is needed for a correct reconstruction, while FROG CRAB traces are usually acquired over a longer time span, thus increasing even more the redundancy of information. Moreover, the retrieval of the modulating electric field offers an additional opportunity to check the validity of the measurement, by comparison with the results of the standard methods for visible pulses. However, FROG CRAB also presents some limitations, that may hinder a correct reconstruction, especially when dealing with sub-100-as pulses or with a main XUV pulse with a residual satellite pulse. The PCGPA, for example, can be too demanding in this case: in fact, the periodic boundary conditions assumed in its reconstruction algorithm are not always satisfied in the case of FROG CRAB traces. In addition, PCGPA needs to operate on square matrices, that is, the number of points on the energy axis must be the same as the one on the delay axis. Most experimental FROG CRAB spectrograms do not satisfy this requirement and the number of steps on the delay axis has to be increased by interpolating the existing ones before feeding the trace to the inversion algorithm. This can cause the appearance of unphysical patterns when fast variations of the spectrogram are present (as in the case of satellite pulses) and the PCGPA fails to retrieve the correct pulse values. In order to overcome these problems, Gagnon and co-workers developed a new retrieval algorithm, called least squares generalized projections algorithm (LSGPA) [10]. This algorithm does not require periodic boundary conditions and obviates the need to interpolate along the delay axis. It was shown that LSGPA is able to correctly reconstruct FROG CRAB traces that PCGPA failed to, and was successfully used to characterize 80-as pulses with a small residual satellite.

### *5.2.1 Experimental Results*

The first experimental demonstration of the attosecond streak-camera method was reported in 2001 by Hentschel et al. [11]. Isolated attosecond pulses were produced by spectrally selecting the cutoff region of the harmonic spectrum generated in neon by 7-fs driving pulses. The XUV beam transmitted by a circular Zr filter, with a size matching the diameter of the harmonic beam, and the co-propagating annular IR beam were focused onto a second gas jet by a concentric piezo-controlled double mirror unit. The central part of the mirror unit was a Mo/Si multilayer acting as a bandpass filter centered at 90 eV (bandwidth $\approx 5$ eV). Upon measuring the evolution of the width of the photoelectron spectrum as a function of the delay between the XUV and IR pulses it was possible to measure a XUV pulse duration of $650 \pm 150$ as. Using the same technique, pulses as short as 250 as were measured in 2004 [12].

The first demonstration of complete temporal characterization of attosecond pulses by the FROG CRAB technique was reported in 2006 by Sansone et al. [13]. Isolated attosecond pulses were generated by using the polarization gating technique in combination with few-optical-cycle driving pulses. Figure 5.2(a) shows the photoelectron spectra as a function of the delay between the XUV and the streaking IR pulses. The periodic oscillation of the FROG CRAB trace follows the temporal evolution of the vector potential of the streaking pulse. The presence of chirp in the XUV pulse results in a narrowing or broadening in the streaked electron spectra at the zero-crossings of the driving vector potential (displayed by the white dashed lines in Fig. 5.2(a)), with a corresponding increase or decrease of the electron count rates, respectively. A nearly transform-limited pulse is characterized by an almost constant electron count rate, as shown in Fig. 5.2(a). The temporal characteristics of the attosecond pulses were retrieved using the principal-component generalized projection algorithm (PCGPA) [8]. In the reconstructed temporal intensity profile of the attosecond pulses, reported in Fig. 5.2(b), the pulse duration was 130 as. Subsequently, the FROG CRAB technique has been applied to the measurement of 80-as isolated attosecond pulses produced by selecting the cutoff portion of the harmonic spectrum generated by sub-1.5-cycle laser pulses [14].

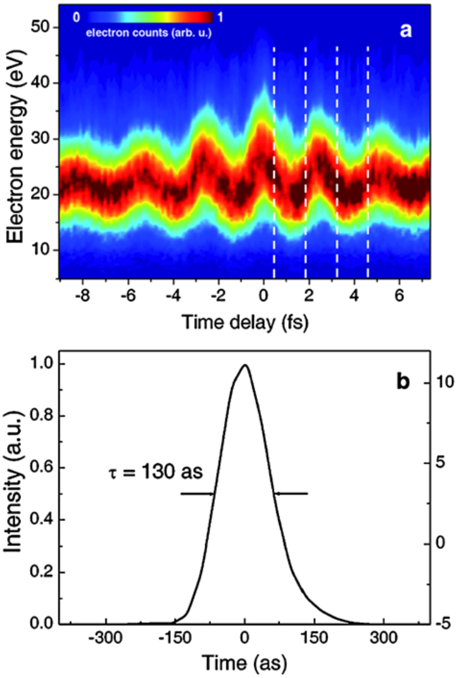

**Fig. 5.2** FROG CRAB measurement and reconstruction: (**a**) complete experimental FROG CRAB trace measured as a function of the temporal delay between the attosecond and the streaking IR pulses. Isolated attosecond pulses were generated by phase-stabilized, 5-fs pulses with modulated polarization state. The white dashed lines mark a few zero-crossings of the driving vector potential: the almost constant electron count rates around these positions is a consequence of the excellent chirp compensation by a 300-nm thick aluminum foil. (**b**) Reconstruction of temporal intensity profile of the attosecond pulses after $5 \times 10^4$ iterations of the PCGPA algorithm

## 5.3 Novel Temporal Characterization Techniques

In 2003 Quéré et al. proposed a technique based on the measurement of the photoelectron wave-packet generated by two replica of the same attosecond pulse and shifted in energy by an intense IR field [15]. The technique can be considered as an extension of the SPIDER (Spectral Phase Interferometry for Direct Electric field Reconstruction) method [16] used in the femtosecond domain, where two replica of the same pulse are delayed and shifted in frequency by sum-frequency generation in a nonlinear crystal using a strongly chirped visible-IR pulse. Simulations showed that the technique could be applied for the characterization of extremely short pulses down to 12.5 as. A similar approach was introduced in 2005 by Cormier et al. analyzing the interferogram generated by two trains of attosecond pulses created by two delayed driving pulses slightly shifted in frequency [17]. From the interference pattern, observed either in the spectral domain (due to the time-delay between the two driving pulses) or in the spatial domain when the two driving pulses are focused to slightly different positions, it is possible to reconstruct the time evolution of the train of attosecond pulses. The latter technique has been dubbed SEA (Spatially Encoded Arrangement) SPIDER. Simulations indicate that this technique could also be applied for the measurement of isolated attosecond pulses. Experimentally it was implemented for the characterization of the 19th harmonic generated by a Ti:Sa laser amplifier [18]. The generation of two isolated attosecond pulses shifted in frequency and with a suitable delay, however, still represents a challenge from the experimental point of view.

Another approach was proposed by Dudovich and co-workers [19] that demonstrated *in situ* characterization of a train of attosecond pulses by adding a small second harmonic field to the fundamental field. Due to the symmetry breaking of the total driving field, even harmonics of the fundamental frequency were generated. By changing the delay between the two fields, their relative phase is varied inducing a modulation in the intensity of the even harmonics signal. By measuring such oscillation as a function of the delay, the relative phase of the odd harmonics can be characterized and the attosecond pulse train can be reconstructed.

### *5.3.1 Phase Retrieval by Omega Oscillation Filtering (PROOF)*

In 2010 a novel technique was proposed that could allow the characterization of broadband attosecond pulses using IR fields characterized by low intensity ($I \sim 10^{11}$ W/cm$^2$). The method, indicated as PROOF (Phase Retrieval by Omega Oscillation Filtering) [20] is closely related to the RABITT (Reconstruction of Attosecond Beating by Interference of Two-photon Transitions) technique, used for the characterization of trains of attosecond pulses [21]. In the case of RABITT the relative phase between two consecutive harmonics, $\omega_{n-1}$ and $\omega_{n+1}$, is retrieved by measuring the photoelectron signal obtained by two-color (XUV+IR) photoionization. Two paths can contribute to the generation of electrons, whose energy is intermediate between the photoelectron signal due to single photon absorption of the two harmonics: absorption of a XUV photon of the harmonic $n+1$ and emission of an IR photon, or absorption of a XUV photon of the harmonic $n-1$ and of an IR photon. As the two paths are indistinguishable they interfere and the photoelectron signal (sideband or order $n$) presents a modulation given by [21–23]:

$$A_f \cos\bigl(2\omega_L\tau + \varphi_{n-1} - \varphi_{n+1} + \Delta\varphi^f_{atomic}\bigr), \tag{5.6}$$

where $A_f$ depends on the matrix dipole moments between the initial and final states, $\omega_L$ is the angular frequency of the IR field, $\tau$ is the delay between the IR and XUV pulses, $(\varphi_{n-1} - \varphi_{n+1})$ is the difference between the phases of the harmonics $n+1$ and $n-1$ and $\Delta\varphi^f_{atomic}$ is the phase difference of the matrix elements corresponding to photoionization from the $n+1$ and $n-1$ harmonics. The physical interpretation of the PROOF technique is closely related to the previous formula, but takes into account that the XUV spectrum is no longer a discrete series of harmonics but a continuum distribution. The photoelectron signal at energy $\omega_v$ is due to the superposition of three terms oscillating at different frequencies:

$$I(\omega_v, \tau) = I_0 + I_{\omega_L} + I_{2\omega_L} \tag{5.7}$$

The three terms on the right-hand side of Eq. (5.7) represent a constant term ($I_0$) and two terms oscillating in time with frequency $\omega_L$ ($I_{\omega_L}$) and $2\omega_L$ ($I_{2\omega_L}$), related to transitions which involve the absorption and the emission of IR photons. From the term oscillating at the IR frequency $\omega_L$, it is possible to extract the phase of the attosecond pulse. Indeed this term is given by four different contributions:

$$\begin{aligned} I_{\omega_L} \propto & -U(\omega_v)U(\omega_v+\omega_L)e^{i[\varphi(\omega_v)-\varphi(\omega_v+\omega_L)]}e^{(i\omega_L\tau)} \\ & + U(\omega_v)U(\omega_v+\omega_L)e^{i[\varphi(\omega_v+\omega_L)-\varphi(\omega_v)]}e^{(-i\omega_L\tau)} \\ & + U(\omega_v)U(\omega_v-\omega_L)e^{i[\varphi(\omega_v)-\varphi(\omega_v-\omega_L)]}e^{(-i\omega_L\tau)} \\ & - U(\omega_v)U(\omega_v-\omega_L)e^{i[\varphi(\omega_v-\omega_L)-\varphi(\omega_v)]}e^{(i\omega_L\tau)} \end{aligned} \tag{5.8}$$

where $U(\omega)$ and $\varphi(\omega)$ are the spectral amplitude and phase of the XUV pulse at frequency $\omega$, respectively. The first term of Eq. (5.8) represents a final state with energy $\omega_v + \omega_L$ that can be reached either by direct photo-absorption of a photon $\omega_v + \omega_L$ or by the absorption on an XUV photon $\omega_v$ and an IR photon $\omega_L$. These two terms interfere depending on the relative phase of the two paths: $\varphi(\omega_v) - \varphi(\omega_v + \omega_L) + \omega_L\tau$. The second term represents a final state with energy $\omega_v$ that can be reached by direct absorption of an XUV photon $\omega_v$ or by a two-color process: absorption of an XUV photon $\omega_v + \omega_L$ and emission of an IR photon $\omega_L$. This term will contribute to the signal at frequency $\omega_v$. The third term corresponds to a signal at frequency $\omega_v - \omega_L$ and the fourth one to a signal at frequency $\omega_v$ involving absorption of a photon $\omega_v - \omega_L$. It is important to observe that this interpretation is closely related to the interpretation of the RABITT signal, the main difference being that in the case of the RABITT no XUV photon at the harmonic order $n$ is present as the XUV spectrum is composed of a discrete series of odd harmonics. In the RABITT and PROOF techniques, the intensity of the IR fields should be limited to the perturbative regime as they rely on the assumption that only paths involving a single IR photon contribute to the signal. Upon increasing the IR intensity, this assumption becomes invalid and systematic errors can be introduced in the reconstruction of the attosecond field. However also in such cases, simulations show that the PROOF method can reconstruct attosecond field waveforms with a precision superior to the FROG CRAB technique [20].

## 5.4 Attosecond Metrology by XUV Nonlinear Optics

A different class of attosecond metrology techniques is based on the use of nonlinear effects, as in the case of femtosecond visible or near-infrared pulses. The extension of nonlinear optics to the XUV spectral region has been so far limited by the low photon yield of the available attosecond sources and by the low nonlinear cross-section in the XUV spectral region. Due to the high photon energy of the XUV pulses, nonlinear processes induced by attosecond pulses necessarily lead to ionization. Since the XUV field intensity does not exceed $10^{16}$ W/cm$^2$, ionization proceeds by multiphoton absorption. For a second-order process the photoelectron yield $Y^{(2)}$ from an interaction volume $V$ with an atomic density $n_a$ is given by $Y^{(2)} = \sigma^{(2)} F^2 \tau n_a V$, where $\sigma^{(2)}$ is the two-photon cross-section, which is of the order of $10^{-49}$ to $10^{-52}$ cm$^4$ s for a range of excess energies from zero to the ionization energy [24], $F$ is the photon flux, and $\tau$ is the pulse duration. In order to have a measurable two-photon ionization yield XUV intensities well exceeding $10^8$ W/cm$^2$ are required. This is the reason why the observation of two-photon processes in the XUV region by using attosecond pulses is a rather demanding experimental problem [25].

Various nonlinear processes have been used so far for the measurement of ultrashort XUV pulse duration: (i) two-photon above threshold ionization (ATI); (ii) two-photon absorption in atoms; (iii) two-photon double ionization; (iv) Coulomb explosion of diatomic molecules via two-photon double ionization. In 2004 Sekikawa et al. reported on the temporal characterization of the ninth harmonic of the driving sub-10 fs pulses of 3.1 eV (central wavelength at 400 nm), by the autocorrelation technique, employing two-photon above-threshold ionization of helium [26, 27]. The photon energy of the ninth harmonic (27.9 eV) is already above the first ionization threshold of He, whereas two-photon absorption of 27.9-eV photons is below the double ionization threshold. In the case of two-photon ATI, a second photon is absorbed beyond the one required for ionization of helium atom. In the experiment, two time-delayed replica of the driving pulse at 3.1 eV were focused, with no spatial overlapping, into an argon gas jet for high-order harmonic generation. The ninth harmonic pulses were focused into helium by an Sc/Si multilayer spherical mirror. The photoelectrons were collected and energy-resolved by using a magnetic bottle photoelectron spectrometer. Upon measuring the number of photoelectrons with energy corresponding to the two-photon ATI peak (at 31.2 eV) as a function of the time delay between the two ninth-harmonic pulses, it was possible to measure the autocorrelation trace, with a minimum pulse duration of $950 \pm 90$ as. The pulse energy of the ninth harmonic was 2 nJ on the target. More recently the temporal phase and intensity profile of the ninth harmonic pulses at 27.9 eV have been measured by using FROG based on two-photon ATI in He [28]. The shortest measured pulse duration was 860 as with a flat phase.

The first observation of two-photon absorption (TPA) ionization of helium induced by high-order harmonics of a Ti:sapphire laser was reported by Kobayashi et al. in 1998 [29]. They measured the autocorrelation trace of the ninth harmonic by acquiring the He$^+$ yield induced by two-photon absorption: the measured pulse duration was 27 fs. In 2003, by using the same nonlinear process, Tzallas et al. demonstrated the first autocorrelation measurement of a train of attosecond pulses [30]. Seventh to fifteenth harmonics generated in a xenon jet and transmitted by an indium filter, were injected into a volume autocorrelator. The XUV beam was divided in two parts by a spherical mirror cut into two halves, which focused the two beams in a helium gas jet. One of the two parts of the mirror was mounted on a piezo-crystal translation unit in order to introduce a controllable delay $\tau$ between the two pulse replica. The He$^+$ yield induced by TPA was measured by a time-of-flight mass spectrometer as a function of $\tau$, and provided the second-order autocorrelation signal. The measured ion yield exhibits a clear attosecond structure, with a periodicity twice that of the driving laser field, from which it was possible to obtain an estimate of 780 ± 80 as for the average duration of the attosecond pulses in the train.

Two-photon double ionization (TPDI) of He induced by femtosecond harmonic pulses was used in 2005 to measure the autocorrelation trace of the 27th harmonic (42-eV photon energy) of Ti:sapphire laser pulses [32]. In this case the two harmonic pulse replicas were obtained by spatially splitting the harmonic beam with a separator of silicon carbide, one of whose parts was mounted on a translation stage in order to introduce a time-delay between the two pulse replicas. The autocorrelation trace was obtained by measuring the yield of doubly charged helium ions as a function of the delay: minimum harmonic pulse duration was 8 fs, with a 24-nJ pulse energy (corresponding to an estimated intensity at the focal point of $1.7 \times 10^{13}$ W/cm$^2$). So far TPDI has not been reported in the attosecond regime.

Coulomb explosion of diatomic molecules via two-photon double ionization has been used for the measurement of the interferometric autocorrelation of an attosecond pulse train [25, 31], due to the larger nonlinear cross section with respect to rare-gas atoms. The experimental apparatus is similar to that used in the case of TPDI of He described above [32]; in this case authors used $N_2$ molecules instead of He atoms, and two-photon absorption was obtained by using high-order harmonics at orders from 9th to 19th. The estimated intensity of the 11th harmonic at the focal point was $3 \times 10^{14}$ W/cm$^2$. The measured time-of-flight mass spectrum shows a two-peak structure corresponding to $N^+$ ions produced by Coulomb explosion of $N_2^{2+}$ ions induced by two-photon double ionization. The two peaks correspond to ions with the same kinetic energy release of 5 eV emitted in the forward and backward directions. The integrated ion yield as a function of the temporal delay between the two XUV pulses displays clear bunches with a periodicity twice that of the driving laser field, which correspond to the interferometric autocorrelation trace of the train of attosecond pulses, with an estimated duration of the pulse envelope of 320 as in full width at half maximum. This value corresponds to $\sim 1.3$ optical cycles of the principal carrier frequency of the 11th harmonic field.

## 5.5 Conclusions

Various schemes for temporal characterization of attosecond pulses have been reviewed in this chapter. Particular emphasis has been devoted to the streak-camera approach, which is at the basis of several important applications of isolated attosecond pulses. The FROG CRAB technique, based on the streaking concept, is now used in various laboratories as a standard method for temporal characterization of attosecond pulses. Advantages and limitations of such a reconstruction method have been pointed out. Recently proposed experimental techniques offer the possibility to extend the attosecond metrology to the sub-100-as temporal regime, where the FROG CRAB approach starts to present limitations.

## References

1. F. Krausz, M. Ivanov, Rev. Mod. Phys. **81**, 163 (2009)
2. M. Nisoli, G. Sansone, Prog. Quantum Electron. **33**, 17 (2009)
3. I. Walmsley, V. Wong, J. Opt. Soc. Am. B **13**, 2453 (1996)
4. Y. Mairesse, F. Quéré, Phys. Rev. A **71**, 011401(R) (2005)
5. F. Quéré, Y. Mairesse, J. Itatani, J. Mod. Opt. **52**, 339 (2005)
6. M. Lewenstein, Ph. Balcou, M.Yu. Ivanov, A. L'Huillier, P.B. Corkum, Phys. Rev. A **49**, 2117 (1994)
7. R. Trebino, *Frequency-Resolved Optical Gating* (Kluwer Academic, Boston, 2000)
8. D. Kane, IEEE J. Quantum Electron. **35**, 421 (1999)
9. H. Wang, M. Chini, S.D. Khan, S. Chen, S. Gilbertson, X. Feng, H. Mashiko, Z. Chang, J. Phys. B, At. Mol. Opt. Phys. **42**, 134007 (2009)
10. J. Gagnon, E. Goulielmakis, V.S. Yakovlev, Appl. Phys. B **92**, 25 (2008)
11. M. Hentschel, R. Kienberger, Ch. Spielmann, G.A. Reider, N. Milosevic, T. Brabec, P.B. Corkum, U. Heinzmann, M. Drescher, F. Krausz, Nature **414**, 509 (2001)
12. R. Kienberger, E. Goulielmakis, M. Uiberacker, A. Baltuška, V. Yakovlev, F. Bammer, A. Scrinzi, Th. Westerwalbesloh, U. Kleineberg, U. Heinzmann, M. Drescher, F. Krausz, Nature **427**, 817 (2004)
13. G. Sansone, E. Benedetti, F. Calegari, C. Vozzi, L. Avaldi, R. Flammini, L. Poletto, P. Villoresi, C. Altucci, R. Velotta, S. Stagira, S. De Silvestri, M. Nisoli, Science **314**, 443 (2006)
14. E. Goulielmakis et al., Science **320**, 1614 (2008)
15. F. Quéré, J. Itatani, G.L. Yudin, P.B. Corkum, Phys. Rev. Lett. **90**, 073902 (2003)
16. C. Iaconis, I.A. Walmsley, Opt. Lett. **23**, 792 (1998)
17. E. Cormier, I.A. Walmsley, E.M. Kosik, A.S. Wyatt, L. Corner, L.F. DiMauro, Phys. Rev. Lett. **94**, 033905 (2005)
18. Y. Mairesse, O. Gobert, P. Breger, H. Merdji, P. Meynadier, P. Monchicourt, M. Perdrix, P. Salières, B. Carré, Phys. Rev. Lett. **94**, 173903 (2005)
19. N. Dudovich, O. Smirnova, J. Levesque, Y. Mairesse, M.Yu. Ivanov, D.M. Villeneuve, P.B. Corkum, Nat. Phys. **2**, 781 (2006)
20. M. Chini, S. Gilbertson, S.D. Khan, Z. Chang, Opt. Express **18**, 13006 (2010)
21. P.M. Paul, E.S. Toma, P. Breger, G. Mullot, F. Augé, Ph. Balcou, H.G. Muller, P. Agostini, Science **292**, 1689 (2001)
22. V. Véniard, R. Taïeb, A. Maquet, Phys. Rev. Lett. **74**, 4161 (1995)
23. V. Véniard, R. Taïeb, A. Maquet, Phys. Rev. A **54**, 721 (1996)
24. L.A.A. Nikolopoulos, P. Lambropoulos, J. Phys. B **34**, 545 (2001)
25. K. Midorikawa, Y. Nabekawa, A. Suda, Prog. Quantum Electron. **32**, 43 (2008)
26. T. Sekikawa, A. Kosuge, T. Kanai, S. Watanabe, Nature **432**, 605 (2004)
27. N. Miyamoto, M. Kamei, D. Yoshitomi, T. Kanai, T. Sekikawa, T. Nakajima, S. Watanabe, Phys. Rev. Lett. **93**, 83903 (2004)
28. A. Kosuge, T. Sekikawa, X. Zhou, T. Kanai, S. Adachi, S. Watanabe, Phys. Rev. Lett. **97**, 263901 (2006)
29. Y. Kobayashi, T. Sekikawa, Y. Nabekawa, S. Watanabe, Opt. Lett. **23**, 64 (1998)
30. P. Tzallas, D. Charalambidis, N.A. Papadogiannis, K. Witte, G.D. Tsakiris, Nature **426**, 267 (2003)
31. Y. Nabekawa, T. Shimizu, T. Okino, K. Furusawa, H. Hasegawa, K. Yamanouchi, K. Midorikawa, Phys. Rev. Lett. **97**, 153904 (2006)
32. Y. Nabekawa, H. Hasegawa, E.J. Takahashi, K. Midorikawa, Phys. Rev. Lett. **94**, 043001 (2005)

# Chapter 6
# Strong-Field and Attosecond Physics with Mid-infrared Lasers

**Anthony D. DiChiara, Shambhu Ghmire, David A. Reis, Louis F. DiMauro, and Pierre Agostini**

**Abstract** This chapter reviews electron energy spectra, multiple ionization, harmonic generation and attophysics as they are modified by scaling the interaction physics to longer driving wavelengths. After a brief outline of the development of mid-infared sources, we discuss findings on Above Threshold Ionization (ATI) and multiple ionization as an (e, ne) process. We then review the properties of high harmonic generation (HHG) in gas phase from the point of view of the highest frequency and the group delay dispersion, both relevant to attophysics. We have explored other generating media and report HHG from crystal and liquid samples. We conclude with a brief outlook of both the laser development and attophysics with MIR sources.

## 6.1 Introduction

Attophysics is about a decade old and, using high harmonic generation (HHG), pulse durations can now reach down to ∼80 attoseconds [1] from sources driven

A.D. DiChiara · L.F. DiMauro · P. Agostini (✉)
Department of Physics, The Ohio State University, Columbus, OH 43210, USA
e-mail: agostini@mps.ohio-state.edu

A.D. DiChiara
e-mail: dichiara@mps.ohio-state.edu

L.F. DiMauro
e-mail: dimauro.6@osu.edu

S. Ghmire · D.A. Reis
SLAC National Accelerator Laboratory, PULSE Institute, Menlo Park, CA 94025, USA

S. Ghmire
e-mail: shambhu@slac.stanford.edu

D.A. Reis
e-mail: dreis@slac.stanford.edu

D.A. Reis
Departments of Photon Science and Applied Physics, Stanford University, Stanford, CA 94305, USA

L. Plaja et al. (eds.), *Attosecond Physics*, Springer Series in Optical Sciences 177,
DOI 10.1007/978-3-642-37623-8_6,

by Titanium sapphire systems at 800 nm. In parallel to the impressive technological progress in the control and diagnostics of such pulses [2] mid-infrared (MIR) drivers have attracted a great deal of interest because they offer, in principle, even better performance thanks to the wavelength scaling properties of strong-field physics. In particular the high harmonic cutoff and group delay dispersion (GDD)[1] which are both pertinent to ultrafast attosecond pulse generation can be significantly improved by increasing the laser wavelength. In fact, increasing the laser wavelength is currently the only known method for *continuously* extending HHG beyond the extreme ultraviolet (XUV) towards the X-ray region of the electromagnetic spectrum.

The philosophy of our group is to approach the study of attophysics by pursuing a better understanding of how an atom behaves in a strong laser field in an interaction scaled by the laser wavelength. We have therefore developed drivers with wavelengths in the range 1–4 µm based on optical parametric amplification (OPA), and Difference Frequency Generation (DFG) to produce intense MIR femtosecond pulses. In this chapter we review the properties of current mid-infrared lasers, with special attention to the OPA and DFG systems in use in our group. We then address the scaling properties of strong-field ionization, multiple ionization and HHG from gas phase systems. The semi-classical rescattering model illustrates a picture that easily scales with wavelength, in particular it addresses, the general structure of the photoelectron energy spectra, the scaling of the harmonic cutoff, which has reached hundreds of eV and should be pushed to the keV range in the near future, and the quadratic spectral phase which controls the optimal bandwidth and the shortest pulse deliverable by a given source of harmonics. Both of these predictions are confirmed quantitatively by the experiment. The success of this model though, does not preclude the occurrence of some unexpected results: for example, the low energy structure in the photoelectron energy spectrum [3]. Testing the semiclassical model domain of validity beyond the gas phase, in which atoms are isolated from each other, is one of the motivations of the exploration of harmonic generation in the liquid and solid phases, briefly reported in the chapter. In the concluding section we discuss current development of an optical parametric chirped pulse amplifier (OPCPA) to bridge the technological gap of OPA-based systems and envision time-resolved imaging techniques allowed by the use of MIR lasers to reach the sub-femtosecond time domain.

## 6.2 Laser Technology: State-of-the-Art and Perspectives

### *6.2.1 The 3.2–3.9 µm Laser System*

The difference frequency generation (DFG) pump and signal beams are generated by separate laser systems: (1) a Ti:Sapphire laser produces 100 fs full-width at half-maximum (FWHM) pulses with a center wavelength of 0.816 µm and 3.0 mJ of energy and (2) a Nd:YLF regenerative amplifier [4] that delivers 16 ps FWHM pulses

---

[1] GDD is the quadratic spectral phase that is also known as *attochirp*.

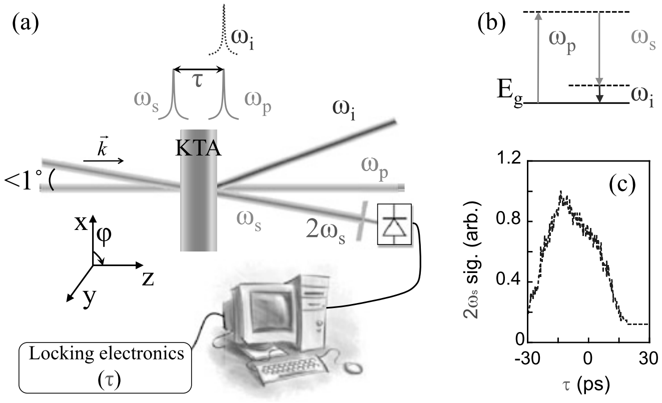

**Fig. 6.1** Overview of our DFG scheme is shown in (**a**) with timing synchronization (see text for details). The beams are incident from *the left*. Second harmonic is produced from the generated signal beam in the KTA and is filtered and monitored with an integrated amplified photodiode. An energy level diagram with photon energies drawn to scale is shown in (**b**). Timing synchronization is monitored with a cross-correlation technique shown in (**c**)

with a center wavelength of 1.053 μm and 0.8 mJ of energy. The kilohertz amplifiers are seeded with commercial oscillators (Time Bandwidth GE-100 [Nd:YLF] and Spectra Physics Tsunami [Ti:Sapph]) that are electronically synchronized, as described in [5]. The amplified pump and signal beams are collimated and sent into the crystal in a near collinear geometry, Fig. 6.1(a), to provide lossless spatial separation of the idler beam. Potassium Titanyle Arsenate (KTA) is used because of its high damage threshold [6] and good transparency to wavelengths from 0.3–5.0 μm [7].

Conservation of energy (see Fig. 6.1(b)),

$$\omega_i = \omega_p - \omega_s, \tag{6.1}$$

implies that the central wavelength of the idler is 3.6 μm. However, we have found that our pump beam undergoes a significant amount of spectral broadening from self phase modulation [8]. The additional bandwidth in turn allows tuning of the idler by adjusting the phase matching angle of the KTA crystal. In practice we can tune continuously from 3.2–3.9 μm with a minimum of 50 μJ of energy and a constant pulse duration of about 100 fs.

Timing stabilization for the two independent lasers is achieved with commercial electronics to ≤3 ps rms jitter or less than 20 % of the 16 ps signal (1.05 μm) pulse width. However, vibrations and other environmental factors limit the synchronization of the pulse trains to approximately 10 ps/(10–30 minutes) drift. The drift is compensated with a feedback loop that monitors the second harmonic (0.527 μm) amplitude of the 100 fs signal beam generated in the DFG KTA crystal, Figs. 6.1(a) and (c).

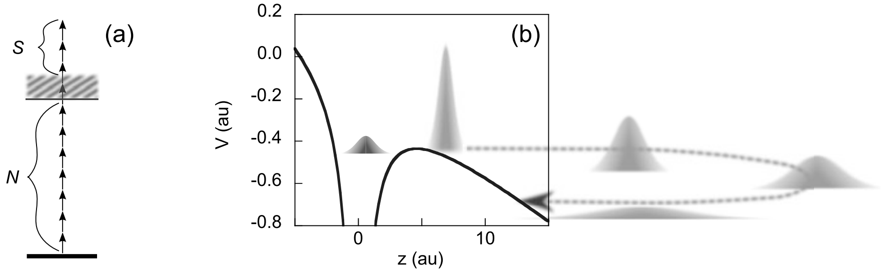

**Fig. 6.2** Models of strong field ionization: (**a**) N-photon ionization + S-photon ATI. (**b**) Keldysh tunneling energy diagram showing the transverse expansion of a Gaussian wave packet [31]

### *6.2.2 The 1.3–2.0 µm Laser System*

The 2 µm radiation source used in the experimental results presented hereafter is based upon a commercial optical parametric amplifier (OPA) (model HE-TOPAS-5/800 built by Light Conversion). The 2 µm OPA is pumped by 5 mJ, 50 fs pulses derived from a Ti:Sapph fs system. The TOPAS starts by using a small amount of pump light to generate a broadband spectrum via superfluorescence. A narrow spectral portion is then used as a seed with the remaining 0.8 µm light. After six passes in two BBO (beta-barium borate) nonlinear crystals 400 µJ of 2 µm radiation is available (on target). Because this is a parametric amplifier that splits one 0.8 µm photon into two lower energy ones, conservation of energy implies that 600 µJ of 1.3 µm idler radiation is also generated.

## 6.3 Photo-ionization and HHG at Long Laser Wavelengths

### *6.3.1 Tunnel Ionization and ATI in the Recollision Model*

One of the first measurements [9] of the ionization rate appeared to depend on the intensity exponentially and not to follow the power law predicted by the usual perturbation theory [10]. This result perhaps suggested to L.V. Keldysh a DC-tunneling ionization. In his famous paper [11], he shows that the ionization rate changes from a power law to an exponential, that depends on the laser intensity $I$, wavelength $\lambda$, and the ionization potential, $I_P$. The change in the rate dependence on intensity follows a transition from the multiphoton regime, Fig. 6.2(a), to the tunneling regime, Fig. 6.2(b). In the low frequency, low intensity limit the Keldysh theory of ionization [11] reduces to a DC-tunneling ionization. To satisfy the limit condition, the field's frequency, $\omega = 2\pi c/\lambda$, is assumed to be small compared to the tunneling frequency. More precisely, this is satisfied when the Keldysh adiabaticity parameter, defined as[2]

$$\gamma = \sqrt{I_P/2U_P} \tag{6.2}$$

is less than one. In the regime where $\gamma < 1$, The ionization rate proceeds as

$$w \propto \exp(-2\gamma/3\omega) \tag{6.3}$$

independent of $\omega$.

Keldysh theory, developed for the hydrogen ground state, was extended to arbitrary states by Ammosov, Delone, and Krainov (ADK) in 1986 [12]. The ADK rate includes an analytical solution for the normalization of the final Volkov state wave function and offers a simple closed-form solution of the ionization rate in a low frequency laser field.

The strong-field interaction of light with atoms first manifested itself in the photoelectron spectra (Above Threshold Ionization (ATI) Karule [13]). Here we will only concentrate on the classical aspects of ATI in the tunneling limit [14]. In that regime, ionization is a subcycle event and electrons are born at $t_0$ near the edge of the combined barrier ($x_i \approx 0$) with initial velocity $v_i = 0$ close to peaks of the laser field. The electron energy spectrum is derived from Newton's equation of motion [15, 16]. For a field $E(t) = E_0 \cos(\omega t)$ the time dependent electron kinetic energy is

$$\mathcal{E}(t) = 2U_P\big[\sin(\omega t) - \sin(\omega t_0)\big]^2. \tag{6.4}$$

Half of the electron trajectories (ignoring the Coulomb attraction of the nucleus) return to the nucleus with a maximum kinetic energy of $3.17U_P$ [17, 18] at $\omega t_0 \sim 0.3$ rad. Electrons returning to the origin at $t_1$ may elastically backscatter acquiring more energy from the field so that after the recollision,

$$\mathcal{E}_{bs}(t_0) = 2U_P\big[2\cos\big(\omega t_1(t_0)\big) - \cos(\omega t_0)\big]^2. \tag{6.5}$$

Equations (6.4) and (6.5) are sufficient to determine the major features of the photoelectron spectra (Fig. 6.3). Electrons born near the peak of the field ($t_0 = 0$) and drifting away from the core have a kinetic energy close to 0. Electrons born (with a very low probability) close to a zero crossing of the field drift with a maximum energy of $2U_P$. Electrons that backscatter can acquire up to $10U_P$ of energy. The simpleman's theory above is closer to reality as the laser wavelength is longer and $\gamma$ smaller. For the limits of validity of the tunneling scheme, see [19]. A numerical solution of the time dependent Schrödinger equation (TDSE) [20] performed for argon at 2 and 0.8 µm (see Sect. 6.4). The extracted trajectory for each wavelength is shown in color while the completely classical trajectory is shown with the solid black line. For 0.8 µm, 0.16 PW/cm$^2$, $\gamma = 0.91$ the multiphoton characteristics and discrepancy with the classical theory are obvious. However, for 2.0 µm

---

[2] $U_P$ is the cycle averaged kinetic energy a free electron gains from an oscillating electric field, and it is defined as $U_P = e^2E_0^2/4m_e\omega^2$, where, $e$ is the charge, and $m_e$ is the mass of the electron, and $E_0$ the electric field. $I_P$ is the ionization potential.

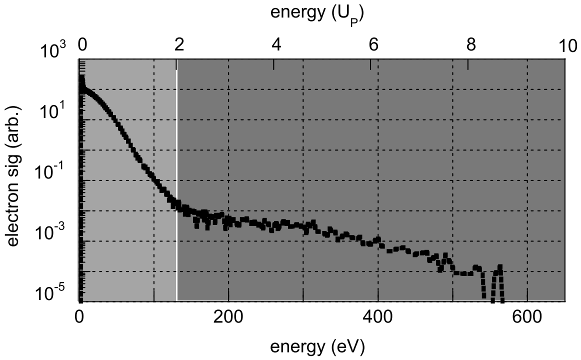

**Fig. 6.3** Strong-field photoelectron spectra of xenon ionized by a 3.6 µm laser field. The peak intensity is inferred as $5.4 \times 10^{13}$ W/cm$^2$. *The light* and *dark grey regions* corresponds to Eqs. (6.4) and (6.5) respectively

at the same intensity $\gamma = 0.36$ and the agreement with classical theory is equally obvious.

### *6.3.2 Non-sequential Ionization with a 3.6 µm Laser Field*

The double (and multiple [21]) ionization of atoms by a short NIR laser pulse cannot, in general, be explained by sequential tunnel ionization. For example, considering double ionization the experimental rate is 5–6 orders of magnitude larger than the ADK rate [22, 23] and corresponds to an appearance intensity that is a factor of 3–5 lower than what is predicted by ADK. Treatments of this problem both quantum [24, 25] or classical [21] have been a challenge for theory. The simple phenomenological approach that explains the photo-electron energy spectra can also be applied to double ionization by (e, 2e) collision [18] and electron ion excitation. The use of long (MIR) wavelength lasers, for which the recollision energy increases as $\lambda^2$, allows the study of higher order processes that may clarify the physics behind multiple ionization.

As an example, the single through quintuple ionization of krypton at 3.6 µm ($\gamma = 0.25$) is shown in Fig. 6.4 along with the yields calculated by numerical integration of the ADK formula for a 100 fs 3.6 µm that is Gaussian in time and space. For the conditions of the experiment the Keldysh parameter is $\gamma = 0.25$ for the maximum intensity measured.

Clearly, the agreement of ADK is satisfactory for Kr$^+$, however the discrepancy of the ADK rate for higher ionization channels is obvious. According to the recollision model, non-sequential ionization (NSI) occurs when an electron wave packet is driven back to the ion core by the strong laser field and results in a collisional event (Fig. 6.2(b)). Surprisingly enough for a process happening in an intense laser field, NSI can be viewed as a *field-free* inelastic (e, ne) collision. We demonstrate this by making a direct correspondence between ionic branching ratios defined as, Kr$^{+n}$/Kr$^+$ for $n > 1$, and field-free cross sections.

We have adopted the procedures of [26, 27] that treat rescattering as the multiplication of an electron wave packet, $W_P$, with an appropriate field-free cross sec-

**Fig. 6.4** Ionization yields of krypton driven by 3.6 μm laser. The results of the full calculation, Eq. (6.7), are shown by *dotted lines*

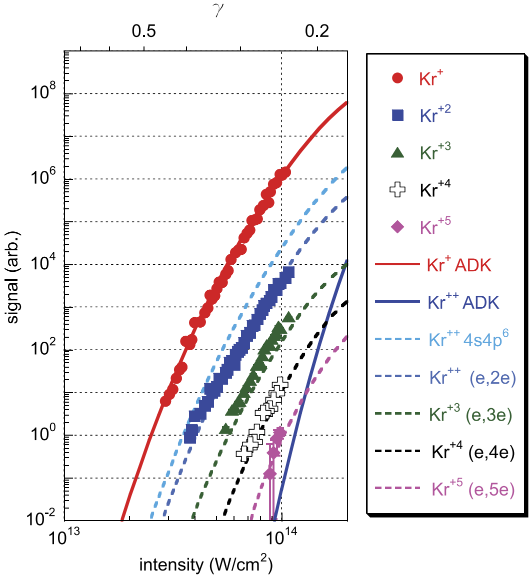

tion, $\sigma$. Here we have used known experimental inelastic cross sections for krypton [28, 29] for double through quadruple ionization, see Fig. 6.5(a). For quintuple ionization and excitation we have used a Lotz fit [30] since this data was not available. Excitation is assumed to lead to prompt ionization [27] and we include only the largest excitation channel of $(\mathrm{Kr}^+)^*$, $4s4p^6$, since double ionization should be dominated by a single excitation channel and direct (e, 2e) ionization. To calculate $W_P$ the laser pulse is sampled in time increments of 1 a.u. and at each point a 1-D trajectory is calculated by solving $\ddot{x} = -(e/m)E(t)$; only trajectories that return to the core are retained. The initial conditions are consistent with the treatment in [27]. Each trajectory is weighted by the ADK yield to account for tunnel ionization and ground state depletion. The free expansion of a tunnel ionized wave packet [31] is taken into account to ensure that each classical trajectory represents a wave packet with the correct area at recollision. The calculation is summed spatially to account for the intensity distribution in a Gaussian laser focus and is shown in Fig. 6.5(b). Figure 6.5(c) shows the measured branching ratios and the inelastic cross sections from Fig. 6.5(a) broadened by our calculated $W_P$,

$$\tilde{\sigma}(I) = \frac{\int dE'\sigma(E')W_P(E'(I))}{\int dE' W_P(E'(I))}. \tag{6.6}$$

Moreover, we have used Eq. (6.6) to calculate the non-sequential ionization probability in the nearly hard sphere approximation [32],

$$P(b, I) = \tilde{\sigma}(I)\frac{\exp(b^2/a_0^2)}{\pi a_0^2}, \tag{6.7}$$

where $a_0 = \sqrt{2/\Delta E}$ and b is the impact parameter. The results (Fig. 6.4) are in very good agreement and strongly support the correspondence of strong-field NSI to a

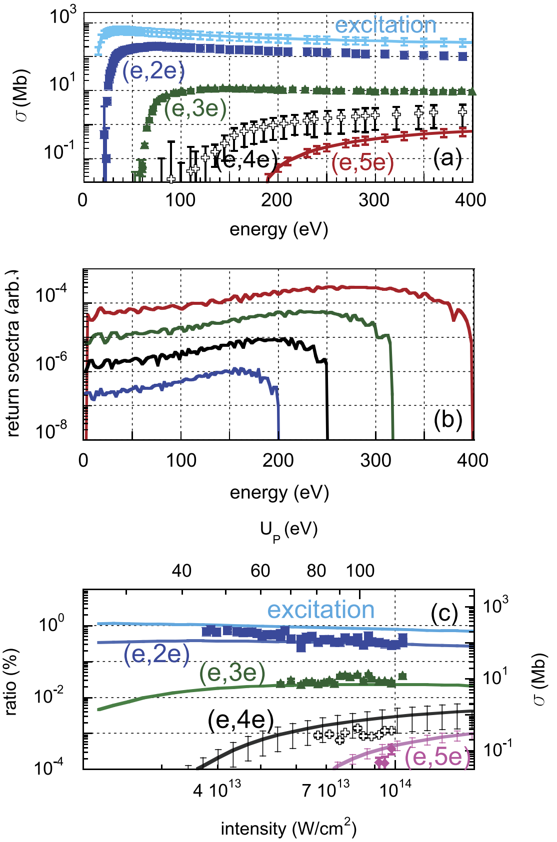

**Fig. 6.5** Panel (**a**) shows (e, ne) collisional ionization cross sections from [28, 29]. See text for details. The return distributions, $W_P$, are shown in panel (**b**) for 100 (*red*), 80 (*green*), 64 (*black*) and 51 (*blue*) TW/cm$^2$. The results of Eq. (6.6) as well as the branching ratios are shown in panel (**b**)

field-free (e, ne) process. This may in part be due to the fact that the recolliding electron returns near the zero of the laser field when the Coulomb potential suffers only a small distortion. We also note that even at the field maximum the region of the potential near $I_P(ion)$ is not significantly distorted. However, in agreement with theory [33] excitation processes are more sensitive to effects of the strong laser field. The success of the field-free cross sections has thus, a simple explanation in the three-step semi-classical model.

## 6.4 HHG and Attosecond Generation at MIR Wavelengths

High harmonic generation (HHG) is the other highly nonperturbative observation of the strong-field interaction. HHG is moreover instrumental in the synthesis of attosecond pulses. The rescatering model [17, 18] immediately explains the harmonic cutoff: quantum mechanically the energy of the emitted photon is equal to the summed energy of the absorbed photons. Classically, the active electron is accelerated in the field and it is this kinetic energy which is converted into radiation.

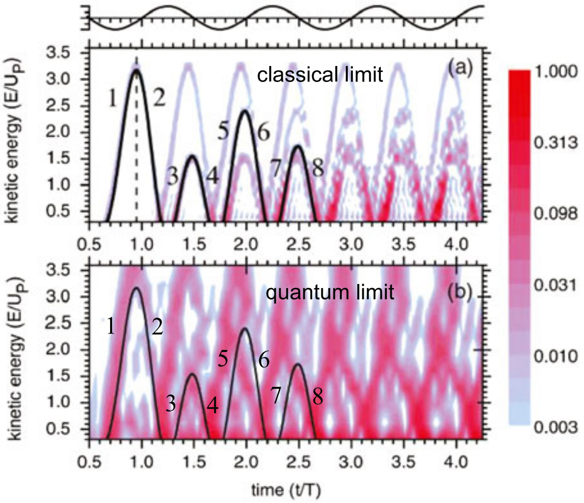

**Fig. 6.6** The TDSE time history of the HHG emission energy for argon excited by (**a**) 2 and (**b**) 0.8 μm driving laser with intensity 0.16 PW/cm$^2$ is shown by *the red* to *blue color scale*. *The solid black lines* are the purely classical prediction for return energy and each numeric label corresponds to the nth trajectory. The top trace shows the electric field of the input pulse, where the time axis is given in units of the laser period, *T*

The so-called harmonic cutoff follows by conservation of energy as $3.17U_P + I_P$ [17]. The maximum energy, proportional to $\lambda^2$ predicts a huge increase of photon energy with mid-infrared drivers.

### 6.4.1 Harmonic Yield

With the most common driving wavelength of 0.8 μm (Ti:Sapph laser) and targets (rare gases), the HHG efficiency is of the order of $10^{-6}$. Both Lewenstein's strong-field approximation and TDSE simulations (Fig. 6.6) indicate that the single-atom dipole decreases rapidly with the laser wavelength [20]. This is most likely due to a combination of the wave packet spreading during the electron trajectory in the continuum and the decrease of the recombination cross section as the electron energy increases. TDSE calculations show that the single atom power spectrum yield scales as $\lambda^{-(5.5\pm0.5)}$ at constant intensity [20] (see also [34]).

The experimental results of Shiner et al. [35] are in agreement with these calculations. Dispersive effects from free electrons, and the intrinsic dipole phase [36] generally result in an even more rapid decrease of the macroscopic yield scaling with wavelength [37] at constant intensity. Fortunately, control parameters such as focusing and target density enable means for global optimization and compensation of the decrease in yield [38, 39].

If the change in harmonic yield in argon between 0.8 and 2 μm is monitored while keeping the other conditions fixed, e.g. intensity, gas density and focusing, and the comparison is confined to a common spectral bandwidth (35–50 eV), then the harmonics generated by the 2 μm driver are observed to be 1000-times weaker than with 0.8 μm and 6-times less than that predicted by 'single atom' calculations

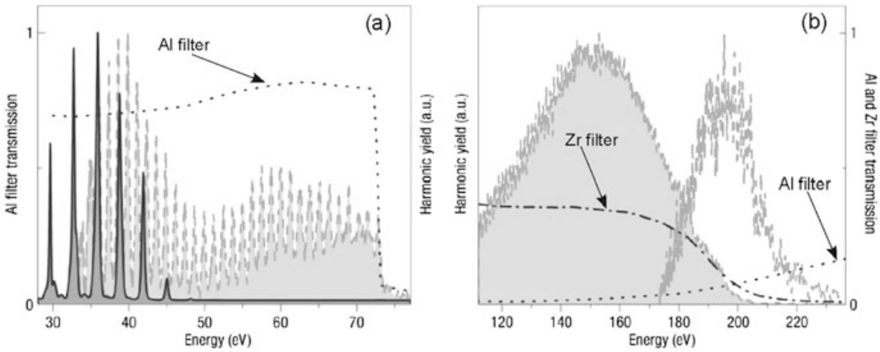

**Fig. 6.7** The high harmonic comb is shown (linear scale) in (**a**) produced in argon for an intensity of 18 TW/cm$^2$ with 0.8 μm (*dashed line-gray filled*) and 2 μmm (*solid line-yellow filled*) pulses through an Al filter (transmission in *dotted line*). The cutoff at 75 eV is due to the Al transmission. In panel (**b**) a Zr (*filled*) and Al (*unfilled*) filters are used together with the filter transmission curves shown as *dot-dash* and *dot*, respectively. The graphs are not corrected for the grating efficiency. The real cutoff (220 eV) is seen in *the unfilled curve*

[20, 38]. Naturally, one has the resource of independent optimization of the parameters. By optimizing the argon density for a maximum harmonic yield at both wavelengths we achieve a yield at 2 μm that is only 85-times weaker than the yield at 0.8 μm. Additional optimization of, particularly, the pump intensity and focusing geometry will further close the gap in yield for the EUV ($\leq 50$ eV) with superior results anticipated for higher photon energies ($50 \leq \hbar\omega \leq 200$ eV) unreachable at 0.8 μm.

High harmonic generation is moreover the only demonstrated route to generating attosecond bursts of radiation [40]. The yield, cutoff, and spectral phase or *attochirp* are critical to the Fourier synthesis of sub-cycle XUV pulses. The following subsections show recent results pertaining to high harmonics from MIR drivers and their properties in the perspective of attophysics.

## 6.4.2 HHG Cutoff and Frequency Content

The harmonic comb consists of an odd-order series of nearly constant amplitude harmonic peaks of the laser fundamental frequency. The comb terminates at an energy defined by the cutoff law, $\hbar\omega_{cutoff} = I_P + 3.17U_P$, previously discussed as the maximum energy a classically driven photoelectron can convert into a photon energy. Verifying the wavelength scaling of the cutoff is the first goal of the experiment [38, 41]. The harmonic spectra at 2 μm are recorded in three independent measurements with different filters which have been separately normalized: aluminum (Fig. 6.7(a)) and zirconium for the low energy portion and aluminum for the high-energy region (Fig. 6.7(b)). First, Fig. 6.7(a) shows the argon harmonic distribution in the extreme ultra-violet (EUV) region driven by 0.8 μm and 2 μm fundamental fields, transmitted by an Al filter [38]. The 0.8 μm distribution shows a 50 eV cutoff (i.e. order 31) consistent with previous measurements, time dependent numerical results [20] and the cutoff law. In contrast, as seen in Fig. 6.7(a) excitation with the longer wavelength produces a denser harmonic comb (consequence of the smaller photon energy) extending to the Al L-edge at ∼70 eV. Using a Zr filter instead, the same argon harmonic comb is observed to extend over the entire Zr filter transmission window (60–200 eV) (Fig. 6.7(b)). The fast structure is the 2 $\hbar\omega$ (1.2 eV) spacing while the overall shape is a convoluted instrumental response. No harmonics are generated in this region using 0.8 μm excitation. A third set of measurements using the second Al-transmission window is necessary to establish that the 2 μm harmonic cutoff is ∼220 eV because the measurement using the zirconium filter is obviously spectrally limited by the transmission drop at short wavelengths. This cutoff value is consistent with the TDSE calculations [20] and extends the cutoff in argon beyond the value found in a previous work at 1.5 μm [37] (Fig. 6.7(b)).

### 6.4.3 Spectral Phase Measurements

A short and a long trajectory are each identified by the total amount of time spent in the continuum between birth and recombination [42]. In the context of attosecond pulses Fourier-synthesized from high harmonics, an inherent GDD exists, due to the relationship between harmonics and the length of the electron trajectories that generates them [43, 44]. The group delay dispersion, which is approximately linear with energy for each class of trajectory, is understood classically as the return energy vs. return time. Since the return energy is quadratic with wavelength and the return time scales with $\lambda$ we immediately recognize that the group delay scales as $1/\lambda$. Thus, increasing the wavelength decreases the group delay suggesting that long wavelength drivers simultaneously move the harmonic comb to higher energies with more favorable intrinsic synchronization conditions. The laser used in this section is our tunable (1.3–2.3 μm) source.

We first addressed the spectral phase measurement by adapting the all-optical method introduced by Dudovich et al. [45]. In this method the high harmonics are generated by a two-color combined field(fundamental driving field and its second harmonic). In such a field, the centro-symmetry of the generation process is lost, resulting in both even- and odd-order harmonics. The amplitude of the even-order harmonics depends on the relative phase of the two-color combined field. By controlling the subcycle delay between the fundamental and second harmonic pulses and recording the resulting oscillations of the even harmonics, it is possible, using the semiclassical model, to retrieve their emission times, and by interpolation, that of the odd orders. In the limit of a sufficiently weak second harmonic beam the emission times correspond to the unperturbed values. It should be stressed that this method yields the *in situ* attochirp. Thus, the spectral phase of the attosecond burst is measured under the conditions of the laser focus without possible propagation affects. The independent of possible subsequent compensation. The phase of the high

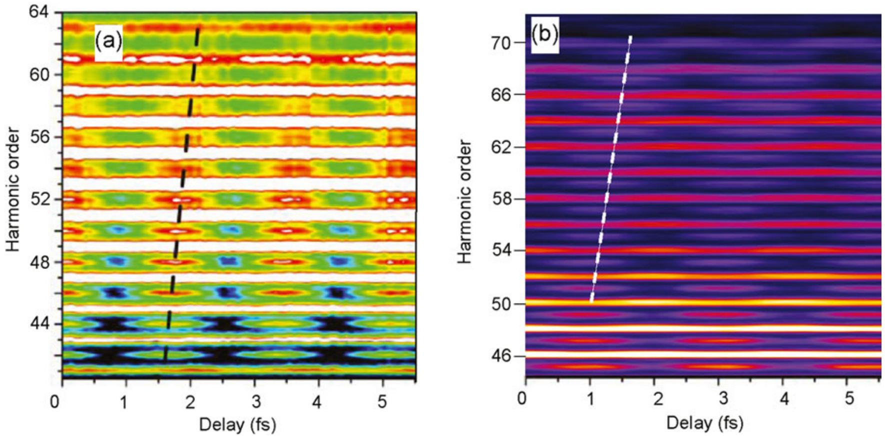

**Fig. 6.8** (**a**) Full scan of $\omega$–$2\omega$ delay obtained in xenon at 2 μm, and an intensity of 21 TW/cm$^2$. The even-order harmonics oscillate at 4 times the fundamental frequency. *The dotted line* serves as a guide for visualizing the shift in the delay that maximizes each even-order harmonic. (**b**) RABBITT spectrogram for 1.3 μm at a laser intensity of 18 TW/cm$^2$. Two individual spectra (line outs of (**a**)) for specific delays maximizing (*solid line*) or minimizing (*dashed line*) the even-order harmonics

harmonic light has been measured with this method in gas jets of argon and xenon at three different driving wavelengths (0.8, 1.3, and 2 μm).

High harmonic spectra are presented in Fig. 6.8(a) for xenon excited by a 21 TW/cm$^2$, 2 μm pulse. The spectra recorded for two different $\omega$–$2\omega$ total fields illustrate the change in amplitude of the even-order harmonics with phase. By contrast, the odd-order harmonics are not modulated. A pair of fused silica wedges provides attosecond control of the relative phase between the $\omega$–$2\omega$ fields. Figure 6.8(a) is a global plot of the harmonic spectra as a function of this relative phase and shows both the periodic oscillations and the shift in the delay that maximizes different even-orders.

The pure wavelength scaling, Fig. 6.9 shows the product of the attochirp and the intensity as a function of the fundamental driving wavelength (to account for the dependence of the chirp on ponderomotive energy and therefore intensity). The figure also includes measurements in argon for 80 TW/cm$^2$, 0.8 μm, and 71 TW/cm$^2$, 2 μm pulses. As previously discussed, the expected $1/\lambda$ dependence is plotted as a solid line. The experiment clearly demonstrates the reduction with fundamental wavelength. The attochirp is reduced by using a longer wavelength driver from a value of 41.5 as/eV at 0.8 μm to 21.5 as/eV at 2 μm. Those values consider the intrinsic attochirp of the generation process only, independently of any subsequent compensation. In those conditions, the optimum pulse duration goes down from 250 as at 0.8 μm to 180 as at 2 μm. This corresponds to an optimal bandwidth of 12.5 eV at 0.8 μm and 20 eV at 2 μm. In theory, the central frequency can be set anywhere in the generated spectra, up to 25 eV at 0.8 μm and 90 eV at 2 μm.

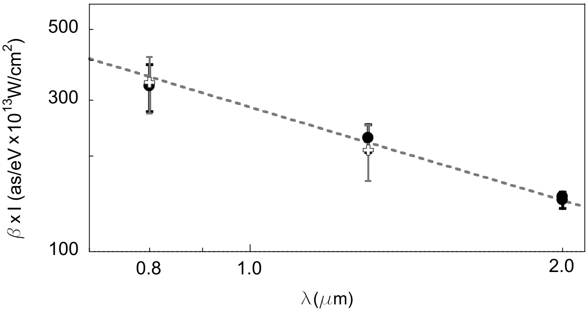

**Fig. 6.9** Scaling of the attochirp as a function of wavelength. The product of the attochirp $\beta$ with the intensity $I$ is plotted in order to remove the effect of the peak intensity (see text for details). *The straight line* corresponds to the predicted scaling $1/\lambda$. *The solid circles* are the result of the *in situ* measurements and the open crosses are the results of the RABBITT method. Both measurements are in agreement for 0.8 and 1.3 μm

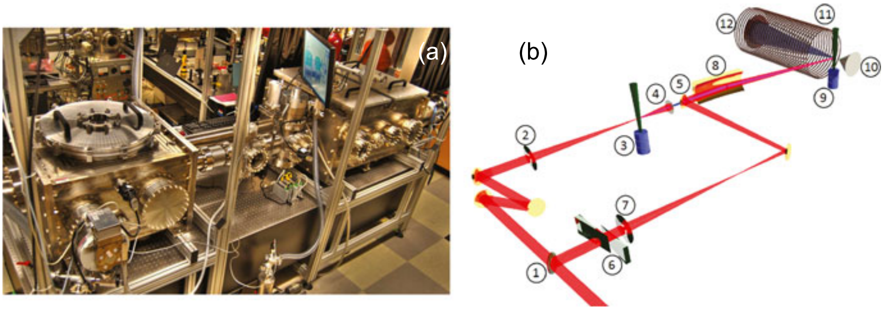

**Fig. 6.10** The OSU attosecond beamline apparatus is shown in panel (**a**) with a detail of our RABBITT scheme shown in panel (**b**). (1) Beam splitter, (2) focusing lens to generate harmonics, (3) generation gas target, (4) metal filter, (5) recombination mirror, (6) glass wedges for delay scans, (7) focusing lens to match divergence, (8) toroidal mirror, (9) detection gas jet, (10) cone-shaped permanent magnet, (11) magnetic bottle solenoid coils, and (12) micro channel plate detector

### *6.4.4 Attosecond Beam Line and RABBITT Measurements*

The ($\omega$–$2\omega$) method depends on a theoretical modelling. It was therefore important to compare its results with an independent method, the RABBITT method [46–48]. The attosecond beamline is illustrated in Fig. 6.10. It is a versatile design which is now incorporating a RABBITT line, that is transport of the attosecond pulse train to a second gas jet where it is superposed to a MIR pulse to ionize a target atom. The method relies on two-photon, three-color ionization process, independent of the HHG theory. Figure 6.9 shows preliminary results which appears to confirm the previous one [44].

## 6.5 Exploration of HHG by Liquids and Crystals

With long wavelength lasers demonstrated as a useful tool for understanding the scaling properties of HHG we now turn to exploratory studies of below threshold harmonics and HHG in condensed phase systems irradiated by our longest wavelength laser. The latter is in part motivated by the simple fact that direct observation of the ionization sequence by constituent charged particle by products in a liquid or solid is limited to surface analysis. Therefore, understanding the strong-field response of bulk condensed phase systems may best be initially pursued by investigating the properties of HHG. Long wavelength lasers are absolutely critical to this research because the low binding potential or energy gap in condensed state systems makes tunnel ionization otherwise inaccessible. While the change in density alone from liquid to solid is minor the structure of a periodic extended lattice has significant ramifications for condensed matter physics. By comparing a common liquid and semiconductor material we will highlight just how significant the long range order of a perfect crystal is in the strong-field sequence as well.

### *6.5.1 Harmonics Generated in Liquids*

In a solid, the breakdown of the medium effectively destroys the integrity of the sample and the order of the system across the extent of the laser focus. In this sense a flowing liquid source presents a high density sample that can be exposed to fields well above the limit of breakdown provided that the sample refresh itself faster than the repetition rate of the laser. These conditions are satisfied by the design of Tauber et al. which, in our version, consists of a 27 cm fluid column constructed from stainless steel tubing, chromatography fittings, custom glassware, and a peristaltic pump to recycle the fluid after the interaction region. At the end of the column is a narrow aperture, 2.7 mm by 0.3 mm, that holds a thin wire loop to provide enough capillarity for the fluid to form a film. With this device we can achieve fluid films as thin as 150 µm with an average linear velocity of 900 µm/ms and corresponds to a Reynold's number of $\mathrm{Re} = 500$. This is well within range of laminar flow ($\mathrm{Re} < 2000$) and the fluid source remained stable over acquisitions of several hours. Light generated from the laser-fluid interaction was delivered to a Czerny-Turner spectrometer with an intensified charge-coupled device placed at the output. The spectrometer has a maximum resolution of 1 nm and is energy calibrated from 200 nm–800 nm within an absolute error of ±50 %. The laser wavelength was tuned to. Figure 6.11(a) shows sample spectra for 3.6 µm laser light with two different fluid samples, water and hexane. In general, the conversion efficiency is very good despite the low harmonic order. For water the conversion efficiency is $3 \times 10^{-6}$ and for hexane it is an impressive $2 \times 10^{-4}$. As described in [49] we believe that despite the very high field strength the density of the fluid effectively shuts down recombination and harmonics are produced through a perturbative mechanism [8]. We also observe that the spatial mode is extremely clean. Spatial mode cleaning is

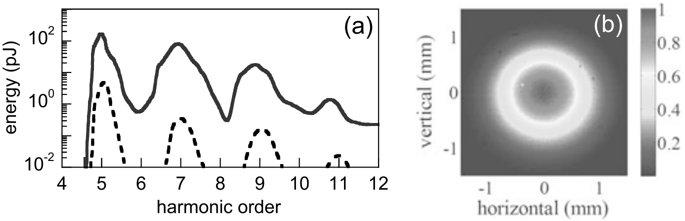

**Fig. 6.11** Panel (**a**) shows two representative harmonic spectra from liquid water (*dash line*) and hexane (*solid line*). The intensity of the laser was 9 × $10^{13}$ W/cm$^2$ and $10^{14}$ W/cm$^2$ respectively. The mode of the fifth harmonic generated in water is shown in panel (**b**) and demonstrates significant mode cleaning of the harmonic beam

known to occur as a result of femtosecond laser filamentation [50] and may indicate that self and cross phase modulation are occurring in the fluid medium. Although, the highest harmonic produced is only ∼4 eV the conversion efficiency and spatial profile make MIR harmonic generation in a fluid medium an intriguing scenario.

### *6.5.2 Harmonic Generation in a Perfect ZnO Crystal*

The long range order of a perfect crystal causes dramatic changes the observed harmonic spectra. Here our experiments are performed with a similar set up as above but with the laser wavelength tuned to 3.25 µm, a 500 µm ZnO crystal, and the entire apparatus from the interaction region to the detector is purged with argon gas to limit atmospheric absorption for photons above 6 eV. A sample spectra is shown in Fig. 6.12. As discussed in [51] the periodicity of the crystal results in rapid field driven Bragg scattering for electrons promoted into the conduction band (equivalent to ionization) by the strong laser field. The nonlinear polarization that results contains high order frequency components that extend over 6 eV above the band edge of the crystal and indicates a distinct breakdown of the perturbative response observed in a liquid media. We also find that the harmonic cutoff scales linearly with the field [51] in stark contrast with the atomic picture. The breakdown of perturbation theory for gas phase harmonic generation has provided decades of fruitful research and can now be extended to an exciting new regime where the structure of a crystal plays a pivotal role in the formation of a harmonic comb.

## 6.6 Conclusion and Outlook

Intense femtosecond mid-infrared lasers have allowed us to investigate the scaling of strong-field single and multiple ionization, and harmonic generation physics and to confirm the wavelength advantages in the prespective of attophysics. Extension from gas phase targets to a solid state system has led to the discovery of a new

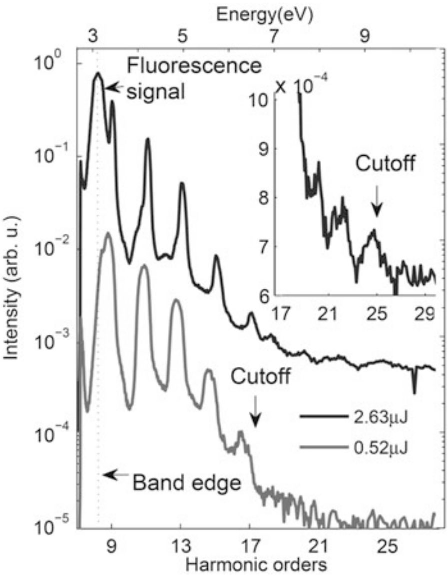

**Fig. 6.12** Harmonic generation from a ZnO crystal. The band edge of the crystal is located at about 3.2 eV as indicated by *the vertical dotted line*. 2.63 μJ (0.52 μJ) corresponds to an estimated intensity of $4.8 \times 10^{12}$ W/cm$^2$ ($9.7 \times 10^{11}$ W/cm$^2$)

cutoff law while liquid targets have produced bright harmonics and a very clean spatial mode.

Another interesting application of MIR laser technology coupled to the strong-field picture lies in using laser driven scattering, e.g. multiple ionization, as a controlled technique to perform sub-femtosecond measurements. In this case we intend to use elastic scattering [52] to pursue laser driven diffractive imaging. Since the scattering process is timed by the period of the laser field laser driven elastic scattering potentially provides a route to perform a new class of time-resolved measurements. It has been the purpose of this chapter to review attophysics from the stand point of advances in MIR laser science and demonstrate the significance of this approach.

Typically, the power produced by an OPA is a limiting factor since the conversion efficiency is low; our HE-TOPAS is about 10 % efficient with respect to production of the idler beam. Increasing the amount of Ti:Sa pump power has an upper limit determined by the size high quality nonlinear crystals can be made with. Moreover, one issue with performing strong-field experiments with long wavelength lasers is the change in the diffraction limited spot size with wavelength. For example, changing the wavelength from 0.8 μm to 2.0 μm results in a factor of 6 decrease in the peak intensity assuming all other pulse parameters remain unchanged. Therefore, OPA's are not well suited for more complicated pump probe scenarios or experiments that may require millijoules of MIR laser power. A practical solution exists with optical parametric chirped pulse amplification (OPCPA) [53] which limits the peak power a nonlinear crystal is exposed to by stretching femtosecond pulses to picoseconds and later compressing them back to the femtosecond time-scale thus allowing more pump photons to be used. Figure 6.13 shows a schematic of the of the OPCPA that is currently under construction at OSU. We anticipate that our OPCPA will provide

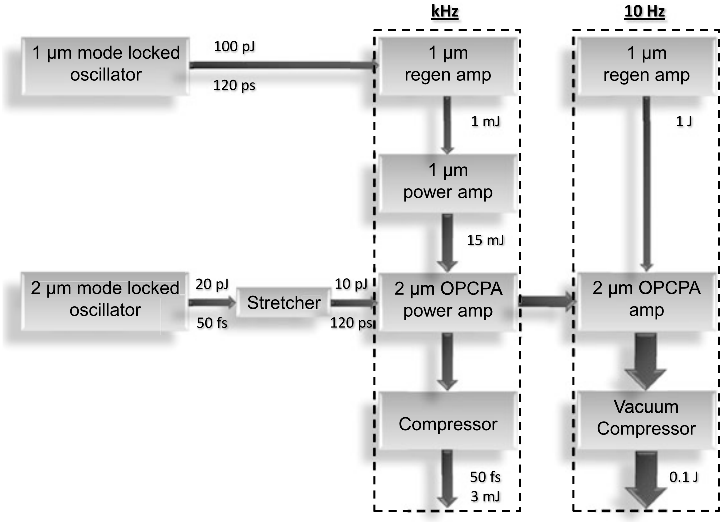

**Fig. 6.13** Diagram of OPCPA currently under construction at OSU

peak powers of 60 Gigawatts or 2 Terawatts at one kilohertz or 10 hertz repetition rates respectively. This will allow the OSU group to perform more complicated pump probe experiments for attoscience as well as address wavelength scaling in high energy density physics and ultrafast filamentation.

**Acknowledgements** This work was carried out with support from the National Science Foundation under contract PHY-1004778 and the Department of Energy under contracts DE-FG-02-04-ER15014 and DE-FG-02-06-ER15833. L.F.D. acknowledges support from the Hagenlocker chair.

## References

1. E. Goulielmakis et al., Science **320**, 1614 (2008)
2. Z. Chang, *Fundamentals of Attosecond Optics* (Taylor & Francis, London, 2011)
3. C.I. Blaga, F. Catoire, P. Colosimo, G.G. Paulus, H.G. Muller, P. Agostini, L.F. DiMauro, Nat. Phys. **5**, 335 (2009)
4. M. Saeed, D. Kim, L.F. DiMauro, Appl. Opt. **29**, 1752–1757 (1990)
5. M.J.W. Rodwell et al., IEEE J. Quantum Electron. **25**, 817–827 (1989)
6. S. Cussat-Blanc et al., Appl. Phys. B **70**, S247–S252 (2000)
7. G. Hansson et al., Appl. Opt. **39**, 5058–5069 (2000)
8. R.W. Boyd, *Nonlinear Optics* (Academic Press, San Diego, 1992)
9. E.K. Damon, R.G. Tomlinson, Appl. Opt. **2**, 546–547 (1963)
10. W. Zernik, Phys. Rev. **135**, A51–A57 (1964)
11. L.V. Keldysh, Sov. Phys. JETP **20**, 1307–1314 (1965)
12. M.V. Amosov, N.B. Delone, V.P. Krainov, Sov. Phys. JETP **64**, 1191–1194 (1986)
13. E. Karule, J. Phys. B, At. Mol. Opt. Phys. **11**, 441–447 (1978)
14. W. Becker et al., Adv. At. Mol. Opt. Phys. **48**, 35–98 (2002)

15. H.B. van Linden van den Heuvell, H.G. Muller, Limiting cases of excess-photon ionization, in *Multiphoton Processes* (Cambridge University Press, Cambridge, 1987), pp. 25–34
16. N.H. Burnett, P.B. Corkum, F. Brunel, Phys. Rev. Lett. **62**, 1259–1962 (1989)
17. K.J. Schafer, B. Yang, L.F. DiMauro, K.C. Kulander, Phys. Rev. Lett. **70**, 1599–1602 (1993)
18. P.B. Corkum, Phys. Rev. Lett. **71**, 1994–1997 (1993)
19. H.R. Reiss, Phys. Rev. Lett. **101**, 043002 (2008)
20. J. Tate et al., Phys. Rev. Lett. **98**, 013901 (2007)
21. P.J. Ho, J.H. Eberly, Phys. Rev. Lett. **97**, 083001 (2006)
22. B. Walker et al., Phys. Rev. Lett. **73**, 1227–1230 (1994)
23. J. Rudati et al., Phys. Rev. Lett. **20**, 203001 (2004)
24. J.B. Watson, A. Sanpera, D.G. Lappas, P.L. Knight, K. Burnett, Phys. Rev. Lett. **78**, 1884 (1997)
25. A. Becker, F.H.M. Faisal, J. Phys. B, At. Mol. Opt. Phys. **38**, R1 (2005)
26. S. Micheau, Z. Chen, A.-T. Le, C.D. Lin, Phys. Rev. A **79**, 013417 (2009)
27. G.L. Yudin, M.Y. Ivanov, Phys. Rev. A **63**, 033404 (2001)
28. K. Tinschert, A. Muller, G. Hofmann, C. Achenbach, R. Becker, E. Salzborn, J. Phys. B, At. Mol. Phys. **20**, 1121–1134 (1986)
29. K. Tinschert, A. Muller, R. Becker, E. Salzborn, J. Phys. B, At. Mol. Phys. **20**, 1823–1838 (1986)
30. W. Lotz, Z. Phys. **206**, 205 (1967)
31. N.B. Delone, V.P. Krainov, J. Opt. Soc. Am. B **8**, 1207 (1991)
32. X.M. Tong, Z.X. Zhao, C.D. Lin, Phys. Rev. A **68**, 043412 (2003)
33. K.C. Kulander, J. Cooper, K.J. Schafer, Phys. Rev. A **51**, 561 (1995)
34. W. Becker, S. Long, J.K. McIver, Phys. Rev. A **50**, 1540–1560 (1994)
35. A.D. Shiner et al., Phys. Rev. Lett. **103**, 073902 (2009)
36. P. Salieres, A. L'Huillier, M. Lewenstein, Phys. Rev. Lett. **74**, 3776–3779 (1995)
37. B. Sheehy et al., Phys. Rev. Lett. **83**, 5270 (1999)
38. P. Colosimo et al., Nat. Phys. **4**, 386 (2008)
39. T. Popmintchev et al., Opt. Lett. **33**, 2128–2130 (2008)
40. P. Agostini, L.F. DiMauro, Rep. Prog. Phys. **67**, 813–855 (2004)
41. B. Shan, Z. Chang, Phys. Rev. A **65**, 011804 (2001)
42. M. Lewenstein et al., Phys. Rev. A **52**, 4747–4754 (1995)
43. Y. Mairesse et al., Science **302**, 1540–1543 (2003)
44. G. Doumy et al., Phys. Rev. Lett. **102**, 093002 (2009)
45. N. Dudovich et al., Nat. Phys. **2**, 781–786 (2006)
46. V. Véniard et al., Phys. Rev. A **54**, 721 (1996)
47. P.M. Paul et al., Science **292**, 1689 (2001)
48. H.G. Muller, Appl. Phys. B **74**, S17 (2002)
49. A.D. DiChiara, E. Sistrunk, T.A. Miller, P. Agostini, L.F. DiMauro, Opt. Express **17**, 20959 (2009)
50. A. Couairon, A. Mysyrowicz, Phys. Rep. **47**, 441 (2007)
51. S. Ghimire, A.D. DiChiara, E. Sistrunk, P. Agostini, L.F. DiMauro, D.A. Reiss, Nat. Phys. **7**, 138 (2011)
52. C.D. lin, A.-T. Le, Z. Chen, T. Morishita, R. Lucchese, J. Phys. B, At. Mol. Opt. Phys. **43**, 122001 (2010)
53. I.N. Ross et al., Appl. Opt. **39**, 2422–2427 (2000)

# Part III
# Attosecond Measurements and Control of Physical Systems

# Chapter 7
# Strong Field Ionization in a Multi-color Field

**T. Balciunas, A.J. Verhoef, S. Haessler, A.V. Mitrofanov, G. Fan,**
**E.E. Serebryannikov, M.Y. Ivanov, A.M. Zheltikov, and A. Baltuska**

**Abstract** We describe several implementations of multi-color shaping of the optical cycles of intense laser pulses, which allow direct control of strong-field dynamics and have important implications for many of their applications. After reviewing a purely optical detection method for attosecond tunneling ionization bursts in gases and transparent solids, we experimentally demonstrate the steering of the induced tunneling electron current via the optical cycle shape of the driving laser pulses.

---

T. Balciunas · A.J. Verhoef · S. Haessler · A.V. Mitrofanov · G. Fan · A. Baltuska (✉)
Photonics Institute, Vienna University of Technology, Vienna, Austria
e-mail: Andrius.baltuska@tuwien.ac.at

T. Balciunas
e-mail: tadas.balciunas@tuwien.ac.at

A.J. Verhoef
e-mail: aart.johannes.verhoef@tuwien.ac.at

S. Haessler
e-mail: stefan.haessler@tuwien.ac.at

A.V. Mitrofanov
e-mail: mitralex@inbox.ru

G. Fan
e-mail: guangyu.fan@tuwien.ac.at

E.E. Serebryannikov · A.M. Zheltikov
M.V. Lomonosov Moscow State University, Moscow, Russia

E.E. Serebryannikov
e-mail: serebryannikov@gmail.com

A.M. Zheltikov
e-mail: zheltikov@phys.msu.ru

M.Y. Ivanov
Department of Physics, Imperial Colledge London, London, UK
e-mail: mivanov@mbi-berlin.de

A.M. Zheltikov
Department of Physics, Texas A&M University, College Station, TX, USA

L. Plaja et al. (eds.), *Attosecond Physics*, Springer Series in Optical Sciences 177,
DOI 10.1007/978-3-642-37623-8_7,

We describe two examples: the control of the electron emission direction in above-threshold ionization, and a new scheme for the efficient generation of tunable THz radiation. Finally, we also describe an application of shaped optical cycles to the generation of ultrafast XUV pulses and present first results on steering of the returning electron trajectories in HHG.

## 7.1 Introduction

Advances in ultrafast laser technology allowed the generation of pulses with intensities that reach electric field strengths comparable to the Coulomb field in atoms, molecules and bulk media. Because the field extrema occur twice per optical cycle and the response of matter to such intensities is extremely fast and nonlinear with respect to the instantaneous field strength, direct observation of attosecond dynamics became possible, giving rise to the new research field of attophysics [1]. An electric field competing in its strength with binding forces can significantly modify the binding potential seen by outer valence electrons, allowing their release into the continuum. Liberation of an electron by the laser field from its bound state is the primary step in strong field—matter interaction [2]. Tunnel ionization and subsequent acceleration of the liberated electron lead to prominent phenomena like above threshold ionization (ATI) [3] or THz field generation [4]. Some trajectories allow the electron to return to the parent ion where it can recombine to the ground state emitting high energy photons, the process known as high order harmonic generation (HHG) [5].

Traditionally, the required field strengths are achieved by using ultrashort laser pulses with a sinusoidal carrier wave. The shape of the waveform determines the instances of ionization and the trajectories of the released electron. For a sinusoidal carrier wave, this dependence famously results in the $3.17U_p$ maximum kinetic energy of a rescattered electron being converted into the highest HHG photon energy [5], as a direct consequence of controlling a returning electron wave packet trajectory with a harmonically oscillating electric field.

The highest peak power of an ultrashort laser pulse is achieved through pulse compression, i.e. elimination of group delay for all colors comprising the pulse. Field evolution control, performed either through tailoring the pulse envelope or through shaping the optical cycles, provides access to changing the outcome of complex strong field matter interactions. Control on the femtosecond time scale can be achieved by tuning the envelope of the driving laser pulse [6]. Control on the attosecond, or sub-cycle, time scale requires shaping the optical cycle of the carrier wave. Basic field shaping methods, without mentioning polarization coding methods are the chirping of the carrier wave [7], control of its phase under a few-cycle envelope [8], or coherent addition of low-order harmonics [9]. The later method corresponds to Fourier synthesis of an optical waveform. The capacity of the lower harmonic superposition method is however limited by a steep decrease in the generation efficiency and the fact that harmonics quickly reach the UV region which is undesirable for driving strong field phenomena. An important improvement of this multicolor method will be to efficiently generate Fourier components downconverted rather than upconverted from the laser frequency. Optical parametric amplification is an efficient and well-developed technology to realize such synthesis.

Here we describe several implementations of multi-color sub-cycle shaping of intense laser fields that allow direct control of strong-field dynamics. The implications of the initial step, tunnel ionization, as the fundamental process behind a plethora of strong field processes, also discussed in [10], are reviewed in Sects. 7.2–7.6 of this chapter. The final part deals with the control of the trajectories of the ionized electrons for tailoring HHG.

## 7.2 Strong-Field Ionization

The ionization rate and timing can be controlled via sub-cycle shaping of the waveform. Keldysh suggested in his revolutionary theoretical work [2], that a valence electron can tunnel through the binding potential barrier, modified by a strong laser field. Since the probability of ionization reaches its maximum near the peaks of the electric field, ionization is predicted to be confined to short intervals of time, lasting a fraction of a half cycle of the light field oscillation. Typically, the tunneling ionization (TI) regime is defined to occur when the Keldysh parameter $\gamma$:

$$\gamma = \frac{\omega_L\sqrt{2m_e I_p}}{|e|E_0} \tag{7.1}$$

is much less than unity $\gamma \ll 1$ ($\omega_L$—laser carrier frequency, $E_0$—amplitude of the electric component of the light field, $I_p$—ionization potential of an atom, $m_e$ and $e$—electron mass and charge respectively). In a later theoretical work [11] Yudin and Ivanov suggested that tunneling remains significant even for $\gamma$ greater than one. The case, when $\gamma \sim 1$ corresponds to the non-adiabatic tunneling regime. Since in this regime the corresponding tunneling time is on the order of the optical half-cycle, the binding potential formed by the atomic field and oscillating laser field varies during tunneling in this regime.

In the regime of TI, the probability of ionization is extremely sensitive to the amplitude of the electric field since only a sufficiently strong field can cause substantial modification of the binding atomic potential. Consequently, the ionization rate becomes strongly sensitive to the absolute phase of the light pulse, which leads to the expectation that the ionization yield reveals a step-wise profile on a sub-femtosecond time scale where each step is locked to a half-cycle of the laser field. Such a behavior of the ionization yield has been recently visualized in an elegant time-of-flight spectrometry measurement [12] where the attosecond steps in the ion yield were detected using an isolated soft X-ray attosecond pump pulse and a few-cycle optical probe. It also demonstrates that the tunneling regime of ionization remains significant even at $\gamma$ values greater than unity (as it was predicted in [11]) since $\gamma \sim 3$ was used in the experiment.

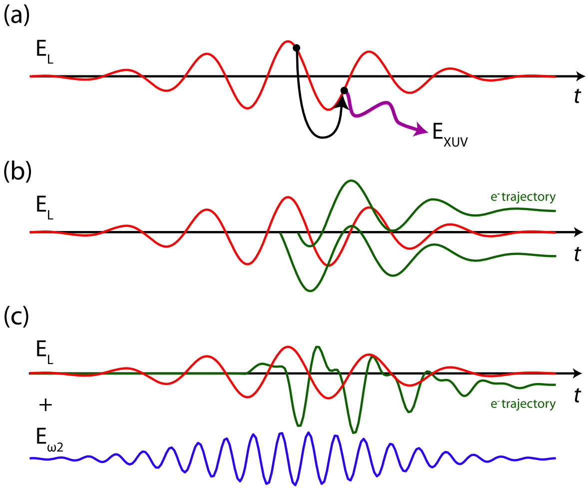

**Fig. 7.1** Ionization in a strong laser field can be viewed as tunneling through a barrier formed by the addition of potential slope caused the laser electric field and the atom's Coulomb potential. After ionization, the motion of the freed electron is forced by the laser's electric field, and thus the freed electron can come back to its parent ion with a high kinetic energy and recombine. Upon recombination a high energetic photon is emitted (**a**). However, the recombination probability is low, and thus most freed electrons remain and gain energy until the laser pulse has passed (**b**). Generally, the electron emission is symmetric with respect to the laser polarization direction. This symmetry can be broken by adding a second laser field with an appropriately chosen different color and phase (**c**). The asymmetric electron emission can give rise to emission of a strong low-frequency (THz) pulse

It is important to emphasize that the direct observation of ions was performed in [12] by means of a time-of-flight measurement. This method is currently successfully used in attosecond physics [13, 14] for investigation of different intra-atomic and intra-molecular process in gases [15] and solid surfaces [16]. This technique implies the detection of charged particles (electrons or ions) that have escaped from the interaction volume and is applicable for gaseous media or solid surfaces. However, it cannot be used for investigation of ionization processes in volume of bulk materials. Therefore, for such materials another method which is not based on direct detection of ionization products has to be developed.

Recently, we have devised an all-optical approach for investigation of ionization dynamics in transparent media, based on the detection of a time-resolved optical signal which uniquely originates from the electron tunneling [17]. This method utilizes a non-collinear optical pump-probe scheme, where ionization dynamics created by a few-cycle pump pulse is read out by a probe pulse in the form of new spectral components. The non-collinear pump-probe scheme allows us to discriminate between the delay-dependent signal in the direction of the probe pulse, originating from ionization, and all possible signals generated through the nonlinear response of the medium. From the nature of TI, one can obviously expect that new frequencies are generated spaced by twice the optical frequency of the ionizing field. This

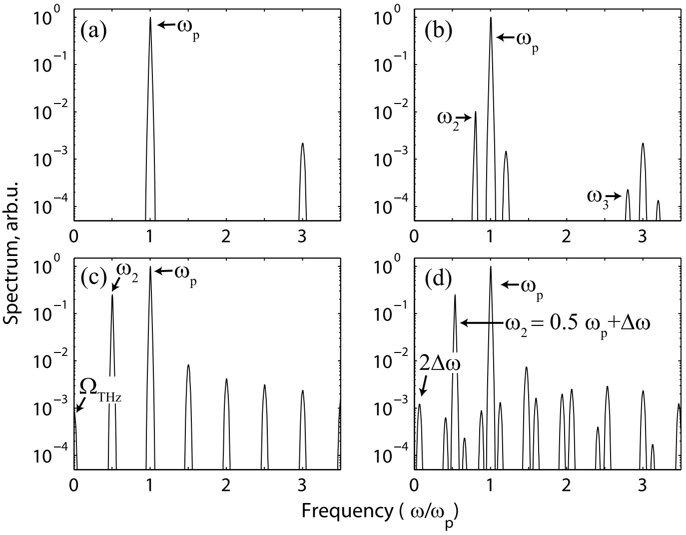

**Fig. 7.2** Sideband generation due to tunnel ionization effects. In a monochromatic laser field, due to tunnel ionization, odd-order harmonics are generated (**a**). When a weak second laser field is added with a slightly different frequency, sidebands spaced by twice the stronger laser field's frequency are generated relative to the weak field's frequency as well (**b**). When the weak laser field's frequency is equal to half the frequency of the strong field, the tunnel ionization is enhanced every other half-cycle of the strong field. The induced asymmetric emission gives rise to sidebands spaced by exactly once the frequency of the strong field, and thus a field with almost zero frequency, i.e. THz emission can be observed as well (**c**). By tuning the weak field's frequency away from $1/2$ the strong field frequency by $\Delta\omega$, the frequency of the generated THz sideband is shifted by $2\Delta\omega$ (**d**)

behavior was first proposed by F. Brunel in 1990 [18], as a mechanism to explain high harmonic generation (HHG). Although later it was shown by P. Corkum [5] that HHG is better explained by recombination of accelerated electrons after TI [19] (see also Fig. 7.1), investigation of harmonic generation following the mechanism proposed by Brunel can offer more insights in the dynamics of TI in the adiabatic regime.

In the pump-probe scheme, it is not required that the pump and probe fields have the same frequency. Thus one may expect that the ionization profile read out by the probe field gives rise to sidebands separated by twice the optical frequencies of the pump field with respect to the frequency of the probe field. When the polarization of the probe field is the same as the polarization of the pump field, and the fields propagate together in the same direction, the modulation on the pump field caused by the probe causes a modulation of the ionization rate, which results in the generation of even more frequencies. The implications of this insight are reviewed in Fig. 7.2.

In this chapter, we present experimental results on optical signals induced by TI, detected in different frequency ranges, and a theoretical model of the generation of new optical frequencies in media ionized by a high-intensity laser field. After the presentation of a semiclassical framework to describe TI in a multicolor laser field and a quantum mechanical interpretation, we present different experiments supporting our model. First of all, we demonstrate using TI in gaseous media that our noncollinear pump-probe scheme allows detecting the new frequency components in the probe field direction, such that the TI induced signal can be separated from other nonlinear responses. In a second step, we show that the method allows detecting the TI induced signal from bulk dielectric media, expanding the field of attosecond physics to systems where direct detection of charged particles is impossible. When the probe beam has the same polarization as the pump, and has a frequency close to half the pump frequency, TI can be suppressed for every other half-cycle, similarly to when the probe frequency is close to the pump second harmonic. In such a case, a sideband close to zero frequency can be observed from gaseous media in the adiabatic TI regime [20]. Such a scheme offers great perspectives for broadband and high peak amplitude THz-pulse generation. We show that the frequency of the THz sideband can be continuously tuned by tuning the frequency ratio of the two color field. Our experimental observations are in good agreement with calculations of the optical response from the ionized medium using semiclassical two-step model. Finally, we show that the directional current in gases induced by incommensurate frequency fields can be directly detected. A classical description of the electron current following TI in a multi-color laser field can at the same time accurately describe the electron kinetic energy spectrum, and the generation of new frequencies from an ionized medium. We also show that the low energy electron spectrum may be used for a more robust carrier-envelope phase detection scheme, since the electron yield at low kinetic energies is orders of magnitude higher than at high kinetic energies.

### 7.2.1 Semiclassical Model of Electron Emission and Sideband Generation in a Two-Color Field

The semiclassical model of Brunel harmonic emission [18] provides an intuitive description of the mechanism of the process. It is based on microscopic electron current production in a field. Brunel proposed a model initially aiming to explain high order harmonic generation. More recently it was shown that the superposition of two colors, namely fundamental frequency and the second harmonic of the laser field, induces a directional current and the model is used to explain the strong THz pulse emission in plasma [21]. In the high-intensity regime, the ionization of atoms or molecules can be described as a tunneling of an electron through the barrier into the continuum. Quantitatively this is calculated using the ADK tunneling rate formula [24]. After the electron is released into a continuum, it is treated as a classical particle and is accelerated in a laser field. The velocity $v_d$ of an electron in a laser field $E(t)$ is given by:

$$v(t) = \frac{q_e}{m_e} \int_{t_0}^{t} E(t') dt' \tag{7.2}$$

The resulting laser-field induced electron current density is then calculated by integrating:

$$J(t) = \frac{q_e^2 \rho}{m_e} \int_{-\infty}^{t} dt_i \Gamma(t_i) \int_{t_i}^{t} dt' E\big(t'\big) \tag{7.3}$$

where $\Gamma$ is the tunneling rate, $\rho$ is the density of gas, $q_e$ and $m_e$ is the charge and mass of an electron. The emission of electromagnetic field is related to the acceleration of the charge and is therefore proportional to the derivative of the induced current density $J(t)$:

$$E_{THz} \propto \frac{dJ(t)}{dt} \tag{7.4}$$

### 7.2.2 Quantum Mechanical Treatment of Brunel Emission

The classical interpretation of the emission by the induced electron current although intuitive, is not rigorous and does have serious limitations. On the other hand full ab initio numerical integration of time-dependent Schrödinger equation was performed to calculate THz emission [22, 23] and shows a good agreement with the experimental data. Initial steps were done to apply a strong field approximation for the calculation of the THz emission using analytical quantum mechanical model [23]. Here we show that there is a bridge between the classical model of the emission due to strong field ionization and charge motion in the laser field and the free-free transitions in the quantum mechanical interpretation. The semiclassical treatment by Brunel is based on several approximations. First, only the interaction of the free electron with the laser field is considered, the Coulomb potential of the core is neglected. The model describes the electromagnetic wave emission that arises from the current $J$ induced by the laser field. The emitted electric field is proportional to the derivative $\dot{J}$ which is can be expressed as a product of the ionization rate and the laser field:

$$\dot{J} \propto E_L(t) n(t) \tag{7.5}$$

where $E_L(t)$ is the laser electric field and $n(t)$ is the time-dependent electron density. In the limit of small depletion and strong field regime the free electron density can be expressed as $n(t) = N \int^t \Gamma(t')dt'$, where $N$ is the density of the atoms or molecules and $\Gamma(t)$ is the static ionization rate. From the quantum mechanical perspective, the induced dipole moment is:

$$d(t) = \big\langle \psi(t) | \widehat{d} | \psi(t) \big\rangle \tag{7.6}$$

The wavefunction of the whole system can be separated into continuum and bound wavepacket parts $\psi = \psi_b + \psi_c$. Similar to the semiclassical model, let us consider only the free electrons and replace the full wavefunction with the continuum wavepacket $\psi_c$. The derivative of the current $\dot{J}$ is associated with the second derivative of the dipole moment:

$$\ddot{d}(t) = \big\langle \psi_c(t) \big| F_{total} \big| \psi_c(t) \big\rangle \tag{7.7}$$

where $F_{total}$ is the total field acting on the electron wavepacket, which can be separated into two parts: $F_{total} = F_L + F_{core}$. The first term corresponds to the force acting on the electron by laser field and the second term is the force due to interaction with the core. By neglecting the latter term, the dipole acceleration becomes:

$$\ddot{d}(t) = F_L \langle \psi_c(t) | \psi_c(t) \rangle \tag{7.8}$$

The right hand side of the equation is just a probability of ionization times the force of the laser field $F_L W_C(t)$. Since $n(t) \approx N W_C(t)$, we see that the expression (7.8) is essentially the same as the derivative of the electron current (7.5) in the semi-classical treatment, which means that the emission mechanism proposed by Brunel arises due to continuum-continuum transitions.

## 7.3 High-Frequency Sidebands in Gas Targets

We experimentally observe the emission of new optical frequency components that are generated following the emission mechanism proposed by Brunel. In a noncollinear pump-probe setup, using 250 μJ, 5 fs horizontally polarized pump pulses, and 1 μJ, 10 fs vertically polarized probe pulses, we have measured the ionization induced high-frequency sidebands as a function of delay between the pump and probe pulses. In a first experiment, we have used krypton at a neutral gas pressure of $\sim$ 250 mbar, and we have observed the TI induced sidebands lying around the 3rd, 5th and 7th harmonic of the pump and probe pulses. The measured spectrally resolved signals as a function of pump-probe delay are shown in Fig. 7.3(a). The temporally integrated signals (Fig. 7.3(b)) are compared with the signal obtained from numerical simulations, that includes gas and plasma dispersion, diffraction, spatial self-action induced by Kerr-nonlinearities, spectral transformation phenomena such as self phase modulation, wave mixing and harmonic generation, as well as ionization induced loss and plasma related nonlinearities. Although the signal-to-noise ratio of the experimental data is rather small, several very important agreements between the experimental data and the numerical simulations can be identified. In Fig. 7.3(b), the experimental data integrated along the delay-axis is compared to the full numerical results (dashed colored curves) are and with the results when no propagation effects are taken into account (black dotted curves). A clear frequency shift away from 'pure' harmonics can be observed when the propagation effects are taken into account. This shift, although the magnitude is different for the different sidebands, is observed in the experimental data as well.

In order to further investigate the TI induced sideband generation, we have performed a more extensive study of the sideband around the 3rd harmonic of our pump and probe pulses. In this study, an argon target was used. While the ionization yield from argon is lower than from krypton, the signal may be expected to be slightly lower. However, since we use a spectrometer that is optimized for detection of light between 200 and 400 nm, the signal-to-noise ratio for these measurements is much higher than for the measurements using krypton, as can be seen in Fig. 7.4.

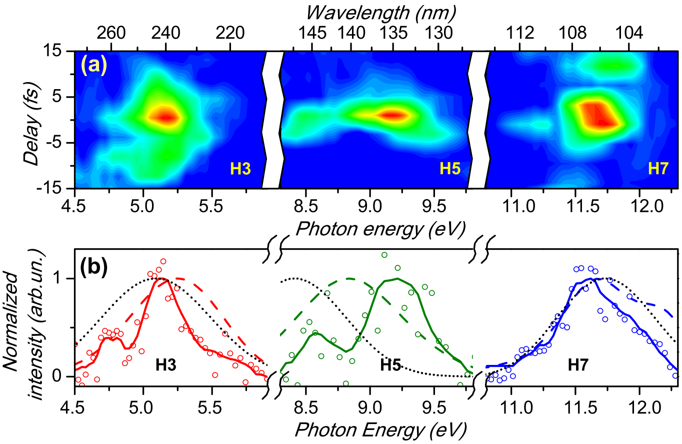

**Fig. 7.3** High frequency sideband generation in krypton. Panel (**a**) shows the measured spectrally resolved signals as a function of the delay between the pump and probe pulses. In panel (**b**) we compare the measured signals integrated along the delay axis with the results from numerical simulations, taking into account all propagation effects (*dashed colored curves*) and without taking into account propagation effects (*black dotted curves*). The frequency shift caused by propagation effects is clearly seen in the numerical results as well as in the measured data

We have investigated the influence of the pump pulse chirp on the measured signal (Fig. 7.4(b)), as well as the influence of the probe energy (Fig. 7.4(c)). For the latter, a linear dependence of the TI induced signal on the probe energy is observed, as may be expected since the probe pulse reads out the modulation induced by the pump pulse. The influence of the pump pulse chirp on the measured signal can be expected to have different implications. First of all, since the periodicity of the ionization steps is disrupted, spectral broadening of the TI induced signal may be expected. However, since the intensity is reduced when a chirp is introduced on the pump pulse, it is clear that the TI induced signal is greatly reduced as well. While we observe a spectral broadening for small amounts of chirp introduced to the pump pulse, the decrease of the TI induced signal for increased chirp on the pump pulse makes a quantitative study of the spectrally resolved signal rather complicated. Therefore we only plot the spectrally integrated TI induced signal as a function of pump pulse chirp, which clearly shows the expected rapid decrease of the signal (see Fig. 7.4(b)).

## 7.4 High-Frequency Sidebands in Bulk Dielectrics

Having us proved the conceptual point about the optical detection of the TI induced signal in gas targets, krypton and argon, we have subsequently performed measurements of the TI induced sideband in the wavelength range from 200 to 300 nm from different bulk dielectrics. Since in many cases the third harmonic generated by the probe beam alone was comparable in strength to the TI induced signal, we have set

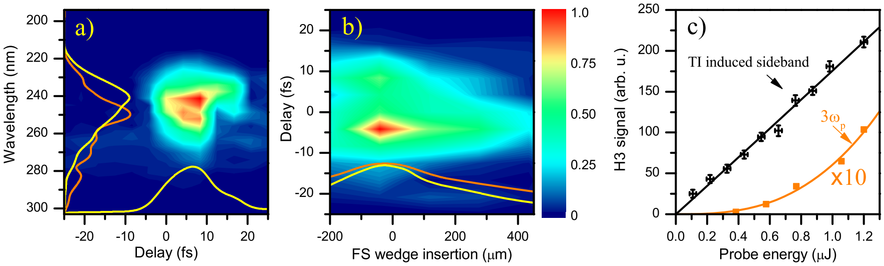

**Fig. 7.4** Investigation of the sideband close to the 3rd harmonic frequency due to tunnel ionization in argon. Panel (**a**) shows the spectrally resolved measured signal as a function of pump-probe delay. *The yellow curves* show the signal integrated along the delay and wavelength axes. *The orange curve* shows the normalized third harmonic of the probe pulse measured in absence of the pump pulses. Panel (**b**) shows the spectrally integrated signal as a function of net material insertion in the pump beam path. The induced chirp lowers the peak intensity, and thus the ionization yield and, therefore, the yield of the ionization induced sideband. *The yellow curve* shows the normalized integrated signal, and *the orange curve* shows the estimated normalized peak intensity of the pump pulses. Panel (**c**) shows the dependence of the sideband signal on the probe pulse energy. *The orange curve* shows the signal in absence of the pump pulse

the central wavelength of the probe pulses to be different from the central wavelength of the pump pulses. This ensures that in addition to the spatial separation of the TI induced signal from other processes, the TI induced signal can be spectrally separated from signals due to other processes that propagate in the same direction as the probe beam. In order to confirm that the spatial and spectral separation works, we have measured the signal with linear polarized pump pulses, as well as with circular polarized pump pulses. In the case of circular polarization, while TI can still be the dominant mechanism for ionization, the free electron density will not increase stepwise (as is the case with linear polarized pump pulses), but smoothly. Thus, in the case of circular polarized pump pulses, no sidebands will be generated. Figure 7.5 shows the measured signal for the case of linear polarized pump pulses (a) and circular polarized pump pulses (b). While the absence of the TI induced sideband in the case of circular polarized pump pulses is notable, one can observe a clear signal due to 4-wave-mixing (FWM) $(\omega_{pump} + 2_{probe})$ as well. While this signal does not propagate in the same direction as the probe beam, however, of all FWM signals possible it propagates closest to the probe beam, and therefore is not completely suppressed by our spatial filtering. It has to be noted, that since the signal at $\omega_{pump} + 2\omega_{probe}$ inherits its polarization from the pump pulses, it is blocked by the polarizer in our setup in the case of linear polarized pump pulses, and that in the case of circular polarized pump pulses, it has a nonzero projection on the probe polarization direction.

Since the ionization rate depends exponentially on the binding potential of the material under investigation, we have performed measurements of the TI induced sideband from different dielectrics, each with a different bandgap (binding potential). For constant pump pulse intensity, a stronger signal is expected from materials with a smaller bandgap. In Fig. 7.6 we show the measured signal from different bulk dielectric materials at a pump pulse intensity of $\sim 20$ TW/cm$^2$. The expectation that

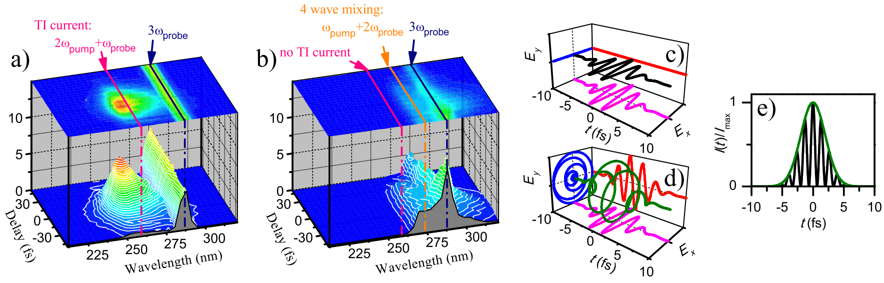

**Fig. 7.5** Tunnel ionization induced sideband generation in a bulk dielectric (fused silica). Since the tunnel ionization rate strongly depends on the instantaneous field strength, the ionization rate in a linear polarized field peaks strongly once per half-cycle. In a circular polarized field, the tunnel ionization rate varies smoothly along the laser pulse, since the field strength never becomes zero. Panel (**a**) shows the tunnel ionization induced sideband generated from fused silica with linear polarized pump pulses. This signal is not observed when the pump pulses have circular polarization (**b**). In this case, the 4-wave mixing signal $w_{pump} + 2w_{probe}$ is not blocked by the polarizer before our spectrometer, and can be used to confirm that the spatial and temporal overlap of the pump and probe pulses is not lost. Panels (**c**) and (**d**) show the temporal evolution of a respectively linear and circular polarized few cycle pulse. Panel (**e**) shows the normalized instantaneous intensity for the pulses shown in panels (**c**) (*black*) and (**d**) (*green*)

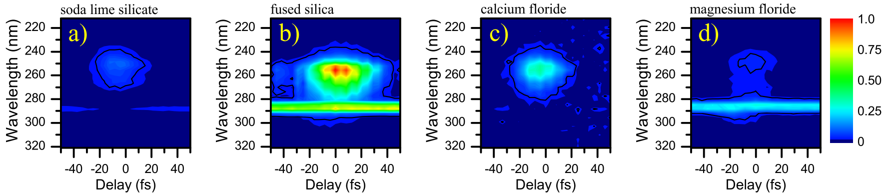

**Fig. 7.6** First tunnel ionization induced sidebands observed from different bulk dielectrics. (**a**) Soda lime silicate—$Na_2O$(22 %)CaO(3 %)$SiO_2$(75 %)—bandgap 6.5 eV. (**b**) Fused silica—bandgap 9 eV. (**c**) $CaF_2$—bandgap 10 eV. (**d**) $MgF_2$—bandgap 11 eV

less signal is expected from material with a higher bandgap is confirmed by these measurements, with the exception of the signal measured from our composite glass soda lime silicate. It has to be noted that it is known that in addition to the size of the band gap, the presence of impurities in the sample under investigation may play a significant role in suppressing or promoting ionization in the laser field. For example, samples with impurities are known to be more prone to optical damage than very pure samples of the same material. Additionally, for crystalline materials the orientation of the crystal axes with respect to the laser polarization can influence ionization as well [25].

## 7.5 Low Frequency Sideband Generation from Gas

In this section we show that the same ideas that were behind the odd-harmonic generation experiments in Sects. 7.3 and 7.4 can be seamlessly extended to explain the emission of low-frequency sidebands in the THz range. In fact, the process can be treated as a special case of wavemixing based on transient nonlinearities and as suggested in Ref. [26] can lead to the emission of THz "Brunel sidebands". Mixing the fundamental field with its second harmonic breaks the symmetry of the cycle and yields to the emission of even harmonics in addition to the odd harmonics. In addition to even high order harmonic generation, this was exploited for the generation of THz pulses in plasma by Cook and Hochstrasser [27].

There exist several interpretations of the process. Originally, the emission of the strong THz transients was attributed to a four wave mixing in air. Later, however, it was shown that the THz emission directly relies on the production of laser induced plasma. Another more accepted interpretation is a semi-classical two-step model. The second color acts as an "AC bias" by breaking the symmetry of the optical cycle and yields production of directional electron current. This directional electron burst was directly observed by means of ATI spectroscopy [28].

The experiments of the THz generation that were done to date were based on the degenerate scheme where the fundamental laser field and its second harmonic are mixed. Here we have used a different scheme based on parametric amplifier for the generation of the second field, whose frequency can be continuously tuned around the degeneracy point. The frequency of the signal wave of the degenerate OPA is half the frequency of the fundamental laser pulse. This $\omega_p + 1/2\omega_p$ scheme is similar to the popular $\omega_p + 2\omega_p$ scheme based on second harmonic generation, except that the lower frequency component is the weaker one. When the frequency of the second field is detuned from the degeneracy point, the drift of the electrons in the laser induced plasma is modulated in time, which shifts the emission peak towards higher frequencies.

An important difference in the case of multi-color pulse superposition using optical parametric amplifier (OPA) as compared to the second harmonic generation case is the phase relation between the constituent colors. In the general case, the superposition of frequency $\omega$ and $\alpha\omega$ fields can be written as follows:

$$E = E_1 \cos(\omega t + \varphi_{CEP}) + E_2 \cos(\alpha\omega t + \beta\varphi_{CEP} + \varphi_{rel}) \tag{7.9}$$

In second harmonic generation both the carrier frequency and the carrier envelope phase (CEP) are doubled ($\alpha = \beta = 2$). In this case the slip of the CEP causes the delay $\tau = \varphi_{CEP} \cdot \omega^{-1}$ of the waveform with respect to the envelope, where $\omega$ is the laser frequency. Therefore, the change is unimportant if the pulse contains many cycles and the effect of the envelope on the cycle is negligible. More generally, in the case of sum frequency generation or n-th harmonic generation, the CEP and the frequency multiplier are the same ($\beta = \alpha = n$) which consequently only causes a shift of the waveform under the envelope. However, in the case of an OPA seeded by a white light super continuum the CEP of the seed pulse is preserved ($\beta = 1$) which causes a change of the fringe shape of the field. The multi-color waveform synthesis using an OPA has the additional advantage that the frequency ratio $\alpha$ can be tuned continuously. The previously mentioned modulation of the electron burst emission direction in time leads to the shift of the sidebands in the frequency domain including the lowest frequency THz sideband as illustrated in Fig. 7.2. In order to

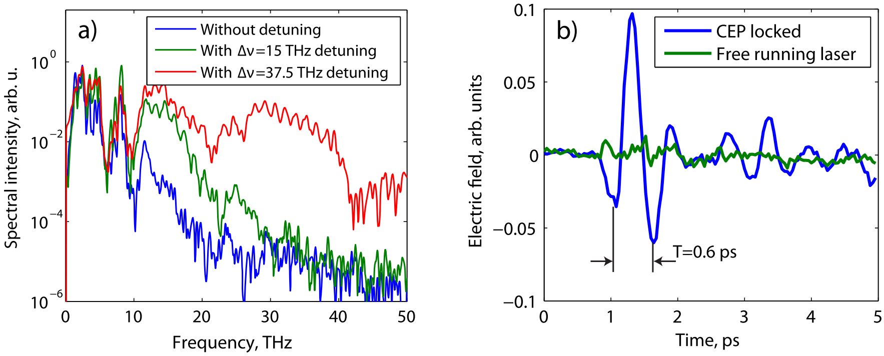

**Fig. 7.7** (**a**) Emission spectrum of plasma excited with $\omega$ and $1/2\omega + 2\pi\Delta\nu$ fields, where $\Delta\upsilon = 2\upsilon_s - \upsilon_p$ is the detuning frequency. The two-color driving laser field is comprised of the fundamental wave ($\lambda_p = 1.03$ µm, 250 µJ) and a tunable signal wave generated in an OPA ($\lambda s = 2.06 - 1.8$ µm, 20 µJ). (**b**) A comparison of the measured THz transient with the CEP of the laser locked and free running

get a reproducible field shape, we needed to actively stabilize the CEP of the pump and signal pulses of the OPA. Since the seed for the signal pulse is derived from the pump pulse, it is enough to stabilize the CEP of the driving laser in order to get all the waves of the OPA phase-locked together.

Tunable THz emission from a plasma was generated using two colors from an OPA, which was pumped by an actively CEP stabilized Yb laser. The measured spectra for different signal and pump pulse frequency ratios are shown in Fig. 7.7. By detuning the OPA from degeneracy, the frequency of the THz sideband can be shifted up to 40 THz. The demonstrated tuning bandwidth was limited by the detection scheme and the optical coatings used for combining the different frequency components of the generating beam. The spectra shown in Fig. 7.7(a) are not corrected for the detection setup response which drops at higher frequencies and yields broadening of the measured spectrum, and thus shifts the apparent maximum to lower frequencies. Figure 7.7(b) shows the effect of the CEP locking of the laser pulse on the measured THz transient. In the case of a free running laser a THz pulse is generated by every laser pulse, but due to random phase of the THz pulse the average signal measured with our field sensitive electro optic (EO) sampling detection setup is zero.

## 7.6 Mapping of Electric Current with ATI Spectroscopy

In addition to the optical detection described in the previous sections, the directional current induced by asymmetric field composed of incommensurate frequencies was also measured directly using electron spectrometry. Combination of several colors provides additional knobs to control the dynamics of sub-cycle ionization. This approach was successfully applied, for example, for the measurement of electron birth time in the HHG process [29] and isolated attosecond pulse generation [30, 31].

Here have extended this approach and combine incommensurate frequency infrared colors to control the timing and the trajectory of the electron in a continuum.

In this section we shall present ATI electron spectroscopy measurements in xenon using intense two-color laser pulses. A two color beam that is composed of a strong 1030 nm and a weaker 1545 nm signal wave is focused into a xenon gas cell. The intensity of approximately $0.6 \times 10^{14}$ W/cm$^2$ is reached in the focus which corresponds to the regime where TI is a dominant process ($\gamma \approx 0.8$). In the strong field regime the electron wave packet evolution in the continuum is mainly determined by the shape of the laser field and the Coulomb interaction with the parent ion can be neglected.

The superposition of two colors can be considered as a train of few-cycle pulses with a DC offset (if the amplitudes of the two fields are not equal). In case of equal amplitudes of two colors $E_1$ and $E_2$, the resulting field is:

$$E = f(t)2\sin\left(\frac{\omega_1+\omega_2}{2}t + \varphi_{CEP} + \frac{\varphi_{rel}}{2}\right)\cos\left(\frac{\omega_1-\omega_2}{2}t - \frac{\varphi_{rel}}{2}\right) \tag{7.10}$$

In the case of combination of pulses with a wavelength of 1030 nm and 1545 nm, the synthesized field can be considered as a train of pulses with the corresponding carrier wavelength $\lambda = 4\pi c/(\omega_1 + \omega_2) = 1.2$ µm and separated by $T = 2\pi/(\omega_1 - \omega_2) = 10$ fs in time.

The experimental results are summarized in Fig. 7.8. The electron spectrum and a lineout at 15 eV shown in panels (a) and (b) are highly dependent on the CEP of the laser pulse. The electron asymmetry modulation depth at 15 eV exceeds 50 %, which indicates good reproducibility of the generated waveforms. The calculated asymmetry map depicted in Fig. 7.8 c) shows the value of the normalized asymmetry parameter $a = (L - R)/(L + R)$ versus energy and CEP of the laser pulse. From this data the phase ellipse is obtained by taking lineouts at two different energy windows [32, 33], which can be used for in-situ calibration of the actual produced waveform.

Usually for the measurement of the CEP value the high energy part of the spectrum corresponding to rescattered electrons is used. The low energy part of the spectrum which is dominated by direct electrons, is also sensitive to the CEP of the pulse. Here we show that the CEP can be measured in-situ not only from the high energy part of the electron spectrum, but also the low energy direct electrons can be used to retrieve the CEP without $\pi$-ambiguity. From the experimental data in Fig. 7.9 a low energy window can be observed where the phase of the retrieved asymmetry varies with electron energy allowing CEP retrieval without $\pi$ ambiguity. The advantage of using low energy electrons over using high energy electrons is that the electron yield much higher allowing for low noise CEP detection without using very high gas densities. Another advantage of using low energy electrons is the better spectral resolution of time of flight spectrometers at lower energies.

## 7.7 High-Order Harmonic Generation

The use of a multicolor multi-cycle driver waveform that can modify the returning trajectory and, simultaneously, accelerate the tunneled-out electron to a higher

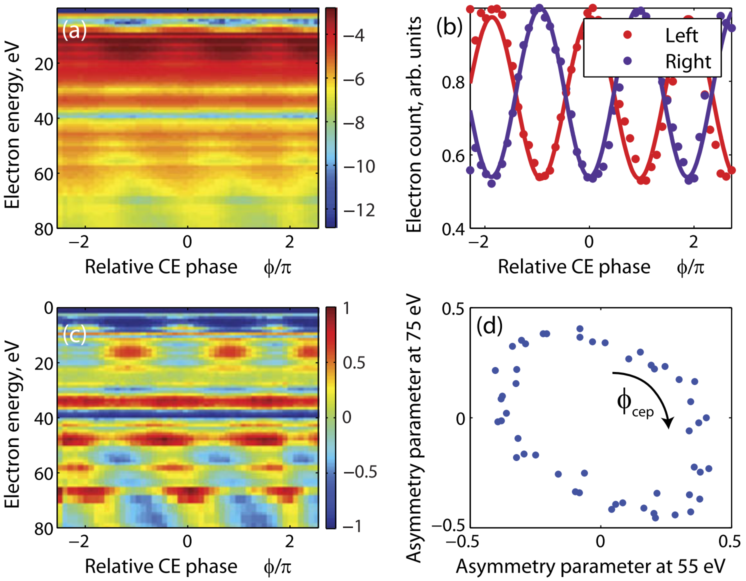

**Fig. 7.8** ATI electron spectrum measurement. (**a**) Phase dependent spectrum of the electrons emitted to the right, (**b**) lineout at 15 eV of the left and right energy spectra for different CEP, (**c**) measured asymmetry parameter dependence on CE phase and electron energy, (**d**) CEP phase ellipse obtained from assymmetry parameters at 55 and 75 eV energy

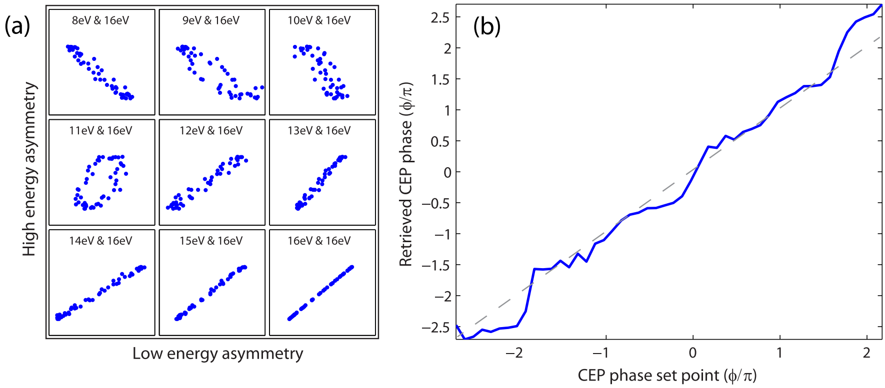

**Fig. 7.9** Phase ellipses obtained by taking lineouts at different positions of the spectrum in the low energy range that is dominated by the direct electrons (**a**). The retrieved CE-phase (*blue line*) is obtained using 11 eV and 16 eV energy windows. *The dashed lined* represents the ideal of perfect phase stability and control

kinetic energy compared to the case of a single-color sinusoidal driver field [34]. The initial suggestion for this optimized re-colliding electron steering, dubbed “the perfect wave” [34], assumed a combination of UV optical harmonics of a 800-nm

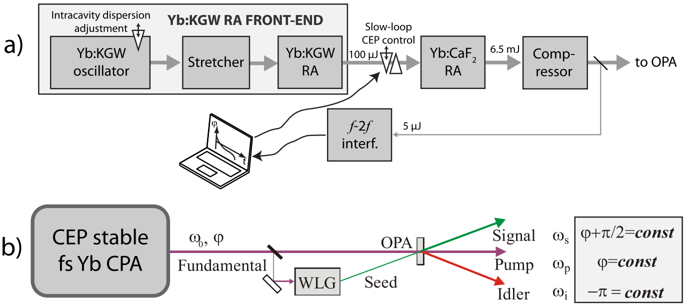

**Fig. 7.10** Concept of a three-wave CEP-stable synthesizer for HHG driving. (**a**) A multi-mJ diode-pumped femtosecond 1 μm CEP-stabilized pump laser; (**b**) collinear mid-IR CEP-stable OPA

laser and included a near-IR sub-harmonic (1600 nm) to demonstrate the feasibility of the cut-off enhancement numerically. An efficient and technically straightforward approach to adding Fourier components at octave frequency spacing can be implemented using a phase-locked parametric amplifier. Shaping of the waveform is achieved via delaying the phases of the different color components and allows controlling the HHG cut-off. Simulations based on SFA [35] shown in Fig. 7.11(c) show the dependence of the cut-off on the carrier envelope phase of the driving laser pulse $\phi_{CEP}$. Here we demonstrate preliminary results of HHG driving with individual colors of multi-color synthesizer.

The general scheme of the experimental setup is depicted in Fig. 7.10. An Yb:KGW CPA laser system is used as a front-end for a high energy Yb:$CaF_2$ regenerative amplifier (RA) [36]. Using an electronic phase-lock loop (PLL), the carrier-envelope-offset phase of the amplifier chain is actively stabilized [37]. A white-light seeded parametric amplifier is pumped with actively CEP stabilized pulses and yields phase locked signal, pump and idler waves that can be coherently combined.

The results of the HHG driven by three incommensurate frequency fields are summarized Fig. 7.12. Firstly, HHG was tested using 180 fs 1.03 μm pulses directly from the Yb laser. Secondly, as a demonstration that the peak power of the system is sufficient for energy demanding applications such as HHG, we measure HHG in argon driven by two waves of our synthesizer individually: the signal wave at 1.545 μm of a KTA OPA and the fundamental wave at 1.03 μm, as shown in Fig. 7.12(a)–(b). A first obvious effect of coherently combining those two color components is obvious in Fig. 7.12(c). Due to a three times larger periodicity of the two-color field as compared to 1 μm wave and asymmetric half-cycles, the density of the harmonic peaks increases six times. Since the amplitude of the individual peaks drops roughly only by a factor of 2, the total flux integrated over the spectrum of the denser-spaced harmonics increases dramatically. Moreover, the spectrum generated using the two-color driver extends beyond the transmission edge of aluminum filter, demonstrating that the cut-off can be pushed above the saturation limit of the

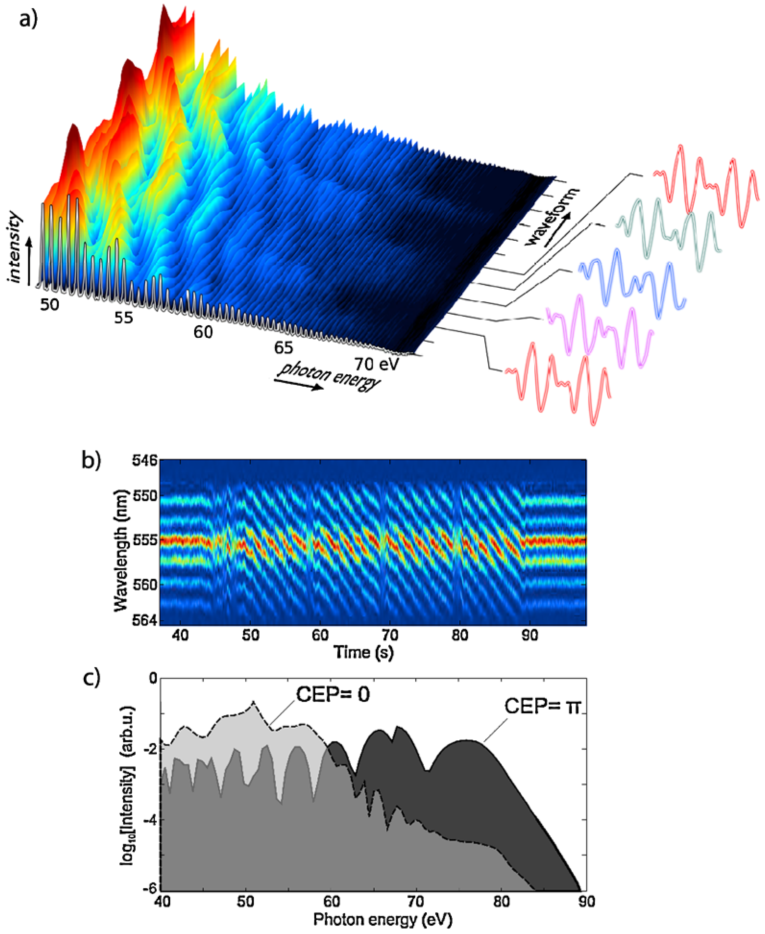

**Fig. 7.11** High order harmonic spectra generated with phase-locked multiple color pulses. (**a**) A series of measured XUV high-order harmonic spectra generated using three colors, which depend upon the shape of the optical cycle of the generating intense infrared synthesized waveforms. The waveform is controlled by scanning the CEP of the driving laser pulse. (**b**) f-2f interference spectrum used for locking the CE phase. The region with slanted line pattern corresponds to the linear ramp of the phase which is used for the measurement of the HHG spectrum dependence vs. phase. (**c**) Simulation of the three-color driven HHG spectra CEP dependence for different relative phases between the 1.545 μm ($\omega/1.5$) and 1.03 μm ($\omega$) waves $\varphi_{rel} = 0$ and $\varphi_{rel} = \pi/2$

1 μm 180 fs pulse. When the third color pulse is added, the HHG spectrum becomes highly CEP-dependent and exhibits phase-dependent cut-off modulation. This CEP dependence signifies that sub-cycle shaping is a potential tool for controlling the dynamics of the electron in a strong laser field. Superposition of these different infrared colors with comparable amplitudes provides a route towards a source of high XUV photon energy and flux.

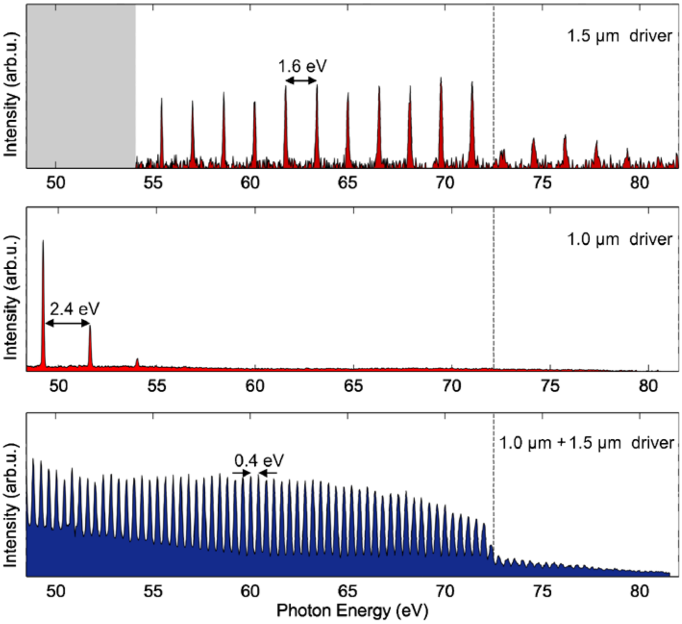

**Fig. 7.12** Multi-color HHG. Comparison of HHG spectrum generated in Argon using single color at (**a**) 1.545 µm, (**b**) 1.03 µm and (**c**) cutt-off region of the HHG spectrum generated using two-color field composed of 1.03 µm ($\omega$) and 1.545 µm ($\omega/1.5$) waves. The spectrum extends beyond the Al filter transmission edge at 72.5 eV

## 7.8 Conclusions

In this chapter, we have shown a pure optical detection of the electron ionization bursts, as well as control of the ionization and steering of the electron current via multi-color waveform synthesis. TI induces attosecond electron bursts that result in emission of new optical signals both at frequencies higher than the ionizing field and at frequencies lower than the ionizing field. In contrast to other attosecond metrology methods, the induced emission can be studied both in gases and bulk dielectrics. The experimental data are in good agreement with a calculations based on the semi-classical model describing ionization in the strong field regime and subsequent motion of the free electrons. We have also presented the first results on steering of the returning electron trajectories in HHG.

## References

1. F. Krausz, M. Ivanov, Rev. Mod. Phys. **81**, 163 (2009)
2. L. Keldysh, Sov. Phys. JETP **20**, 1307 (1965)
3. P. Agostini, F. Fabre, G. Mainfray, G. Petite, N.K. Rahman, Phys. Rev. Lett. **42**, 1127 (1979)
4. H.G. Roskos, M.D. Thomson, M. Kreß, T. Löffler, Laser Photonics Rev. **1**, 349 (2007)
5. P. Corkum, Phys. Rev. Lett. **71**, 1994 (1993)
6. R. Bartels, S. Backus, E. Zeek, L. Misoguti, G. Vdovin, I. Christov, M. Murnane, H. Kapteyn, Nature **406**, 164–166 (2000)

7. Z. Chang, A. Rundquist, H. Wang, I. Christov, H. Kapteyn, M. Murnane, Phys. Rev. A **58**, R30–R33 (1998)
8. A. Baltuška, Th. Udem, M. Uiberacker, M. Hentschel, E. Goulielmakis, Ch. Gohle, R. Holzwarth, V.S. Yakovlev, A. Scrinzi, T.W. Hänsch, F. Krausz, Nature **421**, 611 (2003)
9. F. Calegari, C. Vozzi, M. Negro, G. Sansone, F. Frassetto, L. Poletto, P. Villoresi, M. Nisoli, S. De Silvestri, S. Stagira, Opt. Lett. **34**, 3125 (2009)
10. T. Balciunas, A.J. Verhoef, A.V. Mitrofanov, G. Fan, E.E. Serebryannikov, M.Y. Ivanov, A.M. Zheltikov, A. Baltuska, Chem. Phys. (2013). doi:10.1016/j.chemphys.2012.02.007
11. G. Yudin, M. Ivanov, Phys. Rev. A **64**, 013409 (2001)
12. M. Uiberacker, Th. Uphues, M. Schultze, A. Verhoef, V. Yakovlev, M. Kling, J. Rauschenberger, N. Kabachnik, H. Schroder, M. Lezius, K. Kompa, H.-G. Muller, M. Vrakking, S. Hendel, U. Kleineberg, U. Heinzmann, M. Drescher, F. Krausz, Nature **446**, 627 (2007)
13. E. Goulielmakis, V. Yakovlev, A. Cavalieri, M. Uiberacker, V. Pervak, A. Apolonski, R. Kienberger, U. Kleineberg, F. Krausz, Science **317**, 769 (2007)
14. P. Corkum, F. Krausz, Nat. Phys. **3**, 381 (2007)
15. Th. Uphues, M. Schultze, M. Kling, M. Uiberacker, S. Hendel, U. Heinzmann, N. Kabachnik, M. Drescher, New J. Phys. **10**, 025009 (2008)
16. A. Cavalieri, N. Muller, Th. Uphues, V. Yakovlev, A. Baltuska, B. Horvath, B. Schmidt, L. Blumel, R. Holzwarth, S. Hendel, M. Drescher, U. Kleineberg, P. Echenique, R. Kienberger, F. Krausz, U. Heinzmann, Nature **449**, 1029 (2007)
17. A. Verhoef, A. Mitrofanov, E. Serebryannikov, D. Kartashov, A. Zheltikov, A. Baltuska, Phys. Rev. Lett. **104**, 163904 (2010)
18. F. Brunel, J. Opt. Soc. Am. B **7**, 521 (1990)
19. J.L. Krause, K.J. Schafer, K.C. Kulander, Phys. Rev. Lett. **68**, 3535 (1992)
20. M. Kress, T. Löffler, S. Eden, M. Thomson, H.G. Roskos, Opt. Lett. **29**, 1120 (2004)
21. K.Y. Kim, A.J. Taylor, J.H. Glownia, G. Rodriguez, Nat. Photonics **2**, 605 (2008)
22. N. Karpowicz, X.-C. Zhang, Phys. Rev. Lett. **102**, 093001 (2009)
23. Z. Zhou, D. Zhang, Z. Zhao, J. Yuan, Phys. Rev. A **79**, 063413 (2009)
24. M.V. Amosov, N.B. Delone, V.P. Krainov, Zh. Eksp. Teor. Fiz. **91**, 2008 (1986)
25. M. Gertsvolf, M. Spanner, D. Rayner, P. Corkum, J. Phys. B **43**, 131002 (2010)
26. C. Siders, G. Rodriguez, J.L.W. Siders, F.G. Omenetto, A.J. Taylor, Phys. Rev. Lett. **87**, 263002 (2001)
27. D.J. Cook, R.M. Hochstrasser, Opt. Lett. **25**, 1210 (2000)
28. T. Balčiūnas, D. Lorenc, M. Ivanov, O. Smirnova, A. Pugžlys, A.M. Zheltikov, D. Dietze, J. Darmo, K. Unterrainer, T. Rathje, G.G. Paulus, A. Baltuška, in *Proceedings of the 17th Int. Conference on Ultrafast Phenomena* (2010), p. 658
29. N. Dudovich, O. Smirnova, J. Levesque, Y. Mairesse, M.Yu. Ivanov, D.M. Villeneuve, P.B. Corkum, Nat. Phys. **2**, 781 (2006)
30. E.J. Takahashi, P. Lan, O.D. Mücke, Y. Nabekawa, K. Midorikawa, Phys. Rev. Lett. **104**, 233901 (2010)
31. F. Calegari, C. Vozzi, M. Negro, G. Sansone, F. Frassetto, L. Poletto, P. Villoresi, M. Nisoli, S. De Silvestri, S. Stagira, Opt. Lett. **34**, 3125–3127 (2009)
32. D. Miloševič, G. Paulus, W. Becker, Opt. Express **11**, 1418–1429 (2003)
33. T. Wittmann, B. Horvath, W. Helml, M.G. Schätzel, X. Gu, A.L. Cavalieri, G.G. Paulus, R. Kienberger, Nat. Phys. **5**, 357–362 (2009)
34. L.E. Chipperfield, J.S. Robinson, J.W.G. Tisch, J.P. Marangos, Phys. Rev. Lett. **102**, 063003 (2009)
35. M. Lewenstein, P. Balcou, M.Y. Ivanov, A. L'Huillier, P.B. Corkum, Phys. Rev. A **49**, 2117 (1994)
36. A. Pugzlys, G. Andriukaitis, A. Baltuska, L. Su, J. Xu, H. Li, R. Li, W.J. Lai, P.B. Phua, A. Marcinkevicius, M.E. Fermann, L. Giniūnas, R. Danielius, S. Alisauskas, Opt. Lett. **34**, 2075 (2009)
37. T. Balčiūnas, O.D. Mücke, P. Mišeikis, G. Andriukaitis, A. Pugžlys, L. Giniūnas, R. Danielius, R. Holzwarth, A. Baltuška, Opt. Lett. **36**, 3242 (2011)

# Chapter 8
# Attosecond Electron Interferometry

**Johan Mauritsson, Marcus Dahlström, Kathrin Klünder, Marko Swoboda, Thomas Fordell, Per Johnsson, Mathieu Gisselbrecht, and Anne L'Huillier**

**Abstract** Attosecond extreme ultraviolet light pulses have the potential to resolve the ultrafast electron dynamics that govern basic properties of atoms, molecules, and solids. Here we present three different interferometric pump-probe methods aiming to access not only the temporal dynamics, but also state specific phase information after excitation/ionization using attosecond pulses.

---

J. Mauritsson · K. Klünder · P. Johnsson · A. L'Huillier (✉)
Atomic Physics, Lund University, Box 118, 221 00 Lund, Sweden
e-mail: Anne.LHuillier@fysik.lth.se

J. Mauritsson
e-mail: johan.mauritsson@fysik.lth.se

K. Klünder
e-mail: Kathrin.Klunder@fysik.lth.se

P. Johnsson
e-mail: Per.Johnsson@fysik.lth.se

M. Dahlström
Atomic Physics, Stockholm University, 106 91 Stockholm, Sweden
e-mail: Marcus.Dahlstrom@fysik.su.se

M. Swoboda
B CUBE—Center for Molecular Bioengineering, TU Dresden, Arnoldstrasse 18, 01307 Dresden, Germany
e-mail: marko.swoboda@bcubedresden.de

T. Fordell
Centre for Metrology and Accreditation (MIKES), P.O. Box 9, 02151 Espoo, Finland
e-mail: Thomas.Fordell@mikes.fi

M. Gisselbrecht
Synchrotron Radiation Research, Lund University, Box 118, 221 00 Lund, Sweden
e-mail: Mathieu.Gisselbrecht@sljus.lu.se

L. Plaja et al. (eds.), *Attosecond Physics*, Springer Series in Optical Sciences 177,
DOI 10.1007/978-3-642-37623-8_8,

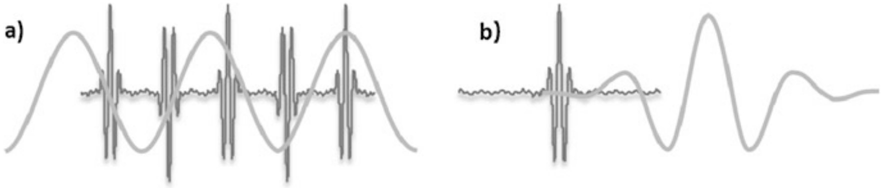

**Fig. 8.1** (**a**) APT plus IR field, (**b**) isolated attosecond pulses plus delayed IR field

## 8.1 Introduction

Attosecond pulses are the shortest available probes to time-resolve processes that occur on the natural time scale of electrons (notably photo excitation processes in atoms) [1, 2]. The bandwidth of these pulses is intrinsically very broad. In order to obtain state specific information we need to achieve a spectral resolution much better than the inverse of the pulse duration. Here we demonstrate that this is achievable by utilizing the coherence of multiple pulses combined with interferometric measurements. We do this by detecting photoelectrons ionized using either an attosecond pulse train (APT), which corresponds to a frequency comb in the spectral domain, or a pair of pulses, analog to traditional Ramsey spectroscopy, with the difference that the pulses have different frequencies, one in the extreme ultraviolet (XUV) and one in the infrared (IR) or visible frequency range. The coherent addition of multiple ionization pathways result in observable interference fringes in the photoelectron spectra that contain both spectral and temporal information about the ionization process. The spectral resolution will, in this case, not be limited by the bandwidth of the pulses, but by the stability and delay range of the pulses.

In this chapter we present three experiments where attosecond electron interferometry is used to obtain both spectral and temporal information. In these experiments we:

1. measure the phase variation of resonant two-color two-photon ionization, which allows us to determine the intensity dependence of the $1s^2$-1s3p transition energy in helium [3];
2. measure the difference in time delay between electrons emitted from the $3s^2$ and $3p^6$ sub-shells in argon [4];
3. characterize an excited electron wave packet in helium composed of the 3p, 4p and 5p states by interfering it with a known reference [5].

In the first experiments (1 and 2) we use an APT and a weak IR probe field (Fig. 8.1(a)), while in the third experiment (3) an isolated attosecond pulse and a few-cycle IR pulse interact with the atom (Fig. 8.1(b)). In all three cases the measurements are based on interferences between photoelectron wave packets at different delays between the attosecond pump pulses and the IR probe pulses. The spectral resolution is not given by the inverse of the duration of the actual pulses but rather by that of the pump-probe delay. We thus reach a resolution that can potentially be orders of magnitude better than the Fourier limit of the excitation pulse.

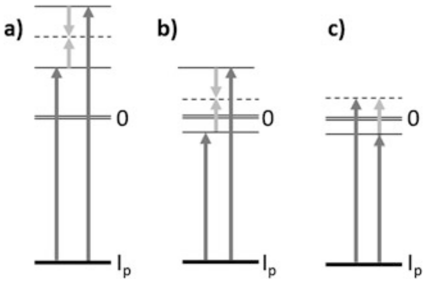

**Fig. 8.2** The pathways in three different cases presented in this chapter

## 8.2 Electron Interferometry

The characteristics of attosecond pulses in terms of coherence, bandwidth, pulse duration and spectral range make the use of traditional spectroscopy methods difficult and new techniques have to be developed [6–15]. The techniques presented in this chapter are based on electron interferometry to perform measurements over large spectral regions. The keywords here are *phase* and *phase variation*. Being able to measure how the phase is varying over large energy spectra is essential to access the attosecond timescale.

In order to do attosecond electron interferometry we need (at least) two ionization pathways to the same final state. In this case the interference is a result of the fact that we do not know, when observing an electron, which way it entered the continuum. If the phase of one pathway is known that path can serve as a reference to the second path whose phase we want to measure.

The different pathways in the three experiments presented can be summarized as follows:

(i) Path 1: absorption of an XUV photon followed by absorption of an IR photon. Path 2: absorption of a more energetic XUV photon followed by emission of an IR photon. In this case we do not know the phase of either pathway and have to compare the interference signal with another signal in order to obtain information about the relative phase difference, Fig. 8.2(a).
(ii) Path 1: the first XUV photon is tuned to be close to a resonance and the system is then ionized by an IR photon. Path 2: absorption of a more energetic XUV photon (sufficient to ionize the system) followed by emission of an IR photon, Fig. 8.2(b).
(iii) Path 1: ionization using an attosecond pulse. Path 2: excitation of one or several bound states using an attosecond pulse, followed by ionization by a phase locked IR pulse. In this scheme phase information about the bound states can be obtained, Fig. 8.2(c).

Already the first demonstration of attosecond pulses [6, 16] utilized electron interferometry as a characterization method. The technique known as RABITT (Reconstruction of Attosecond Beating by Interfering Two-photon Transitions) is used to characterize an average attosecond pulse in a pulse train. In the RABITT method the delay between the APT and an IR probe field is scanned and a photoelectron cross-correlation spectrogram is recorded as a function of delay.

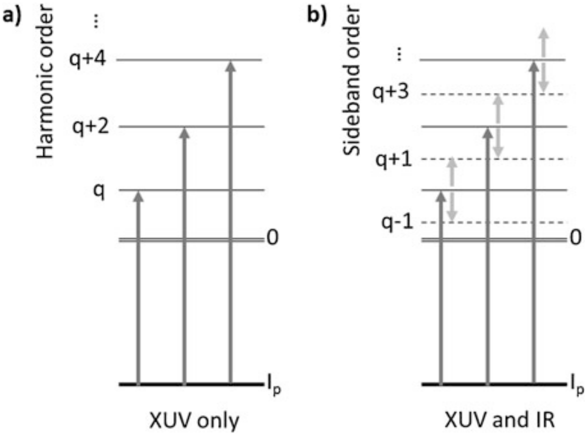

**Fig. 8.3** Rabitt scheme. (**a**) A train of attosecond pulses is used to ionize a gas. If the energy of the individual harmonics is in excess of the ionization potential the atom is ionized via a one photon ionization process. (**b**) When the ionization takes place in the presence of an IR field sidebands can be generated either by absorption or emission of an IR photon. Each sideband can therefore be reached through two different quantum paths that will interfere

Information about the timing of the photoionization process is found in the modulated sidebands, which are reached by two interfering quantum paths, see Fig. 8.3. The first path is absorption of the harmonic with frequency $q\omega$, $V_I^{(q)} \propto \exp(-iq\omega t + i\phi_q)$, followed by absorption of an IR photon $V_{II}^{(+)} \propto \exp(-i\omega t + i\phi_1)$. The second path is absorption of the harmonic with frequency $(q+2)\omega$, $V_I^{(q+2)} \propto \exp[-i(q+2)\omega t + i\phi_{q+2}]$, followed by emission of an IR photon $V_{II}^{(-)} \propto \exp(i\omega t - i\phi_1)$. Both pathways result in the same final energy, $E_k = (q+1)\hbar\omega - I_p$.

The photoelectron signal in the sidebands varies as a function of delay as

$$s(\tau) = A + B\cos\bigl[2\omega(\tau - \tau_{GD} - \tau_I)\bigr],$$

where $A$ and $B$ do not depend on the relative delay $\tau = \phi_1/\omega_1$, $\tau_{GD} \approx (\phi_{q+2} - \phi_q)/2\omega$ is the group delay of the attosecond pulse and $\tau_I \approx (\varphi_I^- - \varphi_I^+)/2\omega$ is a delay introduced by the ionization process involving a two photon transition. The temporal structure of the attosecond pulses can be reconstructed from the spectrum in combination with the group delay. This implies that $\tau_I$ has to be known or assumed to be sufficiently small to be neglected. The delay $\tau_I$ can be calculated numerically by solving the time-dependent Schrödinger equation (TDSE) using a single-active electron approximation [6, 17] and [18]. In the next two sections we focus our attention on measuring $\tau_I$ using attosecond electron interferometry experiments.

## 8.3 Photo Excitation Using an APT and an IR Field

Although the RABITT method presented above was originally developed to characterize APTs, two-photon electron interferometry can be used to measure the atomic properties of the target gas provided the phase variation between all the harmonics

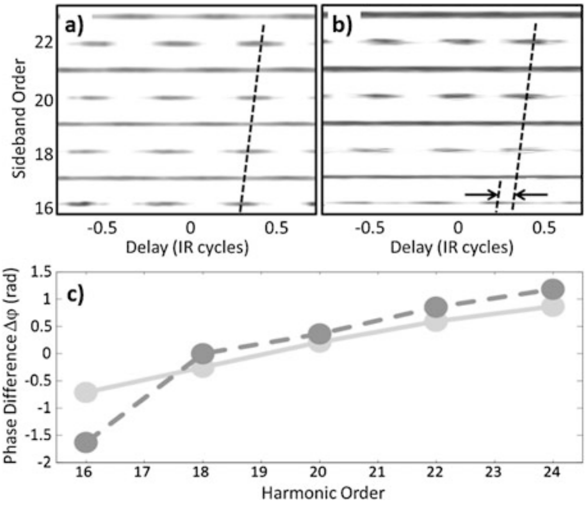

**Fig. 8.4** Electron spectra as a function of delay for argon (**a**) and for helium (**b**) with a detuning of $\delta\omega = 190$ meV. In helium the phase of the modulation of the 16th sideband depends on the detuning while the higher orders do not (see *dashed lines*). (**c**) Measured phase difference as a function of harmonic order for argon (*light grey*) and helium (*dark grey*)

is known [18, 19]. We take benefit of this to study the bound excited state of helium, 1s3p $^1P_1$, dressed by an IR laser field, via resonant two-color two-photon ionization.

The APT is first characterized using argon as calibration gas. In argon all harmonics in the APT from harmonic 15 to harmonic 25 have sufficient energy to overcome the ionization potential. We record the photoelectron spectra as a function of the delay between XUV and IR. In Fig. 8.4(a), the intensity modulation of the sidebands reveals a characteristic linear time-offset due to the phase difference between harmonics. The duration of the reconstructed pulses in the APT is about 260 as.

Once characterized, the same attosecond pulse train is used to ionize helium in the presence of an IR field. The difference now being that harmonic 15 does not have sufficient energy to ionize helium and the energy of this harmonic is close to resonance with the 1s3p $^1P_1$ state. The absorption of one additional IR photon, however, is sufficient to ionize and sideband 16 can, therefore, still be observed. Compared to argon, sideband 16 exhibits a distinct time-offset with respect to higher order sidebands (see Fig. 8.4(b)). This phase variation is a signature of the resonant character of the photo-excitation process in helium.

By comparing the measurements in argon and helium we can extract the phase induced by the state close to resonance. We subtract the linear contribution and set the unaffected phase of higher order sidebands as a reference clock to zero in order to read directly the induced phase shift from the phase of sideband 16, as illustrated in Fig. 8.5.

The induced phase is expected to depend on the detuning from the resonance and experimentally this detuning can be obtained either by changing the frequency of the driving laser and thereby the frequency of harmonic 15, or by changing the intensity of the probe IR field and thereby shifting the resonant state by the ac Stark shift.

We start by detuning the laser nominal frequency keeping everything else constant and calibrate the induced phase shift as a function of detuning, see Fig. 8.6.

**Fig. 8.5** Schematic photo-ionization diagram in Helium. The harmonic phase differences at different dressing intensities are clearly noticeable for sideband 16

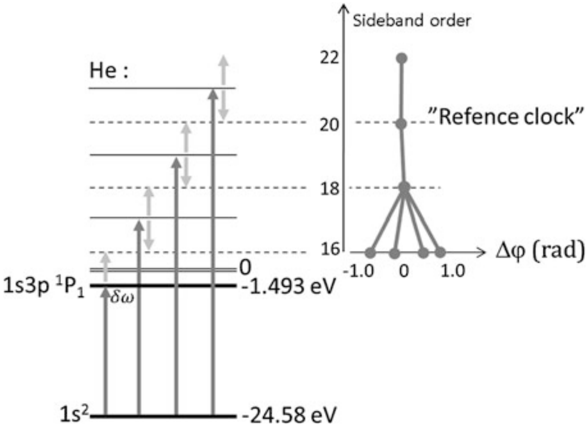

**Fig. 8.6** (**a**) Measurements (*circles*) of the phase as a function of laser detuning. *The dark line* indicates results of a perturbative model while *the lighter grey line* shows results of simulations based on solving the TDSE. (**b**) Phase (*squares*) as a function of intensity, *the solid line* is averaged over six points

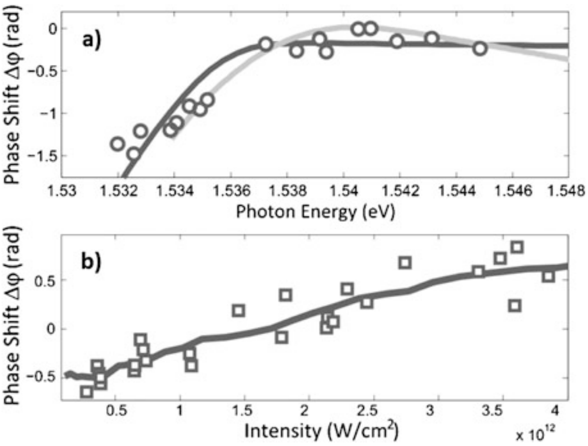

Sideband 16 is very close to the ionization threshold, and only half the resonance (positive detuning) is accessible. For negative detuning, it is not energetically possible to ionize the excited state with only one IR photon. The measurements are compared with the results of two different calculations (solid lines): the dark red line represents a perturbative model considering only the resonant state, while light orange line shows the result of calculations performed by numerically integrating the TDSE in the single active electron approximation [20]. Both calculations are performed in conditions similar to those in the experiment, where we assume Gaussian envelopes for the IR and XUV pulses with FWHMs of 35 and 15 fs, respectively. The result agrees very well with the experiment.

We change now the intensity of the probe field and measure the induced phase shift in order to investigate the bound excited state, 1s3p $^1P_1$ of helium in a dressed IR laser. In Fig. 8.6(b) an almost linear increase of the phase with intensity is observed, and emphasized by the dark red curve obtained by averaging.

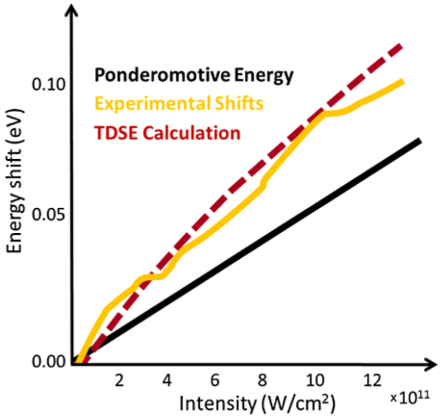

**Fig. 8.7** Measured transition energy of the 1s3p state. Experimental results (*orange line*), compared with the ponderomotive energy (*black*) and TDSE calculation (*dark red line*)

Combining the two phase measurements in Figs. 8.6(a) and 8.6(b), we can determine the intensity dependence of the $1s^2$-1s3p transition energy. Both experimental (orange line) and TDSE (dashed red line) results are shown in Fig. 8.7. Assuming the ac Stark shift of the fundamental state to be very small, we present as guideline the variation of the transition energy if the 1s3p state was moving following the ponderomotive energy (black line). We find that the measured transition energy increases about 40 % more rapidly with the laser intensity than the ponderomotive energy, up to the saturation at about $1.3 \times 10^{12}$ W/cm$^2$. This measurement of the two-photon ionization phase variation in the vicinity of a resonant state allows the investigation of atoms in a dressing field. The method can naturally also be applied to study the dynamics of auto-ionizing states in molecules [14, 21].

## 8.4 Photo Ionization Using an APT and an IR Field

In the experiment presented above the attosecond pulse train was first characterized and then used to do the measurement. An alternative approach is to do the two measurements simultaneously. The same pulse train is then used for both measurements and by subtracting the two results the influence of the pulse structure is removed. We use this approach to study photoionization of argon atoms excited by attosecond pulses and measure the difference in time delays between electrons emitted from the $3s^2$ and $3p^6$ shells at different excitation energies ranging from 32 to 42 eV. The attosecond pulses have a central energy of 38 eV and a bandwidth of 10 eV, corresponding to a compressed duration of 170 as. The actual attosecond pulses were not fully compressed and measured to be 450 as. Interestingly, in this experiment the exact temporal structure of the attosecond pulse is not important since it affects the electrons coming from the two initial states in the same way. A Cr filter is used to select a rather narrow harmonic spectrum, containing harmonic orders from 21 to 25, so that electrons emitted from the $3s^2$ and $3p^6$ shells are separated in energy (see Fig. 8.8).

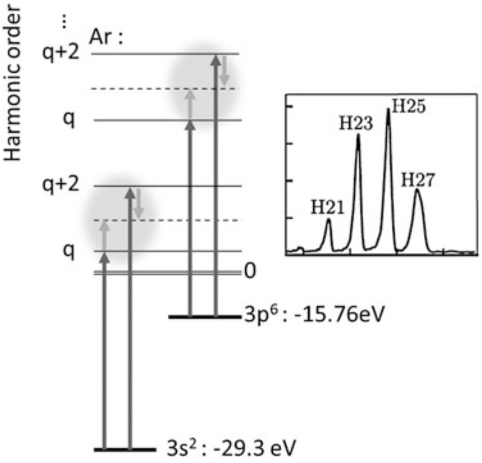

**Fig. 8.8** Principle of the time-delay measurement. Two electron wave packets originating from different shells are simultaneously created using the same comb of high-order harmonics. The outgoing electron wave packets are further probed with a weak IR field. For simplicity only two harmonics are indicated. Also shown is the experimental harmonic spectrum used

Acquiring two interferometric traces at the same time, we can determine the difference in delay in photo emission, $\tau_I(3s) - \tau_I(3p)$, at the position of the sideband peaks. In this experiment we observe three sidebands (with orders 22, 24 and 26). The interpretation of this delay difference requires some theoretical analysis, based on second-order perturbation theory.

A two-photon absorption matrix element can be written in atomic units as

$$M(\vec{k}) = -iF_L F_H \lim_{\varepsilon \to +0} \sum_n \frac{\langle \vec{k}|z|n\rangle \langle n|z|i\rangle}{E_i + \omega_H - E_n + i\varepsilon},$$

where $F_L$ and $F_H$ is the complex field amplitude of the laser and harmonic field respectively, and $\omega_H$ is the frequency of the harmonic. The initial state, $\varphi_i = \langle \vec{r}|i\rangle$, is assumed to be a bound state with energy $E_i$. The final state, $\varphi_{\vec{k}} = \langle \vec{r}|\vec{k}\rangle$, is taken to have an asymptotic momentum along $\vec{k}$ and energy $E_k = k^2/2$ in atomic units. The sum runs over all bound states and continuum states of the atom, $\varphi_n = \langle \vec{r}|n\rangle$, with energy $E_n$.

Making a partial wave expansion of the final state, separating angular and radial parts and for simplicity assuming that the initial state is an s state, the matrix element becomes:

$$M(\vec{k}) = -iF_L F_H \sum_{\ell=0,2} C_{\ell 0} Y_{\ell 0}(\hat{k}) e^{i\eta_\ell(k)} (-i)^\ell \lim_{\varepsilon \to +0} \sum_n \frac{\langle R_{k\ell}|r|R_{n1}\rangle \langle R_{n1}|r|R_{i0}\rangle}{E_i + \omega_H - E_n + i\varepsilon},$$

where $Y_{\ell 0}$ is a spherical harmonic, $C_{\ell 0}$ the corresponding angular coefficient and $\eta_\ell$ the scattering phase of the final state with angular quantum number $\ell$. This expression can be rewritten as

$$M(\vec{k}) = -iF_L F_H \sum_{\ell=0,2} C_{\ell 0} Y_{\ell 0}(\hat{k}) e^{i\eta_\ell(k)} (-i)^\ell \langle R_{k\ell}|r|\rho_{k_a 1}\rangle,$$

where we have introduced the perturbed wave function $\rho_{k_a 1}$, $k_a 1$ denotes the intermediate state wave number and 1 is the intermediate angular momentum quantum

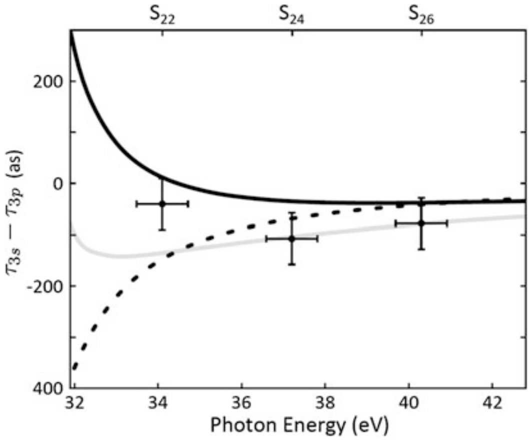

**Fig. 8.9** Comparison between the measured delay differences for ionization of Ar from the 3s and 3p shells (marks with error bars) with calculations performed according to the approximate theory developed in [4] (*light grey line*). Also shown is the delay expected for one-photon ionization (*black line*) and the laser-driven continuum-continuum transition (*dashed line*)

number. The perturbed wave function is an outgoing complex wave function. Approximating the involved continuum wave functions by their asymptotic behavior [4], the phase of the final state cancels out and we obtain the simple result:

$$M(\vec{k}) \propto e^{i\eta_1(k_a)} \times \left(\frac{i}{k_a - k}\right)^{iz} \frac{(2k_a)^{\frac{i}{k_a}}}{(2k)^{\frac{i}{k}}} \Gamma(2 + iz) \equiv e^{i\eta_1(k_a)} \times e^{i\phi_{cc}(k_a)}$$

Combining the two paths leading to a given sideband, labeled with subscripts $a$ and $e$ respectively, we find that the ionization delay introduced previously is the sum of two terms:

$$\tau_I = \frac{\eta_1(k_e) - \eta_1(k_a)}{2\omega} + \frac{\phi_{cc}(k_e) - \phi_{cc}(k_a)}{2\omega} \cong \tau_W + \tau_{cc}.$$

The first term can be interpreted as the group delay of the single-photon ionized photoelectron wave packet, also known as the Wigner-Smith delay [22, 23]. However, there is also a delay coupled to the continuum-continuum transitions between the states reached by one-photon ionization and the sideband states where the measurement is done. Using a classical interpretation, this “continuum-continuum” delay arises from the motion of the electron in a Coulomb potential in the presence of a probe IR field. Figure 8.9 shows experimental results compared to a theoretical prediction based on Hartree-Fock calculations for the Wigner-Smith delay and on asymptotic behaviors for the continuum-continuum part. The agreement is satisfactory, at least for the two points at highest energy. However, let us emphasize the need for more experiments and for a more accurate theoretical treatment of both the continuum-continuum transitions and the Wigner-Smith time delays in a region where correlation effects in the initial and final states should be important [24–27].

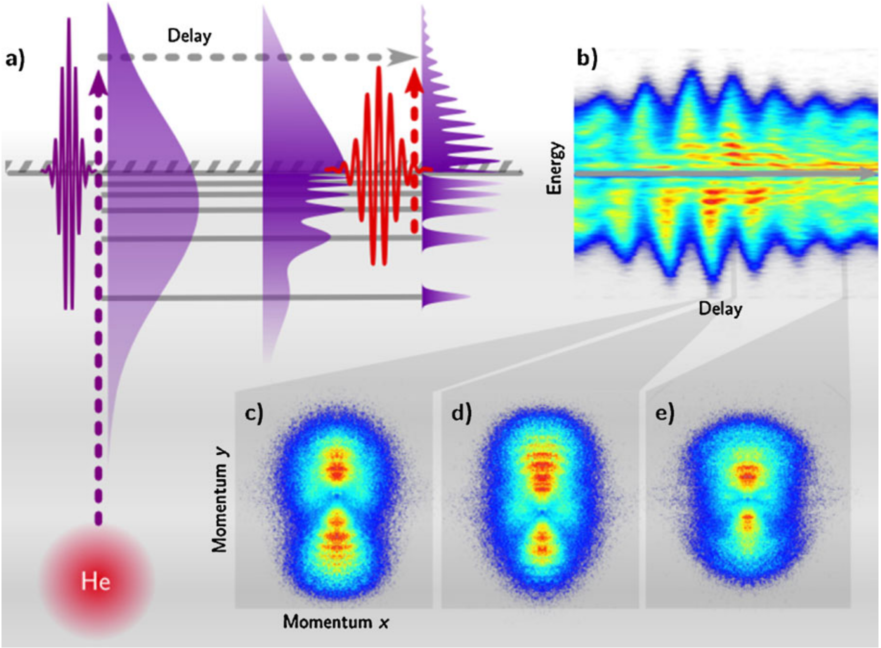

**Fig. 8.10** Principle of attosecond pump-probe interferometry: (**a**) A broadband, isolated attosecond pulse centered on the ionization threshold of Helium is used to coherently excite an electron wave packet consisting of a superposition of bound and continuum $p$-states. After a variable delay the bound part of the wave packet is ionized by a few cycle IR pulse, which is locked in phase to the attosecond pulse. The electron distribution is recorded using a velocity map imaging spectrometer (VMIS). Three VMIS images are shown for different delays in (**c**)–(**e**) and the on-axis electron energy is presented as a function of delay in (**b**). The photoelectron spectra exhibit interference fringes owing to different pathways leading into the continuum

## 8.5 Photo Excitation Using a Single Attosecond Pulse and a Delayed IR Field

The methods presented so far have all used APTs and the spectral resolution obtained is a result of the number of pulses in the trains. When isolated attosecond pulses are used, the interferometry technique is slightly different. In analogy with Ramsey spectroscopy, the spectral resolution is now determined by the separation between the pump and the probe pulses and the stability of the experimental setup. The advantage of using an isolated attosecond pulse is the continuous spectrum that allows us to excite several bound states simultaneously, i.e. to create a wave packet.

In Fig. 8.10 we demonstrate the principle of our method. We use a free wave packet as a reference to measure the amplitudes and binding energies of the states in a bound wave packet. We do this by exciting helium atoms with an attosecond pulse with a bandwidth centered near the ionization threshold, thus creating both a bound and a free wave packet simultaneously. After a variable delay, the bound

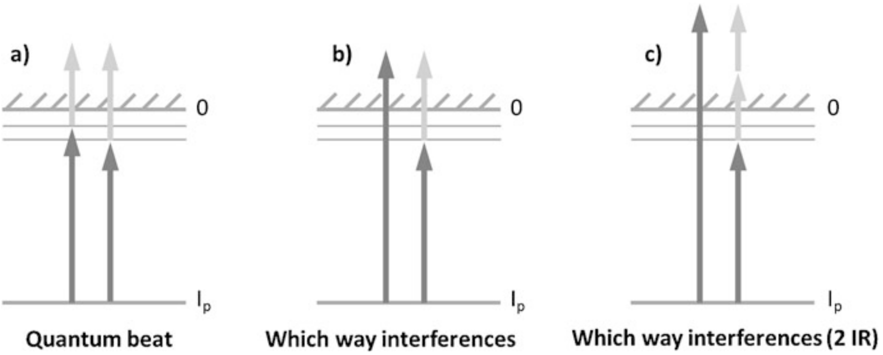

**Fig. 8.11** (**a**) *Quantum beat*; Ionization of both bound states with one IR photon each (slightly different frequencies so that they end up at the same final energy) and detection of the beating between the two outgoing electron waves. (**b**) *Which-way interferometry*; path one: ionization with one XUV photon, path two: ionization with an XUV plus an IR photon. (**c**) *Which-way multi-photon interferometry*; path one: ionization with one XUV photon, path two: ionization with an XUV plus two IR photons

wave packet is ionized by a few-cycle IR laser precisely synchronized to the original attosecond pulse. By measuring the delay-dependent photoelectron spectrum we obtain an interferogram that contains both quantum beats as well as multipath interferences. Analysis of the interferogram allows us to determine the bound wave packet components with a spectral resolution more than two orders of magnitude better than the inverse of the attosecond pulse duration.

The combination of interferometry and angular resolved electron detection enables us to effectively separate the contributions from different pathways, including different bound states and different number of photons used in the ionization process.

The excitation of the bound wave packet and the reference wave packet has to take place at the same time, but there are different ways this can be done. We can, as in our experiment, use an attosecond pulse with a bandwidth centered near the ionization threshold, thereby creating the two wave packets simultaneously, but they could also be excited through a shake-up/shake-off process in which case an electron is rapidly removed and the remaining electron (in the case of helium) finds itself in a perturbed potential and gets excited.

Let us assume that we have created our reference continuum wave packet and a bound wave packet consisting of two states. In order to make these two wave packets interfere we need to ionize the bound wave packet, promoting it to the same continuum energy as the reference wave packet. In this process there are three dominant combinations of pathways that can interfere; these are presented in Fig. 8.11.

We will now consider a shake-up/shake-off process in helium. The description would of course work equally well for direct excitation with an attosecond pulse but would include a few more terms. In the case of shake-up the, abrupt changes in the atomic potential create a perturbation which may ‘shake’ the remaining electron into excited and (shake-off) continuum states. The initial wave packets (both the bound and the reference) will both be $s$-states and can be described as:

$$\psi_{ref} = a(E)e^{-iE\tau}Y_{00}(\theta, \varphi).$$

Here, for simplicity, we assume the radial dependence of the wave packet to be included in $a(E)$. The bound wave packet is still assumed to consist of only two states with binding energies $E_1$ and $E_2$. Once this wave packet is ionized it can be written as

$$\psi_{wp} = \left[b_1(E)e^{-iE_1\tau} - b_2(E)e^{-iE_2\tau}\right]Y_{10}(\theta, \varphi).$$

The states in the reference wave packet and the ionized bound wave packet are orthogonal and at a first glance no interferences might be expected. However, if the angular distribution is measured the interferences appear. The angular resolved photo electron distribution, $F(E, \theta)$, can be decomposed into Legendre polynomials

$$F(E, \theta) = \int_0^{2\pi} d\varphi |\psi_{ref} + \psi_{wp}|^2 = \sum_{\ell=0}^{2} \beta_\ell(E)P_\ell(\cos\theta),$$

where

$$\begin{aligned}
\beta_0 &= \frac{1}{2}\left(|a|^2 + |b_1|^2 + |b_2|^2 + 2Re\left\{b_1 b_2^* e^{i\omega_b\tau}\right\}\right), \\
\beta_1 &= \sqrt{3}\left(Re\left\{a^* b_1 e^{i\Delta\omega_1\tau}\right\} + Re\left\{a^* b_2 e^{i\Delta\omega_2\tau}\right\}\right), \\
\beta_2 &= |b_1|^2 + |b_2|^2 + 2Re\left\{b_1 b_2^* e^{i\omega_b\tau}\right\}.
\end{aligned}$$

Here we find interference terms between the direct and the indirect paths in the first odd polynomial ($\beta_1$) and a beat signal, which is interference between the outgoing waves from the two different states, in the even polynomials. $\Delta\omega_i$ is the energy difference between bound state with index $i$ and the detected electron energy and $\omega_b$ is the energy difference between the two bound states. In general, interference processes that have different parities in the two pathways (see for example Fig. 8.11(b)) will end up in the odd Legendre polynomials and processes with the same parities in the pathways (Figs. 8.11(a) and 8.11(c)) will end up in the even polynomials. Contributions to the odd Legendre polynomials do not affect the total ionization yield, but only the symmetry of the ionization, whereas contributions to the even polynomials (such as the quantum beat) will change the overall ionization signal, but not the symmetry.

Ionization out of the bound states using more than one IR photon (Fig. 8.11(c)) can be treated in a similar fashion. In case of two IR photons the parity of the two pathways will be the same and the interference can be seen in the even Legendre polynomials, i.e. the same Legendre polynomials the quantum beat appear in Figs. 8.12(e) and 8.12(f). These two interference processes (Figs. 8.11(a) and 8.11(c)), furthermore, include the same total number of photons and will, therefore, have comparable strengths and also the same intensity dependence. By plotting the different Legendre polynomials as a function of time it can be seen that different interferences can be clearly distinguished.

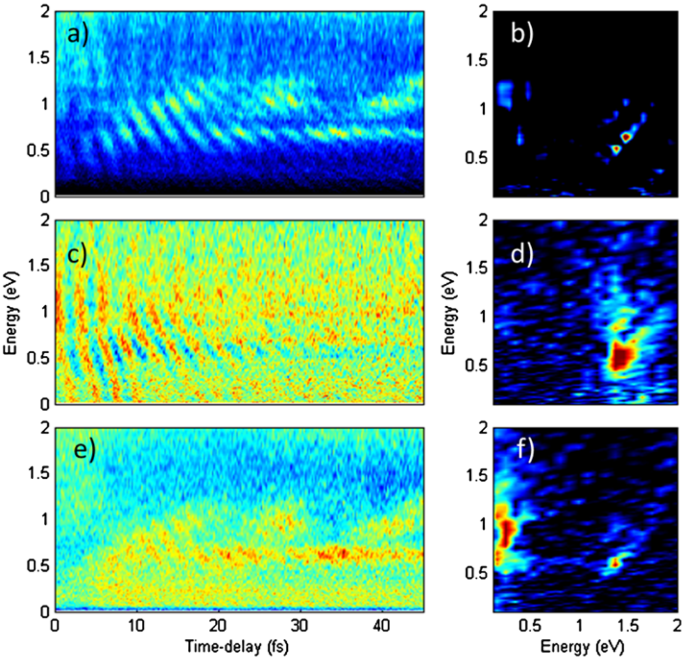

**Fig. 8.12** Partial wave analysis of the experimental angular distributions. (**a**) Experimental interferogram obtained by recording the photoelectrons along the polarization axis and its Fourier transform (**b**). With mainly 4p and 5p excited the beating between the outgoing electron waves has a period of approximately 13 fs (three beat periods can be seen in (**a**)). From the Fourier analysis (**b**) we can resolve the two states and the beating between them, but also see a small hint of the 3p state, which was only weakly excited in this particular experimental scan. The different processes can be separated by a partial wave analysis where the direct–indirect interference appears primarily in the odd expansion coefficients, (**c**) and (**d**), and the quantum beat signal appears exclusively in the even coefficients, (**e**) and (**f**)

## 8.6 Conclusion

In conclusion, the methods demonstrated in this chapter can be used to probe the temporal evolution of bound electron wave packets with high spectral and temporal resolution simultaneously. Our method to measure the phase of resonant two photon ionization process, here demonstrated in He, could be applied to the study of numerous resonant or quasi-resonant processes in atoms and molecules. We believe that the work on the measured time-delays in photo emission will stimulate further experiments, aiming at measuring photoemission delays in a variety of systems, and providing data that could be compared to more advanced theoretical calculations. The interferometric technique presented here, which uses a reference continuum wave packet and a delayed probe excitation, can be used to probe the temporal evolution of bound or quasi-bound electron wave packets, e.g., composed of autoionizing states with high spectral and temporal resolution simultaneously, thus providing an increased precision when doing attosecond experiments. None of the methods rely on the use of intense probing fields, which is important when attosecond techniques are applied to more complex systems.

**Acknowledgements** We thank Kenneth J. Schafer, Marc Vrakking, Alfred Maquet and Richard Taïeb for fruitful discussions. This research was supported by the Marie Curie programs ATTOCO (IEF) and ATTOFEL (ITN), the European Research Council (ALMA), the Swedish Foundation for Strategic Research, the Swedish Research Council and the Knut and Alice Wallenberg Foundation.

## References

1. P.H. Bucksbaum, Science **317**, 766 (2007)
2. F. Krausz, M. Ivanov, Rev. Mod. Phys. **81**, 163 (2009)
3. M. Swoboda et al., Phys. Rev. Lett. **104**, 103003 (2010)
4. K. Klünder et al., Phys. Rev. Lett. **106**, 143002 (2011)
5. J. Mauritsson et al., Phys. Rev. Lett. **105**, 053001 (2010)
6. P.M. Paul et al., Science **292**, 1689 (2001)
7. M. Hentschel et al., Nature **414**, 509 (2001)
8. Y. Mairesse et al., Science **302**, 1540 (2003)
9. R. López-Martens et al., Phys. Rev. Lett. **94**, 033001 (2005)
10. J. Mauritsson et al., Phys. Rev. Lett. **97**, 013001 (2006)
11. P. Johnsson et al., Phys. Rev. Lett. **99**, 233011 (2007)
12. A.L. Cavalieri et al., Nature (London) **449**, 1029 (2007)
13. J. Mauritsson et al., Phys. Rev. Lett. **100**, 073003 (2008)
14. S. Haessler et al., Phys. Rev. A **80**, 011404 (2009)
15. M. Schultze et al., Science **328**, 1658 (2010)
16. V. Véniard, R. Taïeb, A. Maquet, Phys. Rev. A **54**, 721 (1996)
17. E.S. Toma, H.G. Muller, J. Phys. B **35**, 3435 (2002)
18. J. Mauritsson, Phys. Rev. A **72**, 013401 (2005)
19. K. Varju, Laser Phys. **15**, 888 (2005)
20. K.J. Schafer, K.C. Kulander, Phys. Rev. Lett. **78**, 638 (1997)
21. J. Caillat et al., Phys. Rev. Lett. **106**, 093002 (2011)
22. E.P. Wigner, Phys. Rev. **98**, 145 (1955)
23. F.T. Smith, Phys. Rev. **118**, 349 (1960)
24. S. Nagele et al., J. Phys. B, At. Mol. Opt. Phys. **44**, 081001 (2011)
25. C.H. Zhang, U. Thumm, Phys. Rev. A **82**, 043405 (2010)
26. A. Kheifets, I. Ivanov, Phys. Rev. Lett. **105**, 233002 (2010)
27. J.C. Baggesen, L.B. Madsen, Phys. Rev. Lett. **104**, 209903 (2010)

# Chapter 9

# The Attoclock: A Novel Ultrafast Measurement Technique with Attosecond Time Resolution

**Claudio Cirelli, Adrian N. Pfeiffer, Mathias Smolarski, Petrissa Eckle, and Ursula Keller**

**Abstract** The recent progress of the ultrafast laser technology enables to capture and control electrons dynamics, which is the key to understand how energy and charge are transported not only in atoms but also in more complex solid-state and molecular systems. This task calls for the development of novel measurement techniques with attosecond time resolution. The "attoclock" is a relatively simple method, which provides attosecond time resolution without the explicit need of attosecond pulses. In this chapter we review the details of this powerful experimental technique, which was employed in the recent years to investigate electron tunneling dynamics and to study the electron kinematics in strong field single and double ionization.

## 9.1 Introduction

According to Bohr's model of the hydrogen atom, it takes about 150 attosecond (1 attosecond [as] $= 10^{-18}$ s) for an electron in the ground state to orbit around the core. Therefore, the attosecond is the typical time scale for electronic motion. The real-time observation of fundamental processes mediated by electron dynamics like chemical bond breaking and formation, charge transfer, energy transport and many others, requires a measurement technique with attosecond time resolution.

---

M. Smolarski and P. Eckle left academics.

C. Cirelli (✉) · A.N. Pfeiffer · M. Smolarski · P. Eckle · U. Keller
Physics Department, Institute for Quantum Electronics, ETH Zürich, Wolfgang-Pauli-Str. 16, 8093 Zurich, Switzerland
e-mail: cirelli@phys.ethz.ch

A.N. Pfeiffer
e-mail: apfeiff@phys.ethz.ch

U. Keller
e-mail: keller@phys.ethz.ch

*Present address:*
A.N. Pfeiffer
Chemical Sciences Division, Lawrence Berkeley National Laboratory, Berkeley, CA 94729, USA

L. Plaja et al. (eds.), *Attosecond Physics*, Springer Series in Optical Sciences 177,
DOI 10.1007/978-3-642-37623-8_9,

A natural choice is to exploit light pulses in the attosecond time domain: attosecond pulses allow for snapshots of electron dynamics exactly like femtosecond pulses enable observation of molecular dynamics [1].

The first successful generation of light pulses with attosecond time duration was demonstrated in 2001 [2, 3]. Although technically still very challenging, nowadays single attosecond pulses [2, 4–7] or attosecond pulse trains [3, 8, 9] are generated routinely in various labs employing different methods. For time-resolved measurements with attosecond time resolution one would apply the so-called "pump-probe" technique, well established in femtosecond domain [10]: a first pulse (pump) triggers the process under investigation, while a second pulse (probe) measures the induced modifications after a certain, controllable, delay with respect to the pump. Provided that the process is repeatable within a time shorter than the pulse repetition rate, a scan of the delay between the two pulses gives insight into the full dynamics of the system.

With this approach, the time resolution is determined by the duration of the attosecond pulses. With the continued progress of the cutting-edge laser technology, it is nowadays possible to generate attosecond pulses shorter than 100 as in the extreme ultraviolet (XUV) wavelength region [4].

Unfortunately this traditional pump-probe technique is still very limited in the attosecond time domain [11], due to the extremely low average photon flux of the available attosecond sources [12]. In the femtosecond domain pump-probe spectroscopy is performed with pulse energies of few nanojoule and at repetition rates of about 100 MHz. While we can obtain similar pulse energies delivered at the target in attosecond science [13, 14], attosecond pulses are accessible only at a repetition rate in the order of 1 to 10 kHz. As a consequence the time-averaged pump-probe signal, which depends on the square of the instantaneous laser power, drops by several order of magnitudes, imposing unfeasibly long data acquisition times to achieve the same statistics. Furthermore, attosecond pulses lie in the XUV region of the electromagnetic spectrum where the cross-sections for multi-photon interactions are much lower than in the visible or near-infrared where the femtosecond pulses have been successfully applied in the traditional pump-probe technique.

To date, experiments probing ultrafast electron dynamics have been successfully performed by using a single attosecond pulse or attosecond pulse train as pump and a femtosecond infrared pulse as probe or vice versa [1, 15–17]. In the so-called "streaking experiments" [2], the attosecond XUV pulse (pump) ionizes electrons from the target atoms. Just after ionization, the co-propagating femtosecond pulse (probe) alters the momentum of the liberated electrons, depending on the electron's instant of release [18, 19]. The moment in time when the electron is liberated into the continuum becomes mapped onto a change in final energy of the electron; therefore time is mapped to energy. The measurement of attosecond light pulses of 80 as duration [4] and the real-time observation of electron charge transport in solids [20] demonstrates the power of attosecond streaking in exploring electronic motion. However, the technique relies on isolated attosecond light pulses starting the streaking dynamics.

## 9.2 Principle of the Attoclock

A completely different approach is exploited in attosecond *angular* streaking [21, 22]. Here close-to-circularly polarized laser pulses are employed: the electric field vector while rotating in the polarization plane, ionizes and further deflects the electrons in the angular spatial direction, such that the instant of ionization is mapped to the final angle of the momentum vector. Hence, time is mapped to angle. In the case of pulse durations in the two-optical-cycle regime we can assume that most of the ionization is restricted to the central cycle and the time-to-angle mapping is therefore univocal [23]: this is the "minute hand" of the attoclock, which gives the fine timing. In the case of measurements employing laser pulses of longer duration, ionization is achieved during multiple optical cycles and the timing is no longer unambiguous if only the minute hand is considered. However a coarser "hour hand" based on the magnitude of the electron momentum can be used to extract the precise timing [24]. In the multicycle measurement, measuring time is therefore achieved by "counting cycles", such as it is done on a watch face: every hour, the minute hand of a watch points into the same angle (i.e. the mapping to angle is no longer ambiguous) but an univocal timing information can be retrieved by interrogating the hour hand.

The laser-atom interaction process on which the attoclock is based can be divided into two steps in analogy to the three-step-model of high-harmonic generation [25]. In the first step (tunnel ionization) the electron tunnels through the potential barrier that is suppressed in a certain direction by the laser electric field; in the second step (streaking) the electron is accelerated in the radial and angular direction by the rotating electric field of the laser pulse starting with zero kinetic energy.

Both ionization and streaking depend sensitively on the electric field of the laser pulse. The electric field of a laser pulse can be expressed as (atomic units are used throughout all the chapter):

$$\mathbf{F}(t) = \begin{pmatrix} F_x(t) \\ F_y(t) \end{pmatrix} = \frac{f(t)\sqrt{I}}{\sqrt{1+\varepsilon^2}} \begin{pmatrix} \cos(\omega t + \varphi_{CEO}) \\ \varepsilon \sin(\omega t + \varphi_{CEO}) \end{pmatrix} \tag{9.1}$$

where $\omega$ is the central frequency, $I$ is the peak intensity, $f(t)$ the normalized field envelope, $\varepsilon$ is the ellipticity and $\phi_{CEO}$ is the carrier-envelope-offset (CEO) phase [26], also referred to as the carrier envelope phase (CEP). With this definition of the electric field, the $xy$-plane is the polarization plane and the major polarization axis is along the $x$-axis. For a correct interpretation of an attoclock experiment the peak intensity, pulse envelope, CEO phase, ellipticity and orientation of the polarization ellipse are all parameters that need to be controlled precisely. An electron released at the instant of time $t$ with zero kinetic energy will have a final (i.e. after the laser pulse) momentum that can be expressed in atomic units as:

$$\mathbf{p}(t) = -\mathbf{A}(t) = -\int_t^\infty \mathbf{F}(t')dt' \tag{9.2}$$

where $\mathbf{A}(t)$ is the vector potential. Substituting Eq. (9.1) into (9.2) and solving the integral within the slowly-varying-envelope approximation [27] $f'(t)/\omega \ll f(t)$, we can find an expression for the electron momentum:

$$\mathbf{p}(t) = \begin{pmatrix} p_x(t) \\ p_y(t) \end{pmatrix} \approx \frac{f(t)\sqrt{I}}{\omega\sqrt{1+\varepsilon^2}} \begin{pmatrix} \sin(\omega t + \varphi_{CEO}) \\ -\varepsilon\cos(\omega t + \varphi_{CEO}) \end{pmatrix} \tag{9.3}$$

Since the electric field is a vector, whose magnitude and angle with respect to a given axis change as a function of time in the polarization plane, it is useful to write the pulse field components in polar coordinates $(r(t), \phi(t))$:

$$\begin{aligned} \mathbf{F}(t) &= \begin{pmatrix} E_r(t) \\ E_\varphi(t) \end{pmatrix} \\ &= \begin{pmatrix} (f(t)\sqrt{I}/\sqrt{1+\varepsilon^2})\sqrt{\cos^2(\omega t + \varphi_{CEO}) + \varepsilon^2\sin^2(\omega t + \varphi_{CEO})} \\ \arctan(\varepsilon\sin(\omega t + \varphi_{CEO})/\cos(\omega t + \varphi_{CEO})) \end{pmatrix} \end{aligned} \tag{9.4}$$

Also the final momentum vector can be written in polar coordinates $p_r$ and $p_\theta$:

$$\begin{aligned} \mathbf{p}(t) &= \begin{pmatrix} p_r(t) \\ p_\theta(t) \end{pmatrix} \\ &\approx \begin{pmatrix} f(t)\sqrt{I}/(\omega\sqrt{1+\varepsilon^2})\sqrt{\sin^2(\omega t + \varphi_{CEO}) + \varepsilon^2\cos^2(\omega t + \varphi_{CEO})} \\ \arctan(-\varepsilon\cos(\omega t + \varphi_{CEO})/\sin(\omega t + \varphi_{CEO})) \end{pmatrix} \end{aligned} \tag{9.5}$$

Both momentum components carry information that can be divided into coarse timing (hour hand) and fine timing (minute hand).

### 9.2.1 The Minute Hand

If the laser pulse duration is in the two-optical-cycle regime (at 800 nm about 6 fs or below) the ionization events are confined within the central optical cycle. For a perfectly circularly polarized laser pulse, the peak of the electric field vector runs over 360° within one optical cycle. One degree of angular resolution corresponds to 7.4 as at a center wavelength of 800 nm. Measuring the final angle of the electron momentum $p_\theta$ (Eq. (9.5)) enables one to measure time with a precision well below one optical period. In principle there is no fundamental lower limit because electron momentum vectors can be measured with high precision. In Sect. 9.2.1.4 we will discuss about the uncertainties that limit the resolution and the accuracy of the method, which however is well below the shortest pulse duration achieved to date (i.e. $\approx$100 as [4]). Therefore, the “minute hand” of the attoclock provides attosecond timing information without requiring attosecond pulses [28]. Independent measurements give precise knowledge of the temporal evolution of the electric field in the pulse which are required for the interpretation of any attoclock measurement. In Eq. (9.5) we see that the final angle of the electron momentum is dependent on the parameters $\varepsilon$ (the ellipticity value) and $\phi_{CEO}$ (the CEO phase).

#### 9.2.1.1 Quasi-static Tunneling Ionization Rate

In the attoclock technique, the fine timing of the minute hand is obtained by extracting the angle $p_\theta$ (Eq. (9.5)) from the photoelectron (or photoion) momentum distributions arising from strong field ionization. Such final momentum distributions differ qualitatively according to the polarization state of the laser pulse. The reason for that is the strong dependence of the tunnel ionization rate upon the instantaneous value of the electric field magnitude $F_r(t) = |\mathbf{F}(t)| = \sqrt{F_x(t)^2 + F_y(t)^2}$. For laser intensities in the range of $0.1 - 1 \times 10^{15}$ W/cm$^2$ it is commonly accepted that most of the ionization occurs through tunneling: the laser field deforms the binding potential of an atom so strongly, that a potential barrier is created through which an electron may tunnel. According to tunneling theories developed by Perelomov, Popov and Terentev (PPT) [29] on the basis of the pioneering work by Keldysh [30], and further summarized by Ammosov, Delone and Krainov (ADK) [31], the rate of tunneling ionization (TI) reads:

$$W_{TI}(F) = \frac{C_l^2}{2^{|m|}|m|!}\,\frac{(2l+1)(l+|m|)!}{2(l-|m|)!}\,\frac{1}{\kappa^{2Z/\kappa-1}}\left(\frac{2\kappa^3}{F}\right)^{2Z/\kappa-|m|-1} e^{-2\kappa^3/3F} \tag{9.6}$$

where $C_l$ measures the amplitude of the electron wavefunction in the tunneling region and can be derived from the ground-state wavefunction obtained with a model potential [32, 33]; $l$ and $m$ are the angular momentum quantum numbers; and $\kappa = \sqrt{2I_p}$, with $I_p$ being the ionization potential.

It is known that static field ionization rates derived by tunneling theories become invalid in the higher intensity regime, where the atomic potential is bent such that the probability for over-the-barrier ionization (OBI) starts to be no longer negligible. Nevertheless, Eq. (9.6) can still be used provided that an exponential correction factor is considered, as proposed by Tong and Lin [32]:

$$W_{TBI}(F) = W_{TI}(F)e^{-\alpha(Z^2/I_p)/(F/\kappa^3)} \tag{9.7}$$

where the values of the empirical parameter $\alpha$ is tabulated in [32] for different gas targets. Furthermore, for high intensities, ionization occurs at a rate high enough for saturation to become important. This can be accounted for by weighting the ionization rate with the survival probability [34]:

$$W_{sat}(F) = W_{TBI}(F)\exp\left(-\int_{t_0}^{t} W_{TBI}(t')dt'\right). \tag{9.8}$$

Equation (9.8) shows that a variation of 10 % of the electric field amplitude is enough to change the ionization rate by almost one order of magnitude, while keeping all the other parameters constant. For linearly polarized light, the electric field amplitude oscillates rapidly at the carrier frequency, while for purely circularly polarized light it varies slowly following the envelope. As a consequence, the variation of the ionization rate on the time scale of one laser cycle is much smaller for circular than for linear polarization. This leads to different shapes of final momentum distribution in the polarization plane: for linearly polarized light the distribution exhibits

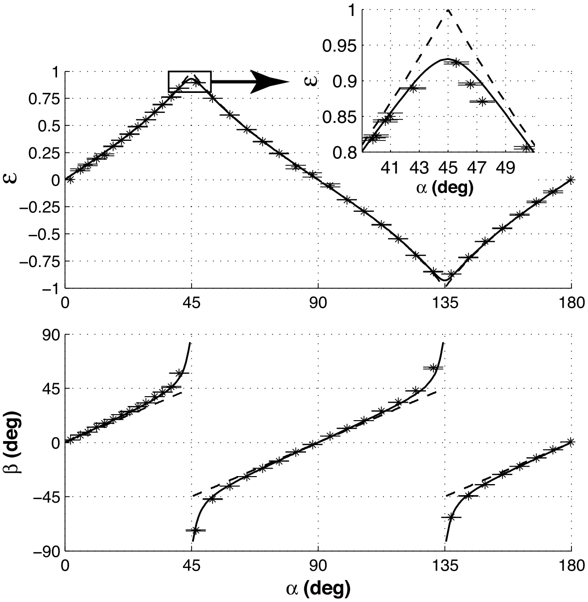

**Fig. 9.1** Polarimetry: the ellipticity $\varepsilon$ and the angle of the polarization ellipse $\beta$. The angle $\alpha$ is the angle between the polarization plane of the linearly polarized incoming pulse and the fast axis of the quarter-wave plate. The data points (*stars* with error bars) are well reproduced by a calculation taking into account the wavelength dependence of the quarter-wave plate (*solid line*). A simple calculation neglecting the wavelength dependence (*dashed line*) shows significant errors at $\varepsilon \approx \pm 1$ (see especially *the inset*)

a Gaussian profile with a maximum in the directions along and orthogonal to the polarization axis; for circularly polarized light a torus builds up, which is equally populated in all angular directions if the CEO phase is not stabilized.

#### 9.2.1.2 Ellipticity Effects

The polarization state of a laser pulse is defined by the value of its ellipticity $\varepsilon$ and the angular orientation of the polarization ellipse. Broadband half and quarter wave plates allow for pulse polarization control, while a polarimetry measurement returns the value of ellipticity and the orientation of the polarization ellipse. Figure 9.1 shows the dependence of the ellipticity $\varepsilon$ and the orientation of the polarization ellipse as a function of the angle of the quarter-wave plate $\alpha$. Ideally, the phase delay between the fast and slow axis of the quarter wave plate should be exactly $\pi/2$ for any wavelength; however, there are no birefringent materials that show such a "flat" retardation property over the whole spectral range covered by few-cycle pulses. Generally, a combination of materials is used for the best possible chromatic correction (referred to as achromatic retardation plates). Still, a slight, wavelength dependent, deviation from $\pi/2$ is unavoidable. The dependence of the phase delay on the wavelength results in a complicated behavior.

In order to obtain the correct behavior in the range of ellipticity close to circularly polarized light ($\varepsilon \approx \pm 1$), the measured input pulse has to be Fourier-transformed into the spectral domain and then numerically propagated through the polarization shaping optics. After projection onto the fast and slow axis of the quarter wave plate, the phase shift is added to the pulse, fully taking into account the material dispersion. After a back-transformation into the time domain, the calculated pulse exhibits

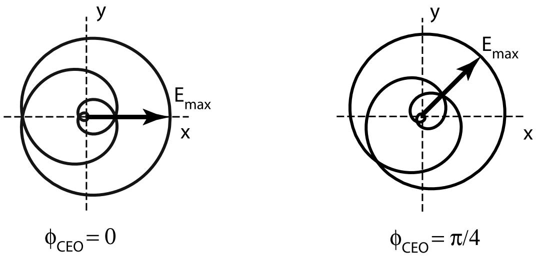

**Fig. 9.2** Spatial evolution of the electric field of a purely circularly polarized laser pulse in the polarization plane ($x$–$y$) for two different values of the CEO phase. A shift of the CEO phase from 0 (*left*) to $\pi/4$ (*right*) causes an anti-clockwise rotation of $\pi/4$ of the pulse field

excellent agreement with the full characterization measurement of the elliptically polarized laser field [35].

### 9.2.1.3 CEO Phase Effects

With laser pulses as short as few optical cycles, CEO phase effects in angular streaking start to become significant [28]. The reason is that the CEO phase governs the electric field waveform through Eq. (9.1) or Eq. (9.4) and consequently the final momentum distributions.

In the case of perfectly circularly polarized light ($\varepsilon = \pm 1$), the temporal evolution of the electric field $E_r(t)$ is independent of the CEO phase. However, the CEO phase determines the angular position of the maximum electric field vector (Fig. 9.2). Equation (9.4) shows that for $\varepsilon = \pm 1$ the electric field components in polar coordinates are simply given by:

$$\begin{pmatrix} E_r(t) \\ E_\varphi(t) \end{pmatrix} = \begin{pmatrix} f(t)\sqrt{I/2} \\ \omega t + \varphi_{CEO} \end{pmatrix}. \tag{9.9}$$

Equation (9.9) indicates that if the CEO phase is shifted by $\Delta\phi$, the pulse field is rotated in space by $\Delta\phi$ (Fig. 9.2). Since most of the ionization occurs in the direction of the electric field maximum (see Eq. (9.6)), the CEO phase controls the direction of emission of the electrons in the polarization plane.

With elliptically polarized pulses, the situation is more complex. Now the electric-field vector follows the polarization ellipse and its magnitude varies in an optical cycle between local minima, when the electric field vector points towards the minor axis of the polarization ellipse and local maxima, when the electric field vector points towards the major axis of the ellipse. The result is that the momentum distributions show two distinct peaks separated by roughly 180°, whose relative intensity changes while varying the CEO phase, as explained in Fig. 9.3.

When the CEO phase value is such that the maximum of the electric field vector points in the direction of the major axis of the polarization ellipse (Fig. 9.3(a)) one dominant peak (labeled A in Fig. 9.3(a)) is created in the rate and in the field evolution (see the inset in Fig. 9.3(a)); this is reflected in the electron momentum distribution, where one of the lobes exhibits higher intensity. When the CEO phase is shifted by $\pi/2$ (Fig. 9.3(b)), the maximum of the electric field vector is along

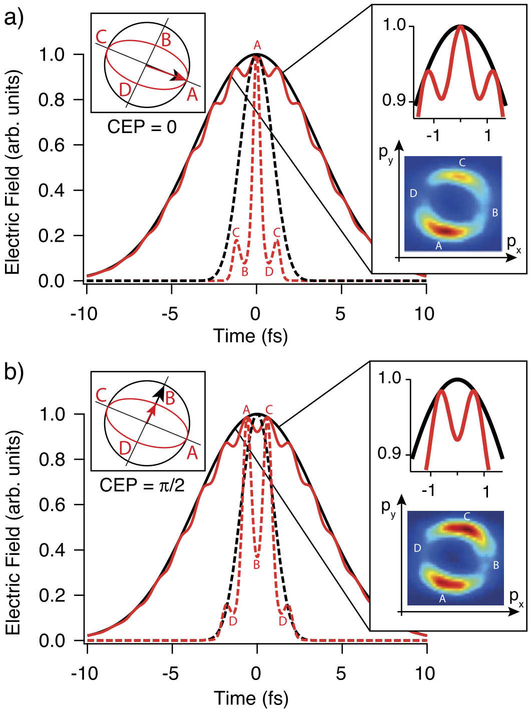

**Fig. 9.3** CEO phase and ellipticity effects. Temporal evolution of the electric field for 5.5-fs pulses for different values of CEO phase, CEP $= 0$ (**a**) and CEP $= \pi/2$ (**b**). The electric field is depicted (*solid line*) together with the corresponding ionization rate, according to Eq. (9.8) (*dashed line*) for purely circularly polarized light (*black*) and elliptical light ($\varepsilon = 0.92$, *red*). *The curves* have been normalized to 1. *The insets on the left* illustrate how the electric field rotates along a circle (*black*) for circular polarization or along an ellipse (*red*) for elliptical polarization and the arrows indicate the direction of the field maximum, according to the value of CEO phase. *The insets on the right* show a closer view into the central optical cycle (where most of the ionization takes place): the electric field magnitude peaks at two instants labeled A and C and reaches local minima at other instants B and D, marked also on the polarization ellipse. This evolution manifests itself directly in the momentum distributions ($p_x$, $p_y$), that have been separately normalized for visualization purposes (adapted from [28])

the minor axis of the polarization ellipse and two equal peaks (labeled A and C in Fig. 9.3(b)) are found in the rate and in the temporal evolution of the pulse; consequently, the two peaks in the electron momentum distribution have the same intensity.

#### 9.2.1.4 Accuracy and Resolution

As reported above, measurements employing perfectly circularly polarized light would allow a robust time-to-momentum mapping in experiments where the CEO

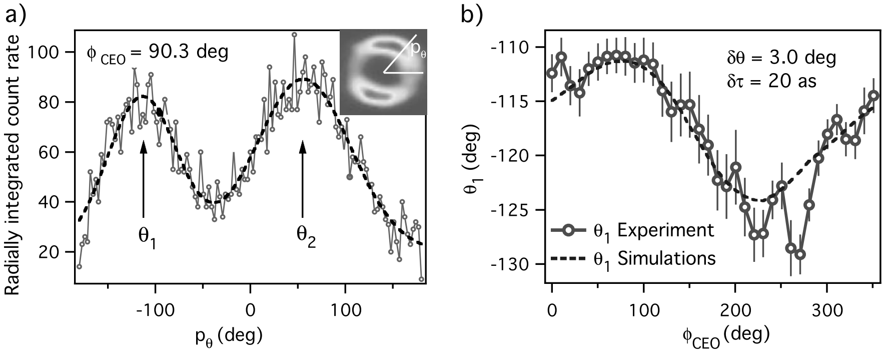

**Fig. 9.4** Temporal localization accuracy. (**a**) Radially integrated momentum distributions; the double peak structure due to the residual ellipticity ($\varepsilon = 0.92$) is clearly resolved for a constant value of CEO phase $= \pi/2$. *The dashed curve* corresponds to a double Gaussian fitting that returns the streaking angle $\theta_1$ and $\theta_2$. (**b**) The angular position of $\theta_1$ is shown as a function of the CEO phase for measured (*open circles*) and simulated (*dashed line*) momentum distributions; the error bars are the root-mean-square errors given by the fitting procedure. The temporal localization accuracy of 20 as follows from the comparison with the simulated curve. Adapted from [28]

phase is stabilized. Figure 9.2 and Eq. (9.4) show that the CEO phase controls the direction of ionization over the full angular spread traced by the rotating electric field vector. Instead, in the case of elliptically polarized light, instead, the time-to-momentum mapping is dictated by the polarization ellipse, with the angular position of the peaks in the momentum distribution varying weakly with a variation of the CEO phase. Nevertheless, the subcycle dynamics have been captured with a temporal localization accuracy of ≈ 20 as. An estimated time resolution of about 200 as can be achieved with the attoclock [28].

The time resolution and the temporal localization accuracy have been obtained as follows. From the CEO phase dependent two-dimensional momentum distributions such as those shown in the insets of Fig. 9.3, a radially integrated distribution is obtained by calculating the angular component of the electron momentum $p_\theta = \arctan(p_y/p_x)$ for each data point. The positions of the peaks of this angular distribution are extracted by a fit with a double Gaussian function, as shown in Fig. 9.4(a). The average root-mean-square error given by the fitting procedure yields the *precision* of the measurement, representing how precisely the peak positions can be determined. For the dataset presented in Fig. 9.4, the precision is much smaller than the actual signal width and amounts to about 2.5°, equivalent to 16 as. This number results from a statistical error and it can be in principle infinitely small for an infinitely large sample size, i.e. for an infinitely long data acquisition time. However, what is more interesting in a measurement technique is its *accuracy*, defined as the degree of closeness of measurements of a quantity to that quantity's actual value. The accuracy is the same as precision as long as no systematic errors in the experiment occur. To check if this is the case in our experiment, the data need to be compared with simulations.

Simulated momentum distributions are obtained within the frame of the semiclassical model, where classical propagation of the electron in the laser field follows tunnel ionization: an electron released at the instant of time $t$ with zero kinetic energy will be driven by the laser field until it acquires the final (i.e. after the laser pulse) momentum $p(t) = -A(t)$, as expressed by Eq. (9.2). Calculating the final momentum according to Eq. (9.3) or Eq. (9.5) for different ionization times, weighted by the tunneling rate given in Eq. (9.8) yields a distribution from which the peak position for different values of CEO phase can be extracted (Fig. 9.4(b)). Even though this simple approach excludes any Coulomb interaction of the electron with the parent ion after ionization, it can be used to check the accuracy of the attoclock, by monitoring how the position of the peaks change scanning the CEO phase. To include the influence of the ion, one has to calculate the classical electron trajectory during the streaking by solving numerically the equation of motion in the combined laser-ion potential. This results in a rotation of the whole $(p_x, p_y)$ distribution by an additional angular offset $\Delta\theta$, which is independent of the CEO phase [36]. This means that the Coulomb correction would manifest itself as a shift of the blue dashed curve shown in Fig. 9.4(b) downwards (or upwards, depending on the helicity of the light). In the present analysis, which excludes electron-ion interaction, the experimental and simulated curves are superimposed by minimizing the root mean square error $\delta\theta$ on the peak position defined as

$$\delta\theta = \sqrt{\frac{1}{N}\sum\left(\theta_{1,2}^{exp} - \theta_{1,2}^{sim}\right)^2}. \tag{9.10}$$

$\delta\theta$ gives an estimate of the highest measurement accuracy achieved. Due to the procedure adopted systematic errors, which cause fixed angular offsets, are not taken into account in this value. Nevertheless, other systematic errors that would induce a different trend of the peak position as a function of CEO phase are included. Figure 9.4(b) shows that the agreement between the experimental data and the simulations is excellent, yielding a temporal localization accuracy of about 3° or 20 as.

In the attoclock we have to distinguish between two different parameters that describe temporal properties: the temporal localization accuracy (tracking the peak of the ionization rate), which has been discussed before, and the temporal resolution (the minimum time difference to separate two independent ionization events that may happen within the same optical cycle). An estimate of the latter can be obtained by calculating the angular uncertainty caused by the tunneling and by an initial momentum distribution of the electron wavepacket at the exit of the tunnel. The initial electron momentum can be assumed to be zero in a first approximation, but in a more detailed picture, the electron must be treated as a wavepacket. It is possible to model the spread of the electron wavepacket, which in the end results in an angular uncertainty, in a semiclassical simulation by an ensemble of trajectories. The key point is to assign a certain initial momentum distribution at the start of the trajectory. If the initial velocity is chosen to match the distribution predicted by ADK tunneling theories [31], the angular uncertainty can be obtained by the width of the peak in the radially integrated momentum distribution. The uncertainty in

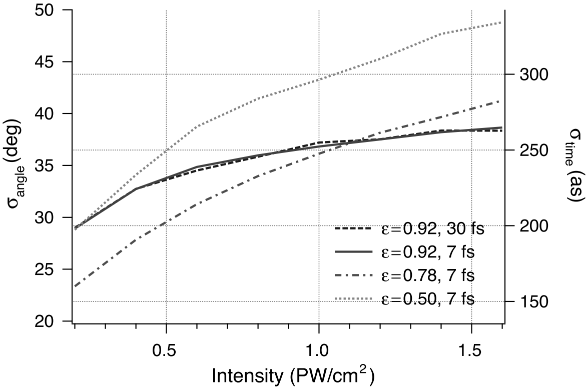

**Fig. 9.5** Angular uncertainty in degrees (on *the left axis*) and corresponding width in time (on *the right axis*) for pulses at a center wavelength of 740 nm for different values of ellipticity. The plot indicates that $\sigma_{time}$ is strongly dependent on ellipticity and intensity but rather weakly influenced by the laser pulse duration

time, which can be calculated by the angular width, has a pure quantum origin since it is due to the inherent electron wavepacket spread. It can be considered a lower limit for the attoclock temporal resolution. Simulations show that it is strongly affected by the pulse intensity and ellipticity but not by its time duration, as depicted in Fig. 9.5 for the Helium ionized with pulses at a central wavelength of 740 nm. Besides this fundamental limit, other experimental uncertainties further degrade this resolution. Generally, the detector resolution is estimated to be around 10 degrees, corresponding to about 70 as (for a discussion of this value, see Sect. 9.3.2). The shot-to-shot CEO phase fluctuations can be measured with an independent f-to-2f interferometer [37] and generally amount to about 6 degrees or 40 as. The gas jet temperature accounts for additional 8 degrees (50 as) because it induces a broadening of the momentum distribution in the radial and angular directions. All these experimental uncertainties come from different parts of the experiment and are assumed to be uncorrelated: they can be added to the estimated width of the electron wavepacket after ionization (Fig. 9.5) to yield an average value of about 240 as for peak laser intensity of 0.4 PW/cm$^2$ and $\varepsilon = 0.92$.

The width of the electron wavepacket after tunnel ionization can be estimated also by quantum mechanical calculations. The time-dependent Schrödinger equation (TDSE) for a helium atom in circularly polarized field is integrated at a peak intensity of $1 \times 10^{14}$ W/cm$^2$, while putting a pulsed source of electrons at the nucleus. This source term can be designed to emit electrons in the same direction as for laser-induced tunneling, thus it mimics the strong-field ionization process. It can be switched on and off rapidly without non-adiabatic effects on the wavefunction inside the atomic potential. With this approach, the narrowest angular spread of the free electrons is 35° corresponding to a resolution of about 240 as for pulses at a center wavelength of 740 nm [28].

The measurements presented above, performed with elliptically polarized and CEO phase stabilized pulses show the potential of the attoclock technique: subcycle dynamics induced by tunnel ionization can be resolved and are directly read out from the momentum distributions of the ionized electrons in the polarization plane. The excellent agreement of the experimental data with the simulations shows that the semiclassical model describes the ionization and streaking processes extremely well and therefore it can be used as the key to extract timing information with a precision of a few attoseconds [22, 24].

If the CEO phase is not stabilized, the counts are accumulated over all the random CEO phase values and the field modulations shown in Fig. 9.3 are washed away in the time domain. However, the momentum distribution still exhibits two dominant peaks, located at a position in the polarization plane determined by the polarization ellipse. The latter remains fixed in space and does not depend on the CEO phase. From an experimental point of view, inverting the time-to-momentum mapping is more robust for purely circular polarization since the counts are equally distributed as a function of angle. On the other hand, as shown above, it is possible to generalize the technique to elliptically polarized pulses, provided that the ellipticity and the orientation of the polarization ellipse are known [35]. In this case, the residual amount of ellipticity turns out to be even beneficial for obtaining measurements with "absolute" timing. The orientation of the ellipse provides the reference for the orientation of the electric-field maximum without the need for determining or locking the CEO phase [22].

With the support of the semiclassical model, one may use the measured electron momenta to extract the timing of the ionization process itself: with the knowledge of the electric field of the pulse given by a polarimetry measurement (see Fig. 9.1), one can trace back the classical electron trajectory in the laser-potential combined field and determine when the trajectory was started. This is exactly the procedure adopted in the work of Eckle et al. [22], who applied the attoclock technique to study one of the fundamental aspects of quantum mechanics: the possibility of particles to pass classically forbidden regions by tunneling through a barrier. Ionization of an atom by strong laser field permits addressing the question of a possible real and measurable tunneling delay time.

The comparison of the measured momentum distributions with the simulated ones, which include the influence of the Coulomb interaction but exclude any hypothetical tunneling delay time, led to the conclusion that the tunneling process is almost instantaneous (an intensity averaged upper limit of 12 as was determined [22]). In fact no additional angular offset, besides the one induced by the Coulomb interaction of the electron with the parent ion, was observed. A real tunneling delay time $\Delta t_D$ would manifest itself as an angular offset. To understand this, it is useful to simplify the problem by neglecting the Coulomb correction. The final electron momentum can then be calculated analytically from Eq. (9.2). If a real tunneling delay time $\Delta t_D$ is considered, an electron that exits the tunnel barrier at $t_0$ would be streaked to a different angle and its final momentum would be $-A(t_0 - \Delta t_D)$ instead of $-A(t_0)$.

### 9.2.2 *The Hour Hand*

If the pulse duration and intensity are such that ionization probability is not confined within the central optical cycle, then the fine timing estimate provided by the minute

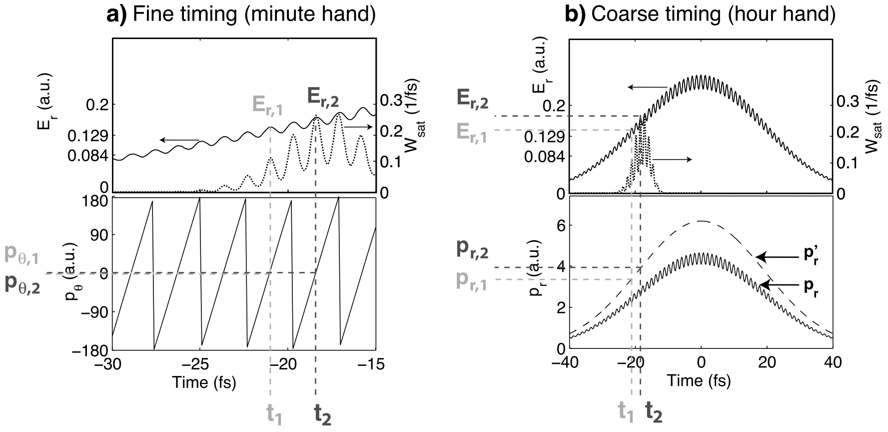

**Fig. 9.6** The hands of the attoclock. (**a**) The minute hand is given by the angle of the final electron momentum $p_\theta$. This angle follows the laser carrier frequency $\omega$, therefore it changes fast with time providing attosecond resolution, see Sect. 9.2.1.4. However, if the ionization rate (*dotted line*), calculated by the electric field (*solid line*) through Eq. (9.8), spans over more than one optical cycle, the one-to-one time to angle mapping is lost. Nevertheless, univocal timing information over an interval of time exceeding the laser period can still be retrieved considering the radial component of the final momentum (**b**); this is the hour hand of the attoclock. In general $p_r$ (*solid line* in the *bottom panel* of (**b**)) is not an injective function of time, due to the oscillations stemming from the ellipticity, but the "ellipticity-corrected" radial momentum $p'_r$ (*dashed line* in *the bottom panel* of (**b**)) preserves the univocal mapping provided that the electron is released before the peak of the pulse

hand is no longer unambiguous. Figure 9.6(a) shows this situation for a 30-fs pulse at peak intensity of 4.5 PW/cm$^2$ and ellipticity 0.77. This plot is similar to those shown in Fig. 9.3 but in the case of multicycle ionization: the tunneling ionization rate (green curve in the plot) as calculated by Eq. (9.8) spans over about 5 optical cycles. As a consequence, two electrons released at $t_1$ and $t_2$ with a time difference of one optical cycle, will be detected with the same angle of the momentum $p_{\theta,1} = p_{\theta,2}$ (Fig. 9.6(a)), because the electric fields $E_{r,1}$ and $E_{r,2}$ at the instant of ionization point in the same direction. This means that the one-to-one time to angle mapping is lost. However, as Fig. 9.6(b) indicates, the radial electron momentum will be different and can be used to extract timing information [24].

For perfectly circularly polarized light ($\varepsilon = \pm 1$), Eq. (9.5) states that $p_r(t)$ is not dependent on the CEO phase and is simply given by $p_r(t) = f(t)\sqrt{I/2}/\omega$. Assuming a Gaussian field envelope $f(t) = \exp[-t^2/(2\tau_p^2)]$, where $\tau_p$ is the laser pulse duration, we can find a momentum-to-time mapping given by:

$$t_{coarse} = \pm\tau_p\sqrt{2\ln\left(\frac{\sqrt{I}}{p_r\omega\sqrt{2}}\right)}. \tag{9.11}$$

In general, this mapping is not univocal, because in Eq. (9.11) two solutions for $t_{coarse}$ can be found for the same value of final radial momentum $p_r$. However, if the ionization event is restricted to the time interval $[-\infty, 0]$, only the negative sign solution in Eq. (9.11) has to be considered and the momentum-to-time mapping is unambiguous. The timing given in Eq. (9.11) is rather coarse, because $p_r(t)$ follows the envelope of the laser pulse field, which changes slowly with time. The temporal resolution achievable with the hour hand of the attoclock is therefore in the order of the optical period of the laser pulse, therefore in the femtosecond time domain.

For elliptical polarization, the radial momentum $p_r$ still follows the envelope of the electric field but sub-cycle oscillations show up, due to the ellipticity (see also Sect. 9.2.1.2). However, a compensation for the non-completeness of the circular polarization is possible, provided that the value of ellipticity and the orientation of the polarization ellipse are known. In this case, one can calculate an "ellipticity-corrected" radial momentum

$$p_r' = \sqrt{\left(1+\varepsilon^2\right)p_x^2 + \frac{1+\varepsilon^2}{\varepsilon^2}p_y^2} \approx \frac{f(t)\sqrt{I}}{\omega} \tag{9.12}$$

which is again an injective function of time, under the assumption that the electron is released before the peak of the pulse.

## 9.3 Experimental Setup

In the attoclock technique the instant of ionization is mapped to a vector momentum, thus requiring a momentum-imaging detector with an appreciable momentum resolution over $4\pi$ solid angle. COLTRIMS ("COLd Target Recoil Ion Momentum Spectroscopy") is an acronym for a technology which provides insight into the complete kinematics of electrons or ions emerging from single atomic or molecular fragmentation, essentially almost independent on the direction and magnitude of their vector momenta [38]. The momentum resolution achieved is at best few percent of an atomic unit, equivalent to ion energy resolution of tenths of μeV. The development of sophisticated delay-line detector systems allowed coincidence measurements of vector momenta of several electrons and ions, making this machine, re-named "Reaction Microscope", an extremely versatile spectrometer [39]. Excellent reviews have been written in the past years, covering all the main characteristics of this detector as well as its most successful applications [38–42]. Here we limit our discussion to those aspects that are especially interesting for the attoclock technique, namely the procedure of calculation of the vector momenta, momentum resolution of ions and electrons, 2 and 3-particle coincidence measurements and others.

### *9.3.1 Calculation of the Momentum Vectors*

High momentum resolution is achieved by preparing the atomic or molecular target in a state with the narrowest possible momentum distribution. This is realized by pre-cooling the target gas with liquid nitrogen and subsequently letting it expand trough a 30 μm nozzle. A cold gas jet is generated by cutting out with a skimmer the "zone of silence", a region with very low internal gas temperature that is formed just after the nozzle. An additional slit further collimates the gas jet, so that its diameter is about 1 mm at the interaction region, where it intersects the laser focus. The Reaction Microscope apparatus has separate time- and position sensitive detectors combined with Micro Channel Plates (MCP) for detecting negatively and positively charged particles; the detectors are installed at the two end of a spectrometer. The spectrometer axis (labeled as $x$ throughout this chapter) is aligned perpendicular to both the gas jet ($y$) and the laser propagation direction ($z$); with this geometry, the polarization plane of the laser pulse is defined as the ($x$–$y$) plane. For further details of the experimental setup see [21] and [43].

The charged fragments created at the interaction region are driven towards the detectors by homogeneous electric and magnetic fields aligned along the spectrometer axis ($x$ axis). The magnetic field, generated by Helmholtz coils located outside the vacuum chamber, is necessary to guide the electrons on helical trajectories, thus ensuring collection from the full solid angle (up to a maximum initial momentum). Compared to the electrons, the ion fragments experience only a small rotation by the magnetic field due to their much heavier mass. The spectrometer electric field strength is about 7 to 8 orders of magnitude smaller compared to the one of the laser pulse. Therefore, during the pulse duration (few femtosecond after ionization), the force exerted by the spectrometer fields is negligible. Within this time, the displacement of the electrons (that are faster than the ions) is in the range of few nanometers. Thus, it is reasonable to assume the particle to be at the instant of time $t_0$ at position ($x = 0$, $y = 0$, $z = 0$) and to have a momentum $p = (p_x, p_y, p_z)$ after the laser pulse has passed. At $t = t_0$ the charged particles start their trajectories and move under the force of the spectrometer fields until they reach the detectors after a Time-Of-Flight (TOF) in the range of typically hundreds of nanoseconds to few tenths of microseconds. When a particle of mass m and charge q collides onto the detector plate at the position ($y$, $z$), it has gained a momentum equal to

$$\begin{aligned} p_x &= \frac{mx}{t - t_0} - \frac{1}{2}Eq(t - t_0) \\ p_y &= -\frac{1}{2}Bq\left[z - \frac{y}{\tan(Bq(t - t_0)/2m)}\right] \\ p_z &= \frac{1}{2}Bq\left[y + \frac{z}{\tan(Bq(t - t_0)/2m)}\right] \end{aligned} \tag{9.13}$$

where $E$ and $B$ are the strength of the spectrometer electric and magnetic field respectively and $t - t_0 = \text{TOF}$. All the parameters on the right side of Eq. (9.13) are known: TOF, $y$ and $z$ are measured by the time and position sensitive detectors and $x$ is the distance between the laser focus and the detector plate. Hence one gets access to the momentum vector of the particle just after the laser pulse has passed.

The values of the spectrometer fields $E$ and $B$, needed to calculate the final momenta according to Eq. (9.13) are determined by the analysis of the raw data.

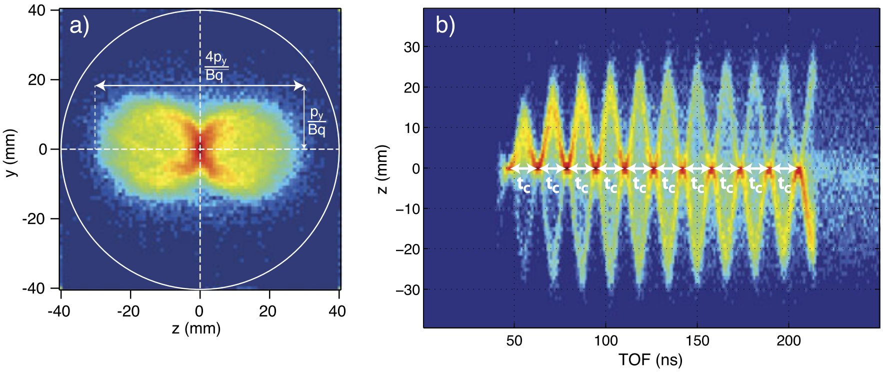

**Fig. 9.7** Magnetic field calibration. (**a**) Electron detector image: for a given value B of the spectrometer magnetic field, the maximum momentum that can be imaged onto the detector (80 mm diameter, *white circle*) is given by Eq. (9.16). (**b**) After each cyclotron period $t_c$ the electrons are refocused in time and come back to the $y = 0$, $z = 0$ position. This leads to periodic nodes in the so-called "fish spectrum". Estimating the value of $t_c$ (equal to 15.77 ns in this case) allows the determination of the magnetic field strength with Eq. (9.15) ($B = 2.266$ mT). The electrons were produced from Ar atoms with almost circularly polarized light (ellipticity equal to 0.95)

First, the raw data are filtered according to the "time sum" of the delay line signals: wherever the particle hits the detector, the sum of duration of the electronic signals traveling to each delayline end must be constant. This ensures that only real events and not signal generated by electronic noise are taken into account. After the filtering, in the ion TOF spectrum, different species can be identified: they reach the detector with appreciable time difference (in the order of few microseconds for standard spectrometer field strength) due to their different mass. Apart from the target gas, smaller and broader peaks of the background gases (mainly hydrogen but also water, nitrogen and oxygen) appear in the TOF spectrum. After associating each ion peak with the respective atomic species, the spectrometer electric field strength $E$ and the instant of ionization $t_0$ can be calculated by solving the equation for at least two values of $t_{ion}$:

$$E = \frac{2m_{ion}x}{q(t_{ion} - t_0)^2} \tag{9.14}$$

The calculation of the magnetic field $B$ is done with the electron data. Indeed the magnetic field affects the electrons' trajectories much more than the ions'. The Lorentz force $F = q[E + (v \times B)]$ constrains the electrons on helical trajectories with the result that they are periodically refocused along the electron TOF axis, passing by the initial position ($y = 0$, $z = 0$). By determining the cyclotron period $t_c$ between the nodes in the TOF spectrum (see Fig. 9.7(b)) the value of the magnetic field can be inferred with the equation:

$$B = \frac{m_{el}}{q}\frac{2\pi}{t_c} \tag{9.15}$$

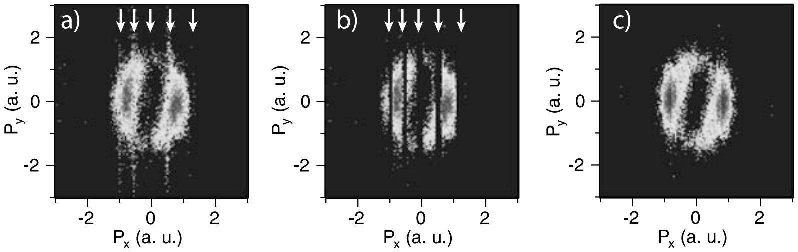

**Fig. 9.8** Electron momentum distributions measured from single ionization of Argon atoms with elliptically polarized light ($\varepsilon = 0.78$) at a peak intensity of $3.5 \times 10^{14}$ W/cm$^2$. (**a**) and (**b**) show the distributions obtained with $E = 418$ V/m: some initial momenta indicated by *white arrows* are not accessible due to the loss of resolution and can be cut out (**b**). Additional measurements taken with different spectrometer $E$ field (not shown here) allow the reconstruction of the full momentum distribution (**c**)

The periodic refocusing in time causes a loss of resolution for certain initial momenta. For TOF $= t - t_0 = t_c$ Eq. (9.13) states that $p_y$ and $p_z$ diverge leading to an impossibility in reconstructing the initial vector momentum. One may use either a lower magnetic field strength, thus increasing $t_c$ and reducing the number of the nodes, or a stronger electric field in order to confine the electron distribution within two of the nodes, at the cost of a slightly worse momentum resolution in the $x$ (TOF) direction. However the approach of using a high electric field and a low magnetic field is not always practicable. The detection of high-momentum electrons puts constraints on the minimum value of the $B$ field to be used and makes it impossible to squeeze all the electron distribution within the cyclotron period $t_c$. Indeed, the lower the magnetic field, the lower is the maximum allowed momentum in the $y$ direction that can be still imaged onto the detector. The latter has to obey the following equation (see also Fig. 9.7(a)):

$$p_y^{\max} < \frac{BqD}{4} \tag{9.16}$$

where $D$ is the diameter of the electron detector (typically 80 or 120 mm). For some applications of the attoclock technique, one may need to detect electrons with momentum up to 3 a.u. in the $x$ and $y$ directions with an 80-mm detector. This results in a minimum B field of about 2 mT (which can be generated with a current of 30 A flowing in the Helmholtz coils, corresponding to a power of almost 1 kW) and a cyclotron period as short as 18 ns.

Due to the loss of resolution for the certain initial momenta, the electron distribution in the polarization plane $(x, y)$ cannot be fully reconstructed. Figure 9.8(a) shows that for some values of $p_x$ indicated by the arrows, a value for $p_y$ is not defined. These are the momenta emerging from the nodes in the TOF, shown in Fig. 9.7; they can be filtered out, as it is done in Fig. 9.8(b), rendering the momentum mapping of the attoclock technique inaccurate. A solution to the problem is given by the acquisition of additional datasets with different values of spectrometer $E$ field. In this way, the positions of the nodes in the TOF still remain (they are determined by the B field), but they correspond to different regions of momentum. By merging 3–4 datasets it is therefore possible to reconstruct the full electron momentum distribution, as shown in Fig. 9.8(c).

### 9.3.2 Single Ionization and Momentum Resolution

The problem of resolution loss for some initial electron momenta can be circumvented if ion momentum distributions are used for the attoclock analysis instead of electron momentum distributions. For the case of ions, due to their mass, the cyclotron period is much larger than the TOF: for helium, for relatively strong magnetic fields, $t_c$ is in the range of 100 µs, thus much longer than the ion TOF, which is typically in the range of few microseconds. On the other hand, the large mass of the ions can be the reason for a lack of resolution of the ion momentum distribution: the error given by the initial thermal spread becomes more significant the heavier the ion is because the latter gains less velocity during the ionization process; in addition supersonic cooling works generally worse for heavy atoms and molecules. Therefore the momentum resolution in the direction of the gas jet ($y$) becomes worse. Consequently, the momentum distribution for circularly polarized light is no longer a torus and the angular streaking analysis becomes meaningless. This imposes that the analysis has to be done on the basis of electron momenta for heavy gas targets (like argon), following the procedure summarized in Fig. 9.8. For light gas targets (like helium), either ion or electron momentum can be exploited. In general, the momentum resolution is better for electron detection than for ions. However, electron momenta are more affected by small error in the determination of the spectrometer parameters like the field strengths, the instant of ionization or the propagation distances. Therefore, the calibration procedure has to be extremely accurate.

The advantage of using indifferently ion or electron momentum distributions comes from the possibility of the simultaneous detection of both offered by the Reaction Microscope, which is the principle of a "coincidence measurement". For the case of single ionization, momentum conservation dictates that the two distributions must be symmetric upon inversion. The ion momentum vector $\mathbf{p}_{ion}$ must equal out the electron momentum vector $\mathbf{p}_{electron}$ because the two particles experience an opposite acceleration during the ionization process, simply due to the different sign of the their charge. As a result the distribution of the sum $(\mathbf{p}_{ion} + \mathbf{p}_{electron})$ has to peak at zero. Figure 9.9 shows coincidence spectra for single ionization of helium. A Gaussian fit of the distributions along the $x$, $y$ and $z$ axis (top of Fig. 9.9) returns the position of the peak and its width. The former, that must be zero, can be used to fine tune the parameters of Eq. (9.13), like the electric field strength $E$, roughly estimated by Eq. (9.14), or the spectrometer's arm lengths $x$ with an iterative procedure. The latter is a measure for the total momentum resolution of the spectrometer (for electrons and ions) and generally it is not the same for the different directions. Which are the most important effects that affect the width of the momentum distributions shown in Fig. 9.9?

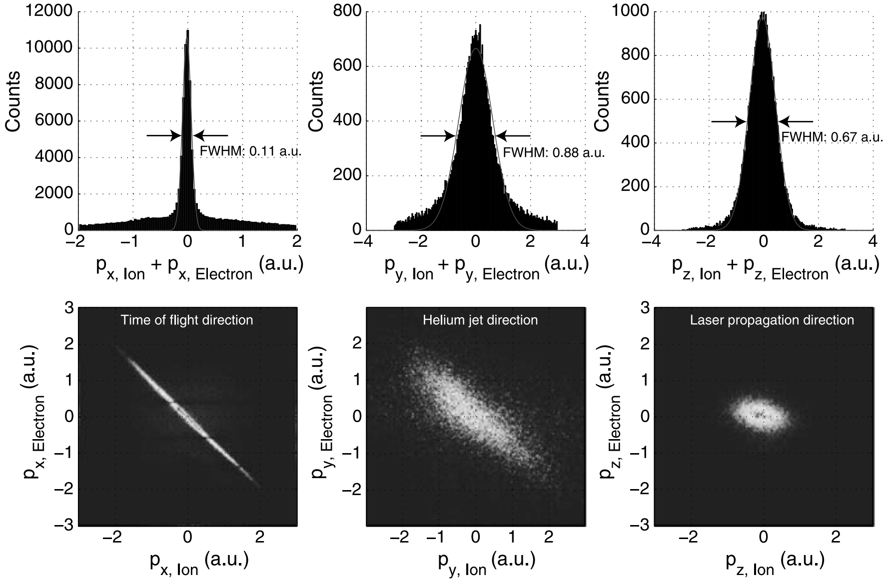

**Fig. 9.9** Coincidence spectra for single ionization of helium at a laser peak intensity of $8 \times 10^{14}$ W/cm$^2$. The width of the ($\mathbf{p}_{ion} + \mathbf{p}_{electron}$) distribution is estimated by a Gaussian curve fitting and is a measure of the spectrometer momentum resolution along the different directions. The 2D representation can be used for the calibration and for an estimation of false coincidences, because the distribution should be along a straight line following the anti-diagonal. Adapted from [43]

1. *Thermal spread.* Fig. 9.9 shows that the resolution is worse along $y$ direction than along $x$ or $z$, mainly because of the thermal spread of the gas jet. The influence of the initial thermal velocity is more important for the detection of ions than of electrons, because the latter are much stronger accelerated by the laser field during the ionization process and therefore an initial velocity distribution has minor weight.
2. *Uncertainty in the origin of ionization.* The calculation of the momenta by Eq. (9.13) is based on the assumption that the origin of the electron (or ion) trajectory is exactly at the center of the coordinate system. However, it may happen that atoms are ionized with a small offset, particularly along the laser propagation direction ($z$), due to the spatial extent of the laser focus. This offset contributes to the broadening of the momentum sum distribution but can be minimized with a tight laser focus geometry.
3. *Detector resolution.* Additional uncertainties may come from the resolution of time- and position sensitive detectors (typically $\Delta x = \Delta t = 0.5$ ns; $\Delta y = \Delta z = 0.5$ mm) and from possible misalignment and inhomogeneity of the spectrometer $E$ and $B$ fields.
4. *Saturation of the detector.* If too many particles hit the MCP at the same time, this may cause a "saturation" of the detectors: particles arriving later onto the same detector position are not detected due to the dead time of the electronics

and the momentum sum distribution becomes wider and asymmetric due to false coincidences (see also Sect. 9.3.3). This is a common problem for the Reaction Microscope apparatuses: in order to have reasonable momentum resolution and reliable measurements, the number of ionization events per laser pulse must be kept much smaller than one. This is achieved for instance by reducing the gas jet density at the inevitable cost of a longer data acquisition time.

For the attoclock technique, the most important observable is the angular component of the momentum in the polarization plane, which is given by $p_\theta = \arctan(p_y/p_x)$ (see Fig. 9.4(a)). An estimate of the angular uncertainty can be obtained by propagating the uncertainties on $p_x$ and $p_y$ determined by the Gaussian fit as shown in Fig. 9.9. The angular uncertainty depends on the value of $p_\theta$ and is the largest for $p_\theta = 0, \pi$ and smallest for $p_\theta = \pi/2, 3\pi/2$. On average, the mean value of all the $\sigma_{p_\theta}$ gives a meaningful estimate of the angular uncertainty. For the particular case of the single coincidence measurement shown in Fig. 9.9, the values of $\sigma_{px}$ and $\sigma_{py}$ result in a final uncertainty $\sigma_{p_\theta}$ equal to about 10 degrees, equivalent to 70 as for pulses at the central wavelength of 740 nm. However, with improved jet stage configurations, a much narrower distribution in the $y$ direction can be obtained, resulting in an uncertainty as small as 20 as (see Sect. 9.2.1.4 and Ref. [22]).

Figure 9.9 can provide additional information regarding the quality of the data, besides an estimate of the momentum resolution. In a single ionization channel particles coming from the same parent atom have to satisfy the equation $\mathbf{p}_{ion} = -\mathbf{p}_{electron}$ imposed by momentum conservation. These are the "real" coincidences that have to be distinguished from the random (or "false") ones. The selection is readily done by checking the momentum conservation plots shown in Fig. 9.9: the diffuse background out of the anti-diagonal in the 2D plot or, equivalently, the pedestal on the sides of the peak at zero are random coincidences from either a different atom or electronic noise. Like in the case of momentum resolution, a low ion (and electron) count rate is beneficial to keep the contribution of false coincidences low. If the count rate is too high, it means that more than one atom is ionized per laser shot. As a consequence one may find in the dataset events where one singly charged ion and two (or more) electrons are detected per laser shot. In this case, the two combinations have to be considered. Both contribute to the coincidence spectra, but necessarily one of the two (if not both, in case the "real" electron was not detected for some reason) has to be a false coincidence, falling out of the anti-diagonal in the 2D plots shown in Fig. 9.9. The situation becomes even worse, when the "false" electron is detected.

### 9.3.3 *Double Ionization*

The multihit capabilities of the delayline anode detectors allow the measurement of more than one particle per laser shot, thus opening the possibility to study double ionization processes of atoms or molecules. With the attoclock technique, it is possible to deduce the timing of release of the first and the second electron by the

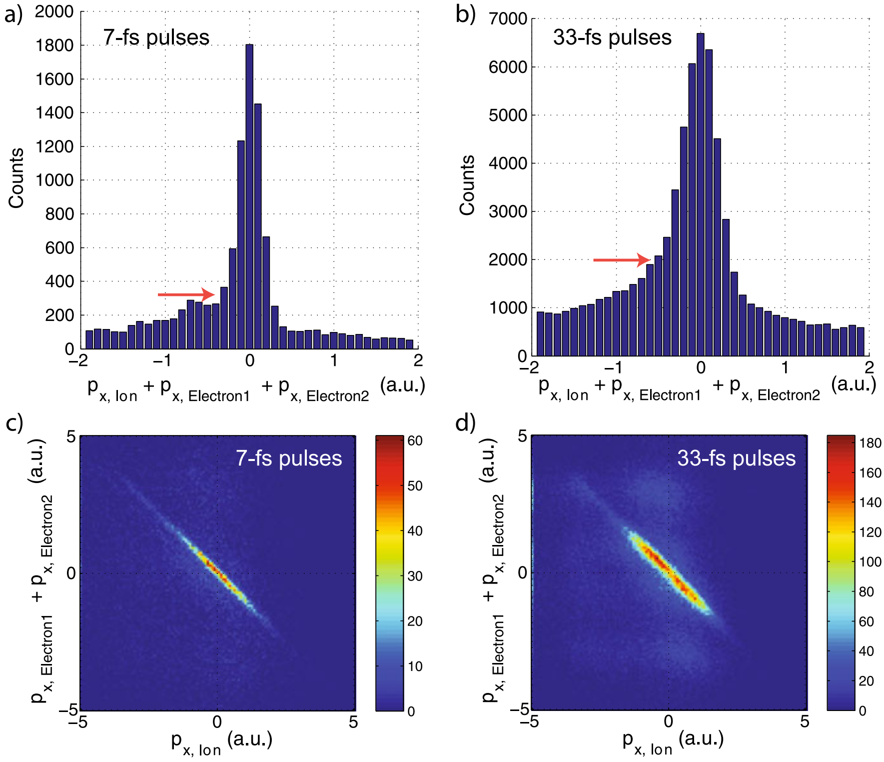

**Fig. 9.10** Coincidence spectra for double ionization of argon for 7-fs (**a**) and (**c**) and 33-fs (**b**) and (**d**) laser pulses, adapted from reference [24]. The spectra are integrated over an intensity range, which is up to 3.5 PW/cm$^2$ for (**a**) and (**c**) and up to 6 PW/cm$^2$ for (**b**) and (**d**). The larger intensities reached with the longer pulses induces a larger amount of false coincidences (relative height of the pedestal, indicated by *an arrow*, larger in (**b**) than in (**a**))

relative angle of the momentum vectors (minute hand, Sect. 9.2.1) and their magnitude (hour hand, Sect. 9.2.2). In order to do that, the momenta of the doubly charged ion and the two electrons need to be measured in coincidence. In this case, momentum conservation laws impose the condition $\mathbf{p}_{ion} + \mathbf{p}_{electron1} + \mathbf{p}_{electron2} = 0$ if the three particles stem from the break-up of a single atom.

When examining a double ionization channel, there are two different methods for data processing.

1. *3-Particle coincidence*. Out of all the detected particles per each laser shot, only groups consisting of one doubly charged ion and two electrons are selected. Like in the case of the single ionization (Fig. 9.9) the momentum conservation equation $\mathbf{p}_{ion} + \mathbf{p}_{electron1} + \mathbf{p}_{electron2} \sim 0$ is exploited to check the quality of the data and estimate the amount of false coincidence, as displayed in Fig. 9.10. The problem is more complicated than in the case of single ionization, because now three particles have to be detected simultaneously. However, this "complete de-

tection” method ensures that the contribution of false coincidences is kept low: in the data shown in Fig. 9.10 false coincidences are about 10 % for low intensities and 20 % for high intensities. The disadvantage of this method is that the detection efficiency results to be inhomogeneous. If the two ionized electrons have the same vector momentum $\mathbf{p}_{electron1} \approx \mathbf{p}_{electron2}$, they will impact onto the electron detector at the same position and at the same time. However, only one of the two electrons will be detected. When the first electron hits the MCP, a blind zone due to the detector dead time builds up around the position of the impact; the second electron that would impact within this blind zone is not detected. As a consequence, this group of particles, consisting of one doubly charged ion and one electron only, will not survive the filtering of the data. In other words, the detection efficiency is much lower for two electrons carrying the same vector momentum than for those having different ones.

2. *2-Particle coincidence.* In this method the filtering of the data is less severe. Groups consisting of one doubly charged ion and only one electron are selected; the momentum conservation equation $\mathbf{p}_{electron2} = -(\mathbf{p}_{ion} + \mathbf{p}_{electron1})$ is now exploited to calculate the vector momentum of the second electron. The advantage of this method is that the detection efficiency is much more homogeneous compared to the 3-particle coincidence method. Also electrons carrying the same vector momentum after ionization are included in the analysis, because only one needs to be measured directly and the second is calculated indirectly. The drawback is the higher contribution of false coincidences, which can be estimated from the momentum sum of the single ionization channel (Fig. 9.9) and the electron rate at the detector [44]. For experimental conditions similar to those of Fig. 9.10 for instance, the false coincidences amount to about 20 % for low intensity to about 27 % for high intensity.

## 9.4 Conclusions and Outlook

Up to now, the attoclock technique has been applied in experiments performed in the tunneling regime exploiting the unique property of resolving attosecond electron dynamics with femtosecond pulses. Experiments providing timing information on the attosecond timescale of strong-field single [22, 36] and double ionization [24, 45] of helium and argon have been presented as first applications. Single attosecond pulses or attosecond pulse trains do not initiate strong-field processes due to their energy photons (in the XUV range) and low intensity. However, they are currently acting as triggers or temporal references in energy streaking experiments where they are used in combination with linearly polarized femtosecond pulses and provide attosecond resolution.

Two recent experiments have investigated the dynamics of single-photon ionization in neon and argon by utilizing such setups in an attempt to answer one of the most fundamental questions in quantum mechanics [46, 47]: how fast can light remove a bound electron from an atom, a molecule or a solid? The outcome of these experiments leads towards the conclusion that single-photon ionization takes a finite amount of time, in contrast to what was inferred by the attoclock experiment for the case of strong-field ionization [22].

The attoclock method can also in principle be employed in a similar manner: a single attosecond pulse induces ionization, while an elliptically polarized femtosecond pulse subsequently probes the dynamics, in a "cleaner" way compared to linearly polarized pulses because additional effects induced by multiple returns of the electron to the core are prevented [48].

Once embedded in a two-color scheme (XUV + infrared), the attoclock technique may become the method of choice to investigate electron dynamics also in more complex systems like molecules and solids.

**Acknowledgements** All the work regarding the development of the attoclock technique was supported by the NCCR Quantum Photonics (NCCR QP) and NCC Molecular Ultrafast Science and Technology (NCCR MUST) programmes, research instruments of the Swiss National Science Foundation (SNSF), by the ETH Research Grant ETH-03 09-2 and by the SNSF R'Equip grant 206021_128551/1. A special acknowledgement goes to L. Gallmann for revising this manuscript. Collaborations with R. Dörner, A. Staudte, L. B. Madsen, H. G. Muller and M. Büttiker are gratefully acknowledged as well as stimulating discussions with L. Cocke.

## References

1. F. Krausz, M. Ivanov, Rev. Mod. Phys. **81**, 163 (2009)
2. M. Hentschel et al., Nature **414**, 509 (2001)
3. P.M. Paul et al., Science **292**, 1689 (2001)
4. E. Goulielmakis et al., Science **320**, 1614 (2008)
5. X.M. Feng et al., Phys. Rev. Lett. **103**, 183901 (2009)
6. E. Goulielmakis et al., Science **305**, 1267 (2004)
7. G. Sansone et al., Science **314**, 443 (2006)
8. T. Remetter et al., Nat. Phys. **2**, 323 (2006)
9. J. Mauritsson et al., Phys. Rev. Lett. **100**, 073003 (2008)
10. A.H. Zewail, J. Phys. Chem. A **104**, 5660 (2000)
11. P. Tzallas et al., Nat. Phys. **7**, 781 (2011)
12. U. Keller, IEEE Photonics J. **2**, 225 (2010)
13. M.J. Abel et al., Chem. Phys. **366**, 9 (2009)
14. F. Ferrari et al., Nat. Photonics **4**, 875 (2010)
15. E. Goulielmakis et al., Nature **466**, 739 (2010)
16. H. Wang et al., Phys. Rev. Lett. **105**, 143002 (2010)
17. M. Holler et al., Phys. Rev. Lett. **106**, 123601 (2011)
18. J. Itatani et al., Phys. Rev. Lett. **88**, 173903 (2002)
19. M. Kitzler et al., Phys. Rev. Lett. **88**, 173904 (2002)
20. A.L. Cavalieri et al., Nature **449**, 1029 (2007)
21. P. Eckle, *Attosecond Angular Streaking* (Südwestdeutscher Verlag für Hochschulschriften, 2008)
22. P. Eckle et al., Science **322**, 1525 (2008)
23. P. Dietrich, F. Krausz, P.B. Corkum, Opt. Lett. **25**, 16 (2000)
24. A.N. Pfeiffer et al., Nat. Phys. **7**, 428 (2011)
25. P.B. Corkum, Phys. Rev. Lett. **71**, 1994 (1993)
26. H.R. Telle et al., Appl. Phys. B **69**, 327 (1999)

27. T. Brabec, F. Krausz, Phys. Rev. Lett. **78**, 3282 (1997)
28. P. Eckle et al., Nat. Phys. **4**, 565 (2008)
29. A.M. Perelomov, V.S. Popov, M.V. Terentev, Zh. Eksp. Teor. Fiz. **50**, 1393 (1966)
30. L.V. Keldysh, Sov. Phys. JETP **20**, 1307 (1965)
31. M.V. Ammosov, N.B. Delone, V.P. Krainov, Sov. Phys. JETP **64**, 1191 (1986)
32. X.M. Tong, C.D. Lin, J. Phys. B **38**, 2593 (2005)
33. X.M. Tong, Z.X. Zhao, C.D. Lin, Phys. Rev. A **66**, 033402 (2002)
34. C.M. Maharjan et al., Phys. Rev. A **72**, 041403 (2005)
35. M. Smolarski et al., Opt. Express **18**, 17640 (2010)
36. A.N. Pfeiffer et al., Nat. Phys. **8**, 76 (2012)
37. A. Guandalini et al., J. Phys. B, At. Mol. Opt. Phys. **39**, S257 (2006)
38. R. Dörner et al., Phys. Rep. **330**, 95 (2000)
39. J. Ullrich et al., Rep. Prog. Phys. **66**, 1463 (2003)
40. J. Ullrich et al., Comments At. Mol. Phys. **30**, 285 (1994)
41. J. Ullrich et al., J. Phys. B, At. Mol. Opt. Phys. **30**, 2917 (1997)
42. R. Dörner et al., in *Advances in Atomic, Molecular, and Optical Physics*, vol. 48 (Academic Press, San Diego, 2002), p. 1
43. A.N. Pfeiffer, Attosecond electron kinematics in strong field single and double ionization, vol. 53. Dissertation at ETH Zurich, Nr. 19565 (2011)
44. T. Weber et al., Nature **405**, 658 (2000)
45. A.N. Pfeiffer et al., New J. Phys. **13**, 093008 (2011)
46. M. Schultze et al., Science **328**, 1658 (2010)
47. K. Klünder et al., Phys. Rev. Lett. **106**, 143002 (2011)
48. P. Dietrich et al., Phys. Rev. A **50**, R3585 (1994)

# Chapter 10
# Studying the Electronic Structure of Molecules with High Harmonic Spectroscopy

**D.M. Villeneuve, J.B. Bertrand, P.B. Corkum, N. Dudovich, J. Itatani, J.C. Kieffer, F. Légaré, J. Levesque, Y. Mairesse, H. Niikura, B.E. Schmidt, A.D. Shiner, and H.J. Wörner**

**Abstract** High harmonic spectroscopy is a tool to study the valence electronic structure of atoms and molecules. It uses the techniques of high harmonic generation, in which a femtosecond laser ionizes the gas sample and XUV radiation is emitted in the forward direction. The XUV intensity, phase and polarization contain information about the orbital from which an electron was removed by the laser. High harmonic spectroscopy reveals details of electron-electron interactions, motion of electronic wave packets, and can follow a chemical reaction.

---

D.M. Villeneuve (✉) · J.B. Bertrand · P.B. Corkum
Joint Attosecond Science Laboratory, National Research Council of Canada and University of Ottawa, 100 Sussex Drive, Ottawa, Ontario K1A 0R6, Canada
e-mail: david.villeneuve@nrc.ca

J.B. Bertrand
e-mail: Julien.Bertrand@nrc-cnrc.gc.ca

P.B. Corkum
e-mail: Paul.Corkum@nrc-cnrc.gc.ca

N. Dudovich
Department of Physics of Complex Systems, Weizmann Institute of Science, Rehovot 76100, Israel
e-mail: Nirit.Dudovitch@weizmann.ac.il

J. Itatani
Institute for Solid State Physics, The University of Tokyo, Kashiwa, Chiba 277-8581, Japan
e-mail: jitatani@issp.u-tokyo.ac.jp

J.C. Kieffer · F. Légaré · B.E. Schmidt
Institut National de la Recherche Scientifique INRS-EMT, 1650, boul. Lionel-Boulet, Varennes, Quebec J3X 1S2, Canada

J.C. Kieffer
e-mail: kieffer@emt.inrs.ca

F. Légaré
e-mail: legare@emt.inrs.ca

B.E. Schmidt
e-mail: schmidtb@emt.inrs.ca

L. Plaja et al. (eds.), *Attosecond Physics*, Springer Series in Optical Sciences 177,
DOI 10.1007/978-3-642-37623-8_10,

## 10.1 Introduction

In recent years, high harmonic generation (HHG) has developed into the main tool of attosecond science. It has permitted the production of attosecond pulses [1], the observation of molecular dynamics [2] and the imaging of molecular orbitals with Ångström resolution [3]. HHG is most simply understood in terms of the three-step model: a molecule exposed to a strong laser field is tunnel ionized, the liberated electron is then accelerated by the field oscillations which can force it to recollide with the parent ion [4]. Recollision is the common step of most strong field processes that permit the observation of dynamical events with attosecond temporal and Ångström spatial resolution [5].

Measuring and understanding the electronic structure and correlated dynamics of matter on its natural time scale represents the main thrust of ultrafast laser science. Understanding the correlated nature of multi-electron systems indeed represents one of the major scientific challenges [6]. Electron correlations affect essential properties of complex systems ranging from configuration interactions in molecules to cooperative phenomena in solids, like superconductivity. Our knowledge of the electronic structure of matter originates from several decades of research on photoionization and photoelectron spectroscopy [7–9], mainly driven by the development of synchrotron-based sources. Recent advances in strong-field physics have opened an alternative approach to probing both the electronic structure [3, 10] and the dynamics [2, 11, 12] of molecules using table-top laser sources. These new methods rely on the recollision of an electron, removed from the molecule by a strong laser field, with its parent ion [4]. The electronic structure of the molecule is

---

J. Levesque
Centre for Operational Research and Analysis, Defence R & D Canada, Department of National Defence, MGen Pearkes Building 6 CBS, Ottawa K1A 0K2, Canada
e-mail: jerome.Levesque@drdc-rddc.gc.ca

Y. Mairesse
CELIA, UMR5107, Université de Bordeaux, CNRS, CEA, 33400 Talence, France
e-mail: mairesse@celia.u-bordeaux1.fr

H. Niikura
Department of Applied Physics, Waseda University, Okubo 3-4-1, Shinjyuku, Tokyo 169-8555, Japan
e-mail: niikura@waseda.jp

A.D. Shiner
Ciena Canada Ltd., 307 Legget Drive, Kanata, Ontario K2K 3C8, Canada
e-mail: andrew.shiner@gmail.com

H.J. Wörner
Laboratorium für Physikalische Chemie, Eidgenössische Technische Hochschule Zürich, Wolfgang-Pauli-Strasse 10, 8093 Zürich, Switzerland
e-mail: woerner@phys.chem.ethz.ch

encoded in the emitted high-harmonic spectrum through the amplitude and phase of the photorecombination matrix elements [11, 13–15] .

The current understanding of processes occurring in a strong laser field relies on the strong-field approximation (SFA) [16] but its shortcomings for quantitative modeling are now becoming apparent. When the electron is far away from the ion core, its motion is dominated by the laser field and therefore its wave function is well represented by plane wave functions or the time-dependent Volkov functions. The difficulty of the coupled Coulomb-Volkov problem is usually addressed by a perturbative treatment of the Coulomb field [17]. We will show that an alternative strategy, treating the ionic potential exactly and neglecting the effect of the laser field during recombination, is very accurate, at least for atoms and small molecules.

## 10.2 Cooper Minimum in Argon Revealed by High Harmonic Spectroscopy

The photoionization cross section of argon atoms exhibits a prominent minimum at a photon energy around 50 eV. We will show that this minimum is also apparent in the high harmonic spectrum of argon [13]. We show that the position of the minimum is not influenced by the strong laser field that is present during the recombination process. This remarkable observation implies that high harmonic experiments can directly measure the field-free electronic structure of the target atom or molecule. Experimentally, we study the argon atom as one of the most frequently used in high-harmonic and attosecond pulse generation and we show that the position of the minimum is independent of intensity and driving wavelength. Theoretically, we develop a method to calculate high-harmonic spectra from field-free continuum functions of an effective potential. The calculation of recombination cross-sections for HHG using scattering functions has been introduced in Ref. [18]. It has subsequently been used to predict harmonic spectra of the rare gas atoms [19] and $H_2^+$ [20]. We show that the minimum observed in HHG in argon atoms lies close to the minimum in the photoionization spectrum that is known as Cooper minimum [21]. Indeed, the last step of HHG is similar to photorecombination of an ion and an electron. We show that our method is capable of quantitatively reproducing the position of the observed minimum in contrast to other methods using plane waves or Coulomb waves.

The experimental setup consists of a chirped-pulse amplification titanium-sapphire laser system (KM Labs), a hollow-core fiber setup for pulse compression and a vacuum chamber for generation and characterization of high-harmonic radiation. The laser system provides pulses of 2 mJ energy and 35 fs duration at a repetition rate of 1 kHz. The pulses are focused into a hollow-core fiber filled with argon to achieve self-phase modulation [22] and are subsequently compressed using chirped mirrors. The typical duration of the compressed pulses was 6–8 fs. These pulses are focused $\sim$1 mm below the orifice of a pulsed nozzle generating a supersonic expansion of argon. This setup minimizes the effects of phase mismatch and reabsorption of the high-harmonic radiation and leads to the observation

**Fig. 10.1** High-harmonic spectra generated in argon using an 8 fs laser pulse centered at 780 nm. The three different panels correspond to the laser intensities $2.5 \times 10^{14}$ W/cm$^2$ (**a**), $2.9 \times 10^{14}$ W/cm$^2$ (**b**) and $3.5 \times 10^{14}$ W/cm$^2$ (**c**). Adapted from [23]

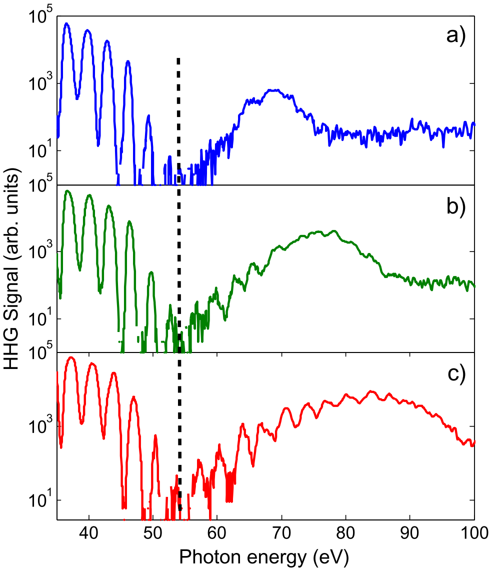

of the single-atom response. The generated high-order harmonics are sent into an XUV spectrometer consisting of an aberration-corrected concave grating that spectrally disperses the harmonics and images them onto a microchannel plate detector. A CCD (charge-coupled device) camera accumulates the spectral image and transfers it to a computer. The image is integrated over the spatial dimension to provide the high harmonic spectrum.

High-harmonic spectra generated in argon using an 8 fs laser pulse centered at 780 nm at different intensities are shown in Fig. 10.1. In the region of low photon energies, the spectrum shows the usual progression of odd harmonics of the fundamental wavelength which turns into a continuum close to the cut-off. The most striking feature of the spectrum is the presence of a deep minimum around the 33rd harmonic.

Different origins are conceivable for minima in high-harmonic spectra. Minima can originate from the structure of the atom or molecule. Their position is approximately independent of the laser intensity as is the case in 2-center interference [24]. A minimum can also originate from dynamics of either the electron in the continuum or of the molecular cation following tunnel ionization and/or the action of the strong laser field. An example of continuum dynamics has been reported using a mixture of helium and neon as nonlinear medium [25]. Such minima are associated with a well defined recollision time and their location in photon energy (i.e. harmonic order) would therefore shift approximately linearly with intensity. It would also depend strongly on the wavelength of the fundamental field.

With increasing intensities the cut-off in the high-harmonic spectra shown in Fig. 10.1 extends clearly, but the position of the minimum is left unchanged. Measurements at longer wavelengths have revealed a minimum at the same photon energies as reported here [26]. This proves that the minimum observed in high-harmonic spectra of argon is associated with the *electronic structure* of the atom rather than with its *dynamics* in the laser field and is independent of the laser source.

We find that the minimum in argon appears at 53 ± 3 eV. This is close to the observed position of the Cooper minimum in the single-photon-ionization efficiency [27]. The minimum in argon has been reported many times in the literature since the early days of HHG [28, 29]. The minimum is much deeper in our spectra because we use an ultra-short pulse that extends the cut-off and places the minimum into the plateau.

We now show that we can accurately model the recombination step in HHG using field-free one-electron procedures commonly used in photoionization spectroscopy. The potential is used to generate both the bound (ground) state and the continuum wave functions, neglecting the laser field at the moment of recombination. Without the laser field, the problem is spherically symmetric. The electronic wave function is represented as a product

$$\Psi(r,\theta,\phi) = \frac{1}{r}\phi_\ell(r)Y_\ell^m(\theta,\phi) \tag{10.1}$$

of a reduced radial wave function $\phi_\ell(r)$ and spherical harmonics. $\ell$ stands for the angular momentum quantum number of the electron and $m$ its projection quantum number. An effective one-electron potential [30]

$$V_\ell(r) = \frac{\ell(\ell+1)}{2r^2} - \frac{1}{r} - \frac{Ae^{-r} + (17-A)e^{-Cr}}{r} \tag{10.2}$$

with $(A = 5.4, C = 3.682)$ is used and spin-orbit interaction is neglected. The ground state wave function (3p) is generated by diagonalizing the Hamiltonian for $\ell = 1$ on a numerical grid. The continuum functions are generated by numerically integrating the Schrödinger equation for a given (positive) kinetic energy of the electron using the Numerov algorithm [31]. The normalization is performed at asymptotically large radial coordinates including the Coulomb tail [32].

Figure 10.2 represents the bound and continuum wave functions for argon. The two-dimensional cut through the continuum wave function was obtained by summing all partial wave components from $\ell = 0$ to $\ell = 50$ that were obtained from numerical integration of the effective potential in Eq. (10.2). The continuum wave function consists of a plane wave propagating along the x axis from left to right and the superimposed scattered wave that strongly distorts the appearance of the plane wave. This highlights the problem of using plane waves to represent the continuum wave function, as we will do in future sections.

Figure 10.3 shows the log base 10 of the photoionization dipole squared as described above. The minimum at about 55 eV is evident. Also shown is the photoionization phase which is seen to have a gradual phase shift over tens of electron volts around the Cooper minimum. The gradual nature is due to the d-wave partial wave component of the transition changing sign around the minimum, but it does not have sufficient magnitude near the minimum to abruptly influence the phase.

The minimum observed in HHG occurs because the total recombination dipole goes through a minimum for a certain value of the electron's kinetic energy. This

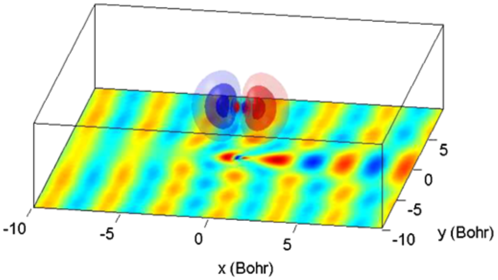

**Fig. 10.2** 3p$_x$ ($m_\ell = 0$) orbital wavefunction of argon and two-dimensional cut through the real part of the continuum wave function for $k = 1.8$ a.u. The atomic orbital was obtained from a quantum chemical *ab initio* calculation using the Hartree-Fock method and the cc-pVTZ basis set. *The two colors* correspond to different signs of the wave function and their intensity of color codes the amplitude. The continuum wave function was calculated from the effective potential given in the text by adding the components $\ell = 0$ to 50. *The color code*, in this later case, represents the amplitude. Adapted from [23]

**Fig. 10.3** *Green line* shows the log base 10 of the calculated photoionization cross section. The Cooper minimum near 55 eV is evident. *The blue line* shows the phase of the photoionization dipole moment. A gradual phase change of somewhat less than $\pi$ occurs centered at the Cooper minimum

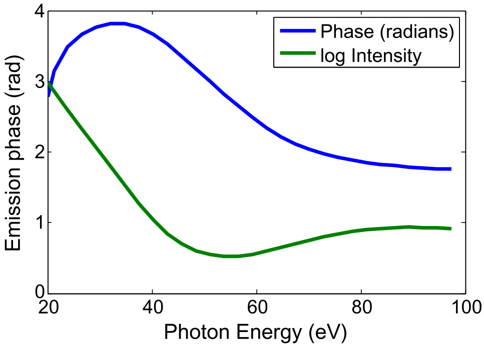

happens because the radial integral for the transition to d wave changes sign. Moreover, the phase of the dipole varies quickly across the minimum position. This will translate to a similar variation in the harmonic phase that should be observable in experiments using the RABBITT technique [33, 34] or mixed gases [25].

The present example enables us to directly compare the information content of a HHG spectrum with that of a photoelectron experiment. The radial integrals are identical for both cases but a photoionization cross section represents an *angle-integrated* measurement and is thus described by an *incoherent* sum over the emitted partial waves whereas HHG is an inherently *differential* technique which is expressed as a *coherent* sum over recombining partial waves. This explains why the minimum seen in HHG is much deeper than the minimum seen in photoionization.

The conversion from the electron's kinetic energy ($k^2/2$ in atomic units) to the photon energy ($\Omega$) has been a subject of debate in recent work, some studies using $\Omega = k^2/2$, others $\Omega = k^2/2 + I_p$ [3, 35, 36]. The disagreement originates from the fact that the kinetic energy of the electron is not clearly defined at the moment of recollision because the electron is accelerated by the ionic potential. The use of plane waves and the relation $\Omega = k^2/2 + I_p$ predicts that the minimum in argon lies around 21 eV. If the other dispersion relation is used, the minimum shifts to 5 eV, so the agreement with experiment is even worse. In the case of exact continuum functions, the dispersion relation can only be $\Omega = k^2/2 + I_p$ because the momentum $k$ of the electron is defined at asymptotic distances from the core where the ionic potential is negligible.

The main approximations of the present method lie in neglecting the laser field which can be justified using a semi-classical argument by comparing the magnitude of the energies involved in the process. The electron corresponding to the observed minimum position has a kinetic energy of 35 eV and the ionic potential is 15.8 eV. However, the variation of the electrostatic potential of the laser field across the region where recombination takes place amounts to a few electron-Volts only. This means that the effect of the laser field on the electron at the moment of recombination is negligible and suggests that field-free continuum wave functions properly describe the region where recombination occurs.

## 10.3 Interchannel Coupling and the Giant Resonance in Xenon

In the previous section, we showed that a structural feature in the photoionization cross section of argon could be clearly seen in high harmonic spectra. We now extend this observation, to show that photoionization cross sections can be recorded up to 150 eV, and that the high harmonic spectrum contains features due to multi-electron processes during photorecombination, specifically interchannel couplings.

We use high harmonic spectroscopy to investigate a new class of collective electronic dynamics—induced and probed by the recombining electron. The kinetic energy of the returning electron is usually much larger than the difference between electronic energy levels of the parent ion. Consequently, inelastic scattering followed by recombination is energetically possible, as illustrated in Fig. 10.4(right). Using the xenon atom as an example, we demonstrate that such processes indeed occur and that they can locally enhance the efficiency of HHG by more than one order of magnitude. We show that such a seemingly complex pathway contributes significantly to the phase matched process. This observation uncovers a new unexpected facet of high harmonic spectroscopy—it provides access to electron correlations which are otherwise very difficult to observe. Our results suggest that electron-electron (e-e) excitations may be ubiquitous in high harmonic spectroscopy experiments. High harmonic spectroscopy gives access to multi-electron dynamics through their spectral signature, much as in photoionization studies, but it offers the additional potential of attosecond temporal resolution.

Until recently, HHG was interpreted within the single-active-electron approximation. HHG experiments in pre-formed, transition-metal plasmas by Ganeev et al. [37] observed significant enhancements of a single harmonic order. These enhancements were recently interpreted by Frolov et al. [38] to be caused by Fano autoionizing resonances and 3d-3p transitions, underlining the importance of multi-electron effects in HHG.

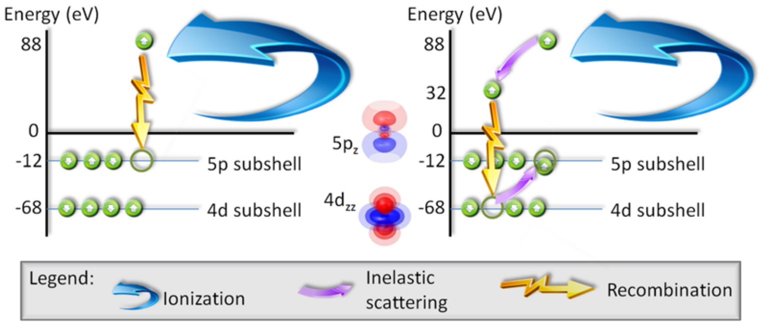

**Fig. 10.4** Steps for harmonic generation. In the usual 3-step model an electron is tunnel ionized from the valance shell, accelerates in the continuum and then recombines to the state from which it came (*left*). With inelastic scattering the returning electron can promote a lower lying electron into the valance band and then recombine to the vacancy in the lower lying state (*right*). In both cases a 100 eV photon is emitted by recombination to a 5p vacancy (*left*) or a 4d vacancy (*right*). Adapted from [39]

We used a novel laser source that is almost ideal for spectroscopic studies [40–42] (see below), having a wavelength of 1.8 μm and a duration of less than 2 optical cycles. With its long wavelength, it creates a recollision electron whose energy can exceed 100 eV, even for low ionization potential systems such as small organic molecules.

HHG spectra were recorded for the noble gases, argon, krypton and xenon, using a thin phase-matched gas jet [39]. Results are shown in Fig 10.5 and demonstrate the smooth spectra that are possible with this laser source. The limit of 160 eV is imposed by the spectrometer. We now show how the photoionization cross section can be measured with these spectra. It has been shown that the three-step model for HHG [4] can be approximately factorized into three terms [3, 15, 43, 44] corresponding to ionization ($I$), electron propagation $W(E)$, and recombination ($\sigma^r$). Although the range of validity for this expression has not been fully explored, it is sufficiently accurate to allow us to compare the HHG spectra of Xe and Kr, both of which involve ionization from p-orbitals.

$$S(E_\Omega) = I(F,\omega)W(E)\sigma^r(E) = \mathbb{W}(E)\sigma^r(E). \tag{10.3}$$

Here $S(E_\Omega)$ is the HHG power spectrum, $E_\Omega = E + I_p$ is the emitted photon energy, $E$ is the electron kinetic energy, $\omega$ is the laser frequency, $F$ is the laser field, and $I_p$ is the ionization potential. The photorecombination cross section $\sigma^r$ is related to the photoionization cross section $\sigma^i$ through the principle of detailed balance [43, 45]. In addition, the differential photoionization cross section in which the photoelectron is ejected parallel to the polarization vector of the electromagnetic field is the appropriate component for photorecombination. The differential cross section is determined from the anisotropy parameter $\beta$ measured in the photoionization experiments, using the relation $\partial\sigma^i/\partial\Omega = \sigma^{total}(1 + \beta P_2(\cos\theta))/4\pi$ for $\theta = 0$.

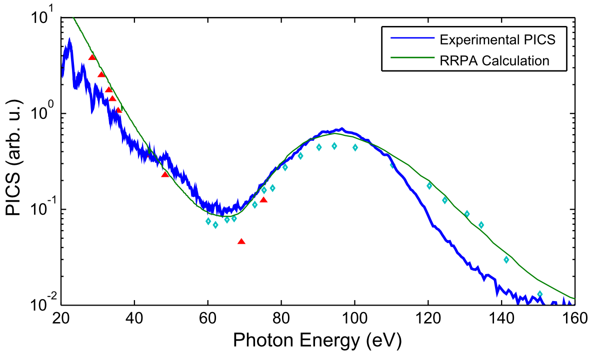

**Fig. 10.5** Experimental HHG spectrum for xenon (*blue line*) obtained with a laser source with a wavelength of 1.8 μm, pulse duration of 11 fs (∼ 1.8 cycles), and intensity of $1.9 \times 10^{14}$ W/cm$^2$. The raw xenon spectrum was divided by the spectrometer calibration. The RRPA calculation of the xenon PICS by Kutzner et al. [47] (*green line*). *The red and green symbols* are PICS measurements by Fahlmann [48] and Becker [49] respectively, each weighted using the anisotropy parameter calculated by Kutzner et al. [47]. Derived from [39]

In order to calibrate the recording system, we use the measured HHG spectrum from krypton $S_{Kr}(E_\Omega)$ and the photoionization cross section $\sigma^i_{Kr}(E_\Omega)$ from the literature [46] to accurately determine the recolliding electron wavepacket spectrum $\mathbb{W}(E)$ by setting $\mathbb{W}(E) = S_{Kr}(E_\Omega)/\sigma^i_{Kr}(E_\Omega)$, using a similar approach to that used by Itatani et al. [3]. We then divide the measured HHG spectrum for xenon with this term, to extract the photoionization cross section for xenon: $\sigma^i_{Xe} = S_{Xe}(E_\Omega)/\mathbb{W}(E)$. Because this procedure divides one spectrum by another, experimental details such as grating reflectivity and detector response cancel out. In addition, the proportionality factor [43, 45] relating $\sigma^i$ and $\sigma^r$ approximately cancel out when the ionization potentials are similar. The correction factor is at most a factor of 2 across the entire spectrum, telling us that the recolliding wave packet is almost flat across the spectrum. The experimentally derived $\sigma^i_{Xe}$ is plotted in Fig. 10.5, together with the photoionization cross section from synchrotron experiments. The excellent agreement shows that the HHG spectrum contains detailed information about the electronic structure of atoms, imprinted through the photorecombination cross section. It is remarkable that the intense laser field can be neglected.

We now study the xenon results, shown in Fig. 10.5. The most striking feature is the pronounced peak around 100 eV. This peak is also seen in the photoionization cross section from synchrotron measurements, also shown in Fig. 10.5. This peak has been extensively studied in the context of photoionization, and led to the development of a theory that included e-e correlations during photoionization [50]. The 100 eV peak is interpreted as being due to the influence of 4d electrons, which have a large photoionization cross section in this region owing to a shape resonance. Energy-resolved measurements [49] have shown that the photoionization cross section of the 5p shell is strongly enhanced around 100 eV through e-e interactions with the 4d sub-shell.

The first step in HHG is tunnel ionization from the most weakly bound electrons, the 5p electrons in the case of xenon. The probability of tunnel ionizing a 4d electron whose binding energy is 68 eV is vanishingly small ($10^{-51}$). So how is it that the photorecombination process in HHG can manifest the influence of the 4d shell? Figure 10.4(right) illustrates the Coulomb interaction between the returning continuum electron and a bound 4d electron. An exchange of energy takes place, resulting in the promotion of a 4d electron to fill the 5p hole. This causes the continuum electron to lose 56 eV (the difference between binding energies of the two sub-shells), and hence to have the correct kinetic energy to experience the quasibound continuum state that enhances the 4d cross section. The decelerated electron then recombines to the 4d hole and emits a photon whose energy is the same as that of the direct channel, due to energy conservation. The smooth green curve in Fig. 10.5 is derived from a complete multi-electron calculation [47] that includes contributions from all sub-shells.

Although we have successfully predicted the observed HHG spectrum in xenon, it is not obvious that the 4d channel will be phase matched, a necessity for HHG. Does the e-e interaction cause a loss of the coherence that is necessary for HHG phase matching? A generalized HHG model [39] shows that coherence is indeed maintained. In SFA, the ion evolves with a phase given by its total energy; the continuum electron gains a phase given by the classical action. After the collisional excitation, both the ion and the continuum electron exchange energy, but the total energy remains the same, meaning that the excitation time does not affect the emission phase, and coherence is maintained.

The observation of the 100 eV peak in xenon in the HHG spectrum is striking in several ways. It reinforces the observation that the HHG spectrum is largely determined by the photoionization cross section [15, 23, 43]. In fact Frolov et al. [15] predicted that the xenon giant resonance will appear in HHG spectra. The agreement between our measured spectrum and the previously measured photoionization cross section is remarkable because it represents a clear observation of e-e correlations and excitation of the ion in HHG. Indeed, it is quite likely that collisional excitation followed by recombination to an inner shell orbital is a general phenomenon in HHG whose experimental evidence has been directly observed for the first time due to the newly developed sub-two cycle IR laser source.

## 10.4 High Harmonics from Aligned Molecules

It has been demonstrated in experiments with aligned molecules that the highest occupied molecular orbital (HOMO) largely determines the shape of the HHG spectrum [51]. It was shown [3] that the process of high harmonic generation could be used to form an image of a single electron orbital wave function of $N_2$, and that the orbitals of rare gas atoms determine the HHG spectrum [36]. These experiments are supported by calculations that show the dependence on the HOMO [52–55]. In this section, we will show that the HHG spectra from aligned $N_2$, $O_2$ and $CO_2$ have

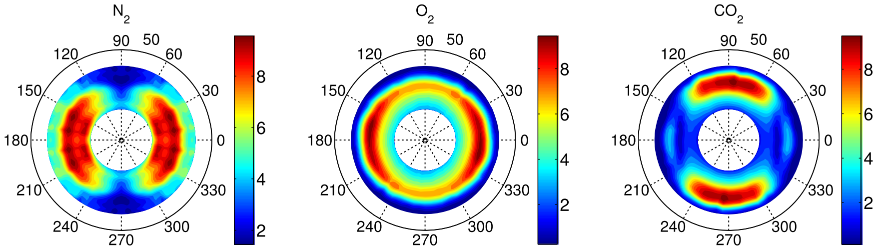

**Fig. 10.6** Experimental high harmonic spectra versus angle between the molecular axis and the laser polarization, from $N_2$, $O_2$ and $CO_2$ molecules. *The colour scale* is the square root of the intensity of each harmonic, divided by the continuum wave function amplitude $\Omega^2 a(\Omega)$. The radius in the polar plot is the harmonic order (from 17th to 43rd), and the polar angle is the angle between the molecular axis and the laser polarization. Derived from [56]

unique features that are determined by the electronic structure of each molecule [56].

The experimental setup has been described previously [3, 57]. Briefly, $N_2$, $O_2$ or $CO_2$ gas was introduced into the vacuum chamber through a pulsed supersonic valve providing a gas density of about $10^{17}$ cm$^{-3}$ with a rotational temperature of about 30 K. A 30 fs duration, 800 nm laser pulse with an intensity of about $5 \times 10^{13}$ W/cm$^2$ created a superposition of rotational states, leading to periodic revivals of molecular alignment [58, 59]. The direction along which the molecular axes were aligned could be rotated by means of a half wave plate. At the peak of the rotational revival, typically 4–20 ps after the first pulse, a second, more intense, laser pulse was focused into the gas to produce high harmonics. Its intensity was approximately 1 to $2 \times 10^{14}$ W/cm$^2$. The HHG spectra were recorded by an XUV spectrometer consisting of a variable groove spacing grating and an MCP and CCD camera.

HHG spectra were obtained for molecules aligned in 5 degree steps in the range of ±100 degrees relative to the intense laser's polarization. The results are presented in Fig. 10.6. The value that is plotted is related to the measured intensity of each harmonic order, $S(\Omega)$, as follows.

In the three step model, the HHG response is a product of the ionization, the propagation, and the recombination. We lump together the first two steps into a term that describes the continuum wave function at the time of recombination, $a(\omega)$. The emitted signal $S(\Omega)$ is given by

$$S(\Omega) = \Omega^4 \left| a(\Omega) D(\Omega) \right|^2. \tag{10.4}$$

Here, $\Omega$ is the emitted XUV frequency, and $D$ is the recombination dipole matrix element. The spectral amplitude of the continuum wave function $a(\Omega)$ was determined by a separate measurement of the harmonic spectrum, $S_{ref}(\Omega)$, taken from a reference atom, argon. Rather than matching the ionization potential of the molecules with individual reference atoms, we used only argon. It was shown in

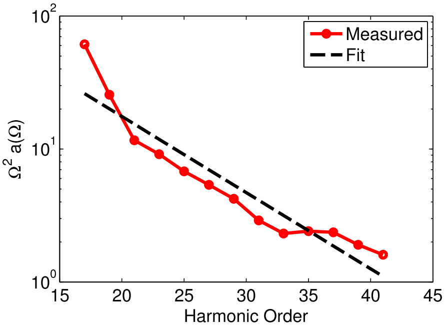

**Fig. 10.7** Calibration of the continuum wave function $\Omega^2 a(\Omega)$ amplitude from the reference argon spectrum. The HHG spectrum of argon is recorded, then is divided by the calculated recombination dipole for the Ar 3p orbital. *A straight line* fit on the semilog scale is used to normalize the spectra presented in Fig. 10.6. Derived from [56]

[36] that atoms as different as He, Ne and Ar, gave essentially the same continuum wave function amplitude,

$$a(\Omega) = \frac{S_{ref}(\Omega)^{1/2}}{\Omega^2 D(\Omega)}.$$

$D$ is evaluated using the 3p orbital of argon calculated by GAMESS [60]

The calibration $\Omega^2 a(\Omega)$ is approximately a straight line on a semilog plot [36] as shown in Fig. 10.7. We fit it to a linear function, $\Omega^2 a(\Omega) = a_1 e^{-a_2 \Omega}$, to avoid any small deviations due to structure in the argon spectrum, for example the Cooper minimum near H31 [13, 21]. Thus in Fig. 10.6 we plot $S(\Omega)^{1/2}/(\Omega^2 a(\Omega))$ .

It should be noted that the alignment dependence of the ionization probability is implicitly included in these measurements. For example, we know that $N_2$ is more easily ionized parallel to its molecular axis, whereas $CO_2$ and $O_2$ preferentially ionize at 45° [61]. In addition, all values are integrated over the distribution of molecular angles that are present in the aligned ensemble.

Each molecule is clearly distinctive, supporting our notion that the valence electronic structure of each molecule is responsible for the HHG emission. $N_2$ shows strongest emission near 0°, whereas $CO_2$ is strongest at 90°. $O_2$ shows less variation with angle, but peaks broadly near 0°.

The $CO_2$ measurements clearly show an amplitude minimum near 0° that is conventionally attributed to two-center interference in the emission process [62–64]. The position of the minimum goes to higher order with increasing molecular angles. For the simple plane wave model, destructive interference of emission from each of the oxygen atoms occurs when $\sin(k \cdot R/2) = 0$, where $R = 2.3$ Å is the distance between the oxygen atoms, and $k$ is the electron wavenumber (or momentum in atomic units) associated with the harmonic order. This can be written as $\cos\theta_{mol} = 2\pi/kR$. For $\theta_{mol} = 0$, the minimum should occur at H27, assuming the “dispersion relation” $\Omega = k^2/2 + I_p$. Measurements of the harmonic phase by the RABBITT technique [65] show a phase jump of about 2 radians in this region, and

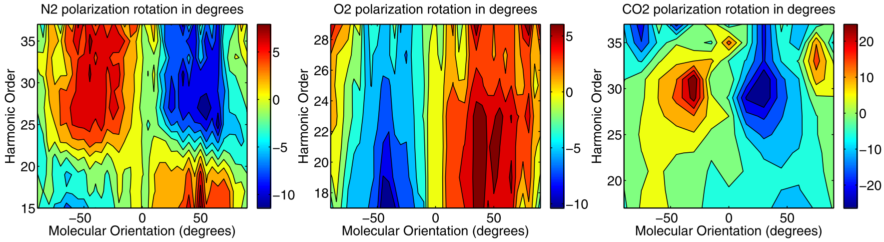

**Fig. 10.8** Measurement of the polarization rotation of harmonics produced in aligned $N_2$, $O_2$ and $CO_2$. *The colour* represents the rotation angle from vertical in degrees. Positive values (*colour red*) mean that the emitted XUV polarization has deviated from the probe laser polarization direction, in the direction of the molecular axis. For an atom, the rotation angle will be zero. To within experimental accuracy, the emitted radiation was linearly polarized. Derived from [68]

the position of the phase jump increases with molecular angle. These observations seem consistent with a two-center interference process that depends on molecular orientation. However it should be noted that there is some disagreement in the location of the interference minimum. Kanai et al. [64] observed the minimum at H25, where Vozzi et al. [63] observed it at H33. This was attributed to an intensity dependence of the interference that is not predicted by the simple model and needs further theoretical investigation. This discrepancy has now been resolved to be due to interferences between emission from different orbitals in $CO_2$, notably the HOMO and HOMO-2 when the laser field is parallel to the molecular axis [11, 66].

The $N_2$ measurements show a minimum around H25. Interestingly, this minimum does not shift to higher orders as the molecule is rotated away from the laser polarization, and even exists in unaligned molecular samples. Measurements of the harmonic phase in randomly aligned [67] and aligned $N_2$ [65] show a phase jump starting at H25, also independent of angle. All these observations are in contradiction with the simple two-center interference model, which predicts a strong angular dependence of the amplitude and phase.

In order to measure the polarization state of the emitted XUV radiation, the previous setup was modified to include a pair of silver mirror at 20° and 25° angles between the grating and the MCP [68]. These mirrors acted as an XUV polarizer [69], although not with perfect extinction. As in the previous section, the direction of the molecular axis could be controlled by waveplate HWP1, and was varied in 5° steps over the range $\pm 100°$. In addition, the polarization of both pump and probe pulses was rotated by HWP2. In a typical polarimetry measurement, the analysing polarizer is rotated; in the present case we keep the analyser fixed and rotate both the molecules and the probe laser polarization. Further details of the experimental setup can be found in Ref. [68]

The results of the polarization measurement [68] for different aligned molecules are shown in Fig. 10.8. We present the polarization direction in the laboratory frame, in which the incoming laser polarization is vertical. It is also possible to present the same data in the molecular frame (not shown). As was the case for the measurement of harmonic intensity, each molecule shows a unique signature.

The polarization rotation measured in $O_2$, shown in Fig. 10.8(b), is rather unremarkable compared with the other molecules studied. The XUV polarization is rotated in the direction of the molecular axis, but its value is largely independent of molecular angle or harmonic order. This implies that there is no change of sign of the recombination dipole vector components.

The polarization measurements for $CO_2$ molecules are shown in Fig. 10.8(c). This molecule shows the greatest amount of polarization rotation of the three molecules studied. It is significant that the direction is opposite to that of $O_2$. The maximum rotation coincides with the harmonic order previously associated with a minimum in the harmonic spectrum in $CO_2$. Thus, polarimetry allows us to attribute this amplitude minimum to the component of the dipole moment that is parallel to the generating laser polarization.

The $N_2$ molecules in Fig. 10.8(a) show a change in behaviour between low and high harmonic orders. For the low harmonics, the polarization direction rotates in the direction of the laser polarization. The high harmonics show a rotation in the opposite direction. This remarkable feature was recently confirmed by other measurements [70]. The point at which the rotation changes sign is around H21, and this point is largely independent of angle. This almost coincides with the order at which the emission amplitude has a minimum, H25, which is also independent of angle. The minimum in amplitude indicates a minimum in the recombination dipole matrix element. The change in polarization direction indicates a sign change in the perpendicular component of the vector recombination dipole. This would seem to be contrary to the conclusion from the experimental measurements in which it seems that the perpendicular component changes sign. However the experimental results are consistent with the model interpretation where the parallel component changes sign. Since the experiment only measures the angle of the polarization modulo $2\pi$, what seems like a rotation of say 20° could in reality be a rotation of $-160°$. Thus the amplitude and polarization measurements contain complementary information about the recombination dipole.

## 10.5 Tomographic Imaging of a Molecular Orbital

Some interpretations of quantum mechanics hold that wave functions do not exist in reality, and that only the square of the wave function has any meaning. Nevertheless scientists use the concept of wave functions to help visualize the electronic structure of atoms and molecules [71]. In particular, single-electron molecular orbital wave functions are mathematical constructs that are used to describe the multi-electron wave function of molecules. The highest lying orbitals are of particular interest since they are responsible for the chemical properties of molecules. Yet they are elusive to observe experimentally. Using the highly non-linear process of tunnel ionization in an intense, femtosecond infrared laser field, we selectively remove the highest occupied molecular orbital electron, and then recombine this electron about 2 fs later. This results in the emission of high harmonics from the molecule that contain information about the shape of the molecular orbital. By aligning the gas phase molecule at a set of angles, the resulting HHG spectra can be tomographically inverted to yield the two-dimensional orbital wave function. The coherent interference between the free electron wave function and the molecular orbital wave function, a form of homodyne detection, enables us to see the actual wave function, not its square [3].

Only a few methods can currently "see" the highest molecular orbitals—electron momentum spectroscopy (EMS) [72] and scanning tunneling microscopy (STM) [73–75]. These experiments have provided valuable data that can be compared with various theoretical descriptions, e.g Hartree-Fock, Kohn-Sham and Dyson orbitals [76]. Other techniques such as electron scattering or x-ray diffraction measure the total electron density of the molecule, not specific orbitals. Yet it is the frontier orbitals that give the molecule its chemical properties.

HHG is usually thought of as a source of attosecond XUV photons that can be used to probe ultrafast dynamics. We will use molecular HHG not as a probe, but as a sensitive signature of the molecular orbit structure. It has been suggested that the HHG spectrum from molecules might contain information on the internuclear separation [77, 78]. We will show that, by recording a series of HHG spectra from molecules held at fixed angles, it is possible to tomographically reconstruct the shape of the highest electronic orbital, including the relative phase of the wave function.

It is possible to align gas-phase molecules in space by means of non-resonant laser fields [79]. It has been demonstrated that medium-sized molecules can be held in space in three dimensions using elliptically polarized fields [80]. Field-free alignment has been demonstrated using an adiabatic pulse that abruptly turns off [81], and by short pulses that produce rotational wavepackets that periodically rephase [82]. Furthermore, polar molecules can be oriented in a particular direction [83, 84].

A proof-of-principle experiment was performed on a simple molecule, $N_2$, whose highest occupied molecular orbital (HOMO) is known to be a $2p\sigma_g$ orbital. More precisely, the $2p\sigma_g$ is the Dyson orbital that is associated with ionization of $N_2$ to the ground state of the cation. The next highest orbitals, about 1 eV below the HOMO, are $2p\pi_u$, and so have distinctly different symmetry. Evidence for emission from lower orbitals of $N_2$ has been reported [85].

In the experiment [3] the output of a Ti:Sapphire laser system (10 mJ, 27 fs, 800 nm, 50 Hz) was split into two pulses with a variable delay. The first pulse served to produce a rotational wave packet in the nitrogen gas emanating from a nozzle [82]. Its intensity was low enough ($< 10^{14}$ W/cm$^2$) that no harmonics were generated. The second laser pulse ($3 \times 10^{14}$ W/cm$^2$) produced the HHG spectrum that was detected with an XUV spectrometer.

During the rotational revivals, there were two distinct times at which the molecules have a clear spatial orientation—parallel (4.094 ps) and perpendicular (4.415 ps) to the laser polarization [82]. We used the parallel alignment time, and rotated the molecular axis relative to the polarization of the HHG pulse using a half-wave plate. In order to remove the sensitivity of the XUV spectrometer and other systematic effects, we have normalized the $N_2$ spectrum to that of argon. Argon has nearly the same ionization potential as nitrogen, and so the ionization process will be very similar. The calibration used is similar to that shown in Fig. 10.7.

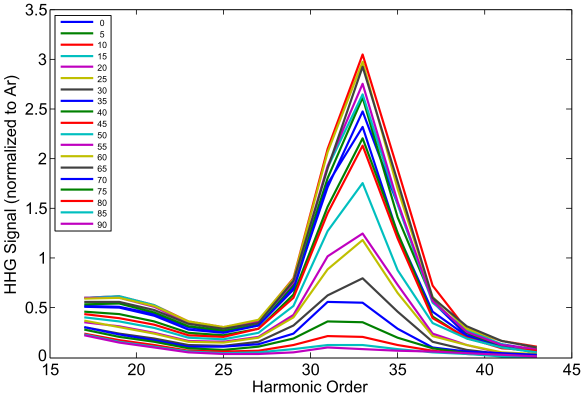

**Fig. 10.9** High harmonic spectra of $N_2$ recorded at 5 degree increments for the angle between the molecular axis and the laser polarization direction. Each spectrum has been divided by the linearized argon reference spectrum to remove the amplitude of the recolliding wave packet. Derived from [56]

It has been shown that the three-step model for HHG [4] can be factorized into three terms [3, 15, 43, 44]. The harmonic signal will be proportional to the square of the dipole moment induced by the returning electron,

$$\mathbf{d} = \langle \psi_m(\mathbf{r}) | \mathbf{r} | \psi_e(\mathbf{r}) \rangle. \tag{10.5}$$

Here, $\psi_m$ is the molecular orbital wave function that was ionized. The outgoing electronic wave function is a complicated Volkov wave [86], but upon return $\psi_e(\mathbf{r})$ is described by a plane wave, $e^{ikx}$. More recent models have described the continuum state as a field-free scattering state. For the sake of simplicity in analysis, we will use the plane wave model. For each harmonic number $n$, we know that the corresponding momentum $k_n$ of the returning electron is $\hbar k_n = \sqrt{2m_e(nE_L - E_i)}$.

In Fig. 10.9 we show the high harmonic spectra recorded for aligned $N_2$ molecules, divided by the argon reference signal. The molecular axis has been rotated by 5 degrees between each measurement, and the fact that each spectral amplitude is different indicates the high degree of alignment achieved.

We now go on to show that the HHG signal can be tomographically inverted to yield a picture of the molecular orbital. We will assume that the laser polarization axis is in the $x$ direction, and that the molecular axis is at an angle $\theta$ with respect to $x$. For a non-planar molecule, this angle can be replaced by the Euler angles that will completely describe its orientation. We then use a rotated version of the wave function to represent the rotated molecule, $\psi_m(\mathbf{r}, \theta)$.

From Eq. (10.5) the dipole magnitude for the $n$-th harmonic can be written as an integral,

$$\mathbf{d}_n(\theta) = \int_{-\infty}^{\infty} \int_{-\infty}^{\infty} \psi_m(\mathbf{r}, \theta) \mathbf{r} e^{ik_n x} dx dy \tag{10.6a}$$

$$= FT \left\{ \int_{-\infty}^{\infty} \psi_m(\mathbf{r}, \theta) \mathbf{r} dy \right\} \tag{10.6b}$$

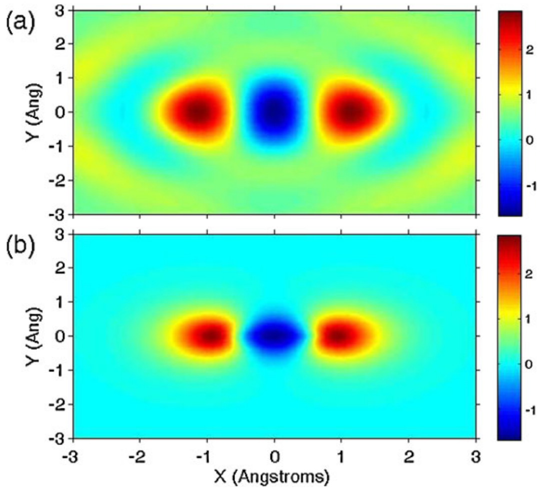

**Fig. 10.10** (**a**) Highest occupied molecular orbital of $N_2$ as reconstructed using the high harmonic emission in Fig. 10.9. Assumptions about a phase jump near H25 and the polarization of the emission were made. (**b**) *Ab initio* calculation of the $3\sigma_g$ orbital of $N_2$. Derived from [3]

where we have dropped the third dimension $z$ for clarity. Note that **d** is a complex vector. It can be seen that this is a spatial Fourier transform in direction $x$ of an integral along $y$ of the molecular wavefunction.

The Fourier Slice Theorem [87] shows that the Fourier transform of a projection $P$ is equal to a cut at angle $\theta$ through the two-dimensional transform $F$ of the object. This is the essence of computed tomography based on the inverse Radon transform. Our dipole is the Fourier transform of a projection of the wave function, and so the parallel between the HHG process and computed tomography is uncanny.

The result of the tomographic deconvolution is shown in Fig. 10.10. The upper panel shows the experimental reconstruction, while the lower panel is the calculated shape of the $3\sigma_g$ orbital of $N_2$. Note that the colour scale includes both positive and negative values, indicating that we are measuring a wave function as opposed to the square of the wave function. The lobes at which the wave function passes through zero are well reproduced in the reconstruction.

It may seem that quantum mechanics forbids the observation of a wave function [71]. Whereas a single quantum system cannot be observed, an ensemble of quantum systems can be measured [88]. In addition, we effectively record the dipole matrix elements of a transition between two states of the system, Eq. (10.5). Since this is an expectation value of a Hermitian operator, it is an observable in quantum mechanics. We determine the molecular orbital wave function to within an arbitrary phase, with a normalization constant and a DC term, because it is effectively a homodyne measurement; part of the bound state electron wave function is removed by the laser, and then interferes with itself when it recombines.

The spatial resolution is limited to the electron wavelength corresponding to the highest attainable harmonic order. This is determined by the ionization potential $E_i$ and the intensity at which the molecule ionizes (not necessarily the peak laser intensity). For $I = 2 \times 10^{14}$ W/cm$^2$ at 800 nm wavelength, $nE_L = 38$ eV and $\lambda_e = 2$ Å. By going to longer wavelengths, such as through the use of optical parametric amplifiers, the cutoff energy is increased. For a laser wavelength of 1.8 µm, $\lambda_e = 0.9$ Å,

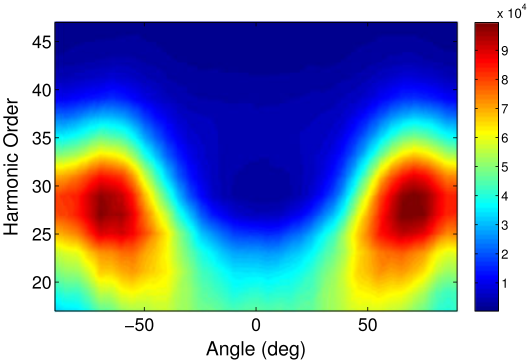

**Fig. 10.11** High harmonic intensities for aligned $CO_2$ molecules using elliptically polarized laser radiation. The HHG signal was obtained for ellipticities for which the spectrum was reduced by $1/3$, averaged for both left and right ellipticities. This removes the effect of the nodal planes, since the recolliding wave packet returns at an angle to the nodal plane

and the highest spatial frequency component is $k = 7\ \mathring{A}^{-1}$. This is usually sufficient to resolve typical molecular orbitals [89].

The mathematical underpinnings of this reconstruction technique have been studied in more detail in [90, 91]. Rather than considering just a single molecular orbital, the more detailed approaches consider all electrons in the system to be indistinguishable, leading to concepts of Dyson orbitals and electron exchange upon recombination. These factors have an effect on the interpretation of the reconstruction, and lead to even better agreement between theory and experiment than shown in Fig. 10.10.

## 10.6 Tomographic Reconstruction of $CO_2$ Molecular Orbital

In the previous section we showed how one can create an image of a single molecular orbital wave function in the case of $N_2$ molecules. In this section we use a similar approach to a different molecule, $CO_2$. The shape and symmetry of the $CO_2$ HOMO ($\Pi_g$) is quite different from that of the $N_2$ molecule ($\Sigma_g$). The presence of nodal planes in $\Pi_g$ symmetry makes the interpretation more difficult. In addition, for a perfectly aligned molecule at 0 degrees, the ionization along the nodal plane direction results in a node in the outgoing continuum electron wave function. Therefore the returning continuum wave function will have a nodal plane, violating the assumption of a plane wave. This violation does not occur at angles other than 0 and 90 degrees. Nevertheless, it makes the reconstruction more complicated. A reconstruction of the HOMO of $CO_2$ was performed by Vozzi et al. [92].

To get around this difficulty, we performed an experiment with aligned $CO_2$ molecules using elliptically polarized 800 nm laser radiation [93]. High harmonic spectra were recorded for each molecular alignment angle, at a range of laser ellipticities. The HHG signal was obtained for ellipticities for which the spectrum was reduced by $1/3$, averaged for both left and right ellipticities. The experimental results are shown in Fig. 10.11.

As was the case for the reconstruction of the $N_2$ wave function, the HHG spectrum from $CO_2$ was divided by the HHG spectrum from reference argon atoms.

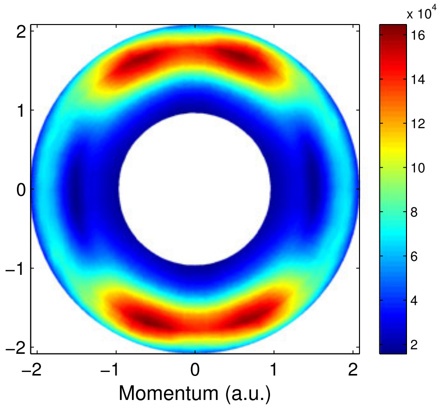

**Fig. 10.12** Polar plot of the square root of the $CO_2$ signal from Fig. 10.11, normalized by the HHG signal from reference argon atoms. The image has been symmetrized into all four polar quadrants

This results in a normalized HHG signal. We plot the square root of this normalized signal in Fig. 10.12. This figure is somewhat different than the results shown in Fig. 10.6 for $CO_2$ which used linearly polarized light to generate HHG. In the present case using elliptical light, there is a small minimum at 90 degrees, whereas for linear light, there is a maximum at 90 degrees. This is probably related to the nodal plane in the HOMO wave function.

We will reconstruct the bound state wave function from this data, using a slightly different procedure than in the previous section. As before, the HHG signal is written as a product of a recombination moment times the amplitude of the recolliding electron wave packet, $a$.

$$S(\omega;\theta) = \left|a(\omega)\right|^2 \left|d_L(\omega;\theta)\right|^2$$

Previously we used the length form of the transition dipole matrix element between the bound state and the continuum wave function which is approximated by a plane wave.

$$d_L(\omega;\theta) = \left\langle \Psi(r;\theta) \middle| r \middle| k(\omega) \right\rangle \tag{10.7}$$

$$= \int dr \Psi(r;\theta) r e^{ikr} \tag{10.8}$$

Instead we use the velocity form of the matrix element,

$$d_v(\omega;\theta) = \Omega \left\langle \Psi(r;\theta) \middle| \hat{p} \middle| k(\omega) \right\rangle \tag{10.9}$$

$$= \Omega \int dr \Psi(r;\theta) \hat{p} e^{ikr} \tag{10.10}$$

$$= \Omega k \Psi(p;\theta) \tag{10.11}$$

since the momentum operator $\hat{p}$ operating on a plane wave of momentum $k$ returns $k$. Therefore the velocity form of the transition dipole matrix element is proportional to the bound state wave function in momentum space. This is just the

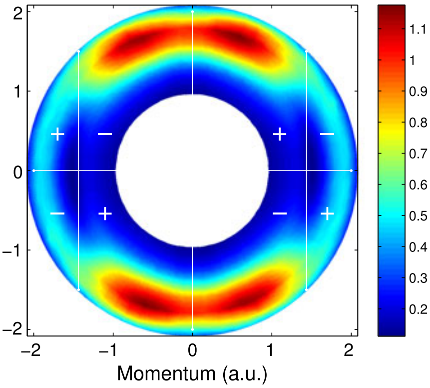

**Fig. 10.13** Polar plot of the square root of the $CO_2$ signal from Fig. 10.11, normalized by the HHG signal from reference argon atoms, as shown in Fig. 10.12. The values have been multiplied by ±1 in different parts of the image, corresponding to where phase jumps are assumed to occur

spatial Fourier transform of the real space wave function. This velocity form approach has the advantage that it does not require knowledge of the two polarization components of the emission; this is also a shortcoming, since it does not take into account the extra information provided by the polarization. In the present experiment using elliptically polarized light, we do not have the polarization information of the XUV radiation.

We lack one vital piece of information, namely the phase of the XUV emission. As in the case of $N_2$, we will assume that the wave function is real, so that the phase will be either 0 or $\pi$. Therefore we multiply the square root of the normalized signal (Fig. 10.12) by ±1, as shown in Fig. 10.13. We assume a phase jump near H25, where there is a minimum in the emission (see Fig. 10.12). We also assume a phase jump at angle 0, 90, 180 and 270 degrees. This assumption is based on the assumption of the symmetry of the bound state wave function. By taking the inverse Fourier transform of Fig. 10.13, we arrive at the spatial image of the bound state wave function of $CO_2$, shown in Fig. 10.14. This indeed looks like the expected $\Pi_g$ orbital of $CO_2$.

The problem with this orbital reconstruction is the assumption of phase jumps. By assuming phase jumps at each quadrant, we have in effect determined the symmetry of the wave function. If we do not put in a phase jump at 90 and 270 degrees, we can reconstruct an orbital with $\Pi_u$ symmetry instead. In fact, if you replace the experimental data in Fig. 10.12 with the value 1 everywhere, but make the same phase change assumptions, then you still obtain an orbital that looks like a $\Pi_g$ wave function. Therefore we should be very suspicious when someone uses this approach to reconstruct the $CO_2$ HOMO wave function.

## 10.7 Following a Chemical Reaction Using High-Harmonic Spectroscopy

Simultaneous imaging of the geometric and electronic structure of a molecule as it undergoes a chemical reaction is one of the main goals of modern ultrafast sci-

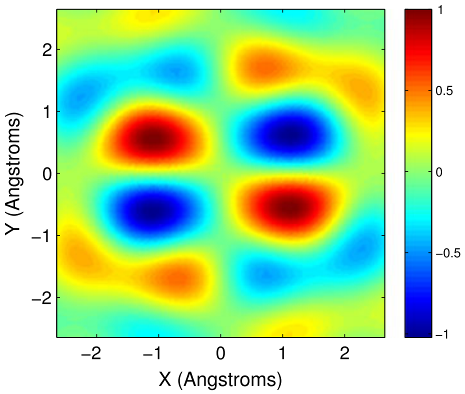

**Fig. 10.14** An inverse Fourier transform of the velocity-form transition moments in Fig. 10.13 is shown. This should be a reconstructed image of the $CO_2$ HOMO wave function. It indeed shows the expected $\Pi_g$ symmetry. Unfortunately, the symmetry of this image is determined by the assumptions of phase jumps that were made in Fig. 10.13. Other assumptions of phase jumps would lead to different symmetries

ence. Techniques based on diffraction [94, 95] measure the position of the atoms within the molecule with high accuracy but are much less sensitive to the electronic structure of the molecule, particularly the valence shell in which the chemical transformations originate. A new complementary approach exploits the rescattering of an electron removed from the molecule by a strong laser field to measure the structure of the molecule [96]. The associated recollision also leads to high-harmonic generation that encodes the structure of the orbital to which the electron recombines [3, 97]. So far, these methods have only been applied to the electronic ground state of molecules [35, 98–100]. Ultrafast dynamics in molecules occur predominantly in excited electronic states which can only be prepared in small fractions when multiphoton processes need to be avoided.

We extend high-harmonic spectroscopy from probing static molecular structure to probing photochemical dynamics. Using the impulsive photodissociation of molecular bromine, we show that the electromagnetic interference between high harmonics generated from the molecular ground state and the excited state occurs on the attosecond timescale. The coherent addition of the emitted radiation results in high visibility of the excited state dynamics despite the low excited state fraction.

The photorecombination step in high-harmonic generation is essentially a time reversal of photoionization. Before describing the HHG experiment, it is useful to compare and contrast the two approaches. In femtosecond photoelectron spectroscopy, single-photon absorption creates a photoelectron which encodes information of the molecule's electronic structure in its spectrum [101, 102]. In femtosecond high-harmonic spectroscopy, similar detailed information [23, 43] is carried in the emitted photon. In photoelectron spectroscopy, different initial (neutral) and final (ionic) electronic states are distinguished through the photoelectron energy. In high-harmonic spectroscopy, the broadband recolliding electron wave can only re-

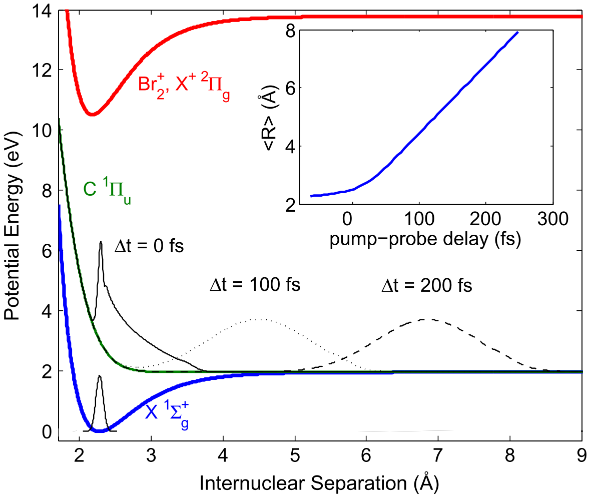

**Fig. 10.15** Potential energy curves of Br$_2$ (X $^1\Sigma_g^+$ ground state and C $^1\Pi_{1u}$ excited state) and Br$_2^+$ (X$^+$ $^2\Pi_g$ ground state). The shape of the nuclear wave packet in the excited state after selected delays $\Delta t$ is also shown. The wave packets were obtained by numerical propagation assuming a 40 fs excitation pulse centered at 400 nm. *The inset* shows the expectation value of the internuclear separation as a function of the pump-probe delay. Derived from [105]

combine to vacant states, which are selectively created by the tunnel ionization step. Tunnel ionization is exponentially sensitive to the binding energy of each ionization channel. The simultaneous measurement of a broad photon spectrum and the selection of the probed state by tunneling both point to greater simplicity for high-harmonic spectroscopy. However, the emitted photons originating from different initial electronic states overlap spectrally, adding an undesirable complexity to the interpretation of high-harmonic spectroscopy. We show that this apparent complexity becomes an advantage as the unexcited molecules can serve as a local oscillator against which we measure the excited state dynamics. Just as in a radio receiver, the local oscillator makes a weak signal that would be otherwise difficult to observe, readily visible. Moreover, the coherent detection provides a high sensitivity to the phase of the radiation, which reflects the evolution of the ionization potential along the dissociation coordinate.

The experimental setup consists of a chirped-pulse amplified titanium-sapphire femtosecond laser system, a high-harmonic source chamber equipped with a pulsed valve and an XUV spectrometer. The laser system provides 800 nm pulses of 32 fs duration (FWHM). The laser beam is split into two parts of variable intensities using a half-wave plate and a polarizer. The minor part of the energy is sent through a 2:1 telescope and used to generate 400 nm radiation in a type I BBO of 60 μm thickness. The major part is sent through a computer-controlled delay stage and is recombined with the 400 nm radiation using a dichroic beam splitter. The combined beams are focused into the chamber using a $f = 50$ cm spherical mirror.

High-order harmonics are generated in a supersonic expansion of Br$_2$ seeded in 2 bars of helium. The helium carrier gas is sent through liquid Br$_2$ kept at room temperature. Bromine molecules are excited by single-photon absorption at 400 nm to the repulsive C $^1\Pi_{1u}$ state (see Fig. 10.15) and high harmonics are generated in the strong 800 nm field. The focus of both beams is placed ~1 mm before the pulsed molecular jet expanding through a nozzle of 250 μm diameter. This setup

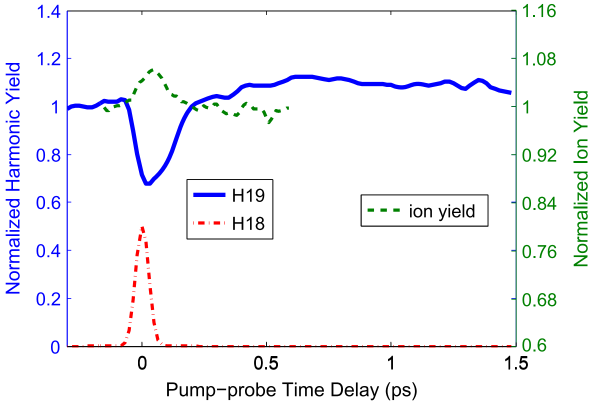

**Fig. 10.16** Intensity of harmonics 19 (*full line*) and 18 (*dash-dotted line*) from excited bromine molecules as a function of the delay between a 400 nm pump pulse and a perpendicularly polarized 800 nm pulse generating high harmonics (*left-hand axis*). The temporal overlap of 400 and 800 nm pulses leads to the emission of even order harmonics, like H18. The total ion yield (*dotted line*, *right-hand axis*) shown as *dashed line* was measured under identical conditions but with higher statistics. Derived from [105]

minimizes the effect of phase-mismatch and reabsorption of the high-harmonic radiation and leads to the observation of the single-molecule response [103]. The typical pulse energies of 1.5 mJ (800 nm) and 5 μJ (400 nm) result in intensities of $1.5 \times 10^{14}$ W/cm$^2$ (800 nm) and $5 \times 10^{11}$ W/cm$^2$, the 400 nm beam having half the diameter of the 800 nm beam. The total number of produced ions is measured by a wire mesh located 10 cm below the nozzle orifice. We have verified that the response of the ion detector was linear. The high-harmonics are spectrally resolved using an aberration-corrected XUV grating and imaged by a micro-channel plate detector backed with a phosphor screen using a charge-coupled device camera. The harmonic intensities are extracted by integrating the images spatially and spectrally.

Figure 10.15 shows the relevant potential energy curves of $Br_2$ and $Br_2^+$. Single-photon excitation at 400 nm from the X $^1\Sigma_g^+$ ground state leads almost exclusively to the repulsive C $^1\Pi_{1u}$ state which dissociates into two bromine atoms in their ground spin-orbit state ($^2P_{3/2}, m_J = 1/2$) [104]. The figure also shows the shape of the vibrational wave function in the ground state and the calculated nuclear wave packet on the excited state surface at selected delays Δt after excitation by a 40 fs pump pulse centered at 400 nm. The $^2\Pi_{3/2g}$ ground state curve of $Br_2^+$ is also shown to illustrate the variation of the ionization potential with the internuclear distance.

Figure 10.16 shows the observed harmonic and ion signals in a pump-probe experiment with perpendicular polarizations. The power of H19 decreases during the excitation, reaches a minimum after the peak of the 400 nm pulse and then recovers to its initial power level. In contrast, the ion yield increases, reaching its maximum after the peak of the 400 nm pulse and subsequently decreases to its initial level. The maximum increase in ion yield amounts to 7 % whereas the harmonic signal is depleted by up to 30 %. The signal of H19 and the ion yield have been normalized to unity at negative delays. This signal level corresponds to all molecules being in the ground electronic state. Temporal overlap of the 800 nm and 400 nm pulses leads to the appearance of even-order harmonics [106] which provide the time origin and a high-order cross-correlation ($\sim$50–60 fs).

When $Br_2$ is excited to the C $^1\Pi_{1u}$ state, the ionization potential for the removal of the most weakly bound electron is reduced from 10.5 to 7.5 eV, explaining the observed increase in the ion yield. The rising part of the ion yield curve reflects the build-up of the excited state population during the excitation pulse. As $Br_2$ dissociates along the repulsive C $^1\Pi_{1u}$ state, the ionization potential increases from 7.5 to 11.8 eV, resulting in a decreasing ionization rate of the excited state. Since the ionization rate increases at early delays, one might expect that the harmonic yield would also increase. However, the opposite is observed. Moreover, the variation of the harmonic signal is much larger than that of the ion signal and exceeds the excitation fraction by a factor of 2.

These results clearly demonstrate a destructive interference between harmonics emitted by the excited molecules and those emitted by the ground state molecules. Destructive interference is the origin of the opposite behavior of ion and harmonic yield. Since the interference between the excited and unexcited molecules involves both phase and amplitude of emission, it is impossible to determine both parameters with a single measurement. In the following section, we utilize a different geometry in order to extract both amplitude and phase.

## 10.8 Transient Grating High Harmonic Spectroscopy

The strong-field approach to molecular imaging relies on an intense femtosecond laser field ($\sim 10^{14}$ W/cm$^2$) to extract an electron wave packet from one of the valence orbitals and drive it back to interfere with the initial bound electronic state. When the electron recombines with the parent ion, it emits extreme-ultraviolet (XUV) radiation in a train of attosecond pulses. All molecules in the sample radiate coherently with the electric field of the driving laser in a phase-matched process. In this section, we demonstrate how HHG can be applied to observe a chemical reaction in real time [89, 107].

We form a sinusoidal grating of excited molecules using two pump beams that cross in the medium, as shown in Fig. 10.17. Horizontal planes of excited molecules alternate with planes of unexcited molecules. We generate high harmonics from this grating with a delayed 800 nm laser pulse (probe). The zero time-delay and the cross-correlation time of 50 fs is monitored through the appearance of even-order harmonics.

From the zeroth and first order diffracted signals, we can uniquely extract the harmonic amplitudes $d_e/d_g$ and phases $|\phi_e - \phi_g|$ of the excited state relative to the ground state (where $d_{g,e}$ and $\phi_{g,e}$ are the harmonic amplitudes and phases of the ground (g) and excited (e) states). We show the experimentally determined values in Fig. 10.18, when the pump and probe pulses are parallel (a) or perpendicular (b).

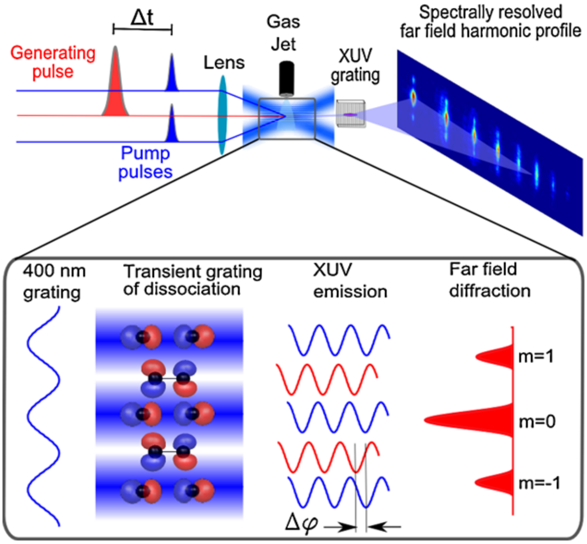

**Fig. 10.17** Schematic of the transient grating excitation geometry. Two 400 nm pump pulses set up a transient grating of excitation in the molecular beam. A delayed 800 nm pulse generates high harmonics. The periodic modulation of the high harmonic amplitude and phase in the near field results in first order diffraction in the far field. Derived from [107]

The different time evolution for the amplitude and the phase is striking. While the phase reaches its asymptotic value after ≈150 fs, the amplitude takes more than 300 fs. It is also striking that the time response of the amplitude changes with the relative polarization of the excitation and harmonic generation pulse. In contrast, while the time-dependent phase is different for the different polarizations, it reaches the same asymptotic value at the same time delay. We will first concentrate on the phase, then discuss the amplitude.

The phase of high-harmonic radiation has two main contributions: (1) The electron and the ion accumulate a relative phase between the moment of ionization and recombination. The phase shift between the same harmonic order $q$ being emitted by two electronic states differing in ionization potential by $\Delta I_p$ can be expressed as $\Delta\phi_q \approx \Delta I_p \bar{\tau}_q$, [25] where $\bar{\tau}_q$ is the average transit time of the electron in the continuum. (2) When the electron recombines, the transition moment imposes an amplitude and a phase on the radiation [11, 23]. The first contribution depends on the electron trajectory (determined by the laser parameters) and the ionization potential. The second contribution characterises the electronic structure of the molecule. It depends on the emitted photon energy and the angle of recombination in the molecular frame [3].

The time evolution of the reconstructed phase in Fig. 10.18 can be split in two regions: the first 150 fs, where the phase undergoes a rapid variation, and the subsequent flat region where the phase is independent of the relative polarizations. The rapid variation of the phase reflects the fast variation of the ionization potentials with delay. The strong dependence of the phase on the relative polarizations (Fig. 10.18(a) vs. (b)) also shows that the phase traces the evolution of the electronic structure of the molecule as it dissociates. This variation occurs because the electrostatic potential into which the electron recombines changes significantly. At asymptotic delays we measure Br atoms relative to ground state molecules. The

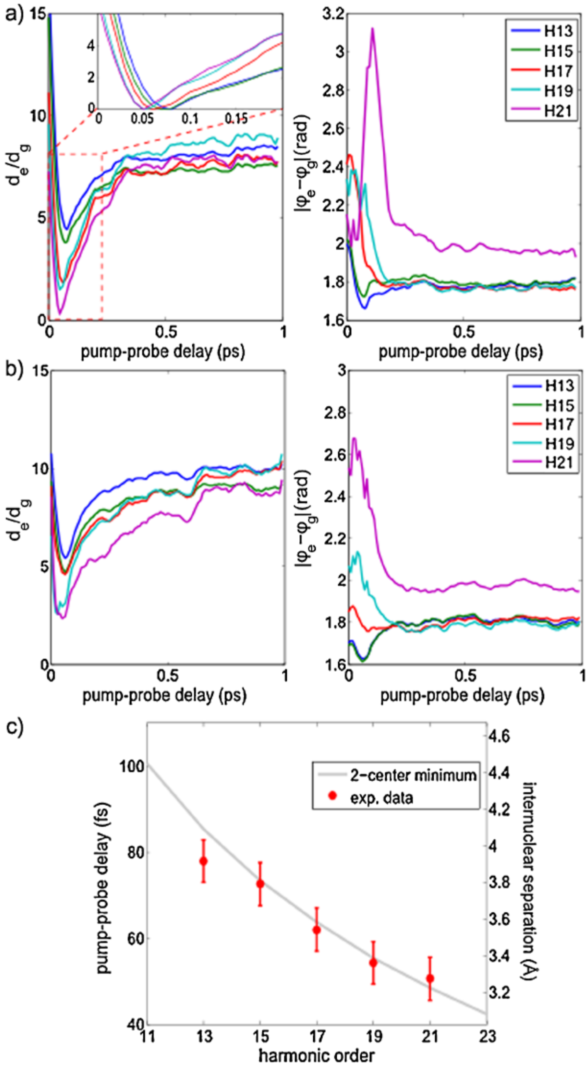

**Fig. 10.18** Reconstruction of high harmonic amplitude and phase. (**a**) shows the reconstructed amplitude (*left*) and phase (*right*) of the excited state emission relative to the ground state, for parallel pump-probe polarizations. (**b**) is the same as (**a**) except the pump-probe polarizations are perpendicular. (**c**) shows the measured internuclear separations as determined by the two-center interference condition for each harmonic order. Derived from [107]

phase shift is independent of the direction of recombination, consistent with the fact that $Br_2$ dissociates into atoms in the $|m_j| = 1/2$ magnetic sub-level [104]. The phase shift is 1.8 radians for H13. Using the relation $\Delta\phi_q \approx \Delta I_p \bar{\tau}_q$, we obtain $\Delta I_p = 1.3$ eV, in good agreement with the known ionization potentials of $Br_2$ and Br.

We now turn to the temporal evolution of the amplitudes. The odd harmonics go through a deep minimum at an early time delay that depends on the harmonic order (see inset of Fig. 10.18(a)). The minimum occurs between 51 ± 5 fs (H21) and 78 ± 5 fs (H13). It measures the stretching of the orbital as the molecule dissociates. Since at early delays the ionization step selects molecules lying parallel to the laser field, we obtain almost identical results in both polarizations. When the electron recombines to the initial state, its de Broglie wavelength $\lambda_q$ can destructively interfere with the initial state wave function. Destructive interference occurs when $R = (2n+1)/2\lambda_q$ ($n$ integer) in the case of a $\sigma_u$ orbital [24]. Using $n = 1$ and the relation $\Omega = k^2/2$ between the photon energy $\Omega$ and the electron momentum $k$, we translate the minimum of H21 to a bond length of 3.3 Å and that in H13 to 3.9 Å—in good agreement with wave packet calculations. Thus, we trace the bond length as a function of time using quantum interference.

As the molecule dissociates, additional minima corresponding to destructive interference with $n > 1$ could be expected. Instead, we observe a slow rise of the amplitude. At delays larger than 150 fs, the four valence molecular orbitals of $Br_2$ formed from the 4p atomic orbitals of Br become nearly degenerate and high-harmonic generation becomes essentially atomic in character. In this regime, the gerade or ungerade states of the ion are degenerate—there should be no quantum interference in ionization nor in recombination. Consequently, it is only the propagation of the electron in the laser field that is affected by the second atom. For perpendicularly polarised pump and probe beams, the interaction of the ionised electron with the neighbouring atom is maximized since the electron trajectory between tunneling and recollision lies in the plane of the disc of dissociating atoms. The slower recovery of the amplitude in Fig. 10.18(b) reflects this fact. This property of high-harmonic spectroscopy is analogous to XAFS (extended X-ray absorption fine structure) and may be useful to probe the chemical environment of a low-$I_p$ species (e.g. a molecule in a helium droplet).

Time-resolved photoelectron measurements of the dissociation of $Br_2$ have beautifully demonstrated how the binding energies shift as the atoms move apart. In Refs. [102, 108, 109] the time delay for the appearance of an atomic-like photoelectron spectrum was determined to lie in the range of 40–85 fs. In high-harmonic spectroscopy, the recollision of the returning photoelectron is sensitive to the electronic structure of the molecule rather than to the binding energy of individual orbitals. The minima between 50–80 fs show that the electron recombines to a 2-centre molecular wave function. The absence of such minima in the range of 100–150 fs suggests that at longer delays the recombination of the electron has become essentially atomic. An analogous transition between two- and one-center signatures has recently been observed in core-shell photoionization of a static molecule [110].

Looking forward, measuring the amplitude and phase of the photorecombination moment relative to a fully characterised ground state reference [3] will allow the dynamic imaging of orbitals in a chemical reaction. The unique properties of high-harmonic spectroscopy will lead to other applications in femtochemistry, reaching from simple dissociation dynamics, to proton transfer, to non-adiabatic reaction dynamics, to complex photochemical processes. For example, the change in electronic structure associated with the crossing of a conical intersection [111, 112] will be mapped into the harmonic radiation. In all these cases, the sensitivity of high harmonic spectroscopy to the electronic structure will provide new insight.

## 10.9 Conclusions

We hope that the reader will recognize the potential of this new spectroscopic technique called high harmonic spectroscopy. We have shown that we can observe electronic structure in atoms and molecules, that we can reconstruct a single molecular orbital wave function, and that we can follow a chemical reaction. As we gain experience with this technique, we learn its advantages and disadvantages. We have recently observed that high harmonic spectroscopy with molecules larger than diatomics is sensitive to the electronic state of the excited molecule, rather than the motion of a nuclear wavepacket; we have shown this for $NO_2$ [113] and recently for $SO_2$, and we believe that this may be a general property. We expect that the advent of mid-infrared few-cycle laser sources will also help in applying high harmonic spectroscopy to larger molecules with low ionization potentials.

## References

1. E. Goulielmakis, M. Schultze, M. Hofstetter, V.S. Yakovlev, J. Gagnon, M. Uiberacker, A.L. Aquila, E.M. Gullikson, D.T. Attwood, R. Kienberger, F. Krausz, U. Kleineberg, Single-cycle nonlinear optics. Science **320**(5883), 1614 (2008). doi:10.1126/science.1157846
2. S. Baker, J.S. Robinson, C.A. Haworth, H. Teng, R.A. Smith, C.C. Chirila, M. Lein, J.W.G. Tisch, J.P. Marangos, Science **312**, 424 (2006)
3. J. Itatani, J. Levesque, D. Zeidler, H. Niikura, H. Pépin, J.C. Kieffer, P.B. Corkum, D.M. Villeneuve, Nature (London) **432**, 867 (2004)
4. P.B. Corkum, Phys. Rev. Lett. **71**, 1994 (1993)
5. H. Niikura, F. Légaré, R. Hasbani, A.D. Bandrauk, M.Y. Ivanov, D.M. Villeneuve, P.B. Corkum, Nature **417**, 917 (2002)
6. Committee on AMO2010, *Controlling the Quantum World: The Science of Atoms, Molecules and Photons* (The National Academies Press, Washington, 2006)
7. J. Berkowitz, *Photoabsorption, Photoionization and Photoelectron Spectroscopy* (Academic Press, New York, 1979)
8. K. Kimura, S. Katsumata, Y. Achiba, T. Yamazaki, S. Iwata, *Handbook of HeI Photoelectron Spectra* (Japan Scientific Societies Press, Tokyo, 1981)
9. U. Becker, D.A. Shirley (eds.), *VUV and Soft X-Ray Photoionization* (Plenum, New York, 1996)
10. R. Torres, N. Kajumba, J.G. Underwood, J.S. Robinson, S. Baker, J.W.G. Tisch, R. de Nalda, W.A. Bryan, R. Velotta, C. Altucci, I.C.E. Turcu, J.P. Marangos, Phys. Rev. Lett. **98**(20), 203007 (2007)
11. O. Smirnova, Y. Mairesse, S. Patchkovskii, N. Dudovich, D. Villeneuve, P. Corkum, M.Y. Ivanov, Nature (London) **460**(7258), 972 (2009)
12. H.J. Wörner, J.B. Bertrand, D.V. Kartashov, P.B. Corkum, D.M. Villeneuve, Nature (London) **466**, 604 (2010)
13. H.J. Wörner, H. Niikura, J.B. Bertrand, P.B. Corkum, D.M. Villeneuve, Phys. Rev. Lett. **102**(10), 103901 (2009). doi:10.1103/PhysRevLett.102.103901
14. A.-T. Le, R.R. Lucchese, M.T. Lee, C.D. Lin, Phys. Rev. Lett. **102**(20), 203001 (2009)
15. M.V. Frolov, N.L. Manakov, T.S. Sarantseva, M.Y. Emelin, M.Y. Ryabikin, A.F. Starace, Phys. Rev. Lett. **102**(24), 243901 (2009). doi:10.1103/PhysRevLett.102.243901
16. M. Lewenstein, P. Balcou, M.Y. Ivanov, A. L'huillier, P.B. Corkum, Phys. Rev. A **49**, 2117 (1994). doi:10.1103/PhysRevA.49.2117

17. O. Smirnova, M. Spanner, M. Ivanov, Phys. Rev. A **77**(3), 033407 (2008). doi:10.1103/PhysRevA.77.033407
18. Z.B. Walters, S. Tonzani, C.H. Greene, J. Phys. B **40**(18), 277 (2007)
19. T. Morishita, A.-T. Le, Z. Chen, C.D. Lin, Phys. Rev. Lett. **100**(1), 013903 (2008). doi:10.1103/PhysRevLett.100.013903
20. M.F. Ciappina, C.C. Chirila, M. Lein, Phys. Rev. A **75**(4), 043405 (2007). doi:10.1103/PhysRevA.75.043405
21. J.W. Cooper, Phys. Rev. **128**, 681 (1962)
22. J.S. Robinson, C.A. Haworth, H. Teng, R.A. Smith, J.P. Marangos, J.W.G. Tisch, Appl. Phys. B **85**, 525 (2006)
23. H.J. Wörner, H. Niikura, J.B. Bertrand, P.B. Corkum, D.M. Villeneuve, Phys. Rev. Lett. **102**(10), 103901 (2009)
24. M. Lein, N. Hay, R. Velotta, J.P. Marangos, P.L. Knight, Phys. Rev. Lett. **88**, 183903 (2002)
25. T. Kanai, E.J. Takahashi, Y. Nabekawa, K. Midorikawa, Phys. Rev. Lett. **98**, 153904 (2007)
26. P. Colosimo, G. Doumy, C.I. Blaga, J. Wheeler, C. Hauri, F. Catoire, J. Tate, R. Chirla, A.M. March, G.G. Paulus, H.G. Muller, P. Agostini, L.F. Dimauro, Nat. Phys. **4**, 386 (2008)
27. J.A.R. Samson, W.C. Stolte J. Electron Spectrosc. Relat. Phenom. **123**, 265 (2002)
28. A. L'Huillier, P. Balcou, Phys. Rev. Lett. **70**, 774 (1993)
29. S. Minemoto, T. Umegaki, Y. Oguchi, T. Morishita, A.-T. Le, S. Watanabe, H. Sakai, Phys. Rev. A **78**(6), 061402 (2008)
30. H.G. Muller, Phys. Rev. A **60**, 1341 (1999)
31. D.J. Tannor, *Introduction to Quantum Mechanics: A Time-Dependent Perspective* (University Science Books, Sausalito, 2007)
32. A.F. Starace, Theory of atomic photoionization, in *Handbuch der Physik*, vol. 31, ed. by W. Mehlhorn (Springer, Berlin, 1981), pp. 1–121
33. P.M. Paul, E.S. Toma, P. Breger, G. Mullot, F. Augé, P. Balcou, H.G. Muller, P. Agostini, Science **292**, 1689 (2001)
34. Y. Mairesse, A. de Bohan, L.J. Frasinski, H. Merdji, L.C. Dinu, P. Monchicourt, P. Breger, M. Kovacev, R. Taieb, B. Carré, H.G. Muller, P. Agostini, P. Salières, Science **302**, 1540 (2003)
35. C. Vozzi, F. Calegari, E. Benedetti, J.-P. Caumes, G. Sansone, S. Stagira, M. Nisoli, R. Torres, E. Heesel, N. Kajumba, J.P. Marangos, C. Altucci, R. Velotta, Phys. Rev. Lett. **95**(15), 153902 (2005). doi:10.1103/PhysRevLett.95.153902
36. J. Levesque, D. Zeidler, J.P. Marangos, P.B. Corkum, D.M. Villeneuve, Phys. Rev. Lett. **98**(18), 183903 (2007). doi:10.1103/PhysRevLett.98.183903
37. R.A. Ganeev, J. Phys. B, At. Mol. Phys. **40**, R213 (2007). doi:10.1088/0953-4075/40/22/R01
38. M.V. Frolov, N.L. Manakov, A.F. Starace, Phys. Rev. A **82**(2), 023424 (2010). doi:10.1103/PhysRevA.82.023424
39. A.D. Shiner, B. Schmidt, C. Trallero-Herrero, H.J. Wörner, S. Patchkovskii, P.B. Corkum, J.-C. Kieffer, F. Légaré, D.M. Villeneuve, Nat. Phys. **7**(7), 464 (2011)
40. M. Giguère, B.E. Schmidt, A.D. Shiner, M.-A. Houle, H.C. Bandulet, G. Tempea, D.M. Villeneuve, J.-C. Kieffer, F. Légaré, Opt. Lett. **34**(12), 1894 (2009)
41. B.E. Schmidt, P. Béjot, M. Giguère, A.D. Shiner, C. Trallero-Herrero, É. Bisson, J. Kasparian, J. Wolf, D.M. Villeneuve, J. Kieffer, P.B. Corkum, F. Légaré, Appl. Phys. Lett. **96**(12), 121109 (2010). doi:10.1063/1.3359458
42. B.E. Schmidt, A.D. Shiner, P. Lassonde, J.-C. Kieffer, P.B. Corkum, D.M. Villeneuve, F. Légaré, Opt. Express **19**, 6858 (2011)
43. A.-T. Le, R.R. Lucchese, S. Tonzani, T. Morishita, C.D. Lin, Phys. Rev. A **80**(1), 013401 (2009). doi:10.1103/PhysRevA.80.013401
44. M.V. Frolov, N.L. Manakov, T.S. Sarantseva, A.F. Starace, J. Phys. B, At. Mol. Opt. Phys. **42**(3), 035601 (2009)
45. L.D. Landau, E.M. Lifshitz, *Quantum Mechanics Non-relativistic Theory*, 3rd edn. Course of Theoretical Physics, vol. 3 (Pergamon, New York, 1977), p. 553

46. K.-N. Huang, W.R. Johnson, K.T. Cheng, At. Data Nucl. Data Tables **26**(1), 33 (1981). doi:10.1016/0092-640X(81)90010-3
47. M. Kutzner, V. Radojević, H.P. Kelly, Phys. Rev. A **40**(9), 5052 (1989). doi:10.1103/PhysRevA.40.5052
48. A. Fahlman, M.O. Krause, T.A. Carlson, A. Svensson, Phys. Rev. A **30**(2), 812 (1984). doi:10.1103/PhysRevA.30.812
49. U. Becker, D. Szostak, H.G. Kerkhoff, M. Kupsch, B. Langer, R. Wehlitz, A. Yagishita, T. Hayaishi, Phys. Rev. A **39**(8), 3902 (1989). doi:10.1103/PhysRevA.39.3902
50. M.Y. Amusia, J.-P. Connerade, Rep. Prog. Phys. **63**, 41 (2000)
51. R. Torres, N. Kajumba, J.G. Underwood, J.S. Robinson, S. Baker, J.W.G. Tisch, R. de Nalda, W.A. Bryan, R. Velotta, C. Altucci, I.C.E. Turcu, J.P. Marangos, Phys. Rev. Lett. **98**, 203007 (2007)
52. X.X. Zhou, X.M. Tong, Z.X. Zhao, C.D. Lin, Phys. Rev. A **71**, 061801 (2005)
53. X.X. Zhou, X.M. Tong, Z.X. Zhao, C.D. Lin, Phys. Rev. A **72**, 033412 (2005)
54. T. Morishita, A.-T. Le, Z. Chen, C.D. Lin, Phys. Rev. Lett. **100**, 013903 (2008)
55. M. Lein, J. Phys. B **40**, 135 (2007)
56. Y. Mairesse, J. Levesque, N. Dudovich, P.B. Corkum, D.M. Villeneuve, J. Mod. Opt. **55**(16), 2591 (2008)
57. J. Itatani, D. Zeidler, J. Levesque, M. Spanner, D.M. Villeneuve, P.B. Corkum, Phys. Rev. Lett. **94**, 123902 (2005)
58. F. Rosca-Pruna, M.J.J. Vrakking, Phys. Rev. Lett. **87**, 153902 (2001)
59. P.W. Dooley, I. Litvinyuk, K.F. Lee, D.M. Rayner, M. Spanner, D.M. Villeneuve, P.B. Corkum, Phys. Rev. A **68**, 023406 (2003)
60. M.W. Schmidt, K.K. Baldridge, J.A. Boatz, S.T. Elbert, M.S. Gordon, J.J. Jensen, S. Koseki, N. Matsunaga, K.A. Nguyen, S. Su, T.L. Windus, M. Dupuis, J.A. Montgomery J. Comput. Chem. **14**, 1347 (1993)
61. D. Pavicic, K.F. Lee, D.M. Rayner, P.B. Corkum, D.M. Villeneuve, Phys. Rev. Lett. **98**, 243001 (2007)
62. M. Lein, N. Hay, R. Velotta, J.P. Marangos, P.L. Knight, Phys. Rev. A **66**(2), 023805 (2002)
63. C. Vozzi, F. Calegari, E. Benedetti, J.-P. Caumes, G. Sansone, S. Stagira, M. Nisoli, R. Torres, E. Heesel, N. Kajumba, J.P. Marangos, C. Altucci, R. Velotta, Phys. Rev. Lett. **95**, 153902 (2005)
64. T. Kanai, S. Minemoto, H. Sakai, Nature **435**, 470 (2005)
65. W. Boutu, S. Haessler, H. Merdji, P. Breger, G. Waters, M. Stankiewicz, L.J. Frasinski, R. Taieb, J. Caillat, A. Maquet, P. Monchicourt, B. Carre, P. Salieres, Nat. Phys. **4**(7), 545 (2008)
66. H.J. Wörner, J.B. Bertrand, P. Hockett, P.B. Corkum, D.M. Villeneuve, Phys. Rev. Lett. **104**(23), 233904 (2010). doi:10.1103/PhysRevLett.104.233904
67. H. Wabnitz, Y. Mairesse, L.J. Frasinski, M. Stankiewicz, W. Boutu, P. Breger, P. Johnsson, H. Merdji, P. Monchicourt, P. Salières, K. Varju, M. Vitteau, B. Carré, Eur. Phys. J. D **40**, 305 (2006)
68. J. Levesque, Y. Mairesse, N. Dudovich, H. Pépin, J.-C. Kieffer, P.B. Corkum, D.M. Villeneuve, Phys. Rev. Lett. **99**(24), 243001 (2007)
69. P. Antoine, B. Carré, A. L'Huillier, M. Lewenstein, Phys. Rev. A **55**(2), 1314 (1997)
70. Y. Mairesse, S. Haessler, B. Fabre, J. Higuet, W. Boutu, P. Breger, E. Constant, D. Descamps, E. Mével, S. Petit, P. Salières, New J. Phys. **10**, 025028 (2008)
71. W.H.E. Schwarz, Angew. Chem., Int. Ed. Engl. **45**, 1508 (2006)
72. C.E. Brion, G. Cooper, Y. Zheng, I.V. Litvinyuk, I.E. McCarthy, Chem. Phys. **270**, 13 (2001)
73. M.F. Crommie, C.P. Lutz, D.M. Eigler Science **262**, 218 (1993)
74. L.C. Venema, J.W.G. Wildöer, J.W. Janssen, S.J. Tans, H.L.J.T. Tuinstra, L.P. Kouwenhoven, C. Dekker, Science **283**, 52 (1999)
75. J.I. Pascual, J. Gómez-Herrero, C. Rogero, A.M. Baró, D. Sánchez-Portal, E. Artacho, P. Ordejón, J.M. Soler, Chem. Phys. Lett. **321**, 78 (2000)
76. E.K.U. Gross, R.M. Dreizler, *Density Functional Theory* (Plenum Press, New York, 1995)

77. M. Lein, N. Hay, R. Velotta, J.P. Marangos, P.L. Knight, Phys. Rev. Lett. **88**, 183903 (2002)
78. M. Lein, P.P. Corso, J.P. Marangos, P.L. Knight, Phys. Rev. A **67**, 23819 (2003)
79. H. Stapelfeldt, T. Seideman, Rev. Mod. Phys. **75**, 543 (2003)
80. J.J. Larsen, K. Hald, N. Bjerre, H. Stapelfeldt, T. Seideman, Phys. Rev. Lett. **85**, 2470 (2000)
81. J.G. Underwood, M. Spanner, M.Y. Ivanov, J. Mottershead, B.J. Sussman, A. Stolow, Phys. Rev. Lett. **90**, 223001 (2003)
82. P.W. Dooley, I.V. Litvinyuk, K.F. Lee, D.M. Rayner, M. Spanner, D.M. Villeneuve, P.B. Corkum, Phys. Rev. A **68**, 23406 (2003)
83. H. Sakai, S. Minemoto, H. Nanjo, H. Tanji, T. Suzuki, Phys. Rev. Lett. **90**, 083001 (2003)
84. L. Holmegaard, J.H. Nielsen, I. Nevo, H. Stapelfeldt Phys. Rev. Lett. **102**, 023001 (2009)
85. B.K. McFarland, J.P. Farrell, P.H. Bucksbaum, M. Gühr, Science **322**, 1232 (2008)
86. M. Lewenstein, P. Balcou, M.Y. Ivanov, A. L'Huillier, P.B. Corkum, Phys. Rev. A **49**, 2117 (1994)
87. A.C. Kak, M. Slaney, *Principles of Computerized Tomographic Imaging* (SIAM, Philadelphia, 2001)
88. A. Royer Found. Phys. **19**, 3 (1989)
89. V.-H. Le, A.-T. Le, R.-H. Xie, C.D. Lin, Phys. Rev. A **76**(1), 013414 (2007)
90. S. Patchkovskii, Z. Zhao, T. Brabec, D.M. Villeneuve, Phys. Rev. Lett. **97**, 123003 (2006)
91. S. Patchkovskii, Z. Zhao, T. Brabec, D.M. Villeneuve, J. Chem. Phys. **126**, 114306 (2007)
92. C. Vozzi, M. Negro, F. Calegari, G. Sansone, M. Nisoli, S. De Silvestri, S. Stagira, Nat. Phys. **7**, 822 (2011)
93. Y. Mairesse, N. Dudovich, J. Levesque, M.Y. Ivanov, P.B. Corkum, D.M. Villeneuve, New J. Phys. **10**, 025015 (2008)
94. R. Neutze, R. Wouts, D. van der Spoel, E. Weckert, J. Hajdu, Nature **406**(6797), 752 (2000)
95. H. Ihee, V.A. Lobastov, U.M. Gomez, B.M. Goodson, R. Srinivasan, C.-Y. Ruan, A.H. Zewail, Science **291**(5503), 458 (2001). doi:10.1126/science.291.5503.458
96. M. Meckel, D. Comtois, D. Zeidler, A. Staudte, D. Pavičić, H.C. Bandulet, H. Pépin, J.C. Kieffer, R. Dörner, D.M. Villeneuve, P.B. Corkum, Science **320**, 1478 (2008)
97. S. Baker, J.S. Robinson, M. Lein, C.C. Chirila, R. Torres, H.C. Bandulet, D. Comtois, J.C. Kieffer, D.M. Villeneuve, J.W.G. Tisch, J.P. Marangos, Phys. Rev. Lett. **101**(5), 053901 (2008)
98. T. Kanai, S. Minemoto, H. Sakai, Nature (London) **435**(7041), 470 (2005)
99. N.L. Wagner, A. Wüest, I.P. Christov, T. Popmintchev, X. Zhou, M.M. Murnane, H.C. Kapteyn, Proc. Natl. Acad. Sci. USA **103**(36), 13279 (2006). doi:10.1073/pnas.0605178103
100. W. Li, X. Zhou, R. Lock, S. Patchkovskii, A. Stolow, H.C. Kapteyn, M.M. Murnane, Science **322**(5905), 1207 (2008)
101. L. Nugent-Glandorf, M. Scheer, D.A. Samuels, A.M. Mulhisen, E.R. Grant, X. Yang, V.M. Bierbaum, S.R. Leone, Phys. Rev. Lett. **87**, 193002 (2001)
102. P. Wernet, M. Odelius, K. Godehusen, J. Gaudin, O. Schwarzkopf, W. Eberhardt, Phys. Rev. Lett. **103**(1), 013001 (2009). doi:10.1103/PhysRevLett.103.013001
103. A.D. Shiner, C. Trallero-Herrero, N. Kajumba, H.-C. Bandulet, D. Comtois, F. Légaré, M. Giguere, J.-C. Kieffer, P.B. Corkum, D.M. Villeneuve, Phys. Rev. Lett. **103**(7), 073902 (2009)
104. T.P. Rakitzis, T.N. Kitsopoulos, J. Chem. Phys. **116**(21), 9228 (2002)
105. H.J. Wörner, J.B. Bertrand, P.B. Corkum, D.M. Villeneuve, Phys. Rev. Lett. **105**(10), 103002 (2010). doi:10.1103/PhysRevLett.105.103002
106. H. Eichmann, A. Egbert, S. Nolte, C. Momma, B. Wellegehausen, W. Becker, S. Long, J.K. McIver, Phys. Rev. A **51**(5), 3414 (1995)
107. H.J. Wörner, J.B. Bertrand, D.V. Kartashov, P.B. Corkum, D.M. Villeneuve, Nature **466**(7306), 604 (2010). doi:10.1038/nature09185
108. L. Nugent-Glandorf, M. Scheer, D.A. Samuels, A.M. Mulhisen, E.R. Grant, X. Yang, V.M. Bierbaum, S.R. Leone, Phys. Rev. Lett. **87**(19), 193002 (2001). doi:10.1103/PhysRevLett.87.193002

109. L. Nugent-Glandorf, M. Scheer, D.A. Samuels, V.M. Bierbaum, S.R. Leone, J. Chem. Phys. **117**, 6108 (2002)
110. B. Zimmermann, D. Rolles, B. Langer, R. Hentges, M. Braune, S. Cvejanovic, O. Geszner, F. Heiser, S. Korica, T. Lischke, A. Reinkoster, J. Viefhaus, R. Dörner, V. McKoy, U. Becker, Nat. Phys. **4**(8), 649 (2008). doi:10.1038/nphys993
111. W. Domcke, D.R. Yarkony, H. Köppel (eds.), *Conical Intersections: Electronic Structure, Dynamics and Spectroscopy*. Adv. Ser. in Phys. Chem., vol. 15 (World Scientific, Singapore, 2004)
112. P.H. Bucksbaum, Science **317**(5839), 766 (2007)
113. H.J. Wörner, J.B. Bertrand, B. Fabre, J. Higuet, H. Ruf, A. Dubrouil, S. Patchkovskii, M. Spanner, Y. Mairesse, V. Blanchet, E. Mével, E. Constant, P.B. Corkum, D.M. Villeneuve, Science **334**, 208 (2011)

# Chapter 11
# Attosecond Molecular Spectroscopies with XUV Harmonic Radiation

**R. Guichard, J. Caillat, S. Haessler, Z. Diveki, T. Ruchon, P. Salières, R. Taïeb, and A. Maquet**

**Abstract** When irradiated by an intense pulse of an infrared (IR) laser, molecules emit a coherent radiation composed of a frequency comb of harmonics of the pump laser frequency, ranging from ultraviolet (UV) up to soft X-rays. These harmonics are emitted during extremely short time windows, within the attosecond range. The properties of harmonic emission are of much interest when applied to issues of relevance to AMOP (Atomic, Molecular and Optical Physics) and they have opened a new domain of investigation in the emerging field of attophysics. In the spectral domain, analyzing high harmonic spectra provides original information on the electronic structure of the outer orbitals that are active in the generation process. In the time domain, the use of attosecond pulses of Extreme Ultra-Violet (XUV) harmonics within a pump-probe scheme opens unique opportunities to develop a new time-resolved spectroscopy of transient excited molecular states. In this review, we shall report on recent advances in the field and we shall address several issues of interest with the objective to go beyond the "proof-of-principle" demonstrations that have been reported so far.

## 11.1 Introduction

Uncovering time-dependent aspects of chemical reactivity with unprecedented time resolution, in the attosecond range, has become achievable through the recent advent of harmonic-based sources of XUV radiation. In this context, two distinct kinds of applications of these new sources have been explored so far. In a chronological

---

R. Guichard · J. Caillat · R. Taïeb · A. Maquet (✉)
Laboratoire de Chimie Physique-Matière et Rayonnement (LCPMR), UPMC Université Paris 6, UMR 7614, 11 rue Pierre et Marie Curie, 75231 Paris Cedex 05, France
e-mail: alfred.maquet@upmc.fr

Z. Diveki · T. Ruchon · P. Salières
Service des Photons, Atomes et Molécules, CEA-Saclay, IRAMIS, 91191 Gif-sur-Yvette, France

S. Haessler
Photonics Institute, Vienna University of Technology, Gusshausstrasse 27/387, 1040 Vienna, Austria

L. Plaja et al. (eds.), *Attosecond Physics*, Springer Series in Optical Sciences 177,
DOI 10.1007/978-3-642-37623-8_11,

order, the first one has been the detailed analysis of the harmonic spectra generated by aligned molecular systems. This provides valuable information about the electronic molecular states (dominantly the outer valence states) involved into the generation process. Moreover, the analysis of such time-resolved harmonic spectra is expected to provide new insights in the dynamics of the electronic processes at work when generated by a system in the course of a chemical change. The second one is the use of harmonics as a photoionization probe, to extend the XUV measurements performed with synchrotron sources. A typical example includes the study of the resonances embedded within the atomic or molecular continuum: synchrotron measurements display the spectral signatures of autoionizing states as well as of the so-called shape resonances. As we shall report, a most interesting feature of harmonic-based measurements is that they give direct access to the temporal characterization of these phenomena.

In the context of this class of attosecond-resolved measurements performed with coherent XUV radiation, it turns out that the intensities of the harmonic lines can be measured quite straightforwardly, while the harmonic phases are a priori less accessible. The precise determination of these latter provides the key to explore the time domain, as their energy derivative gives access to characteristic time delays, with attosecond time resolution, in the system under consideration. Several techniques have been implemented so far to measure the harmonic phases. Among them, we shall focus the presentation on a multicolor IR-XUV photoionization scheme dubbed RABBIT (Reconstruction of Attosecond Beating By Interference of Two-photon transitions) technique [1–3]. In the following, we will describe some of the recent advances that have been achieved with the help of this technique, both from the theory and experimental standpoints.

Focusing first on the characterization of High Harmonic Generation (HHG) spectra in aligned molecules, it is well established now that the phases and intensities of the spectral components are very sensitive probes of the molecular states involved in the generation process. The first milestone in this direction has been the "tomographic imaging" of a molecular *orbital*, derived from the analysis of the harmonic emission by aligned $N_2$ molecules with different orientations of the internuclear axis with respect to the polarization of the pump field. This procedure, based on the analysis of the scaled harmonic intensities with assumptions for the harmonic phases, has initially permitted to image the $\sigma_g$ HOMO (Highest Occupied Molecular Orbital) which is dominantly involved in the generation process [4]. A more detailed characterization of such HHG emission, including the determination of the spectral phases, has revealed that the HHG process results in fact from a delicate combination of contributions originating from both the $\sigma_g$ HOMO and from the nearest underlying orbital $\pi_u$ HOMO-1 [5]. In specific laser conditions, i.e. when a particular laser intensity is chosen, disentangling the contributions of each orbital to the harmonic signal is made possible as the net result of all phase contributions is close to $\pi/2$, therefore encoding them in the real and imaginary parts of the harmonic dipole, respectively. However, when the pump laser intensity is varied, this distinction becomes unclear as the mixing of the two contributions appears to be spectrally and intensity dependent [6].

Still regarding HHG in aligned molecules, another important question has emerged about the possibility to *control* the attosecond emission by changing the molecular response. The basic idea relies on the dependence of the harmonic generation on the orientation of the molecular axis with respect to the polarization of the pump laser. For instance, in two-center systems, interference phenomena are expected to take place depending on the internuclear distance, the molecular alignment and the de Broglie wavelength of the recombining electron. It is expected that these parameters govern the harmonic intensities and phases, allowing a pulse shaping of the attosecond emission in given spectral regions. Interferences resulting from multi-orbital contributions could also allow such pulse shaping. This has been demonstrated in the test case of the linear $CO_2$ molecule [7].

A second (more recent) field of investigations deals with the molecular response to the attosecond pulses of harmonic XUV radiation generated in an auxiliary gas jet. Clearly, under such conditions, molecules can experience various excitation processes, including ionization and dissociation. However, given the unique temporal properties of harmonic pulses, the possibility arises to uncover the dynamics of excited "vibronic" molecular states. This implies to disentangle the electronic and nuclear degrees of freedom in reactive species. We shall show below that the RABBIT technique is again an efficient tool to achieve this goal [8, 9].

Central as an investigation tool in all the above listed topics is the RABBIT technique. It has been implemented in several experiments to realize the combined measurements of the phases and amplitudes of harmonic signals. For the sake of completeness, we shall devote Sect. 11.2 to a brief description of the technique. In Sect. 11.3, we shall discuss how molecular data can be extracted from the analysis of harmonic spectra generated in aligned molecules. Subsections will concentrate on multichannel (or multi-orbital) contributions and on the control of harmonic emission in the time domain. The main features of the recently developed attosecond XUV spectroscopy of molecular excited states will be outlined in Sect. 11.4, with applications to the relation between RABBIT phases and the timing of photoelectron emission in near-threshold transitions. The chapter will end in Sect. 11.5 with a brief discussion of the perspectives opened by these recent advances.

## 11.2 RABBIT Analysis of Harmonic Spectra

The RABBIT technique has been designed first with the objective to measure the relative phases of consecutive odd harmonics, as generated in a system with central symmetry. It is based on the multicolor ionization of an auxiliary atomic or molecular gas sample, in the simultaneous presence of an attenuated beam of the pump IR laser with frequency $\omega_L$ together with a comb of its odd XUV harmonics with frequencies $\Omega_{\pm} = (2q \pm 1)\omega_L$, [1–3]. In these conditions, the photoionization spectrum displays equidistant lines labelled $\ldots, H_{2q-1}, H_{2q+1}, \ldots$, that are associated to the absorption of single harmonic photons, and intermediate sidebands

$\ldots, \mathrm{SB}_{2q}, \ldots$ resulting from the exchange of one additional IR photon. In the moderate IR intensity regime considered, the sidebands result from two-photon IR-XUV ionization transitions.

Still in this regime, it turns out that two distinct quantum paths contribute dominantly to the formation of a given sideband $\mathrm{SB}_{2q}$: (i) sequential absorption of $\mathrm{H}_{2q-1}$ and of the fundamental and (ii) sequential absorption of $\mathrm{H}_{2q+1}$, followed by the stimulated emission of the fundamental. Two other quantum paths also participate which are associated to transitions with reversed time-ordering but, in the context considered here, their contributions are much smaller [1–3]. The dominant XUV-IR processes correspond to two-photon "Above-Threshold Ionization" (ATI) transitions. Then, RABBIT measurements consist in monitoring the variations of the sideband magnitude when the IR-XUV delay $\tau$ is varied. One shows that, as a result of the two quantum paths interferences', it can be written under the generic form below, which evidences that each sideband signal $S_{2q}$ oscillates periodically as a function of $\tau$:

$$S_{2q} = \alpha + \beta \cos(2\omega_L \tau + \Delta\phi_\Omega + \Delta\theta) \tag{11.1}$$

where $\alpha$ and $\beta$ are real quantities, $\Delta\phi_\Omega = \phi_{2q+1} - \phi_{2q-1}$ is the difference between the intrinsic phases of the two consecutive harmonics and $\Delta\theta$ is a contribution that is characteristic of the ionized system. The latter term originates from the fact that the second-order transition amplitudes associated to ATI transitions are complex numbers, with phases that depend on the quantum path followed by the system to reach the sideband. Thus when clocked against the IR laser cycle, the periodic variations of the cosine term in the expression Eq. (11.1) contains both the phase informations about the harmonics as well as intrinsic molecular data contained in the $\Delta\theta$ term. If the continuum structure of the system under study is smooth, $\Delta\theta \approx 0$ and the measurement of the phases of the oscillations gives a direct access to the relative phases of the harmonics $\Delta\phi_\Omega$ and, by extension, to their emission time, with attosecond resolution [10, 11].

To make the connexion between phase differences and time delays clearer, it is convenient to rewrite the formula in Eq. (11.1) under the form:

$$S_{2q} = \alpha + \beta \cos\bigl[2\omega_L(\tau + \tau_{2q} + \tau_I)\bigr] \tag{11.2}$$

where $\tau_{2q} = (\phi_{2q+1} - \phi_{2q-1})/2\omega_L$ is a finite difference approximation to the group delay $GD = \partial\phi/\partial\omega$ of the harmonic radiation at the considered frequency, which is also called the "emission time", and $\tau_I = \Delta\theta/2\omega_L$ is an intrinsic time delay resulting from the analytical structure of the two-photon ATI transition amplitude in the system under consideration. For the sake of completeness we turn now to a succinct presentation of the origin of this additional phase or, equivalently, of this time delay.

The RABBIT technique is implemented with radiation fields with intensities moderate enough so that lowest-order time-dependent perturbation theory applies. Then, the structure of the relevant transition amplitudes dominantly involved in the process is the one of a second-order matrix element associated to a two-photon ATI transition . Each matrix element contains angular factors that may be complex quantities, but it turns out that they average out when performing the angular integration of the squared amplitude that is required to reproduce the photoelectron signal. The phase difference $\Delta\theta$ in Eq. (11.1) originates from the radial parts of the amplitudes, which are complex numbers for ATI transitions.

This can be seen from their expression which is associated to the transition from an initial bound state with radial component $|R_{n_i,\ell_i}\rangle$ with negative energy $\varepsilon_i$ towards a final state in the continuum $|R_{k_{2q},\ell_f}\rangle$ associated to photoelectrons in the sideband $\mathrm{SB}_{2q}$, with kinetic energy: $\varepsilon_{2q} = k_{2q}^2/2 = \varepsilon_i + 2q\omega_L$. The transition results from the sequential absorption of one harmonic XUV photon $\Omega_\pm$ followed by the exchange of the IR photon $\omega_L$. Thus, the radial component of the transition amplitude is of the following form:

$$T^{\pm}_{\ell_f,\ell,\ell_i}(\varepsilon_i + \Omega_\pm) = \sum_n \frac{\langle R_{k_{2q},\ell_f}|r|R_{n,\ell}\rangle\langle R_{n,\ell}|r|R_{n_i,\ell_i}\rangle}{\varepsilon_i + \Omega_\pm - \varepsilon_n} + \lim_{\epsilon\to 0^+}\int_0^{+\infty} d\varepsilon_k \frac{\langle R_{k_{2q}\ell_f}|r|R_{k,\ell}\rangle\langle R_{k,\ell}|r|R_{n_i,\ell_i}\rangle}{\varepsilon_i + \Omega_\pm - \varepsilon_k + i\epsilon}. \tag{11.3}$$

In this expression, we have made explicit the structure of the sum running over the whole atomic spectrum, by separating the contributions of the discrete states with negative energies $\varepsilon_n > \varepsilon_i$ and radial component $|R_{n,\ell}\rangle$ and of the states in the continuous spectrum, with energies $\varepsilon_k$ and radial wave function $|R_{k,\ell}\rangle$. We note that the angular momentum algebra imposes the selection rules $\ell = \ell_i \pm 1$ and $\ell_f = \ell_i, \ell_i \pm 2$. Also, the radial wave functions are real quantities, so that, in the first term, the sum over the discrete spectrum is also real, with denominators which stay positive as $\Omega_\pm > |\varepsilon_i|$. By contrast, the second term, i.e. the integral over the continuous spectrum, is a complex number. This is because of the presence of a pole on the positive energy real axis located at $\varepsilon_k = \varepsilon_i + \Omega_\pm$. This implies that the integral acquires an imaginary component according to the prescription:

$$\lim_{\epsilon\to 0^+}\int_{-\infty}^{+\infty} \frac{dx}{x + i\epsilon} = \mathcal{P}\int_{-\infty}^{+\infty} \frac{dx}{x} - i\pi\delta(x) \tag{11.4}$$

where the Cauchy principal part in the first term is a real quantity while the second term with the delta function is pure imaginary. The consequence is that the amplitude attached to each quantum path leading to the sideband of interest acquires a phase, i.e.

$$T^{\pm}_{\ell_f,\ell,\ell_i}(\varepsilon_i + \Omega_\pm) = \left|T^{\pm}_{\ell_f,\ell,\ell_i}(\varepsilon_i + \Omega_\pm)\right| e^{i\theta_\pm}. \tag{11.5}$$

The quantity $\Delta\theta$ introduced in Eq. (11.1) is the difference $\Delta\theta = \theta_+ - \theta_-$ between the phases of the quantum path amplitudes leading to a given sideband. As we shall show below, this analytical structure of the RABBIT amplitudes play a most important role to address several phenomena of interest in attophysics that are investigated with the help of harmonics.

## 11.3 Harmonic Emission by Aligned Molecules

### *11.3.1 Multichannel Contributions to Harmonic Emission*

Typical harmonic spectra generated in atoms exhibit the following general features: a rapid decay at the lowest orders, followed by a plateau where the harmonic intensity is roughly constant, and a final decay beyond the cutoff location. When generated in molecules, intensity minima and corresponding phase jumps appear in the emitted high-order harmonic signal. Three distinct classes of intensity minima, related either to structural or dynamical origins, have been evidenced. A representative type of "structural" minimum has been documented in two-center molecules [12, 13]. It appears when destructive interferences take place between XUV radiation emissions from each center. The harmonic frequency at which such minima are located depends on the molecular alignment with respect to the laser polarization $\theta$, as well as on the internuclear distance $R$. It can be linked to the angular dependence of the recombination dipole moment of each contributing channel [7, 14, 15] and its position does not change with the laser parameters [12, 16]. Another type of minimum is referred to as "Cooper-like", since its presence can be related to the minima observed in the photoionization cross section of the species under study. They involve destructive interferences between either distinct angular momentum components of the unbound electron wave packet when it recombines with the initial state [17], or from the nodal structure of the initial state. The position of such minima is independent of any laser parameter—especially the intensity $I_L$, [18]. A third type of minima, referred to as "dynamical", occurs when several molecular orbitals (or channels) contribute to HHG. In the specific situations where two contributions end up with a $\pi$-phase difference and thus interfere destructively, a marked minimum appears in the harmonic spectrum. Varying the driving laser parameters—either intensity or wavelength—shifts their relative phase and thus modifies the spectral position of the dynamical minima [19, 20].

The discrimination between the different types of minima is therefore based on two main experimental parameters: $\theta$ and $I_L$. The presence of a so-called dynamical minimum indicates that several orbitals, typically the valence molecular orbitals (HOMO-1, ...) lying close below the highest-occupied one (HOMO), are energetically high enough to contribute to the first stage of HHG, namely the tunneling ionization process (step (i)). During the continuum excursion (step (ii)) prior to recombination (step (iii)), they leave the molecular ion in a coherent superposition of the ground (X) and excited states (A, B, ...). All these ionization channels finally coherently contribute to the harmonic emission [20, 21] which encodes the ultrafast dynamics occurring in the molecular ion during the emission process, giving access, e.g., to the rearrangements taking place in the electronic shells within less than one laser cycle [22, 23].

Disentangling the contributions of the different ionization channels thus requires an advanced characterization of the harmonic emission, including the measurements, not only of the spectral intensities of the harmonic components [14, 15, 19, 21, 24, 26], but also of their relative phases. As explained in Sect. 11.2, this can be achieved with the help of the RABBIT technique. For the sake of illustration,

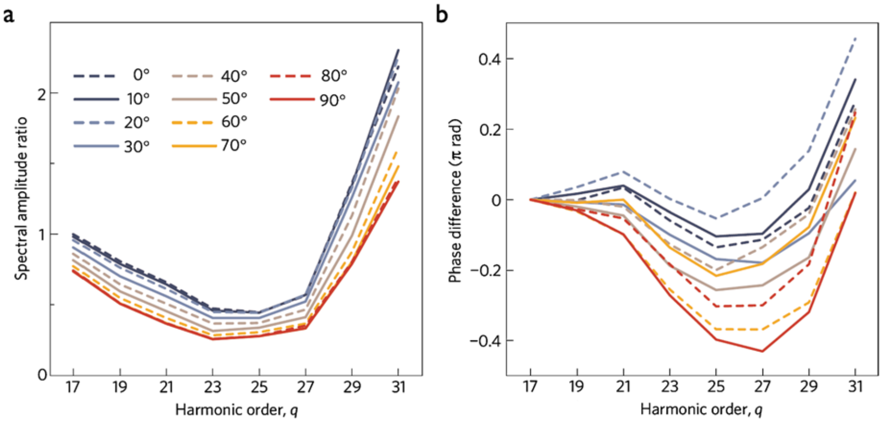

**Fig. 11.1** Experimental recombination dipole for $N_2$ molecules. Amplitude (**a**) and phase (**b**) of the complex soft-X-ray field for $N_2$ at various alignment angles normalized by that for argon. For perpendicular alignment ($\theta = 90°$), the phase decreases by $\pi/2$ between harmonic $H_{17}$ and $H_{27}$. This change gradually disappears when rotating the molecules towards parallel alignment ($\theta = 0°$). For all angles, the phase increases by $\pi/2$ from $H_{27}$ on, which might be the beginning of a larger jump not completely contained in our spectral range. The phase difference is set to 0 at the lowest harmonic order $H_{17}$

we present the measurements of the angular dependence of the harmonic yields and phases, in the specific case of $N_2$ as generating medium, at a fixed intensity ($1.2 \times 10^{14}$ W/cm$^2$) in Fig. 11.1 [5].

In that system, the global phase difference between the contributions of the HOMO and of the HOMO-1 orbitals for harmonic 25 is close to $\pi/2$ [5]. Therefore, their contributions to the normalized molecular dipole are practically disentangled in the imaginary and real part respectively. A more detailed analysis of the complex dipole structure allows the exploitation of the measured data: (i) to simulate the temporal profiles of the attosecond emission, (ii) to reconstruct the involved orbitals by a tomographic procedure, and, merging the temporal and structural aspects, (iii) to image, at the instant of recombination, the dynamical "hole" formed by the coherent ionization channels [5].

Pursuing that type of investigation by varying the laser intensity $I_L$, one can evidence the changes in HHG when exploring frequencies below and above the cut-off. Again, in the case of $N_2$, this is achieved when varying $I_L$ between $0.7 \times 10^{14}$ W/cm$^2$ (cut-off at $H_{21}$) and $1.3 \times 10^{14}$ W/cm$^2$ (cut-off at $H_{29}$). One can observe a fast variation of the harmonic phase as a function of the harmonic order, while the harmonic intensity presents a shallow $I_L$-independent minimum, as shown in Fig. 11.2 [6].

Two mechanisms were identified to explain this measured non-trivial phase evolution. First, the difference in the continuum dynamics of the two channels controls the harmonic phase in the cut-off region. Second, the remarkably fast—sub-cycle—nuclear dynamics occurring on the attosecond timescale in the A channel strongly affects its contribution to HHG. Typically, in $N_2$, the non-trivial HHG phase changes

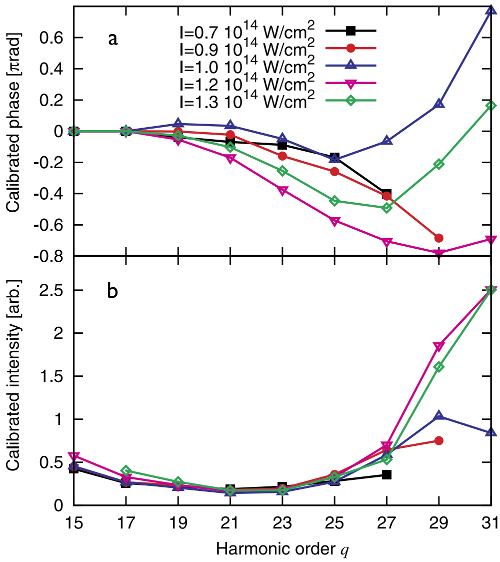

**Fig. 11.2** Pump laser intensity-dependent harmonic phases (**a**) and intensities (**b**) measured for $N_2$ at $\theta = 90°$ and respectively calibrated with Ar quantities for different driving laser intensities indicated in units of $10^{14}$ W/cm$^2$. All phases are moved to 0 at $H_{15}$

over the spectral range are attributed to variations of the X- and A-channel relative amplitudes and phases, up to a situation where the A channel contribution is significantly reduced. Therefore, the relative magnitudes of the contributions of different orbitals (here principally the HOMO and HOMO-1) to HHG can be controlled through a fine tuning of the laser intensity.

### *11.3.2 Control in Time of Harmonic Emission*

Generating attosecond pulse trains in aligned molecules does not only provide a signal that encodes information about the molecular structure and dynamics, but it also provides a mean to coherently control the attosecond time profile of the XUV emission. This has been demonstrated on the example of the attosecond high harmonic emission from aligned $CO_2$ molecules [7]. Again, much similarly to the previously discussed case of $N_2$, the laser intensity appears as a key parameter to control the different orbital contributions.

Figure 11.3 shows spectral intensities and emission times measured with the RABBIT method for $CO_2$ molecules, the internuclear axis of which has been aligned at varying angles $\theta$ with respect to the driving laser polarization direction. These data have been obtained with a driving laser pulse of 55 fs duration and an intensity of $0.95 \times 10^{14}$ W/cm$^2$. The spectral intensities show a strong dependence on alignment angle around the harmonic orders 23 and 25: for the parallel alignment ($\theta = 0°$), their intensities are suppressed by about one order of magnitude as compared to perpendicular alignment ($\theta = 90°$). Correlated with this suppression, a “hump” on the emission time curves is observed, which appears on top of the usual linear increase with harmonic order, typical for the short trajectory contribution to

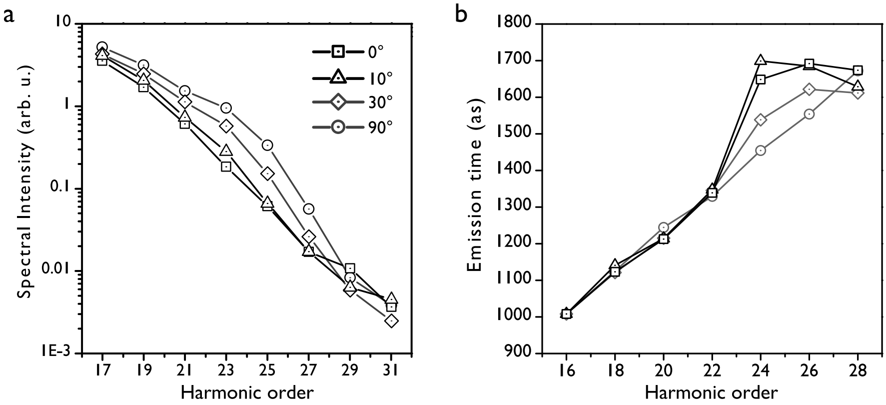

**Fig. 11.3** Spectral Intensities (**a**) and emission times (**b**) for $CO_2$ aligned at $\theta = 0°$ (*squares*), 10° (*triangles*), 30° (*diamonds*) and 90° (*circles*). These data are taken from the series of measurements also used for Fig. 3 in [7]

HHG. The emission times are the derivative of the harmonic spectral phase with respect to frequency—namely the group delay, i.e. the hump corresponds to a rapid phase increase, or a phase jump. In these experiments, the value of this phase jump has been found to be $(2.0 \pm 0.6)$ rad in a series of 8 independent measurements for $\theta = 0°$. The angle-dependent intensity minimum correlated to a phase jump is a clear sign for destructive quantum interference taking place in HHG. While in [7], structural interference appearing around harmonic photon energies of 60 eV [24, 25] has been initially proposed as the main origin, it later turned out that dynamic interference of the two channels involving the HOMO and HOMO-2 of $CO_2$ [20] is the most likely explanation of the observations.

Indeed, whatever the physical process behind, the destructive interference can however be controlled by the choice of the molecule, the alignment, and possibly the driving laser intensity. This opens the possibility to control the temporal profile of the emitted attosecond pulses. Figure 11.4(a) and (b) shows reconstructions of the temporal intensity profiles of the attosecond pulses emitted by $CO_2$ molecules aligned at varying angles $\theta = 0°, 10°, 20°, \ldots, 90°$ for two different spectral ranges. The data used for these reconstructions is from the same series of RABBIT scans, of which Fig. 11.3 shows a selection. Including only harmonic orders below the phase jump in the attosecond pulse reconstruction leads to pulses whose shape and timing are independent of the molecular alignment. They also have the same duration of 320 as FWHM and timing as the attosecond pulses generated in the ‘reference atom’ krypton, which has the same ionization potential as $CO_2$. However, including only the harmonic orders undergoing the phase jump in the attosecond pulse reconstruction, the obtained intensity profile for $\theta = 0°$ is delayed by 150 as with respect to the krypton emission, and gradually evolves in agreement with the reference atom as the molecules are rotated towards perpendicular alignment ($\theta = 90°$) [7]. The delayed emission is due to the spreading of the phase jump over several harmonic orders, which leads to the corresponding emission times being shifted to larger values.

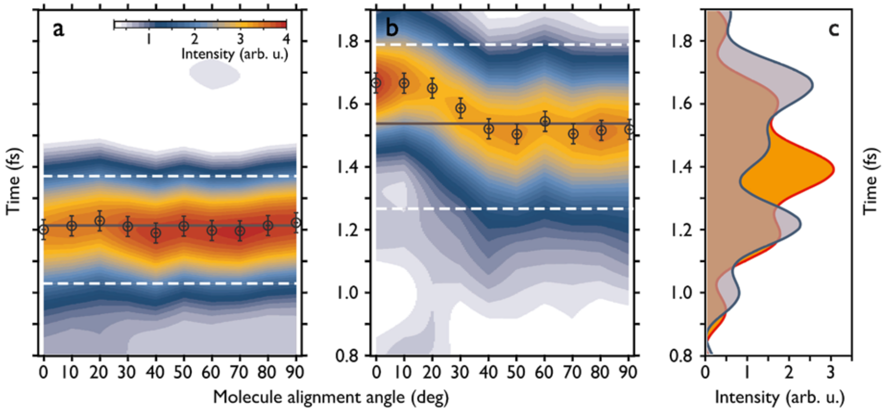

**Fig. 11.4** Intensity of a typical attosecond pulse in the generated train, mapped as a function of the alignment angle $\theta$ and time $t$, with $t = 0$ at the maximum of the generating laser field. *Circles* give the peak position of the pulse in a series of RABBIT scans, and the error bars represent the standard deviation of the emission time of sideband $SB_{16}$, indicating the error in absolute timing of the attosecond pulses. *Black and dashed white lines* indicate the positions of peak and half–maximum, respectively, of the attosecond pulse generated in krypton under the same experimental conditions. (**a**) Using harmonics $H_{17}$–$H_{23}$, located below the phase jump, and (**b**), using harmonics $H_{23}$–$H_{29}$, undergoing the phase jump. (**c**) Using harmonics $H_{17}$–$H_{29}$ and assuming constant spectral amplitudes for $\theta = 0°$ (*blue*) and $\theta = 90°$ (*orange*). (Figure adapted from [7])

Assuming that with spectral filters we are able to transform our measured spectral amplitudes into flat ones and including the whole spectral range (harmonics $H_{17}$–$H_{29}$) into the reconstruction, strongly distorted pulse time profiles are obtained, as shown in Fig. 11.4(c). For $\theta = 0°$ and thus for a strong phase jump, destructive interference between the parts of the spectrum before and after the phase jump causes a dip in the temporal intensity. This dip appears just at the temporal position where constructive interference of all spectral components builds up the pulse peak in the case of $\theta = 90°$, where there is no phase jump. Rotating the molecules can thus switch the pulse time profile from a single to a double peak structure.

What are the possible applications of this pulse shaping method? XUV pulse shaping can be achieved, of course, partly by amplitude shaping using filters or specifically designed mirrors. Including only certain harmonic orders in the APT reconstruction is already a ‘virtual’ amplitude shaping. The most interesting feature of aligned molecules as an APT source is the phase jump that can be switched on and off and placed at a chosen spectral position according to the molecule, its alignment, and possibly the driving laser intensity. The capability of adding a phase jump, close to $\pi$, at some spectral position is a central element in any pulse shaping scheme [27], which has until recently not been available in the XUV regime. Such a phase jump, placed at the transition energy, can serve to transiently enhance a resonant transition [28], which is one of the simplest coherent control schemes. Below- and above-resonance contributions to the excited state population then interfere constructively and result in so called coherent transients. The phase jump in the XUV emission from aligned molecules can thus be used to drive a transient enhancement of the population of a spectrally large resonance in the XUV region.

## 11.4 Molecular Photoionization with Attosecond XUV Harmonic Pulses

As explained in the previous sections, the RABBIT method was developed (and successfully applied) to characterize ultrashort XUV pulse trains produced in HHG, through the retrieval of the harmonic phases $\Delta\phi_\Omega$ (see Eq. (11.1)). To achieve this goal, the implementation of the RABBIT technique assumes that the harmonics are detected in a reference gas with known or negligible atomic/molecular phases $\Delta\theta$.

However, the method was recently used in a non-conventional way, where a gas is ionized with characterized harmonics and the atomic/molecular phases $\Delta\theta$ are deduced from RABBIT measurements [8, 9, 29, 30]. This came with new issues concerning the interpretation of the experimental data: What information is encoded in $\Delta\theta$? To be more specific, what can be learned from these phases in terms of ionization dynamics? Up to date, two different—but not contradictory—answers were proposed. In [30], it was shown that, close to the ionization threshold with the constraint that $\Delta\theta$ varies smoothly with energy, it gives access to a characteristic time-delay $\tau_I$ (see Eq. (11.2)) that is reminiscent of the so-called "Wigner time-delay". The latter is defined as the energy derivative of the scattering phase shift of the photoelectron wave function [31]. In this section, we focus on a complementary interpretation, introduced in [9], which relates the *spectral derivative* of $\Delta\theta$ to the sideband formation delay [32].

### 11.4.1 RABBIT Phase and Time Delays

The two paths leading to a given sideband can be seen as two "quantum slits" through which the released electron wave-packet is coherently formed. The phase $\Delta\theta$ is nothing but the phase difference accumulated by the wave packet *during its formation* through each of the paths, irrelevant of the IR and XUV fields phases.

This translates into the time domain by assigning, to each path leading to a given sideband $\mathrm{SB}_{2q}$, a "generalized group delay" defined as

$$\tau_\pm = \frac{1}{2q \pm 1} \frac{\partial \theta_\pm}{\partial \omega_L}, \tag{11.6}$$

where $\theta_\pm$ are the phases of the two-photon matrix elements associated to each path, as defined in Eq. 11.5 [32]. These delays then appear in the spectral variations of the $\mathrm{SB}_{2q}$ RABBIT phase as:

$$\frac{1}{2q} \frac{\partial \Delta\theta}{\partial \omega_L} = \frac{1}{2q} \left( \frac{\partial \theta_+}{\partial \omega_L} - \frac{\partial \theta_-}{\partial \omega_L} \right) \tag{11.7}$$

$$= \frac{2q+1}{2q} \tau_+ - \frac{2q-1}{2q} \tau_- . \tag{11.8}$$

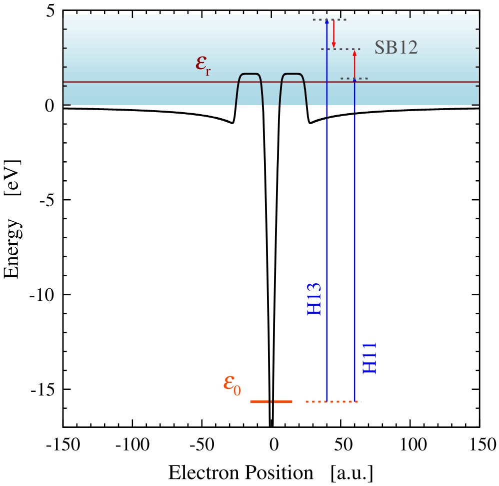

**Fig. 11.5** Model system. The potential (*full black line*) is composed of a soft-coulomb binding term, adjusted for a ground state energy $\varepsilon_0 = -15.65$ eV, to which a symmetric barrier is added to create a shape resonance of width $\Gamma_r \approx 10$ meV at $\varepsilon_r = 1.22$ eV. Starting from the ground state, the 11th harmonic of a $\sim 800$ nm laser hits the vicinity of the resonance, while the 13th harmonic reaches a smooth region of the continuum. This model potential corresponds actually to a cut in the potential of the more elaborate molecular model used in Ref. [9]

For sufficiently large orders $q$, the latter can be approximated as

$$\frac{1}{2q}\frac{\partial \Delta\theta}{\partial \omega_L} \simeq \tau_+ - \tau_- \tag{11.9}$$

The RABBIT phase derivative thus provides the sideband group delay difference, through each of the interfering paths.

## 11.4.2 Physical Meaning of the Delays

The physical meaning of these delays was evidenced in [9], in numerical experiments where the delays derived from RABBIT simulations were compared to wavepacket "times-of-flights (TOF)", as suggested by Eq. (11.9). The simulations were performed on a model molecule accounting for the essential vibronic features of $N_2$, on which preliminary experimental results had been reported, in a situation where one of the paths leading to the sideband strongly differs from the other [8].

Here, we illustrate the method with similar simulations on a simple, one-dimensional (1D), model system (see Fig. 11.5). The model potential was designed to present a shape resonance with energy $\varepsilon_r = 1.22$ eV above threshold, i.e. at about 17 eV above the ground state ($\varepsilon_0 = -15.65$ eV). The energy difference corresponds to the energy of the 11th harmonic of a 800 nm Ti:Sapph laser ($\omega_L \approx 1.55$ eV). When simulating a RABBIT experiment, the path leading to $SB_{12}$ through $H_{11}$ is

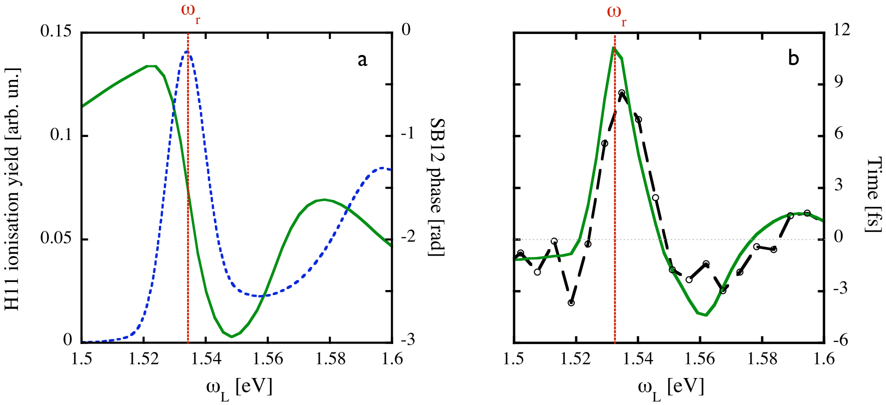

**Fig. 11.6** (**a**) Probability to photoionize the system with $H_{11}$ as a function of the fundamental frequency $\omega_L$ (*blue dashed curve*); $SB_{12}$ RABBIT phase obtained by photoionizing the system with $H_{11}$, $H_{13}$ and the fundamental (*green full curve*). (**b**) Group delay difference $\tau_+ - \tau_-$ retrieved through numerical differentiation of the RABBIT phase according to Eq. (11.9) (*green full curve*); Photoionization delay difference $\tilde{\tau}_+ - \tilde{\tau}_-$ obtained by TOF-like detection of the $SB_{12}$ wave-packets (*empty circles* linked by *black dashed lines*). The frequency $\omega_r$ at which $H_{11}$ hits the sharp resonance is indicated by a *vertical red dotted line*

therefore affected by the resonance, in contrast with the upper path involving $H_{13}$ through a smooth continuum. Such simulations were realized by solving ab initio the corresponding time-dependent Schrödinger equation (TDSE) for the system. The laser frequencies were chosen to explore the vicinity of the resonance with field intensities kept low enough to make negligible the transitions involving more than two photons.

In a first stage, we computed the ionization probability with $H_{11}$ only, when varying the *fundamental* frequency $\omega_L$ between 1.5 and 1.6 eV. This provides a clear picture of the structure of the system's spectrum in the vicinity of the resonance. The result is displayed on frame (a) of Fig. 11.6(dashed blue curve). The resonance we are interested in is responsible for the prominent peak localized at $\omega_r = (\varepsilon_r - \varepsilon_0)/11 \approx 1.53$ eV. Its width is governed by the spectral width of the $H_{11}$ pulse, which exceeds the resonance's width $\Gamma_r$ by about one order of magnitude. In addition, a broader resonance is revealed at higher energies, for $\omega_L \approx 1.6$ eV.

Then, we simulated the photoionization of the model system in the presence of the XUV harmonics 11 and 13, as well as of the fundamental IR. Electron spectra were obtained by a spectral Fourier analysis of the final wave-function, and RABBIT phases were retrieved from the $SB_{12}$ oscillations observed when tuning the XUV-IR delay $\tau$ (see Sect. 11.2). The procedure was repeated for a set of frequencies in the range of interest. The results are presented in Fig. 11.6. The vertical dashed line indicates the resonant laser frequency $\omega_r$, for which $\Omega_- = 11 \times \omega_L = 16.87$ eV. We see that the RABBIT phase (frame (a) of Fig. 11.6) undergoes a $-\pi$ jump when $\Omega_-$ crosses the resonance. This corresponds to the change of sign of the denominator in the term (thus by far dominant) associated to the resonant state $n = r$

in the corresponding two-photon transition matrix element shown in Eq. (11.3). Another negative, but less pronounced, jump takes place as $H_{11}$ enters the vicinity of the second, broader, resonance. In addition, a third jump (now positive) takes place *between* the resonances, around $\omega_L \approx 1.56$ eV. The latter results from an almost zero in the two-photon transition probability, where the contributions from the two consecutive resonances compensate each other, leaving only the contribution from the smooth continuum. Note that the two *vibronic* resonances identified in [9] correspond to two vibrational states associated to the same electronic resonance, while here they correspond to two different electronic states of our simpler 1D model. By contrast, we have checked that a typical—resonance-free—RABBIT phase varies by less than few tenths of radians within this range of laser frequencies.

We now turn to the generalized group delay difference $\partial \Delta\theta/(12\partial\omega_L)$ as given by Eq. (11.9), obtained by numerical differentiation of the RABBIT phases. It is displayed as the green full curve in frame (b) of Fig. 11.6. Each jump observed in the phase translates into a delay difference of several femtoseconds, up to $\approx 10$ fs at $\omega_r$: On the time scale of photoionization, it is a dramatic change in duration, as compared e.g. to Wigner-like delays which typically do not exceed a few tens of attoseconds [30, 33].

Whether such a delay difference—derived from a set of RABBIT phases—has any physical reality, was checked with the help of another series of simulations, where the model system was photoionized by either $H_{11}$ or $H_{13}$, in addition to the fundamental. This corresponds respectively to the lower and upper paths leading to $SB_{12}$ in the previous RABBIT simulations. Here we have performed "numerical time-of-fligth (TOF)" evaluations by computing, for each path, the electron flux at a given distance from the core. The latter was chosen large enough to make sure that the electron wave-packet associated to $SB_{12}$ reaches the virtual detector when the interaction with the XUV and IR fields is over. At each considered frequency, the flux temporal profile reflects the pulse shape (not shown). The time at which it is maximum is a good indicator of the $SB_{12}$ wave-packet arrival time at the virtual detector (noted $\tilde{\tau}_-$ and $\tilde{\tau}_+$ for the lower and upper paths respectively). Note that, while the values of $\tilde{\tau}_+$ and $\tilde{\tau}_-$ obviously depend on the detector's position, the difference $\tilde{\tau}_+ - \tilde{\tau}_-$ does not, because the two wave-packets evolve with the same total energy, along the same potential.

We have reported the arrival time difference $\tilde{\tau}_+ - \tilde{\tau}_-$ as a function of $\omega_L$ in frame (b) of Fig. 11.6(empty circles connected by black dashed lines), and found an excellent agreement with the RABBIT derived group delay difference (green full curve, same plot).

Comparing these two sets of data demonstrates that the group delay differences derived from RABBIT data uncover the presence of a chronology in two-photon ATI transitions, which is not measurable otherwise with current TOF technologies. As both wave-packet components evolve identically once formed, this group delay difference can be ascribed to a difference of time spent prior to their release, i.e. during their formation. This can therefore be viewed as a time during which the system is "trapped" in the intermediate stage of the two-photon absorption, although the XUV and IR pulses act simultaneously, i.e. in an a priori non-sequential regime. An interesting point, besides the possibility to measure such delays, is that the transition duration can be controlled by tuning the laser frequency around resonances.

## 11.5 Conclusions

In this chapter, we have presented recent experimental and theoretical results on the study of a new class of molecular processes that have been uncovered with the help of coherent XUV harmonic radiations. We have reported advances realized in two main domains of applications that have been explored so far: (i) Characterization and control of the harmonic emission, with applications to molecular structure issues; (ii) Use of harmonic radiation to evidence temporal aspects of the non-linear response of molecular systems. Thanks to the temporal structure of the harmonic pulse trains, it is now feasible to follow the temporal evolution of such systems, at the attosecond level. Here, the emphasis has been on the IR-XUV RABBIT technique which has revealed itself as an efficient tool to follow in time the changes in the electronic distribution within a molecule. So far, these studies have been conducted in simple molecules and, as such, they should be considered as proofs of principle. In any case, they open most interesting perspectives towards the study in real time of electronic processes in reactive systems.

## References

1. V. Véniard, R. Taïeb, A. Maquet, Phys. Rev. Lett. **74**, 4161 (1995)
2. V. Véniard, R. Taïeb, A. Maquet, Phys. Rev. A **54**, 721 (1996)
3. H.G. Muller, Appl. Phys. B **74**, S17 (2002)
4. J. Itatani, J. Levesque, D. Zeidler, H. Niikura, H. Pépin, J.C. Kieffer, P.B. Corkum, D.M. Villeneuve, Nature **432**, 867 (2004)
5. S. Haessler, J. Caillat, W. Boutu, C. Giovanetti-Teixeira, T. Ruchon, T. Auguste, Z. Diveki, P. Breger, A. Maquet, B. Carré, R. Taïeb, P. Salières, Nat. Phys. **6**, 200 (2010)
6. Z. Diveki, A. Camper, S. Haessler, T. Auguste, T. Ruchon, B. Carré, P. Salières, R. Guichard, J. Caillat, A. Maquet, R. Taïeb, New J. Phys. **14**, 023062 (2012)
7. W. Boutu, S. Haessler, H. Merdji, P. Breger, G. Waters, M. Stankiewicz, L.J. Frasinski, R. Taïeb, J. Caillat, A. Maquet, P. Monchicourt, B. Carré, P. Salières, Nat. Phys. **4**, 545 (2008)
8. S. Haessler, B. Fabre, J. Higuet, J. Caillat, T. Ruchon, P. Breger, B. Carré, E. Constant, A. Maquet, E. Mével, P. Salières, R. Taïeb, Y. Mairesse, Phys. Rev. A **80**, 011404 (2009)
9. J. Caillat, A. Maquet, S. Haessler, B. Fabre, T. Ruchon, P. Salières, Y. Mairesse, R. Taïeb, Phys. Rev. Lett. **106**, 093002 (2011)
10. P.M. Paul, E.S. Toma, P. Breger, G. Mullot, F. Augé, Ph. Balcou, H.G. Muller, P. Agostini, Science **292**, 1689 (2001)
11. Y. Mairesse, A. de Bohan, L.J. Frasinski, H. Merdji, L.C. Dinu, P. Monchicourt, P. Breger, M. Kovačev, R. Taïeb, B. Carré, H.G. Muller, P. Agostini, P. Salières, Science **302**, 1540 (2003)
12. M. Lein, N. Hay, R. Velotta, J.P. Marangos, P.L. Knight, Phys. Rev. Lett. **88**, 183903 (2002)
13. M. Lein, N. Hay, R. Velotta, J.P. Marangos, P.L. Knight, Phys. Rev. A **66**, 023805 (2002)
14. C. Vozzi, F. Calegari, E. Benedetti, J.-P. Caumes, G. Sansone, S. Stagira, M. Nisoli, R. Torres, E. Heesel, N. Kajumba, J.P. Marangos, C. Altucci, R. Velotta, Phys. Rev. Lett. **95**, 153902 (2005)

15. T. Kanai, S. Minemoto, H. Sakai, Nature **435**, 470 (2005)
16. E. van der Zwan, M. Lein, Phys. Rev. A **82**, 033405 (2010)
17. J. Higuet, H. Ruf, N. Thiré, R. Cireasa, E. Constant, E. Cormier, D. Descamps, E. Mével, S. Petit, B. Pons, Y. Mairesse, B. Fabre, Phys. Rev. A **83**, 053401 (2011)
18. H.J. Wörner, H. Niikura, J.B. Bertrand, P.B. Corkum, D.M. Villeneuve, Phys. Rev. Lett. **102**, 103901 (2009)
19. H.J. Wörner, J.B. Bertrand, P. Hockett, P.B. Corkum, D.M. Villeneuve, Phys. Rev. Lett. **104**, 233904 (2010)
20. O. Smirnova, Y. Mairesse, S. Patchkovskii, N. Dudovich, D. Villeneuve, P. Corkum, M.Y. Ivanov, Nature **460**, 972 (2009)
21. B.K. McFarland, J.P. Farrell, P.H. Bucksbaum, M. Gühr, Science **322**, 1232 (2008)
22. O. Smirnova, S. Patchkovskii, Y. Mairesse, N. Dudovich, M.Y. Ivanov, Proc. Natl. Acad. Sci. USA **106**, 16556 (2009)
23. Y. Mairesse, J. Higuet, N. Dudovich, D. Shafir, B. Fabre, E. Mével, E. Constant, S. Patchkovskii, Z. Walters, M.Yu. Ivanov, O. Smirnova, Phys. Rev. Lett. **104**, 213601 (2010)
24. R. Torres, T. Siegel, L. Brugnera, I. Procino, J.G. Underwood, C. Altucci, R. Velotta, E. Springate, C. Froud, I.C.E. Turcu, S. Patchkovskii, M.Yu. Ivanov, O. Smirnova, J.P. Marangos, Phys. Rev. A **81**, 051802 (2010)
25. C. Vozzi, M. Negro, F. Calegari, G. Sansone, M. Nisoli, S. De Silvestri, S. Stagira, Nat. Phys. **7**, 823 (2011)
26. A.-T. Le, R.R. Lucchese, C.D. Lin, J. Phys. B **42**, 21 (2009)
27. A. Monmayrant, S. Weber, B. Chatel, J. Phys. B **43**, 103001 (2010)
28. N. Dudovich, D. Oron, Y. Silberberg, Phys. Rev. Lett. **88**, 123004 (2002)
29. M. Swoboda, T. Fordell, K. Klünder, J.M. Dahlström, M. Miranda, C. Buth, K.J. Schafer, J. Mauritsson, A. L'Huillier, M. Gisselbrecht, Phys. Rev. Lett. **104**, 103003 (2010)
30. K. Klünder, J.M. Dahlström, M. Gisselbrecht, T. Fordell, M. Swoboda, D. Guénot, P. Johnsson, J. Caillat, J. Mauritsson, A. Maquet, R. Taïeb, A. L'Huillier, Phys. Rev. Lett. **106**, 143002 (2011)
31. E.P. Wigner, Phys. Rev. **98**, 145 (1955)
32. M. Vacher et al. in preparation (2013)
33. M. Schultze, M. Fieß, N. Karpowicz, J. Gagnon, M. Korbman, M. Hofstetter, S. Neppl, A.L. Cavalieri, Y. Komninos, Th. Mercouris, C.A. Nicolaides, R. Pazourek, S. Nagele, J. Feist, J. Burgdörfer, A.M. Azzeer, R. Ernstorfer, R. Kienberger, U. Kleineberg, E. Goulielmakis, F. Krausz, V.S. Yakovlev, Science **328**, 1658 (2010)

# Chapter 12
# Observation and Control of Electron Dynamics in Molecules

**Andreas Becker, Feng He, Antonio Picón, Camilo Ruiz, Norio Takemoto, and Agnieszka Jaroń-Becker**

**Abstract** The technological development of ultrashort laser pulses makes it possible to monitor and control the dynamics of the electrons in atoms and molecules. In this Chapter we first review recent experimental and theoretical progress towards tracking and understanding of electron motion in nature's simplest molecule, the hydrogen molecular ion, on its natural time scale. A complex and counterintuitive dynamics appears due to a strong coupling between different electronic states and of the electron with the external field. Different approaches for the observation of these single-active electron effects in the hydrogen molecular ion as well as of electron rearrangement in the valence shell of more complex molecules are presented. Based on these new insights we then turn to a discussion of recently proposed strategies to control electron localization in molecules with carrier-envelope phase locked pulses, attosecond pump-probe set-ups as well as circularly polarized laser pulses. In particular, results of experiments, in which the asymmetry of local-

---

A. Becker (✉) · A. Picón · A. Jaroń-Becker
JILA and Department of Physics, University of Colorado, 440 UCB, Boulder, CO 80309-0440, USA
e-mail: andreas.becker@colorado.edu

A. Picón
e-mail: Antonio.Picon@uab.es

A. Jaroń-Becker
e-mail: jaron@jila.colorado.edu

F. He
Key Laboratory for Laser Plasmas (Ministry of Education) and Department of Physics and Astronomy, SJTU, Shanghai 200240, People's Republic of China
e-mail: fhe@sjtu.edu.cn

C. Ruiz
Centro de Laseres Pulsados CLPU, Edificion M3, Parque Cientifico, C/ Adaja s/n, 37185 Villamajor, Spain
e-mail: camilo@usal.es

N. Takemoto
Department of Chemical Physics, Weizmann Institute of Science, 76100 Rehovot, Israel
e-mail: norio.takemoto@weizmann.ac.il

L. Plaja et al. (eds.), *Attosecond Physics*, Springer Series in Optical Sciences 177,
DOI 10.1007/978-3-642-37623-8_12,

ization probabilities at the protons in the hydrogen molecular ion is observed, are complemented with theoretical results and analysis from ab-initio numerical simulations.

## 12.1 Introduction

One of the central goals of ultrafast intense laser science is to observe, understand and control the dynamics of the components of matter on their natural time scale. Real-time observation and control of the motion and rearrangement of atoms in molecules and condensed matter have been achieved using femtosecond laser techniques in the past (for a review of the field of femtochemistry, see [1]). The advent of attosecond laser pulse technology promises to improve the temporal resolution towards the shorter attosecond time scale of electron dynamics in atoms and molecules. Insights into attosecond electron motion, including that driven by the intense laser pulse itself, may provide new or refined understanding of basic phenomena, such as ionization or higher-order harmonic generation, the coupling between electronic and nuclear dynamics as well as the control of charge localization and charge transfer in and between molecules.

Much progress in this direction has been done recently for the simplest molecules, namely the hydrogen molecular ion and the hydrogen molecule (as well as their isotopes). For these systems theoretical analysis can be performed with high accuracy using elaborate numerical calculations. On the other hand, detailed observation of the electron as well as the coupled electron-nuclear dynamics, involving the detection of the momenta of all charged particles in coincidence, has become possible or is on the verge to emerge. Thus, these molecules are an ideal meeting ground for experiment and theory to analyze sub-femtosecond electron dynamics and its control by the electric field of an ultrashort intense laser pulse. Recent results provide vivid examples of the potential of attosecond physics in this respect. This includes surprising and even counterintuitive new insights into seemingly well-understood processes, such as laser-induced ionization of a molecule.

In the next section we will discuss how intramolecular electron dynamics on the attosecond time scale can influence the ionization process in a molecule. A theoretical analysis of this phenomenon, based on results of numerical solutions of the time-dependent Schrödinger equation, will be complemented with actual experimental observations and theoretical proposals for future experiments. We will also discuss recent experimental and theoretical efforts to visualize electron rearrangement in other di- and triatomic molecules. We will then turn to the question how the electron in the simplest chemical bond can be controlled and the electron can be localized at one of the two protons in the hydrogen molecular ion. Different theoretical concepts will be contrasted with available experimental data. Finally, we will briefly discuss recent progress towards steering electronic dynamics in more complex molecules.

## 12.2 Attosecond Laser Driven Intramolecular Electronic Dynamics

Ionization of atoms and molecules by a laser field is the doorway state to many phenomena in strong-field science, e.g. the generation of higher-order harmonics and attosecond pulses (for a review, see [2]), molecular dissociation and its control [3] and ultrafast molecular imaging [4]. Widely used ionization pictures and theories, such as tunneling ionization or multiphoton ionization, make use of quasistatic or cycle-averaged approximations for the interaction of the electrons with the laser electric field. Up to now, little attention has been given to the sub-cycle dynamics of the electron driven by the oscillating laser electric field inside the atom or molecule before or during the ionization process. Attosecond technology has shifted this perspective since the electron dynamics can now be probed, sometimes with surprising and counterintuitive results.

### *12.2.1 Charge-Resonance-Enhanced Ionization on the Attosecond Time Scale*

Arguably, the most popular ionization models in the interaction of ultrashort laser pulses with matter are based on the quasistatic approximation of the laser electric field. In this approximation it is assumed that the change of the electric field of the laser in time happens slowly as compared to the electron dynamics in the process under consideration [5]. For example, in the tunnel ionization picture, the combination of the potentials due to the Coulomb attraction of the atomic or molecular core and the laser electric field form a barrier through which the electron can escape from the atom or molecule. According to this picture, one expects that the probability for ionization is largest when the potential barrier becomes thinnest. In a linearly polarized laser field this coincides with the moments in time when the electric field is strongest, i.e., over the envelope of the field amplitude at its peak and during one oscillation of the field at the extrema. Attosecond probing of the ionization of neon atoms during the interaction with a near-infrared laser pulse provided strong support of this picture in the atomic case [6].

Some molecules, such as the hydrogen molecular ion, show more complex ionization mechanisms, which are however still explained based on the quasistatic approximation of the laser electric field. A strong coupling between a pair of quasi-degenerate states with opposite parity, also called charge-resonant states [7], can lead to a strong enhancement of the ionization probability of the molecule [8, 9]. In the hydrogen molecular ion the ground state of $1s\sigma_g$-symmetry and the first excited state of $2p\sigma_u$-symmetry form such a pair of states when the molecular ion is stretched to intermediate separations of the protons. As shown in Fig. 12.1(a), the coupling between the states lifts the energy level at one of the protons while the energy level at the other proton is decreased by the laser electric field. At high field

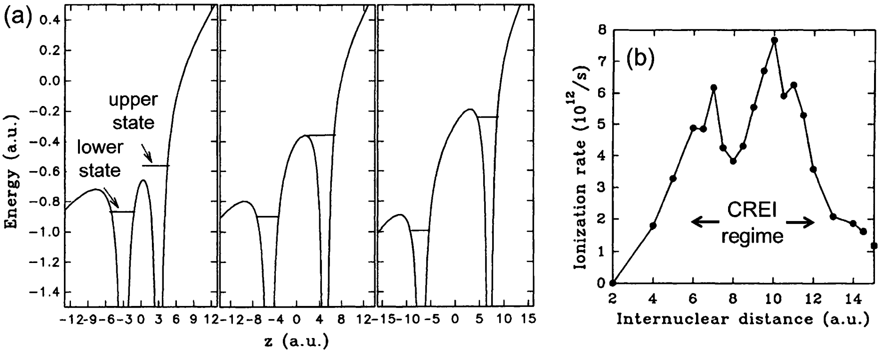

**Fig. 12.1** Mechanism and results for charge-resonance-enhanced ionization (CREI) in the hydrogen molecular ion by T. Zuo and A.D. Bandrauk [8]: (**a**) Lowest energy levels (see text) in hydrogen molecular ion induced by a static electric field of $E_0 = 0.0533$ a.u. (corresponding to an intensity of $I = 10^{14}$ W/cm$^2$) at internuclear separations of 6 a.u., 10 a.u. and 14 a.u. (*from left to right*); (**b**) Results of ab-initio numerical simulations for the ionization rate of hydrogen molecular ion in a linearly polarized laser field (peak intensity: $10^{14}$ W/cm$^2$, wavelength: 1064 nm). The CREI regime is indicated (adapted from [8])

strengths, the upper state lies above the internal Coulomb barrier between the protons and the electron is ionized efficiently, which leads to a strong enhancement of the ionization probability at intermediate internuclear distances (see Fig. 12.1(b)). The corresponding ionization mechanism was theoretically predicted and termed charge-resonance-enhanced ionization (CREI) [8, 9] before the dependence of the ionization probability on the internuclear separation was observed in the experiment [10].

In the original CREI picture ionization of the hydrogen molecular ion is viewed on the femtosecond time scale of nuclear dynamics. On the attosecond time scale it has the same features as the tunneling ionization picture because of the inherent quasistatic field approximation. This means that in a linearly polarized laser field the ionization probability is expected to be largest whenever the external field is strongest. However, recent results of numerical solutions of the time-dependent Schrödinger equation capturing the interaction of the hydrogen molecular ion with an intense laser pulse do not agree with the expectation of the quasistatic CREI picture [11]. As shown in Fig. 12.2(b), over one half cycle of the oscillation of the laser electric field the ionization rate of the hydrogen molecular ion can have two maxima but a minimum near the peak of the field. This unexpected multiple ionization burst phenomenon in case of the hydrogen molecular ion becomes specifically apparent when compared to results of a quasi-static ionization theory for the hydrogen atom, which exhibit the expected maxima in ionization rate at every maximum of the field (Fig. 12.2(a)). Indeed, further theoretical analysis shows that even more than two ionization bursts can occur within a half cycle of the oscillation of the field depending on the parameters of the field [12].

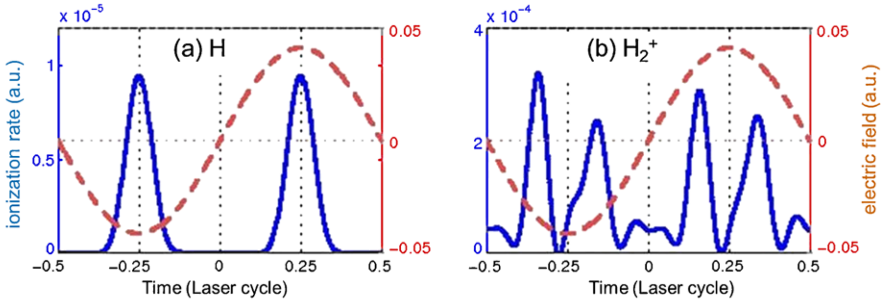

**Fig. 12.2** Ionization rates (*solid blue curves*) of (**a**) the hydrogen atom and (**b**) the hydrogen molecular ion as a function of time over one cycle of a laser pulse [11]. The molecular ionization rates, as obtained by numerical solution of the corresponding time-dependent Schrödinger equation, are accumulated over internuclear separations between 6.75 a.u. and 7.25 a.u. The electric field of the laser pulse is represented by *the dashed red curves* and the field parameters were wavelength: 800 nm, peak intensity: $6 \times 10^{13}$ W/cm$^2$ and pulse duration: 26.69 fs (adapted from [11])

Based on numerical results, Kawata et al. first noticed an ultrafast laser-driven intramolecular electron dynamics between the two protons such that the electron population at each of the protons is maximized more than once over a half cycle of the field [13]. With the increasing interest in attosecond electron dynamics it was shown that this phenomenon is the physical origin for the multiple ionization bursts [11] and the intensity-dependent electron localization in the dissociating hydrogen molecular ion [14] (see Sect. 12.4.2). An explanation of the sub-laser-cycle electron dynamics is given by a strong-field modulated diffraction effect in the molecule (c.f., Fig. 12.3). The intramolecular electron transfer between the protons is gated at specific electron momenta, as can be seen from a phase-space analysis in terms of the Wigner distribution[1] [14]:

$$\begin{aligned} W(z, p_z; t) = \frac{1}{\pi} \int\int \rho d\rho dR \int_{-\infty}^{\infty} dy \Psi^*(R, z+y, \rho; t) \Psi(R, z-y, \rho; t) \\ \times \exp(2 i p_z y) \end{aligned} \tag{12.1}$$

where $\Psi(R, z, \rho; t)$ is the solution of the corresponding Schrödinger equation of the hydrogen molecular ion interacting with the field and $p_z$ is the momentum along the polarization direction of the field. Figure 12.3 shows snapshots of the Wigner distributions at four time instants over a field cycle (rows) and three different laser intensities (columns). The red spots in the distributions correspond to the maxima of the electron population, while the blue spots mark forbidden regions in the phase-space. Following the evolution of the Wigner distribution at the lowest intensity (left hand column) we see that the population moves from the proton centered at $z \approx 3.5$ a.u.

---

[1] Throughout this chapter, we use atomic units: Bohr radius $a_0 = 1$, mass of electron $m_e = 1$, Planck's constant $\hbar = 1$, charge of electron $q_e = 1$ and Bohr magneton $\mu_B = 1/2c$ with $c$ is the speed of light.

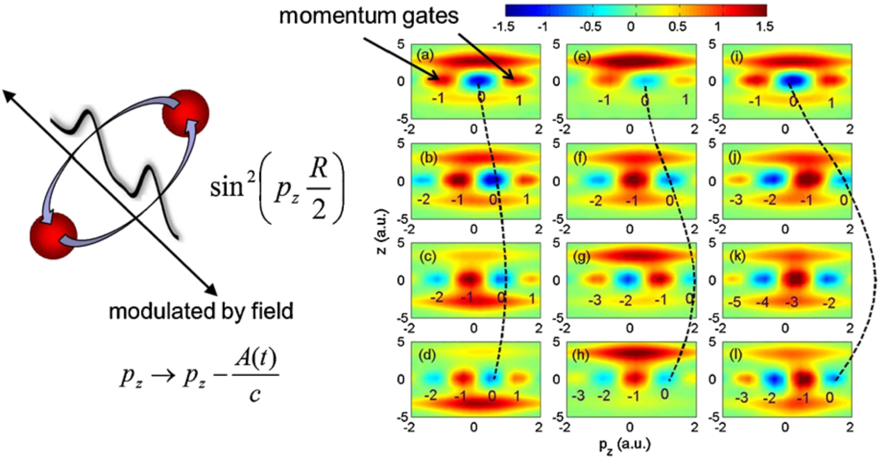

**Fig. 12.3** Wigner distributions (on a linear color scale) for the interaction of a dissociating hydrogen molecular ion with an infrared laser pulse at 800 nm and a pulse length of 5.3 fs [14]. The four snapshots in each of the columns are taken over about one cycle of the oscillating electric field at intensities: $3 \times 10^{12}$ W/cm$^2$ (*left column*), $2 \times 10^{13}$ W/cm$^2$ (*middle column*) and $10^{14}$ W/cm$^2$ (*right column*). *The red spots* indicate the momentum gates due to diffraction effects (molecular structure factor $\sin^2(p_z R/2)$), which are modulated by the strong field along the momentum axis. *The dashed lines* indicate the oscillation of the central point in the momentum distribution (adapted from [14])

at discrete momenta to the other proton, located at $z \approx -3.5$ a.u. The discrete momenta correspond to diffraction peaks (or, momentum gates [14]) in the electron momentum distribution, which can be factorized into an atomic momentum distribution and a two-center structure factor (in the present case, $\sin^2(p_z R/2)$) [14, 15]. In the field the momentum gates are shifted back and forth with the period of the driving laser period, since according to the minimum coupling principle the electron momentum $p_z$ is replaced by $p_z - A(t)/c$ where $A(t)$ is the time-dependent vector potential of the laser pulse. At small field intensities the momentum shift is small and the electron distribution oscillates between the two protons following the oscillating electric field. However, if $A(t)$ exceeds the field-free values of the momentum gates, the electronic flux between the protons reverses and opposes the classical laser-electric force. At high field intensities the momentum gates are shifted across the favored $p_z \approx 0$ region several times, resulting in a bunching of the electronic flux within the molecule over one half-cycle of the oscillation of the laser field. A detailed analysis of the gating effect in terms of Bohmian trajectories has been given recently as well [16].

Complementary insight into the multiple ionization burst phenomenon was gained by analyzing the complex electron dynamics in a model consisting of the two charge resonant states ($1s\sigma_g$ and $2p\sigma_u$ in the case of hydrogen molecular ion). Based on an analysis of the general solution of the time-dependent Schrödinger equation of the model in terms of the two Floquet states expressed in form of a series expansion, the time instants $t_{loc}$ for maximum localization of the electron distribution at one of the protons was derived as [11, 12]:

$$A(t_{loc}) = -c\frac{m\pi + \xi}{2d_{gu}}, \quad \text{with } m = 0, \pm 1, \pm 2, \dots \tag{12.2}$$

The time instants depend on the mixing angle $\xi$ of the two Floquet states as well as the dipole transition matrix element $d_{gu}$ between the two states. The two-state model used in the analysis is valid when these two states are coupled much more strongly with each other than with the other states in the molecule. In the case of $H_2^+$ at small internuclear separations around the equilibrium distance, the absolute value of the transition dipole element between the ground $1s\sigma_g$-state and the first excited $2p\sigma_u$-state is comparable to those between these states and other excited states. Hence, the traditional tunnel ionization picture is expected to appear. However, as the internuclear separation gets larger in the process of dissociation, the energy levels of the pair of state ($1s\sigma_g$ and $2p\sigma_u$) become almost degenerate and isolated from the other states, and $d_{gu}$ grows proportionally to the internuclear distance [17]. This validates the derivation of Eq. (12.2) within the two-state model. For large $d_{gu}$, the condition can be fulfilled for more than one value of $t_{loc}$ in a half cycle of the oscillation of the electric field which results in a bunching of the electron localization and corresponding multiple ionization bursts (for a detailed derivation and discussion, see Ref. [12]). Comparison of the time instants for electron localization predicted by the simple condition (12.2) with the numerical results in Fig. 12.2 shows a good agreement. Although the result has been derived and confirmed for the specific case of the hydrogen molecular ion, it is expected to hold for other molecules with pair(s) of quasi-degenerate charge resonant states as well.

### *12.2.2 Observation of Intramolecular Electron Dynamics in Hydrogen Molecular Ion*

Attosecond laser pulse technology potentially allows to take snapshots of the electron dynamics in an atom or molecule on its natural time scale. The complex laser-driven dynamics, discussed in the previous section, provides a particularly interesting and challenging example, since it leads to counterintuitive phenomena such as multiple ionization bursts. Below, we first discuss theoretical studies on probing the asymmetry of the electron density in the molecule via attosecond photoionization in opposite directions along the molecular axis. This theoretical concept is then extended such that the polarization direction of the attosecond pulse is set perpendicular to the molecular axis and two-center interference patterns are used for retrieving the quantum states. Finally, we will review how traces of the attosecond intramolecular electronic dynamics can be mapped onto the electron momentum distribution generated by a femtosecond circularly polarized laser field using the attoclock concept.

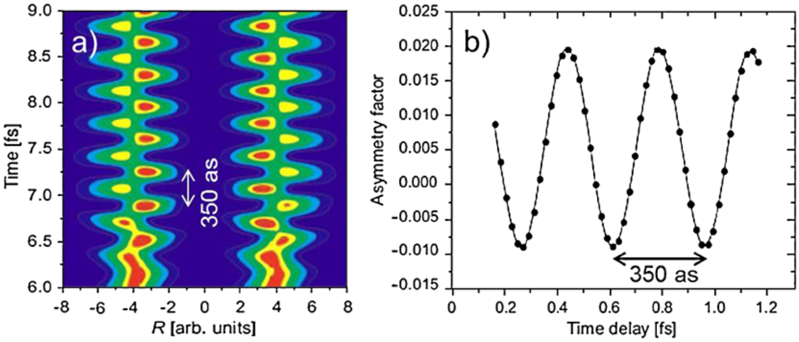

**Fig. 12.4** Numerical results by A.D. Bandrauk et al. [18] for (**a**) the electron probability density as a function of time for a coherent superposition of two electronic states in the hydrogen molecular ion at an internuclear separation of 8 a.u. and (**b**) the asymmetry in the photoelectron emission along the internuclear axis as a function of time delay between a pump pulse (115 nm, 0.8 fs) and an ionizing probe pulse (20 nm, 100 as) (adapted from [20], original result in [18])

#### 12.2.2.1 Theoretical Proposals for Tracing Attosecond Electron Dynamics

Several theoretical proposals how to track electron motion in molecules are based on the application of an attosecond laser pulse to ionize the electron and measure the angular distribution of the photoelectron momentum. In order to explore this idea Bandrauk and coworkers [18, 19] created in their numerical simulations coherent superpositions of different electronic states in the hydrogen molecular ion with a sub-fs vacuum ultraviolet (VUV) pulse. The induced electron wavepacket dynamics between the two protons (Fig. 12.4(a)) is then probed with a second attosecond pulse, which photoionizes the molecular ion along the internuclear axis. The oscillation of the electron population is mapped onto the asymmetry in the photoelectron emission along the molecular axis, $(P_+ - P_-)/(P_+ + P_-)$, where $P_\pm$ is the probability to observe the electron along the positive or negative direction, respectively (Fig. 12.4(b)). A similar concept has been applied theoretically to ionization of the hydrogen molecule followed by dissociation of the ion as well [21].

Conceptually, the partial electron waves ejected from the two atomic centers of a diatomic molecule take the role of the coherent light waves emerging from the two slits in the Young's experiment [22]. This analogy, first discussed by Cohen and Fano [23], was recently applied to attosecond photoionization of a dissociating hydrogen molecular ion [24–26]. On the femtosecond time scale, the photoionization yield as a function of the internuclear separation shows oscillations, which are a characteristic feature of the two-center interference effects [27–29]. Results of numerical calculations for an attosecond pump-probe scenario show that information about the nuclear wave packet, such as the velocity, the internuclear separation and the width of the wave packet, can be retrieved from the oscillation and the decrease of its amplitude (see, Fig. 12.5) [26].

Beyond the information about the slower nuclear dynamics, the two-center interference effects in the electron momentum distributions exhibit information about

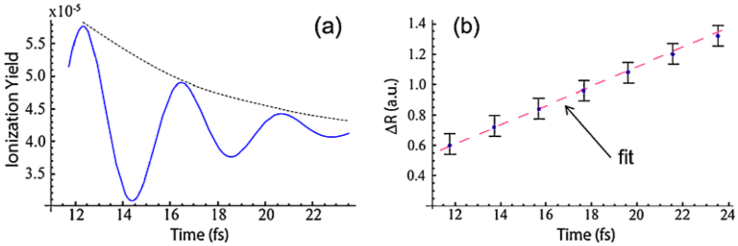

**Fig. 12.5** (**a**) Results of numerical simulations [26] for a pump-probe scenario, in which the first pulse (wavelength: 117 nm, pulse length: 1.2 fs, intensity: $8 \times 10^{12}$ W/cm$^2$) excites the hydrogen molecular ion to the dissociative $2p\sigma_u$-state and the time-delayed second pulse (frequency: 22 nm, pulse length: 73 as, intensity: $1.35 \times 10^{14}$ W/cm$^2$) ionizes the dissociating molecular ion. (**b**) Spreading of the nuclear wave packet, as obtained from the results of the numerical simulations (*points* with error bars) and the decrease of the amplitude of the oscillation in the ionization yield (fit, *dashed line*) (adapted from [26])

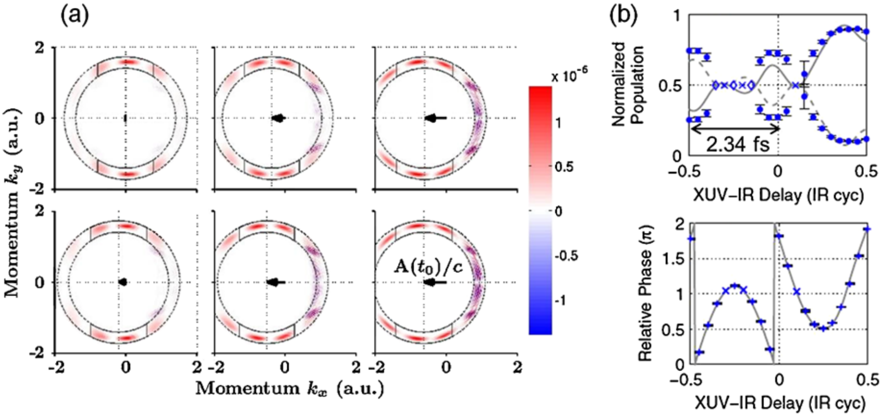

**Fig. 12.6** (**a**) Results of numerical simulations for the photoelectron momentum distributions following ionization of hydrogen molecular ion at an internuclear separation of 7 a.u. with an intense XUV pulse (25 nm, $1 \times 10^{12}$ W/cm$^2$, 500.3 as) [11]. The electron probability distribution in the hydrogen molecular ion was driven by an IR laser field at 1400 nm, peak intensity of $1.5 \times 10^{13}$ W/cm$^2$, and a pulse duration 14.01 fs. The momentum distributions are obtained for the following time delays between the two pulses (from *the upper left* to *the lower right*): 0, 0.05, 0.1, 0.15, 0.2, 0.25 IR laser cycles. (**b**) Normalized populations (*upper panel*) and relative phase of the amplitudes (*lower panel*) at the two protons, as retrieved from the momentum distributions (*markers*), in comparison with the results of the ab-initio numerical simulations [11] (adapted from [11])

the electron dynamics in the molecule itself. As an example, Fig. 12.6(a) shows results of a numerical experiment in which the electron in a hydrogen molecular ion is driven by an infrared laser pulse, polarized along the internuclear axis, and being probed by a sub-fs extreme ultraviolet (XUV) laser pulse, polarized perpendicular to the internuclear axis, at six different delay times of the two pulses over a quarter of the infrared (IR) laser cycle [11]. The momentum distributions clearly show that the interference patterns vary which is due to the changes in the IR-laser driven electron wavefunction. Using a two-state model of the hydrogen molecular ion the complex electron dynamics, discussed in Sect. 12.2.1, can be retrieved from the interference patterns (see, Fig. 12.6(b)) [11].

Recently, observable traces of intramolecular electron dynamics have been predicted to occur in higher-order harmonic generation as well [30]. Results of numerical calculations show a high sensitivity of the spectra to the coupled electron-nuclear dynamics, which allows to separate contributions from the coherent superposition of two or more states in the hydrogen molecular ion. Furthermore, concepts for the generation of attosecond electron pulses, which would provide the required temporal and spatial resolution for diffraction experiments, have been brought forward recently [31]. Based on these developments, it has been shown theoretically that the time-dependent localization and delocalization of the electron probability distribution can be imaged on the differential cross section for elastic scattering of an electron pulse of a diatomic molecule [32].

#### 12.2.2.2 Experimental Observation Using the Attoclock Concept

Using a different concept the electron motion inside the molecule can be indirectly captured. To this end, a femtosecond circularly polarized laser pulse is applied to induce ionization of the electron from the target. In a long circularly polarized pulse the magnitudes of the electric field and the vector potential of the laser are almost constant near the peak and only their directions rotate once every 2.6 fs for a near-infrared laser operating at about 800 nm. Assuming that the escaping electron will be accelerated from rest after the ionization in the field, the final momentum distribution $\mathbf{p}_f = \mathbf{A}(t_i)/c$, where $\mathbf{A}(t_i)$ is the vector potential at the instant of ionization $t_i$, is a measure of the release time of the electron from the target [33]. More precisely, it is the angular resolution (angular streaking) of the photoelectron momentum distribution which provides the attosecond temporal resolution in this concept, which is also called attoclock [34] and has been used for other attosecond measurements on atoms before [34, 35].

Applied to a target with a spherical symmetric electron probability density, such as e.g. an atom, the electron will be released at a constant rate as the electric field rotates. One therefore expects a donut-shaped electron momentum distribution of radius $|\mathbf{p}_f| = A_0/c$ where $A_0$ is the peak amplitude of the vector potential. In contrast, for the hydrogen molecular ion with an initial state distribution in its ground state elongated along the internuclear axis it is expected that the ionization rate is largest when the electric field is aligned along the molecular axis. Consequently, the momentum distribution should peak along the corresponding direction of the vector potential at this time instant, namely perpendicular to the molecular axis on the ring $|\mathbf{p}_f| = A_0/c$ (see, Fig. 12.7(a)). However, recent experimental observations, presented in Fig. 12.7(b), show that the electron momentum distribution is tilted in the same direction as the rotation of the laser electric field and peaked at lower momenta than expected [36]. This indicates that the instant of ionization as well as the initial

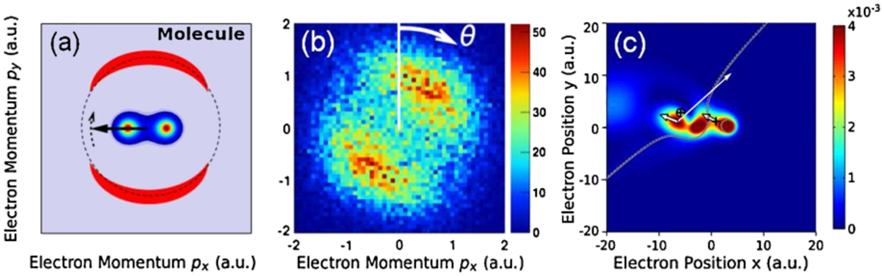

**Fig. 12.7** Photoelectron momentum distribution (**a**) as expected for ionization of the hydrogen molecular ion in its $1s\sigma_g$ ground state and (**b**) as observed in the experiment (laser parameters: $6 \times 10^{14}$ W/cm$^2$, 780 nm, and 35 fs) [36]. (**c**) Snapshot of the calculated electron probability density in hydrogen molecular ion at a time instant of 356 as after the electric field vector was aligned along the axis connecting the protons, which are located at $(x, y) = (\pm 3.5\ \text{a.u.}, 0)$ [36]. *The grey solid* and *dashed lines* are the contour lines of the potential at the field free energies of the two lowest energy states. The + signs mark the saddle points of the instantaneous potential. *The bold white arrow* and *the thin white arrow* indicate the initial momentum of the electron wave packet and $\mathbf{A}(t_i)/c$, respectively (adapted from [36])

momentum of the electron is at odds with the expectation from previously assumed (quasistatic) ionization models.

Results of ab-initio numerical simulations reproduce the tilted peak as the main contribution in the calculated electron momentum distribution. Moreover, the snapshot of the electron probability density in Fig. 12.7(c) captures the time instant when the electron wave packet is released from the molecular ion [36]. The snapshot shows that the laser electric field is not aligned along the internuclear axis at the moment of ionization and the wave packet has an initial velocity with a component opposite to the acceleration by the field. The late emission of the electron wave packet is induced by the strong coupling between the ground and first excited states of the molecular ion, as discussed in Sect. 12.2.1. This induces a complex electron dynamics in the molecule, which leads to the attosecond time lag and the initial momentum in the electron emission. The experiment maps these features of the electron dynamics onto the tilt angle and the magnitude of the observed electron momentum distribution.

## 12.3 Tracing Electron Rearrangement in Larger Molecules

In Sect. 12.2 we considered electron dynamics in nature's simplest molecule, the hydrogen molecular ion having just one electron. In view of the goal of attosecond physics to provide new insights into chemical reactions or charge transfer processes in molecules at the level of electrons, it is important to develop techniques which visualize the rearrangement of the entire valence shell in molecules during a process. There have been at least three promising approaches to time resolve the electron rearrangement during the dissociation of a molecule proposed recently, which are schematically depicted in Fig. 12.8, namely (a) photoelectron spectroscopy [37],

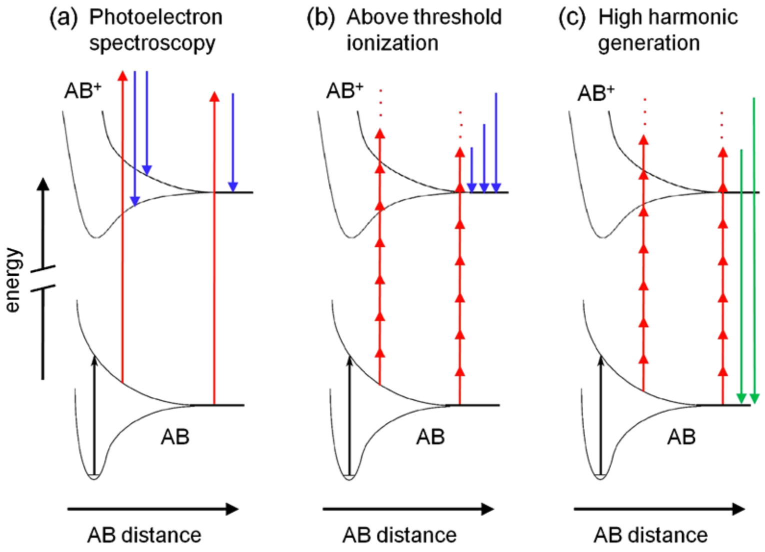

**Fig. 12.8** Concepts for time-resolved measurements of electron rearrangement during the transformation of a diatomic molecule AB to two atoms. The electronic dynamics is probed at a time delay after the initiation of molecular dissociation by (**a**) photoelectron spectroscopy [37], (**b**) strong–field ionization [38] or (**c**) higher-order harmonic generation [39]

(b) strong-field above threshold ionization [38] and (c) higher-order harmonic generation [39]. The potential of each of these approaches has been demonstrated for the dissociation of di- or triatomic molecules, which is usually induced by excitation of an electron from the ground state to one or a superposition of a few excited state(s) at the equilibrium distance of the molecule.

In the first approach, called time-resolved photoelectron spectroscopy (Fig. 12.8(a)), the dissociating molecule is probed by a VUV (or, XUV) pulse via single photon ionization and photoelectron spectra are recorded. By variation of the pump-probe delay the time evolution of the excited state can be monitored [37, 40–42]. Detailed insights into certain aspects of a dynamical process, such as, for example, predissociation via asymmetric stretching in case of the carbon disulfide molecule could be gained [41]. This technique is particularly useful to probe dissociation dynamics, shifts in the binding energy and changes in the electronic density at small internuclear distances in the molecule. On the other hand the linear response of the method makes it challenging to follow changes at internuclear separations at which potential energy curves become quasi-degenerate.

The nonlinear nature of strong-field processes, such as above threshold ionization (Fig. 12.8(b)) or higher-order harmonic generation (Fig. 12.8(c)), promises to provide an alternative to time-resolved photoelectron spectroscopy. Both methods have in common that an ultrashort intense laser pulse is applied as the time-delayed probe pulse. It is well known from past work that harmonic spectra [4, 43–46] as well as ion yields [15, 47–49] reflect the symmetry of the molecular orbital involved in the process due to characteristic interference effects. It has been demonstrated

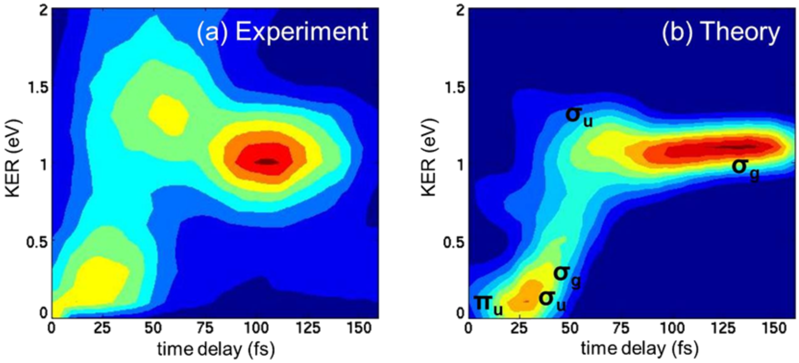

**Fig. 12.9** Comparison of (**a**) experimental ion yields and (**b**) calculated ionization rates of bromine molecule as a function of the kinetic energy release and the time delay after the dissociating pulse [38]. According to the theoretical analysis contributions from different orbitals in the valence shell dominate the ionization signal as the time delay increases. Laser parameters: 400 nm, $2 \times 10^{11}$ W/cm$^2$ and 40 fs (dissociating pulse); 800 nm, $4 \times 10^{13}$ W/cm$^2$ and 30 fs (adapted from [38])

that, in particular, harmonic spectra can reveal the changes in the nuclear and orbital structure up to attosecond time resolution as the configuration of the molecule changes [50, 51] or the molecule dissociates [39]. While the high harmonic signal usually reflects a single-active-electron response, traces of multielectron rearrangement in the valence shell could be observed in the dissociation of bromine molecule using strong-field ionization as a probe signal during the dissociation [38]. Figure 12.9 shows the yields of the ionic fragments as a function of the kinetic energy release and the time delay between the pump and the probe pulses. Experimental data (panel (a)) and theoretical results for ionization rates using the molecular strong-field approximation [15, 48] (panel (b)) are in good agreement. As indicated, the calculations reveal that the response from different orbitals in the valence shell of the dissociating bromine molecule varies as the time delay increases. Surprisingly, one can observe changes in the electron density up to time delays of about 150 fs after the excitation of the molecule, at which the molecule has stretched to more than twice its equilibrium distance. The results therefore show the encouraging perspective that the nonlinear interaction of ultrashort intense laser pulse with the molecule can probe the electronic structure changes even if the potential energy curves are nearly degenerate [38].

## 12.4 Control of Charge Distribution in Molecules

Controlling the dynamics of all constituents in a reaction is a fascinating goal in photochemistry. Due to the rapid progress in femtosecond laser technology it has become possible to accurately change phase, amplitude, and polarization of the different frequency components of a femtosecond laser pulse (for a recent review, see [52]). Such pulses are nowadays an effective tool to control the fragments of a laser

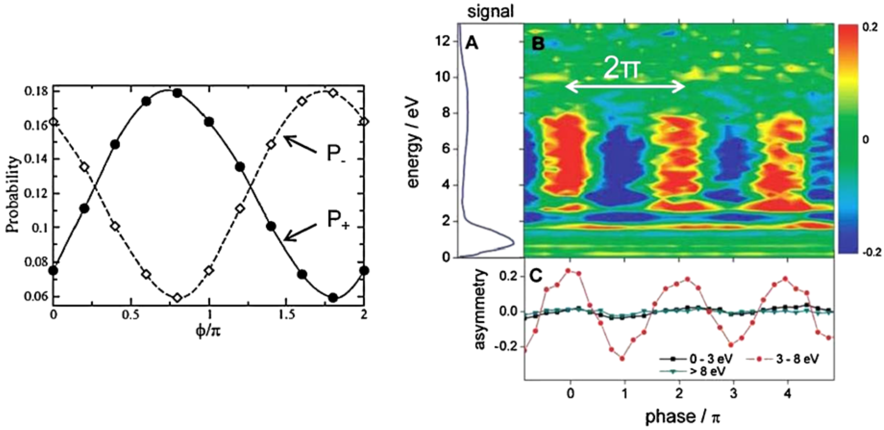

**Fig. 12.10** *Left*: Theoretical predictions by V. Roudnev et al. [56] for a strong asymmetry in the electron localization in positive and negative direction along the internuclear axis in a dissociating hydrogen molecular ion as a function of the carrier-envelope phase of a linearly polarized laser pulse at 800 nm, $9 \times 10^{14}$ W/cm$^2$ and 10 fs. *Right*: Asymmetry parameter $A = (P_+ - P_-)/(P_+ + P_-)$ for electron localization in positive and negative direction along the internuclear axis in dissociation of deuterium molecular ion with a 5 fs, $10^{14}$ W/cm$^2$ laser pulse [57]. (**A**) Without stabilization of the carrier-envelope phase as a function of kinetic energy release, (**B**) as a function of carrier-envelope phase and kinetic energy release and (**C**) as a function of the carrier-envelope phase integrated over several ranges of the kinetic energy release spectrum (adapted from [56] and [57])

induced reaction on the time scale of atomic motion [3, 53]. The development of carrier-envelope phase-locked few-cycle pulses [54] and sub-femtosecond pulses [55] has prepared the ground to go a step further and control the electron dynamics in the molecule itself and in between molecules. In this section we will review different theoretical concepts and experimental realizations of controlling the localization of an electron in a dissociating molecule. As for the observation of intramolecular electron dynamics (see Sect. 12.2) much work has been devoted to the simplest molecules.

### 12.4.1 Control with Carrier-Envelope Phase-Locked Pulses

One method to control electron localization in a dissociating molecule uses few-cycle laser pulses with a controlled evolution of the electric field via a locked carrier-envelope phase. Initial studies in the framework of the time-dependent Schrödinger equation showed that the carrier-envelope phase of an ultrashort intense laser pulse does influence the electron localization probability during the dissociation of the hydrogen molecular ion [56]. The results for the angular distribution of the products in the dissociation, namely the hydrogen atom and the proton, show a strong asymmetry of the localization of the electron at one of the protons with variation of the carrier-envelope phase (left panel of Fig. 12.10).

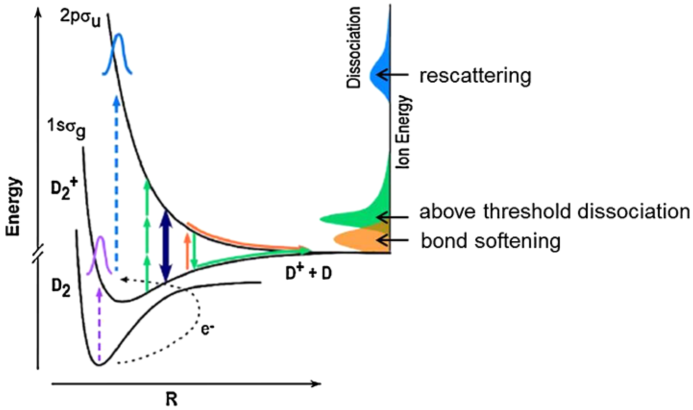

**Fig. 12.11** Dissociation of the deuterium molecular ion due to ionization of the neutral molecule followed by excitation of the ion by the recolling ion (RES, *dashed arrow*) or traditional laser–driven dissociation processes such as bond softening (BS) and above-threshold-dissociation (ATD) (adapted from [58])

Experimental results, in general, confirm the pronounced dependence of the electron localization on the carrier-envelope phase (part C in right hand panel of Fig. 12.10). However, one has to consider that in the experimental studies the hydrogen molecular ion (or, the deuterium molecular ion) is usually produced from the neutrals by the laser pulse itself [57–59] or a preceding few-cycle pulse [60, 61]. Recent experimental studies show that the ionization step from the neutral to the molecular ion itself does not influence the control over the localization of the electron in the dissociating ion [59]. However, the electron set free during the ionization may return to the parent ion. Thus, in the experiments the excitation to the $2p\sigma_u$-state, which starts the dissociation of the molecular ion, may either be induced by the rescattering electron (RES) or by the laser field itself, e.g. via bond softening (BS) or above-threshold-dissociation (ATD) [62]. Experimentally, these pathways can be distinguished in the kinetic energy release (KER) spectrum of the fragments (see Fig. 12.11). Rescattering of the electrons predominantly occurs within one cycle after the ionization event and, hence, at rather short internuclear separations in the molecular ion (corresponding to a higher kinetic energy release) [63]. On the other hand, dissociation by the laser pulse itself is predominantly induced at larger internuclear separations (corresponding to a lower kinetic energy release). The time scale of vibrational motion in the electronic ground state of the ion depends on the mass of nuclei. Therefore dissociation of the light hydrogen molecular ion is found to be predominantly induced by the laser [59], while rescattering induced dissociation appears to be the dominant mechanism for the deuterium molecular ion in ultrashort few-cycle pulses [57]. Consequently, the control over the electron localization has been observed for fragments at low or high kinetic energy release in the respective experiments (for control via the pathway of rescattering induced dissociation, see right panel in Fig. 12.10) .

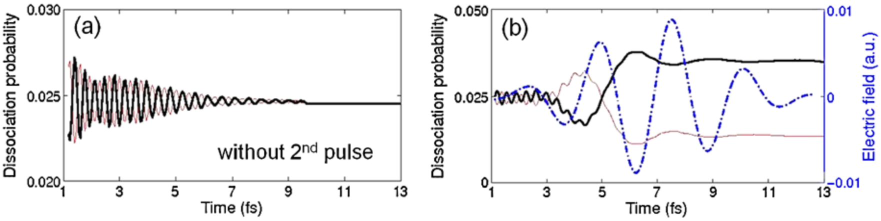

**Fig. 12.12** Electron localization probabilities in the two-pulse control scheme (see Sect. 12.4.2) in positive (*thick line*) and the negative (*thin line*) direction along the internuclear axis (**a**) without controlling second pulse and (**b**) with second time delayed pulse (represented by its electric field as *dashed dotted line*). Laser parameters were: 106 nm, $10^{13}$ W/cm$^2$ and 0.425 fs (for the exciting VUV pulse) and 800 nm, $3 \times 10^{12}$ W/cm$^2$ and 3.8 fs (for the controlling infrared pulse). The time delay between the pulses was 6.9 fs (adapted from [66])

Taking account of effects induced by the rescattering electron requires the development of theoretical approaches which include electron correlation. Models to describe this two-electron dynamics have been proposed recently [63, 64]. However, in most of the theoretical studies on electron localization in the hydrogen molecular ion (and its isotopes) by carrier-envelope phase locked pulses so far, the ionization step and the “first” electron is neglected. Of course, such single-active-electron models do account for the pathways via laser induced dissociation only. In particular, the above-mentioned mass effect has been studied theoretically in Ref. [65].

Once the molecular ion is excited into the $2p\sigma_u$-state field-free dissociation would lead to equal localization probabilities at either one of the two nuclei (for results of related simulations in the two pulse scenario, discussed in Sect. 12.4.2, see Fig. 12.12(a), [66]). Further interaction with the controlled evolution of the field as the nuclei start to separate however creates a coherent superposition of the $1s\sigma_g$- and the $2p\sigma_u$-states, which equivalently can be viewed as coherent superposition of states localized at the two nuclei. The asymmetry of electron localization depends on the ratio of the amplitudes and the relative phase of the population in the two states as the internuclear separation grows. Mixing of the two states should occur at internuclear separations at which there is a resonant transition between the two states. However, it is known that the transition dipole matrix element between the two charge resonant states increases linearly with the internuclear separation [17], which does make a mixing at intermediate internuclear distances beyond the region of resonant transitions feasible as well. As the internuclear distance increases further (to about 6–10 a.u.), the potential barrier between the nuclei rises until the electron density probability finally remains localized at the nuclei [57, 66].

The time it takes for the nuclei to reach this localization region depends on the dissociation pathway (RES, BS, ATD etc.). Thus, the phase of the field at the moment of localization of the electron will depend on the specific pathway as well, which gives rise to significant differences in the observed asymmetries of the localization at the two nuclei. This interpretation is strongly supported by experimental and theoretical data for the localization asymmetries in case of the deuterium molecular ion in a two-color field (superposition of 400 nm and 800 nm radiation

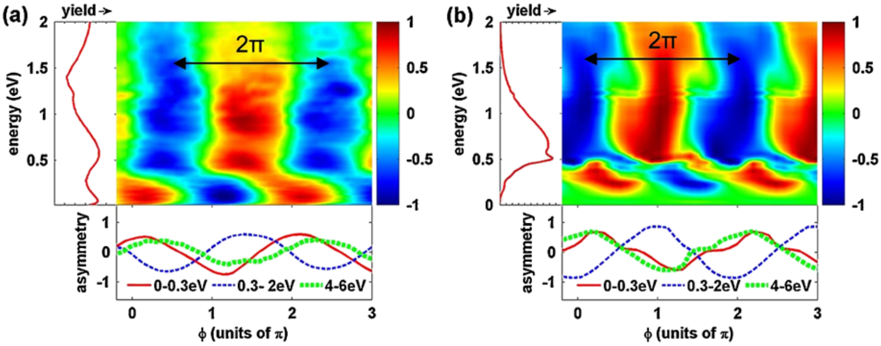

**Fig. 12.13** Comparison of (**a**) experimental and (**b**) theoretical data for the asymmetry of the electron localization in the dissociating deuterium molecular ion as a function of kinetic energy release and relative phase between intense laser pulses at 800 nm and 400 nm [58]. *The panels* show energy spectra integrated over all phases (*left*) and asymmetries integrated over different regions of the kinetic energy release (*bottom*) (adapted from [58])

fields) [58]. The results corresponding to dissociation via bond softening (KER below 0.3 eV), above-threshold-dissociation (KER between 0.3 eV and 2 eV) and rescattering (KER between 4 eV and 6 eV) clearly show a different dependence on the relative phase between the two fields (see Fig. 12.13). Other theoretical studies [67] confirm that the sign of the electric field at the moment of promotion of the electron to the dissociative state is an essential factor which determines whether the electron localizes at the left or the right nucleus.

The degree of the localization can be efficiently enhanced in a pump-probe set-up with two ultrashort carrier-envelope phase locked pulses [60, 61]. The first pulse is used to create a coherent superposition of vibrational states in the electronic ground state of the hydrogen molecular ion, which for strong field ionization can differ from the usually expected Franck-Condon-like distributions [68, 69]. Change of the time delay for the second pulse, which induces the dissociation and controls the electron localization, results in a strong variation of the degree of localization. These experimental data indicate that the control mechanism strongly depends on the form of the nuclear wave packet as it passes the region of coupling between the two states [61]. A control over the internal quantum state (here, the vibrational state) of the molecular ion would be therefore desirable. A coherent control scheme of the population in the vibrational state based on the application of infrared laser pulses has been proposed recently [70].

Understanding of control mechanisms in more complex molecules requires a more efficient theoretical approach than the often used ab-initio simulations of the time-dependent Schrödinger equation in case of the hydrogen molecular ion. Such a model has been recently proposed [67] and successfully applied to analyze experiments on carrier-envelope phase controlled electron localization in deuterium molecule [67], carbon monoxide [71] and deuterium chloride [72]. In the model an electronic wavefunction is defined based on the populations in the relevant electronic states and interference terms between the states at a given internuclear distance. The nuclear dynamics is determined via calculations of potential energy surfaces using elaborate quantum-chemical program packages. The temporal evolution of the electronic wavefunction results then from the changes in the orbitals with internuclear distance. This approach, in which the coupling of electronic to nuclear dynamics is considered in style of the Born-Oppenheimer approximation, allows for the desired efficient calculation of the localization dynamics in larger molecules.

### *12.4.2 Control with an Attosecond Pump Pulse (Train) and an Infrared Probe Pulse*

An alternative approach to control the electron localization in the hydrogen molecular ion makes use of two time-delayed coherent pulses [66]. The first attosecond pulse initiates the dissociation of the hydrogen molecular ion, either by excitation to the $2p\sigma_u$-state from the ground state of the ion [66] or by ionization of the neutral hydrogen molecule accompanied by excitation to the dissociative state of the ion [73, 74]. The time-delayed second pulse is then used to steer the electron between the protons by effective mixing of the population in the ground and the first excited electronic state at intermediate internuclear separations of the protons. The results of numerical solutions of the time-dependent Schrödinger equation in Fig. 12.12 show how the electric field of the second time-delayed pulse breaks the symmetry in electron localization for a field-free dissociation (panel (a)) and drives the electron in the molecule, which results in a high degree of control over the electron localization at one of the protons in the dissociating hydrogen molecular ion (panel (b)) [66].

In the two-pulse scenario the carrier-envelope phase of the second pulse is used to steer the electron localization independent of the dissociation step, which may enhance the asymmetries in the localization probabilities [75]. Results of numerical simulations confirm the importance of two parameters, the time delay between the pulses and the carrier-envelope phase of the second probe pulse, for the control of the electron localization (see Fig. 12.14) [76]. However the control mechanism, and hence the dependence of the localization probabilities on the control parameters becomes significantly more complex, when the intramolecular electron dynamics varies strongly at high field strengths, as discussed in Sect. 12.2.1 [14].

General features of the two-pulse control strategy are confirmed in recent experiments [73, 74]. The excitation of the molecular ion to the dissociative $2p\sigma_u$-state, accompanied in the experiment by ionization of the initially prepared deuterium molecules, is induced by either a single attosecond pulse [74] or an attosecond pulse train [73]. An interesting aspect of the latter study is that a control of the localization can be achieved only, if the pulses in the train are separated by the full cycle of the infrared field (see Fig. 12.15(a)), which can be achieved by mixing the driving field with its second harmonic [77, 78]. This dependence on the time delay of pulses in the train was theoretically predicted [79] and can be readily explained by the results of numerical simulations, presented in Figs. 12.15(b) and (c). For a separation of the attosecond pulses by a full cycle (panel (b)) the individual electron wave packets, generated by the pulses in the train, are directed by the control field to the same

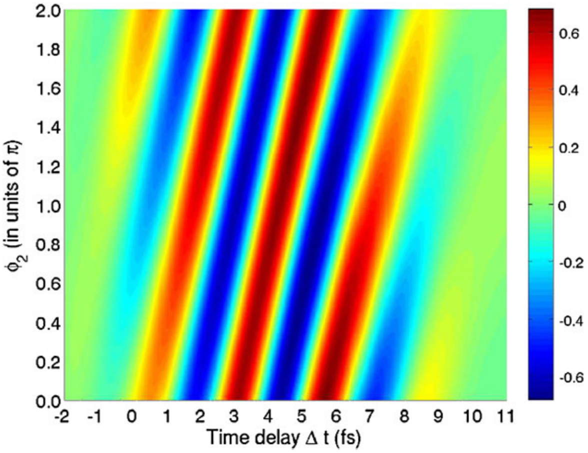

**Fig. 12.14** Results of numerical simulations for the asymmetry parameter $A = (P_- - P_+)/(P_- + P_+)$, where $P_\pm$ is the differential ionization probability in positive and negative direction along the internuclear axis, as a function of the time delay $\Delta t$ between the two pulses and the carrier-envelope phase $\phi_2$ of the second pulse in a two-pulse control scheme [76]. The parameters of the two laser pulses in the simulations were: $10^{13}$ W/cm$^2$ (peak intensity), 106 nm (wavelength) and 0.425 fs (pulse length) for the exciting VUV first pulse and $3 \times 10^{12}$ W/cm$^2$ (peak intensity), 800 nm (wavelength) and 5.8 fs (pulse length) for the controlling second infrared pulse

nucleus as they are in phase with the control field. On the other hand electron wave packets generated by pulses separated by a half cycle of the driving pulse are out of phase with the control field and directed to opposite nuclei (panel (c)). Thus, while in both scenarios there is control over each of the electron wave packets, a variation of the total asymmetry parameter will occur in the previous case only [79]. A similar analysis holds when the molecular ion is excited by a series of rescattering events [58]. In this case excitation once every cycle is as well achieved by superimposing the driving field with its second harmonic (see results at KER between 4 eV and 6 eV in Fig. 12.13).

Recently, experimental studies of the two-pulse scenario were performed with unequaled time resolution using a single attosecond pulse of 300–400 as in duration together with an infrared laser pulse having a pulse length of about 5 fs. The experimental data were analyzed on the basis of high-precision numerical simulations taking account of all electronic and vibrational degrees of freedom [74]. The combined experimental and computational efforts revealed another, previously undetermined, complex localization mechanism, in which the infrared pulse induces a quantum mechanical interference between different states in the ion, including autoionizing states, at short internuclear separations close to the equilibrium distance. These results show that attosecond pulse technology can become a powerful technique to control electron dynamics even in systems with strong couplings between many electronic-vibrational levels.

The fascinating idea to guide an electronic wavepacket has been recently studied in more complex molecules as well [80–83]. For example, new mechanisms for the

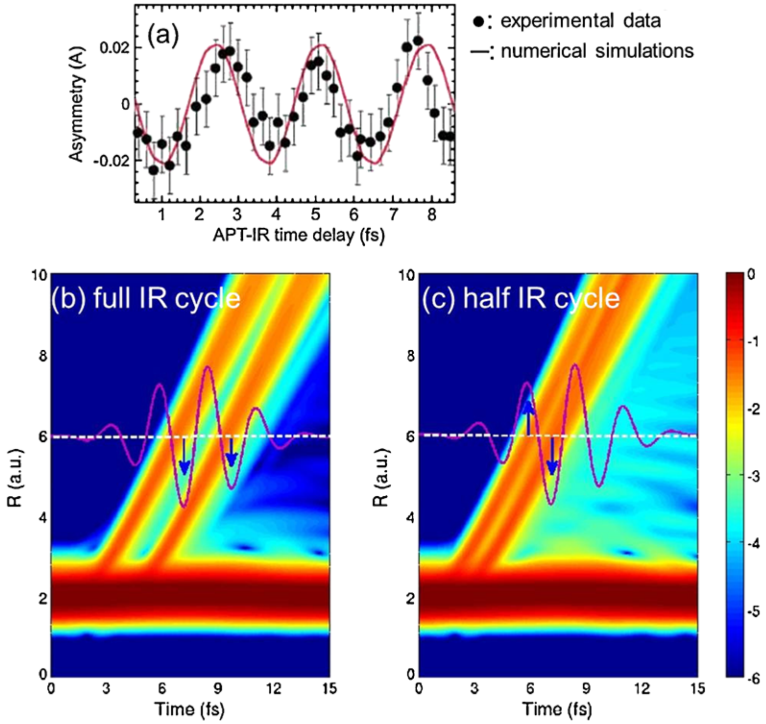

**Fig. 12.15** (**a**) Comparison of experimental data (*circles* with error bars) with results of numerical simulations (*line*) for the asymmetry parameter $A$ of electron localization in deuterium molecular ion as a function between the exciting attosecond pulse train (pulse duration: 400 as for the individual pulse) and the controlling infrared pulse (800 nm, $5 \times 10^{13}$ W/cm$^2$, 40 fs) [73]. (**b**), (**c**) Integrated electron probability density as a function of the internuclear separation $R$ and the time delay after initiation of the dissociation of the hydrogen molecular ion by an attosecond pulse train in which the pulses are either separated by a full cycle (panel (**b**)) or a half cycle (panel (**c**)) of the controlling infrared laser pulse [79] (adapted from [73] and [79])

**Fig. 12.16** Theoretical result by I. Barth et al. [81] for an electronic ring current in an oriented Mg-porphyrin molecule, which is induced by a circularly polarized laser pulse. Laser parameters: 3.42 eV (frequency), $1.28 \times 10^{12}$ W/cm$^2$ (peak intensity) and 9.67 fs (pulse duration) (adapted from [81])

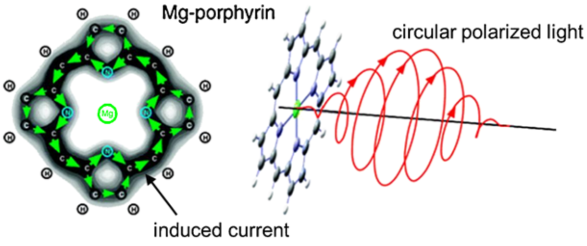

induction of electronic ring currents have been proposed and theoretically demonstrated in Mg-porphyrin [81] and chiral aromatic molecules [83]. An example of the induced electronic dynamics is shown in Fig. 12.16. The flux in the oriented Mg-porphyrin molecule is driven by a circularly polarized UV $\pi$ laser pulse on the time scale of the pulse duration of a few femtoseconds.

**Acknowledgements** We appreciate collaborations and discussions with many colleagues on the topics presented in this Chapter. In particular we like to acknowledge in this respect A. Bahabad, J. Biegert, S.L. Chin, C.L. Cocke, R. Dörner, F.H.M. Faisal, H.C. Kapteyn, H. Kono, W. Li, M.M. Murnane, M. Odenweller, and U. Thumm. We further acknowledge financial support by the US National Science Foundation (JILA Physics Frontier Center under Grant No. 1125844, Engineering Research Center for Extreme Ultraviolet Science and Technology and Grant No. 1068706), US Department of Energy (Chemical Sciences, Geosciences, and Biosciences Division, Office of Basic Energy Sciences, Grant No. DE-FG02-09ER16103), the National Science Foundation of Shanghai (Grant No. 11ZR1417100), the Pujiang Scholar Foundation (Grant No. 11PJ404800), the National Science Foundation of China (Grant No. 11104180, 11175120) and the Spanish Ministry of Science via their postdoctoral program.

## References

1. A.H. Zewail, J. Phys. Chem. A **104**, 5660 (2000)
2. T. Popmintchev, M.C. Chen, P. Arpin, M.M. Murnane, H.C. Kapteyn, Nat. Photonics **4**, 822 (2010)
3. A. Assion, T. Baumert, M. Bergt, T. Brixner, B. Kiefer, V. Seyfried, M. Strehle, G. Gerber, Science **282**, 919 (1998)
4. J. Itatani, J. Levesque, D. Zeidler, H. Niikura, H. Pepin, J.C. Kieffer, P.B. Corkum, D.M. Villeneuve, Nature **432**, 867 (2004)
5. L.V. Keldysh, Zh. Eksp. Teor. Fiz. **47**, 1945 (1964). Engl. Transl. in Sov. Phys. JETP **20**, 1307 (1964)
6. M. Uiberacker, Th. Uphues, M. Schultze, A.J. Verhoef, V. Yakovlev, M.F. Kling, J. Rauschenberger, N.M. Kabachnik, H. Schröder, M. Lezius, K.L. Kompa, H.-G. Muller, M.J.J. Vrakking, S. Hendel, U. Kleineberg, U. Heinzmann, M. Drescher, F. Krausz, Nature **446**, 627 (2007)
7. R.S. Mulliken, J. Chem. Phys. **7**, 20 (1939)
8. T. Zuo, A.D. Bandrauk, Phys. Rev. A **52**, R2511 (1995)
9. T. Seideman, M.Yu. Ivanov, P.B. Corkum, Phys. Rev. Lett. **75**, 2819 (1995)
10. G.N. Gibson, M. Li, C. Guo, J. Neira, Phys. Rev. Lett. **79**, 2022 (1997)
11. N. Takemoto, A. Becker, Phys. Rev. Lett. **105**, 203004 (2010)
12. N. Takemoto, A. Becker, Phys. Rev. A **84**, 023401 (2011)
13. I. Kawata, H. Kono, Y. Fujimura, J. Chem. Phys. **110**, 11152 (1999)
14. F. He, A. Becker, U. Thumm, Phys. Rev. Lett. **101**, 213002 (2008)
15. J. Muth-Böhm, A. Becker, F.H.M. Faisal, Phys. Rev. Lett. **85**, 2280 (2000)
16. N. Takemoto, A. Becker, J. Chem. Phys. **134**, 074309 (2011)
17. K.C. Kulander, F.H. Mies, K.J. Schafer, Phys. Rev. A **53**, 2562 (1996)
18. A.D. Bandrauk, S. Chelkowski, H.S. Nguyen, Int. J. Quant. Chem. **100**, 834 (2004)
19. G.L. Yudin, S. Chelkowski, J. Itatani, A.D. Bandrauk, P.B. Corkum, Phys. Rev. A **72**, 051401(R) (2005)
20. F. Krausz, M. Ivanov, Rev. Mod. Phys. **81**, 163 (2009)
21. S. Gräfe, V. Engel, M.Yu. Ivanov, Phys. Rev. Lett. **101**, 103001 (2008)
22. T. Young, Philos. Trans. R. Soc. Lond. **94**, 1 (1804)
23. H.D. Cohen, U. Fano, Phys. Rev. **150**, 30 (1966)
24. G.L. Yudin, S. Chelkowski, A.D. Bandrauk, J. Phys. B, At. Mol. Opt. Phys. **39**, L17 (2006)
25. S. Chelkowski, A.D. Bandrauk, Phys. Rev. A **81**, 062101 (2010)
26. A. Picón, A. Bahabad, H.C. Kapteyn, M.M. Murnane, A. Becker, Phys. Rev. A **83**, 013414 (2011)

27. A.V. Davis, R. Wester, A.E. Bragg, D.M. Neumark, J. Chem. Phys. **118**, 999 (2003)
28. R. Mabbs, K. Pichugin, A. Sanov, J. Chem. Phys. **122**, 174305 (2005)
29. R. Mabbs, K. Pichugin, A. Sanov, J. Chem. Phys. **123**, 0534329 (2005)
30. T. Bredtmann, S. Chelkowski, A.D. Bandrauk, Phys. Rev. A **84**, 021401 (2011)
31. S.A. Hilbert, C. Uiterwaal, B. Barwick, H. Batelaan, A.H. Zewail, Proc. Natl. Acad. Sci. USA **106**, 10558 (2009)
32. H.-C. Shao, A.F. Starace, Phys. Rev. Lett. **105**, 263201 (2010)
33. P.B. Corkum, N.H. Burnett, F. Brunel, Phys. Rev. Lett. **62**, 1259 (1989)
34. P. Eckle, M. Smolarski, P. Schlup, J. Biegert, A. Staudte, M. Schöffler, H.G. Muller, R. Dörner, U. Keller, Nat. Phys. **4**, 565 (2008)
35. A.N. Pfeiffer, C. Cirelli, M. Smolarski, R. Dörner, U. Keller, Nat. Phys. **7**, 428 (2011)
36. M. Odenweller, N. Takemoto, A. Vredenborg, K. Cole, K. Pahl, J. Titze, L.Ph.H. Schmidt, T. Jahnke, R. Dörner, A. Becker, Phys. Rev. Lett. **107**, 143004 (2011)
37. O. Geßner, A.M.D. Lee, J.P. Shaffer, S.V. Levchenko, A.I. Krylov, J.G. Underwood, H. Shi, A.L.L. East, D.M. Wardlaw, E.T.H. Chrysotom, C.C. Hayden, A. Stolow, Science **311**, 219 (2006)
38. W. Li, A.A. Jaroń-Becker, C.W. Hogle, V. Sharma, X. Zhou, A. Becker, H.C. Kapteyn, M.M. Murnane, Proc. Natl. Acad. Sci. USA **107**, 20219 (2010)
39. H.J. Worner, J.B. Bertrand, D.V. Kartashov, P.B. Corkum, D.M. Villeneuve, Nature **466**, 604 (2010)
40. A.S. Sandhu, E. Gagnon, R. Santra, V. Sharma, W. Li, P. Ho, P. Ranitovic, C.L. Cocke, M.M. Murnane, H.C. Kapteyn, Science **322**, 1081 (2008)
41. C.Z. Bisgaard, O.J. Clarkin, G. Wu, A.M.D. Lee, O. Geßner, C.C. Hayden, A. Stolow, Science **323**, 1464 (2009)
42. Ph. Wernet, M. Odelius, K. Godehusen, J. Gaudin, O. Schwarzkopf, W. Eberhardt, Phys. Rev. Lett. **103**, 013001 (2009)
43. M. Lein, N. Hay, R. Velotta, J.P. Marangos, P.L. Knight, Phys. Rev. Lett. **88**, 183903 (2002)
44. P. Torres, N. Kajumba, J.G. Underwood, J.S. Robinson, S. Baker, J.W.G. Tisch, R. deNalda, W.A. Bryan, C. Altucci, I.C.E. Turcu, J.P. Marangos, Phys. Rev. Lett. **98**, 203007 (2007)
45. M.F. Ciappina, A. Jaroń-Becker, A. Becker, Phys. Rev. A **76**, 063406 (2007)
46. X. Zhou, R. Lock, W. Li, N. Wagner, M.M. Murnane, H.C. Kapteyn, Phys. Rev. Lett. **100**, 073902 (2008)
47. X.M. Tong, C.D. Lin, Phys. Rev. A **66**, 033402 (2002)
48. A. Jaroń-Becker, A. Becker, F.H.M. Faisal, Phys. Rev. A **69**, 023410 (2004)
49. A. Jaroń-Becker, A. Becker, F.H.M. Faisal, Phys. Rev. Lett. **96**, 143006 (2006)
50. W. Li, X. Zhou, R. Lock, S. Patchkovskii, A. Stolow, H.C. Kapteyn, M.M. Murnane, Science **322**, 1207 (2008)
51. S. Baker, J.S. Robinson, M. Lein, C.C. Chirila, R. Torres, H.C. Bandulet, D. Comtois, J.C. Kieffer, D.M. Villeneuve, J.W.G. Tisch, J.P. Marangos, Phys. Rev. Lett. **101**, 053901 (2008)
52. A. Weiner, Opt. Commun. **284**, 3669 (2011)
53. R.S. Judson, H. Rabitz, Phys. Rev. Lett. **68**, 1500 (1992)
54. C.P. Hauri, W. Kornelis, F.W. Helbing, A. Heinrich, A. Couairon, A. Mysyrowicz, J. Biegert, U. Keller, Appl. Phys. B **79**, 673 (2004)
55. M. Hentschel, R. Keinberger, Ch. Spielmann, G.A. Reider, N. Milosevic, T. Brabec, P. Corkum, U. Heinzmann, M. Drescher, F. Krausz, Nature **414**, 509 (2001)
56. V. Roudnev, B.D. Esry, I. Ben-Itzhak, Phys. Rev. Lett. **93**, 163601 (2004)
57. M.F. Kling, Ch. Siedschlag, A.J. Verhoef, J.I. Khan, Th. Uphues, Y. Ni, M. Uiberacker, M. Drescher, F. Krausz, M.J.J. Vrakking, Science **312**, 246 (2006)
58. D. Ray, F. He, S. De, W. Cao, H. Mashiko, P. Ranitovic, K.P. Singh, I. Znakovskaya, U. Thumm, G.G. Paulus, M.F. Kling, I.V. Litvinjyuk, C.L. Cocke, Phys. Rev. Lett. **103**, 223001 (2009)
59. M. Kremer, B. Fischer, B. Feuerstein, V.L.B. de Jesus, V. Sharma, C. Hofrichter, A. Rudenko, U. Thumm, C.D. Schröter, R. Moshammer, J. Ullrich, Phys. Rev. Lett. **103**, 213003 (2009)

60. C.R. Calvert, R.B. Kling, W.A. Bryan, W.R. Newell, J.F. McCann, J.B. Greenwood, I.D. Williams, J. Phys. B, At. Mol. Opt. Phys. **43**, 011001 (2010)
61. B. Fischer, M. Kremer, T. Pfeifer, B. Feuerstein, V. Sharma, U. Thumm, C.D. Schröter, R. Moshammer, J. Ullrich, Phys. Rev. Lett. **105**, 223001 (2010)
62. A. Zavriyev, P.H. Bucksbaum, H.G. Muller, D.W. Schumacher, Phys. Rev. A **42**, 5500 (1990)
63. X.M. Tong, C.D. Lin, Phys. Rev. Lett. **98**, 123002 (2007)
64. S. Gräfe, M.Yu. Ivanov, Phys. Rev. Lett. **99**, 163603 (2007)
65. J.J. Hua, B.D. Esry, J. Phys. B, At. Mol. Opt. Phys. **42**, 085601 (2009)
66. F. He, C. Ruiz, A. Becker, Phys. Rev. Lett. **99**, 083002 (2007)
67. D. Geppert, P. von den Hoff, R. de Vivie-Riedle, J. Phys. B, At. Mol. Opt. Phys. **41**, 074006 (2008)
68. X. Urbain, B. Fabre, E.M. Staicu-Casagrande, N. de Ruette, V.M. Andrianarijaona, J. Juretta, J.H. Posthumus, A. Saenz, E. Baldit, C. Cornaggia, Phys. Rev. Lett. **92**, 163004 (2004)
69. E. Goll, G. Wunner, A. Saenz, Phys. Rev. Lett. **97**, 103003 (2006)
70. A. Picón, J. Biegert, A. Jaroń-Becker, A. Becker, Phys. Rev. A **83**, 023412 (2011)
71. I. Znakovskaya, P. von den Hoff, S. Zherebtsov, A. Wirth, O. Herrwerth, M.J.J. Vrakking, R. de Vivie-Riedle, M.F. Kling, Phys. Rev. Lett. **103**, 103002 (2009)
72. I. Znakovskaya, P. von den Hoff, N. Schirmel, G. Urbasch, S. Zherebtsov, B. Bergues, R. de Vivie-Riedle, K.-M. Weitzel, M.F. Kling, Phys. Chem. Chem. Phys. **13**, 8653 (2011)
73. K.P. Singh, F. He, P. Ranitovic, W. Cao, S. De, D. Ray, S. Chen, U. Thumm, A. Becker, M.M. Murnane, H.C. Kapteyn, I.V. Litvinyuk, C.L. Cocke, Phys. Rev. Lett. **104**, 023001 (2010)
74. G. Sansone, F. Kelkensberg, J.F. Pérez-Torres, F. Morales, M.F. Kling, W. Siu, O. Ghafur, P. Johnsson, M. Swoboda, E. Benedetti, F. Ferrari, F. Lépine, J.L. Sanz-Vicario, S. Zherebtsov, I. Znakovskaya, A. L'Huillier, M.Yu. Ivanov, M. Nisoli, F. Martin, M.J.J. Vrakking, Nature **465**, 763 (2010)
75. F. He, A. Becker, J. Phys. B, At. Mol. Opt. Phys. **41**, 074017 (2008)
76. F. He, C. Ruiz, A. Becker, unpublished
77. J. Mauritsson, P. Johnsson, E. Gustafsson, A. L'Huillier, K.J. Schafer, M.B. Gaarde, Phys. Rev. Lett. **97**, 013001 (2006)
78. N. Dudovich, O. Smirnova, J. Levesque, Y. Mairesse, M.Yu. Ivanov, D.M. Villeneuve, P.B. Corkum, Nat. Phys. **2**, 781 (2006)
79. F. He, C. Ruiz, A. Becker, J. Phys. B, At. Mol. Opt. Phys. **41**, 081003 (2008)
80. P. Krause, T. Klamroth, P. Saalfrank, J. Chem. Phys. **123**, 074105 (2005)
81. I. Barth, J. Manz, Y. Shigeta, K. Yagi, J. Am. Chem. Soc. **128**, 7043 (2006)
82. F. Remacle, R.D. Levine, Proc. Natl. Acad. Sci. USA **103**, 6793 (2006)
83. M. Kanno, H. Kono, Y. Fujimura, S.H. Lin, Phys. Rev. Lett. **104**, 108302 (2010)

# Chapter 13
# Attosecond Time-Resolved Photoemission Spectroscopy in Condensed Matter—Photoelectron Wave Phase Shifts and Time Delays

**Ulrich Heinzmann**

**Abstract** The chapter reviews the first attosecond time-resolved photoemission experiment performed on a tungsten single crystal surface and discusses the status and the limitations of this research field in condensed matter. It also discusses the relationship between photoelectron wave phase shifts obtained in spin-resolved photoemission experiments and attosecond Wigner time delays of the photoelectron emission for certain orbital angular momenta. Finally it reviews similar ESCA (electron spectroscopy for chemical analysis) photoemission measurements recently performed on a solid as well as on a molecular adsorbate with some femtosecond time and 0.1 eV energy resolution.

## 13.1 Introduction

For about 100 years the photoemission process has been one of the most important analyzing methods for studying the electronic structure of matter. Where light intensities are not too strong each absorbed photon creates one free electron which may leave the solid crystal and its surface as a photoelectron. The kinetic energy of this photoelectron is given by the light energy minus the work function (difference between the vacuum energy level and the Fermi energy) minus the binding energy with respect to the Fermi energy. Visible and UV-light is used to eject non-localized electrons from the conduction band and XUV radiation is used to additionally eject electrons localized in the inner-shell of a certain atom in the bulk of the crystal or on its surface.

The motion of electrons in metallic solids, i.e. conductivity, is the basis of modern electronic technology; the absorption of photons triggers the excitation of bound electrons to the conduction band and can be used as a fast switch [1]. Photoelectrons only from the first few atomic layers are able to leave the crystal [2] and thus photoemission has been demonstrated as being a very surface-sensitive experimental tool for the broad field of surface chemistry and surface physics [3]. The successful

---

U. Heinzmann (✉)
Faculty of Physics (Molecular and Surface Physics), University of Bielefeld, P.O. Box 10 01 31, 33501 Bielefeld, Germany
e-mail: uheinzm@Physik.Uni-Bielefeld.de

L. Plaja et al. (eds.), *Attosecond Physics*, Springer Series in Optical Sciences 177,
DOI 10.1007/978-3-642-37623-8_13,

development of fs-lasers in the ultraviolet (UV) and soft x-ray in the past decades has allowed the study of processes of chemical reactions at the surface [4] and thus of related electronic transitions on metal surfaces [5], molecular adsorbates [6], interfaces [7], magnetic adlayers [8] and semiconductors [9]: Two-photon photoemission experiments (2PPE) have enabled measurement of the lifetime of excited states [10], coherent electronic wave-packets on metal surfaces have been observed [11], laser assisted photoemission studies on a metal surface have been performed [12] and surface photo-voltage transients on a semi-conductor surface have been studied experimentally with fs-time resolution [13].

## 13.2 Sub-femtosecond Time-Resolved Photoemission Experiments

In 2005 the life-time of a Koster-Kronig decay in an adsorbate was measured with sub-femtosecond resolution by means of core-hole clock spectroscopy (CHC) [14]: A core electron of an atom, for example sulphur in this case, adsorbed on a Ru(0001) surface is promoted by resonant excitation from the ground state 2s to the 3p state above the Fermi energy but below the vacuum level creating a core-hole with a life time of 500 as. But the adsorbate bound to the surface is not isolated so it can exchange charge and energy. If the status of the resonantly excited electron changes during the lifetime of the core level, the coherence of excitation and decay is lost. By quantitative cross-comparison of the intensities for the resonant Auger (also called Auger Resonant Raman Effect, ARRE) and the normal Auger processes, the charge transfer time for electron transfer from the adsorbate to the solid is given by the ratio of both intensities in units of the core hole lifetime. Thus with CHC-spectroscopy by means of CW-radiation (for example synchrotron radiation) it was possible to indirectly study the dynamics of an electron transfer between different parts of an adsorbate system resolved in time with attosecond accuracy by cross-comparing the intensities of different Auger electrons emitted.

In 2007 the first real attosecond time-resolved photoemission experiment in condensed matter with ultrashort XUV laser radiation was performed on the W(110) surface [15]. The photoemission process is often described in the three-step model: (i) photoexcitation to an upper band as an intermediate bound state; (ii) transport of the electron through the crystal in the presence of a screened hole state; (iii) escape through the surface accompanied by creation of an image charge. In the past, the timescale on which these processes occur was inaccessible to experiments. On the one hand it was possible to calculate the transport time of a 60 eV electron from a bulk atom to the surface using a classical approach as being about 200 as, taking into account that the electron escape depth for these energies is just a few atomic layers, i.e. about 0.5–1 nm [2]. On the other hand the escape through the surface has been seen up to now to be instantaneous in time, like the tunnel process in atoms whose time dynamics has recently become a matter of topical research [16]. The motion of electrons in the upper conduction band to the surface takes place as an ultrashort wave-packet with a certain group velocity. In order to describe single-electron motions in many-electron bands as a single particle flow, the effective mass $m^*$ which may be different from sub-band to sub-band has to be used instead of the free-electron mass $m$ keeping its charge $e$ constant. During photoemission, the hole state is screened by the non-localized neighbouring electrons. Furthermore, the photoelectron leaves the metal surface in the presence of an image charge. The time dynamics of hole-screening and image charge creation and decay have been studied theoretically [5, 17] and offer now access to experimental studies in condensed matter physics. None of the above-mentioned femtosecond methods, however, have shown the dynamics of electron emission in time directly. The sequential emission of photoelectrons from different bands of a metal solid on an attosecond timescale, and the duration of the photoelectron pulse, were the showcase examples of [15] and opened up the new field of attosecond spectroscopy of solids.

Attosecond resolved photoionization of free-atoms in an atomic beam had already been performed prior to 2007 by use of an ultrashort near-IR-light pulse (NIR) [18] with a stabilized carrier envelope phase as the clock: A single 250 attosecond long pulse of extreme ultraviolet radiation (XUV) from NIR laser-induced High Harmonic Generation was used to photoionize the atom and to trigger the motion of the emitted photoelectron with respect to the phase of the oscillating electric field underneath the ultrashort NIR light pulse [19]. Since the duration of the photoelectron pulse (250 as) was short compared with the oscillating period of the NIR pulse (2.3 fs), the emitted electrons were accelerated or decelerated like ballistic particles by the phase-stabilized, non-jittering electric field of the NIR pulse. Thus the atomic photoelectrons either won or lost kinetic energy up to 20 eV additionally as in a conventional streak camera. The existence of such "streaking curves" i.e. oscillation of the photoelectron kinetic energy as a function of the delay between attosecond XUV-pulse and NIR-pulse demonstrated the attosecond duration of the atomic photoelectron pulse and presented the delay of the NIR-pulse as a real-time clock to determine experimentally the delays of emission times for the different kinds of electrons emitted (for example Auger vs. photoelectrons) [20]. Very recently the delay of different photoelectrons in atomic photoionization has been experimentally identified as being 21 as [21]. These attosecond-resolved photoelectron emission experiments on isolated atoms in the gas-phase gave rise to the question as to whether such an attosecond time-resolved photoemission experiment could in principle be performed on a solid crystal directly opening up attosecond spectroscopy for application in condensed matter physics. It is the objective of the present chapter to review this first attosecond resolved photoemission experiment [15] using a tungsten single crystal as a photoelectron emitter and to discuss the status of the field today.

What is completely different between photoemission from a metal crystal compared with atomic photoionization?

1. The radiation hits $10^8$ times more atoms in the condensed matter case than in atomic beam experiments. The atoms have a neighbour distance of about 0.3 nm so that the outermost atomic orbitals overlap creating a conduction band with

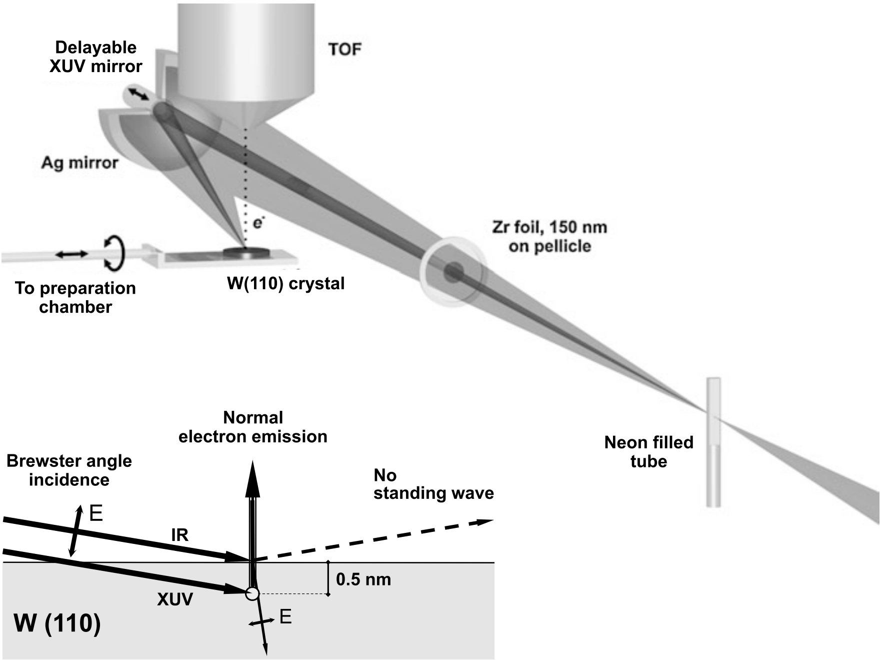

**Fig. 13.1** Experimental set up of the attosecond time-resolved photoemission experiment with W(110) (adapted from Ref. [15]). The 5 fs laser pulse produces the XUV 300 as pulse (HHG) in the neon-filled tube and co-propagates with the XUV via the delayable double mirror system to the W(110) crystal surface in Brewster geometry (*inset*). The photoemission in the direction normal to the surface in the presence of the linearly polarized IR pulse is studied by means of the time of flight (TOF) spectrometer as a function of the delay between IR and XUV pulse (streaking technique)

many non-localized electrons in the initial state. The electron spectrum in photoemission from core states is additionally complicated by a core level shift of the surface atoms compared to the bulk atoms—in this case of W(110) 4f state it is 0.3 eV [22, 23]—i.e. the source of photoelectrons has different locations in the solid; they also have different binding energies for the same electronic states and they have different velocities in the solid before they escape through the surface compared to the case outside the crystal.

2. The streaking technique as a time-clock uses a NIR pulse whose electric field accelerates or decelerates the photoelectrons in a free-free transition. Is this different in the presence of a metallic surface? The decision was made to use a set-up involving a collinear input of XUV and NIR at a grazing incidence angle in order to have the electric field of the NIR light nearly perpendicular to the surface (p-light geometry) (see Fig. 13.1, inset). Furthermore a Brewster angle geometry was used in order to avoid standing waves at the surface due to constructive interference of the incoming and reflected NIR and thus E-field nodes which obviously would make the streaking technique impossible.

3. Unlike atoms with only a few electronic states at certain energies, condensed matter has bands with many occupied and unoccupied states, also far beyond the Fermi energy. Thus multiphoton excitations and above-threshold ionization processes occur on account of the presence of the strong NIR pulse alone. This increases dramatically the unwanted background with respect to the single XUV-photoelectron spectra and free-free transitions due to the NIR laser-pulse as a streaking clock. Furthermore a compromise had to be made between the energy resolution for photoelectron spectroscopy necessary in order to discriminate between the different solid state bands and time-resolution. Being presented the opportunity of varying the multilayer XUV-optics to determine radiation bandwidths of between 1 and 15 eV corresponding to 2 fs [24] to 150 as [25, 26] led to the decision to use a multilayer XUV mirror for 91 eV radiation energy with a 6 eV bandwidth which corresponded to a time resolution of 300 as.

Figure 13.1 describes schematically the set up of the new experiment. Tungsten has been used as the photoemission target, since unlike other solids the electron escape depth (mean free path) for photoelectron kinetic energies around 90 eV is lower (2 atomic layers) than at 50 eV (3 atomic layers) [27] with the consequence that the slower photoelectrons escape later not only due to the smaller velocity but also due to their location of birth deeper in the crystal.

A linearly polarized, waveform-controlled 5 fs, 0.4 mJ, 750 nm ($T_0 = 2.5$ fs) laser pulse with carefully optimized values of carrier envelope phase produced one isolated single XUV pulse at the high energy end of the High Harmonic spectral comb at $(\hbar\omega_{XUV})_{mean} = 91$ eV in a gas of neon atoms. The XUV pulse copropagated with the laser pulse in a collinear, laser-like beam to a W(110) crystal under the grazing Brewster angle of 15 degrees placed in the focus of a spherical, two-component, Mo/Si multilayer mirror of 120-mm focal length [28]. It was separated from the NIR in the inner part of the laser beam by a zirconium pellicle, which blocked the NIR but not the XUV. The inner mirror reflected XUV radiation over a band of $\sim$ 6 eV, centred at $\sim$91 eV. Consequently, the XUV pulse created photoelectrons with a kinetic energy of $p_i^2/2m = \hbar\omega_{XUV} - W_b$, (where $W_b$ is the electron's binding energy, plus the work function of the crystal) spread over a 6 eV band, with $p_i$ being the momentum of the electron. The volume of the light-field probing was defined laterally by the $< 10$ μm diameter of the XUV beam at its focus and longitudinally by the escape depth of the photoelectrons as being about 1 nm which is well confined within the focal volume of the laser beam (diameter $> 60$ μm). For $p_i^2/2m \approx 100$ eV, the electrons travelled less than 100 nm within 10 fs and hence remained safely confined to the region of constant laser field amplitude outside the crystal surface. Inside the crystal a constant laser field was also approximatively assumed within the 1 nm layer thickness where the photoelectrons could only escape the crystal surface. But due to refraction of the IR laser radiation at the surface (outermost conduction band of the first row of atoms), there was no acceleration of the electrons emitted normal to the surface inside the crystal because of the linear polarization nearly parallel to the surface (see inset in Fig. 13.1).

Once placed in the electric field of a linearly polarized wave, the change of the electrons momentum $\Delta p(\mathbf{r},t)$ at the location $\mathbf{r}$ and time $t$ along the direction of the electric field is given by

$$\Delta p(\mathbf{r},t) = e\int_t^{\infty} E_L\big(\mathbf{r},t'\big)dt' = eA_L(\mathbf{r},t)$$

where $A_L(\mathbf{r},t)$ is the vector potential of the electric field $E_L(\mathbf{r},t) = E_0\varepsilon_L(\mathbf{r},t) \times \cos(\mathbf{kr} - \omega_L t + \varphi)$, where $E_0$ is the maximum field amplitude and $\mathbf{k}$ is the wave vector. Thus the change of the kinetic energy due to the interaction with the NIR is given by $\Delta W(t) \approx e(p_i/m)A_L(t)$.

These considerations suggest that the electron probe needs to be localized not only in time to a tiny fraction of the wave period $T_0$, but also in space to a tiny fraction of the wavelength $\lambda_L$ of the light. The latter requirement can be substantially relaxed if the electron release is triggered with an energetic photon pulse that co-propagates with the NIR laser wave in a collinear beam. This was certainly true outside the crystal. Thus the timing of the probe electrons relative to the light field was invariant to space along the laser propagation in this case. The field-induced variation of the final energy spectrum of the photoelectrons versus delay between the XUV burst and the laser pulse revealed, without the need of any detailed analysis, that probing was implemented by a single burst of sub-femtosecond duration that was synchronized with sub-femtosecond accuracy to the NIR laser field.

The complete photoemission experiment was performed in Ultra-High Vacuum (UHV, $10^{-9}$ mbar). The W crystal was heated in front of an $O_2$ doser to about 1400 K (local pressure in front of the crystal was approximately $10^{-6}$ mbar, pressure in chamber $< 3 \cdot 10^{-8}$ mbar) followed by repeated flashing to about 2200 K in order to clean it. The visibility of the 4f peak in photoemission was an indication as to how long the crystal surface remained sufficiently impurity-free since the peak disappeared if the impurity had an adsorbate thickness of more than 1 nm, corresponding to the escape depth of the electrons. It took no longer than one hour to run through the photoemission experiment, following which the cleaning procedure of the crystal surface was repeated in a special preparation chamber, separated from the main UHV-chamber. The crystal was mounted on a rotatable and movable manipulator and was grounded in order to avoid charging and to define zero energy. All streaking measurements were performed with NIR laser radiation at a constant intensity in order to avoid changes of space charge due to multi-photon photoemission of the NIR. The intensity of the NIR was limited such that the NIR induced multi-photon photoelectron signals did not dominate the time-of-flight (TOF) spectra and the photoelectrons from the W 4f band were quantitatively discriminated against the NIR-induced background. The photoelectrons emitted normally to the W(110) surface were spectrally analysed with respect to their kinetic energy by means of the TOF. By using a piezo translation stage connected with the movable inner part of the focussing mirror, the time delay of the XUV 300 as pulse was increased or

**Fig. 13.2** Raw streaking spectrum of W(110): the dependence of photoelectron kinetic energy as a function of the delay between the IR and the 91 eV XUV pulse. The photoelectrons from the 4f core states and from the d conduction band close to the Fermi energy follow with their energies the oscillation of the electric field of the IR pulse (adapted from Ref. [15])

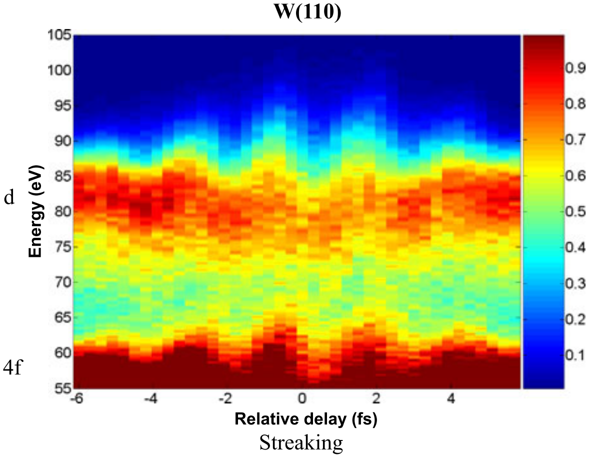

decreased in steps of 50 nm corresponding to 300 as with respect to the NIR pulse with its stabilized carrier envelope phase.

Figure 13.2 shows the photoelectron spectra of W(110) measured in this way as a function of the delay over the whole duration of the NIR pulse [15]. Positive relative delay means that the XUV arrived earlier than the NIR, and negative delay indicates the opposite. In Fig. 13.2 no background was subtracted, only the time spectra of the time-of-flight spectrometer were converted into photoelectron energy spectra. An approximately 10 eV broad conduction band could be observed below the Fermi edge at about a photoelectron kinetic energy of 87 eV, and the 4f band of W(110) at about 60 eV. For both bands the emitted photoelectrons showed a pronounced streaking structure with the delay to the phase stabilized NIR laser pulse. This could be observed over the whole NIR pulse of about 3 laser oscillation periods. We limited the energy range shown in Fig. 13.2 to energies above 55 eV where the NIR-induced background was negligible in order to demonstrate that, even in this raw spectra, a time delay shift of about one experimental step between the two streaking curves (Fermi edge electrons and 4 f electrons) can easily be observed with the eye: Maxima and minima of the Fermi edge streaking (sine-oscillation of kinetic energy) are shifted to the left side compared to the streaking of the 4f edge. This has shown for the first time that different types of photoelectrons from different bands leave the crystal sequentially at different times. Furthermore, it is evident that the photoelectrons even from the non-localised d-band at the Fermi edge which have been emitted by means of a 300 as XUV pulse also show a sub-femtosecond pulse duration; were this not the case the streaking in Fig. 13.2 could not be observed. The streaking signal (oscillation of the photoelectron kinetic energies as a function of the delay following the E field structure of the IR radiation) was expected for the 4f band, since it is a localized atomic like state, but not at all for the conduction band since it was believed that many electron effects in the conduction band and their non-localization described by Bloch waves would smear out all time memories and thus any streaking signal. Obviously this picture was wrong: The 300 as

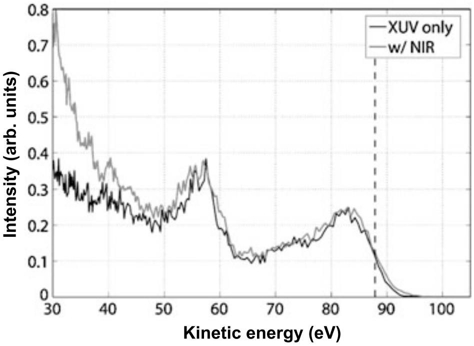

**Fig. 13.3** Photoelectron spectrum of W(110) with and without the near infrared pulse obtained using a 91 eV XUV pulse. *The dashed vertical line* marks the kinetic energy for photoelectrons emitted from states at the Fermi energy. *Straight lines* between the measured intensity values at 50 eV and 65 eV as well as at 65 eV and 95 eV mark the background contribution (see text) (adapted from Ref. [15])

excitation and the fast transport through only 2 to 3 atomic layers of the solid was too fast for the electron cloud in the conduction band to cancel the time memory. In order to gain better access to these observations, fit procedures of the raw data had to be performed.

The first step was to detect and to subtract the background electron spectrum from the raw measured data. The measured electron spectra have a form of two peaks existing on top of a background. This background appears due to two processes. First, the NIR probe field can create electrons with kinetic energies reaching 100 eV by a process which is analogous to the above threshold ionisation process (ATI) in isolated atoms. For brevity this part of the background is referred to as "ATI background". Second, an electron ejected by the extreme-ultraviolet (XUV) pulse can experience inelastic collisions before it leaves the metal. Comparison of photoelectron spectra recorded with and without the presence of the NIR streaking field provides an insight into the properties of the XUV-induced and the ATI background signals. Spectra recorded with and without the presence of the NIR streaking field are shown in Fig. 13.3. It is worth noting that in the streaking experiment the IR intensity has been dramatically reduced to such a value that the ATI background vanishes at the f band at about 50 eV kinetic energy.

In Fig. 13.4 a smoothed photoelectron spectrum of W(110) as a function of the binding energy is shown for a delay value where the NIR laser pulse shows a vanishing E-field, after the background of Fig. 13.3 has been subtracted. Here the 4f-band with electrons from the localized 4f atomic states and consisting of four sub-bands is at about 32 eV binding energy, as highly resolved photoemission experiments have demonstrated [22, 23, 29, 30]. There are two spin orbit split fine structure components $f_{7/2}$ and $f_{5/2}$ which are separated by 2.18 eV and each of them in turn are separated in a surface and a bulk peak by the core level shift of 0.3 eV (the branching ratio $f_{7/2}$ to $f_{5/2}$ has been fitted to be 1.6). The conduction band (predominantly itinerant d-like states) can be seen below the Fermi edge. It is worth noting that the

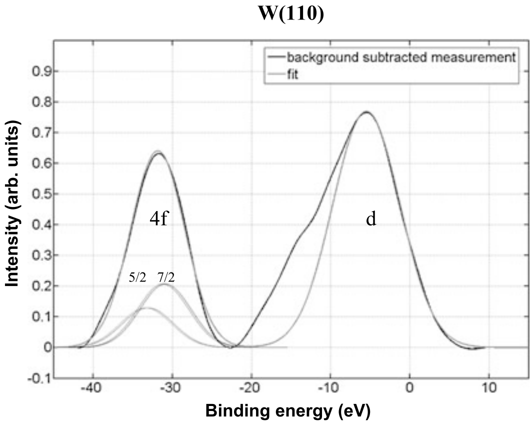

**Fig. 13.4** Background subtracted results of Fig. 13.2 according to the procedure given in Fig. 13.3 describing the 4f core state and conduction band (d) photoemission intensity as a function of the binding energy for W(110) with Gauss peak fits for the $f_{7/2}$, $f_{5/2}$ bulk and surface parts and the conduction band

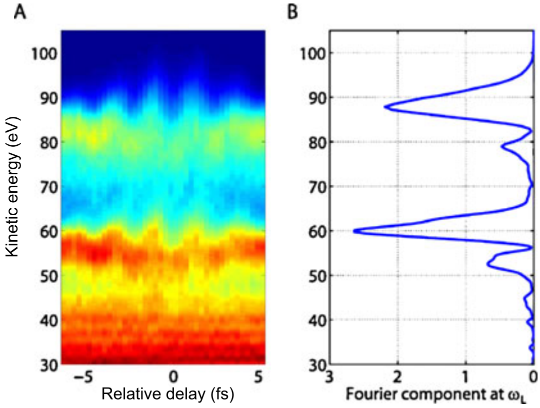

**Fig. 13.5** ATI background subtracted streaking spectrum of W(110) according to Fig. 13.2 (*left*) in cross-comparison with its Fourier analysis at the IR laser frequency $\omega_L$ (*right*) (adapted from Ref. [15])

bands shown in Fig. 13.4 do not show their natural bandwidths since the photoemission experiment has been performed by means of an ultrashort XUV pulse of 300 as duration corresponding to a bandwidth of 6 eV. In Fig. 13.4 also the individual fits of the four 4f sub-bands described above are drawn together by using Gaussian curves to produce a fit of the total ensemble of 4f bands as well as of the band at the Fermi edge.

Fourier analysis was used to study the raw spectra and any time-dependence of the background subtraction procedure. The results of this Fourier analysis are summarized in Fig. 13.5. The magnitude of the Fourier component at the carrier laser frequency $\omega_L$ is maximal at the slopes of the peaks, where a small spectral shift causes the largest change in the spectral intensity. It is clear from this analysis that no periodic modulation at the laser frequency is observed in regions containing only background, specifically at energies below the 4f peak or in between the peaks. Therefore, streaking of the XUV-produced background was determined as being negligibly small in the measurements.

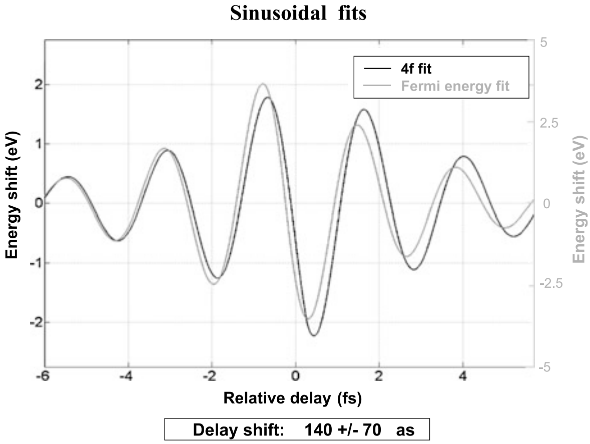

**Fig. 13.6** Sinusoidal fit of the streaking curves of the data in Fig. 13.2 in connection with the background subtraction as given in Figs. 13.3 and 13.4 for the photoelectrons emitted from the 4f core level states and from the band at the Fermi energy of W(110). They are shifted in delay by 140 ± 70 as

This static behaviour of the background electrons could be expected for several reasons. Most importantly, streaking can only be observed if the duration of the streaked electron wave packet is sufficiently small. Ideally, the wave packet should be much shorter than the period of the streaking field. While the electrons that compose the photoemission peaks come from the first atomic layers, the background electrons can originate from much deeper in the material, so they need more time to reach the surface, which broadens their emission time and therefore weakens the effect of streaking.

Figure 13.6 presents a cross-comparison of the streaking fit data of the maxima of the 4f band with that of the Fermi energy given by the inflection points of the electron spectra as given in Fig. 13.3 and Fig. 13.4. Both curves demonstrate a streaking, i.e. an oscillation in energy over 4 eV and 8 eV for 4f and Fermi energy electrons, respectively, with the time dependence of the electric field distribution of the NIR pulse. Additionally as already shown in Fig. 13.2 and discussed above, the streaking curve of the 4f shows an overall shift of 140 ± 70 as (single standard deviation) to the streaking curve of the Fermi edge. This means that the electrons from the non-localized band are emitted about 140 as earlier than the localised 4f electrons. This has shown for the first time that different types of photoelectron from different bands are emitted sequentially at different times.

Since the two fits in Fig. 13.6 do not have exactly the same but a shifted structure, a second evaluation of the raw data was performed and published in [15] by looking at the streaking oscillation of the centre of mass of the two peaks at 45 to 65 eV and 65 to 100 eV. The advantage is that the centre of mass of a peak is more stable with respect to background fluctuations, the disadvantage is that it does not fit the streaking of the conduction band at the Fermi energy but at a kinetic energy which is about 8 eV lower, thus other parts of the conduction band become the subject of the streaking analysis. The results of the evaluation obtained by cubic-spline interpolation using a smoothed and not background corrected spectrum (shown in Fig. 13.7 with this centre of mass analysis) are shown in Fig. 13.8. Once again, both streaking curves are shifted, now with a time shift of 110 ± 70 as. It is worth not-

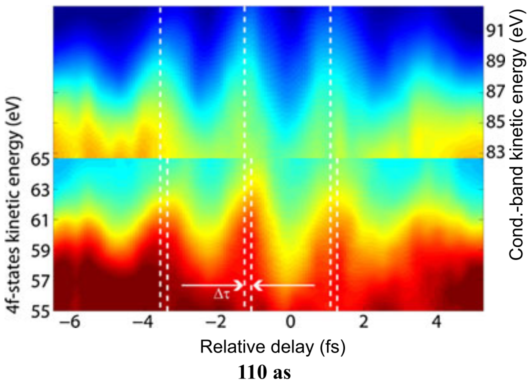

**Fig. 13.7** Smoothed streaking spectrum of W(110) after cubic spline interpolation of the oscillation of the kinetic energies as given in Fig. 13.2 as a function of the delay between IR and XUV pulse (adapted from Ref. [15])

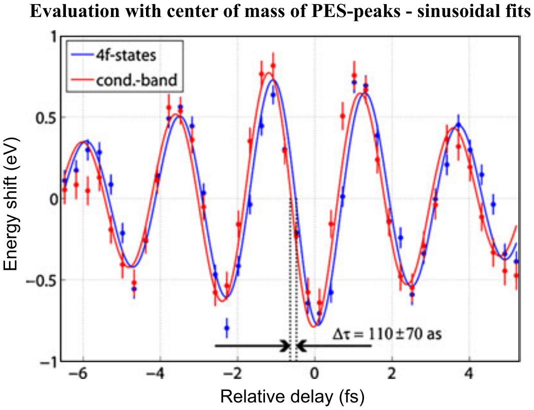

**Fig. 13.8** Fit through the streaking oscillations in Fig. 13.7 of W(110) at the centre of mass of the 4f state peak and of the conduction band peak. They are shifted in delay by 110 ± 70 as (adapted from Ref. [15])

ing that the oscillation amplitude of the streaking in Fig. 13.8 (centre of mass) is smaller than in Fig. 13.6 (background corrected peaks directly). It is also worth noting that the experiment has recently been repeated [31] with a much shorter XUV pulse of 80 as duration where a streaking shift of 85 ± 35 as between the 3d conduction band and the 4f band has been found for W(110). Although the three different time shifts measured—(140 ± 70 as, 110 ± 70 as and 85 ± 35 as)—agree within their error bars, they all refer to different parts of the conduction band, the 85 as pulse has a bandwidth of 20 eV shifting the energy range of study further away from the Fermi energy and averaging it out over the whole conduction band which is indeed a composition of 5d, 5p and 6sp band parts. The energy dependence of the phase shifts, and thus the time delays, for different orbital angular momenta in time-resolved photoemission are further discussed later in this chapter. It is worth noting that very recently (2012) Stefan Neppl (TU Munich) has repeated the attosecond-time-resolved photoemission experiment with W(110) at a higher XUV photon and thus higher photoelectron energy and measured a pronounced shorter emission time shift (not yet published).

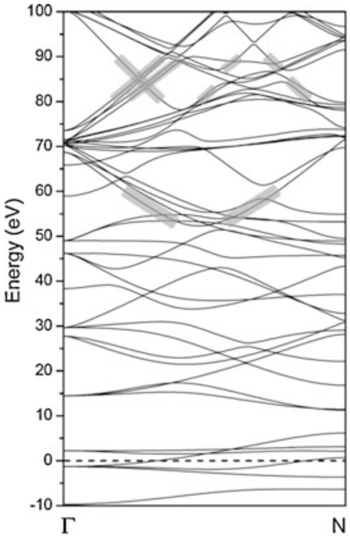

W (110) calculated band structure

**Fig. 13.9** Static band structure calculation of bcc tungsten along $\Gamma N$ momentum direction [110]. Zero on the energy axis is the Fermi energy. Electrons from the 4f states are photoexcited by the 88–94 eV XUV peak into the upper conduction band that is shaded and centred at about 58 eV. Similarly, electrons from the conduction band reach bands with energies around 85 eV. The slope of the upper conduction bands estimates the group velocities of the electrons inside the crystal (adapted from Ref. [15])

## 13.3 Interpretations of the Emission Time Differences

The experimentally observed delays of the photoelectrons emitted from different bands of W(110) may have different reasons, since the electrons have different kinetic energies and they may originate from locations at different distances with respect to the surface. Five different theoretical approaches to describe the dynamics of the photoemission process at W(110) exist so far, all yielding delays between 42 and 110 as for the core and the conduction band electrons photoemitted. The first theoretical approach by Echenique used a static band structure calculation as given in Fig. 13.9 [15] and explained the different delayed emission by different group velocities of the final states given as slopes $dE/dp$ with $p = kh/2\pi$ as the electron momentum. This classical model used the assumption of a sudden refraction of the IR laser beam as shown in Fig. 13.1 at the surface with the consequence that there is no streaking effect inside the crystal since the electric field of the IR laser and the velocities of the photoelectrons observed normal to the surface are perpendicular to each other. Thus a delay results from electron flight time differences in the location of photoexcitation up to the surface. Ref. [15] found that electrons of 85 eV kinetic energy need about 60 as to propagate a distance of 0.4 nm in the crystal while electrons of 58 eV need 150 as, which is in good agreement with the experiment. The critical point of this approach was of course the use of a static band structure which might not be valid for an ultrashort photoemission process.

By taking the delocalization of the 4f and 5d states of tungsten into account differently, using a quantum mechanical approach and assuming that the IR laser radiation does not penetrate into the crystal, Kazansky and Echenique [32] found that the concept of group velocities could be ruled out for small time intervals. The main effect of the delay is attributed to the localized nature of the core electrons in contrast to the conduction band electrons which are completely delocalized. Contrary to this approach Baggesen and Madsen [33] found in a quantum mechanical approach using Volkov waves as final states that the delay originates from the travel through the surface. Zhang and Thumm [34] assumed a localized core state and delocalized electrons in the conduction band in a jellium approximation under the circumstance that the streaking laser field inside the solid is included. The photoemission by XUV was dealt with by the first order perturbation theory, whereas the streaking itself was not treated with the perturbation theory; they took into account interfering contributions from different lattice layers to the dipole matrix elements of the optical transition under the circumstance that the core electrons were delocalized within the jellium model. They calculated a delay of 110 as in agreement with the experiment.

Lemell et al. [35] used a classical transport theory, neglecting the penetration of the IR laser field into the crystal but using different group velocities for electrons from 4f, 6s and 5d states. They found a delay of 110 as in agreement with the experiment with group velocities as given in [15] or alternatively 42 as with a free particle dispersion relation. Summarizing, with the given theoretical approaches so far, the real nature of the delay is not yet quantitatively understood. There is however no doubt that it exists: Electrons of different states excited by an ultrashort attosecond pulse leave the crystal surface at different times.

The fact that electrons from different bands with different symmetries i.e. orbital angular momenta (s, p, d, f) may have different group velocities, even if they have the same kinetic energies [35], gives rise to the general question as to which parts of the full Hamilton operator influence the time delays of emitted photoelectrons measured by means of streaking experiments. Very recently, Zhang and Thumm [36] discussed theoretically the relationship of streaking and Wigner time delays. Based upon the essence of the time delay introduced by Wigner and Smith [37, 38] they discussed theoretically how phase shifts of individually travelling plane wave components lead to spectral delays: $\tau = d\varphi/d\varepsilon$ with $\tau$ being the Wigner time delay, $\varphi$ the phase shift and $\varepsilon$ the photoelectron kinetic energy. The Wigner relationship is based upon the definition of the group velocity mentioned above $\upsilon = dE/dp$. This means in practice that a delay of photoelectron wave packets $t$ is given by the derivative of the phase shift $\varphi$ with respect to the electron energy as being $t = 658\text{ as} \cdot d\varphi/dE$ with $E$ in units of eV. Phase shifts $\varphi$ between different partial waves thus automatically create a delay of the electron wave packets $t_1 - t_2$ if they show a different dispersion $t_1 - t_2 = 658\text{ as} \cdot d(\varphi_1 - \varphi_2)/dE$. Furthermore, this poses the question of how phase shift resolved photoemission experiments can be performed in reality.

## 13.4 Phase Shift Resolved Photoemission and Its Relation to Time Delays

Indeed, phase shift resolved photoelectron emission experiments have been successfully performed with free atoms and molecules, adsorbates and solids in the past

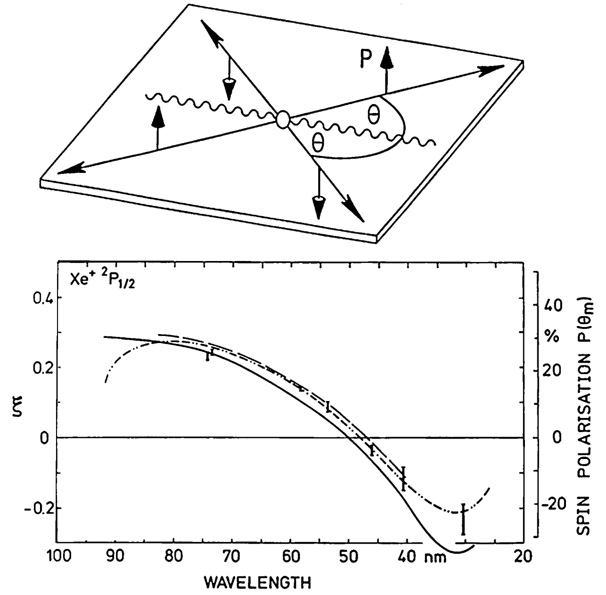

**Fig. 13.10** Reaction plane of spin resolved photoemission of atoms by means of unpolarized radiation given by the momenta of the photon and photoelectron. The so-called dynamical spin polarization P is perpendicular to this plane, its value varies with the emission angle $\theta$ (*upper part*). Spin polarization P measured at the magic angle $\theta_m = 54°$ for photoelectrons from free xenon atoms with respect to the $5p_{1/2}$ orbital leaving the ion in the $^2P_{1/2}$ state as a function of the light wavelength in cross comparison with different theories (*curves*) [39, 40] (*lower part*). $\xi$ is the so-called dynamical spin parameter which is given by $P(\theta_m)$

decades by the group of the author of this chapter [39–47]. These experiments have used cw-radiation in the XUV region like the core hole clock spectroscopy (CHC) mentioned above, but they have also gained access to the phase shifts and thus to the time dynamics via the dynamical spin polarization of the photoelectrons emitted. It has been experimentally verified in more than 60 systems studied so far, that photoelectrons emitted by circularly polarized radiation are in general spin polarized up to 100 % by means of the spin polarization transfer from the photons absorbed onto the photoelectrons due to the existence of the spin-orbit interaction. It has been shown experimentally, however, that this degree of polarization can also be achieved by using a linearly polarized or even unpolarized radiation for one component of the spin polarization vector, the so-called dynamical spin polarization perpendicular to the reaction plane, spanned by photon and electron momenta as shown in Fig. 13.10 (upper part), if the influence of the spin-orbit interaction is experimentally resolved in the photoelectron spectrum [39, 40]. This dynamical spin polarization, which varies with the photoelectron emission angle $\theta$ and is proportional to $\sin\theta \cdot \cos\theta$ [41], is shown in Fig. 13.10 (lower part) for $\theta_m = 54°$ as a function of the radiation wavelength for photoelectrons of free xenon atoms leaving the xenon ion back in

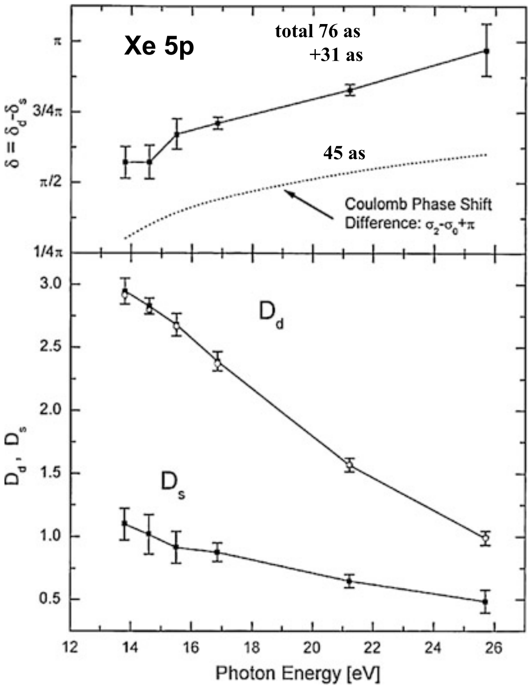

**Fig. 13.11** Measured phase shift differences (*upper part*) and dipole matrix elements (*lower part*) (error bars) [39, 40] of photoelectrons from Xe 5p with respect to transition into the energy degenerate d and s continua as a function of the photon energy. *The dashed curve* shows the calculated Coulomb phase shift $\sigma_d - \sigma_s - \pi$. *The full curve* connects the experimental data points, its derivative $d\delta/dE$ is the Wigner time delay between the partial wave packets d and s given in numbers in *the upper part* (see text)

the ${}^2\mathrm{P}_{1/2}$ state. The existence of this dynamical spin polarization is based upon the quantum mechanical interference of the $d$ and $s$ continuum wave functions reached by the optical transition from the $p_{1/2}$ atomic orbital according to the selection rules. Its value is directly proportional to the sine of the phase shift difference of these two partial photoelectron waves $\delta_d - \delta_s$:

$$\mathrm{P}(54^\circ) = \frac{D_d \cdot D_s}{D_d^2 + D_s^2} \cdot \sin(\delta_d - \delta_s)$$

The matrix elements $D_d$ and $D_s$ have been determined experimentally by means of the spin polarization values, when circularly polarized radiation is used, and by means of the photoionization cross-section. Thus a so-called quantum mechanical "complete" photoemission experiment has been performed, which means that experimentally all individual matrix elements and phase shift differences have now been determined separately. The results for the xenon atom are shown in Fig. 13.11. The phase shift difference given in the upper part of Fig. 13.11 as a function of the energy is the sum of the Coulomb phase shift difference $\sigma_d - \sigma_s - \pi$, which describes the influence of the pure Coulomb potential of the core (hydrogenic part), and of the phase shift difference influenced by the many electron system of the xenon atom. The slope of the phase shift difference curves as a function of the energy directly gives the time delays of the photoelectrons emitted in the individual continuum channels d and s to be 45 as for the Coulomb phase shift alone and 76 as = 45 + 31 as in total at

**Fig. 13.12** Analytically calculated energy dependence of the energy slope of the Coulomb phase shift $\sigma_d - \sigma_s - \pi$ given as time delay

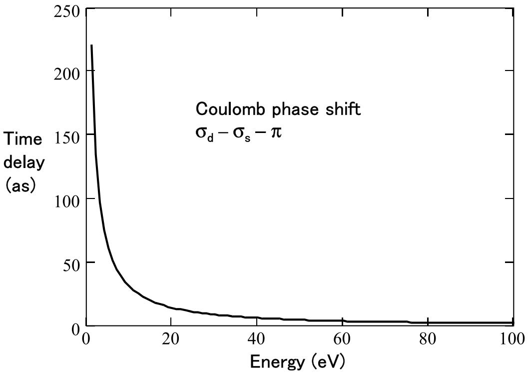

the joint kinetic energy of 7 eV (20.5 eV photon energy), as given in Fig. 13.11. Figure 13.12 shows that the time delay due to this Coulomb phase shift strongly decreases with increasing kinetic energy and is negligible (<8 as) for kinetic energies higher than 30 eV. With respect to the time-resolved photoemission of f-core level bands and of the conduction band of W(110) discussed above, Figure 13.13 shows phase shift differences of $f_{7/2}$ and $f_{5/2}$ continuum waves with respect to a $p_{3/2}$ continuum wave of the photoelectron emission of mercury atoms (lower part of Fig. 13.13) together with the corresponding matrix elements [45]. Note that the phase shifts describe only the non-hydrogenic part, after the Coulomb phase shifts have been subtracted; they are given as differences of quantum defects $\Delta\mu$ in units of $\pi$ [40]. In the energy range presented in Fig. 13.13 the non-Coulombic phase shift differences have a slope which defines a time delay between f and p waves to be 77 as and 59 as for the Hg atoms $d_{3/2}$ and $d_{5/2}$ initial states, respectively. It is worth being noted that the phase shift differences $f_{7/2} - f_{5/2}$ as well as $p_{3/2} - p_{1/2}$ in Fig. 13.13 do not show any dispersion with the consequence that the spin orbit interaction alone, as a part of the total potential in which the photoelectron leaves, does not create any time delay. Obviously the main part of the time delay with respect to f and p waves is due to the different centrifugal term $l(l+1)/r^2$ in the Schrödinger equation.

In the photoemission of metal surfaces there is a prominent showcase example of a pronounced dynamical spin polarization and thus of a large phase difference and time delay: a $\sin\phi \cdot \cos\phi$ dependent dynamical spin polarization exists with respect to the azimuthal rotation angle $\phi$ in the photoemission of Pt(110) in normal electron emission and in normal incidence of linearly polarized radiation. The electric vector **E** and the crystal $[1\bar{1}0]$ direction define the reaction plane in this case, as given in Fig. 13.14. The spin polarization varies between −10 % and +10 %; using all experimental data, a phase shift difference is obtained as a function of the binding energy for a fixed photon energy of 11.8 eV, as given in the right part of Fig. 13.14 [44]. Its slope versus energy gives the high value of 4.7 fs for the time delay of electrons from the two bands $\Sigma_5^3$ and $\Sigma_5^4$ [44, 46, 47]. This value of a time delay for photoelectrons from different bands is so high because the kinetic energy

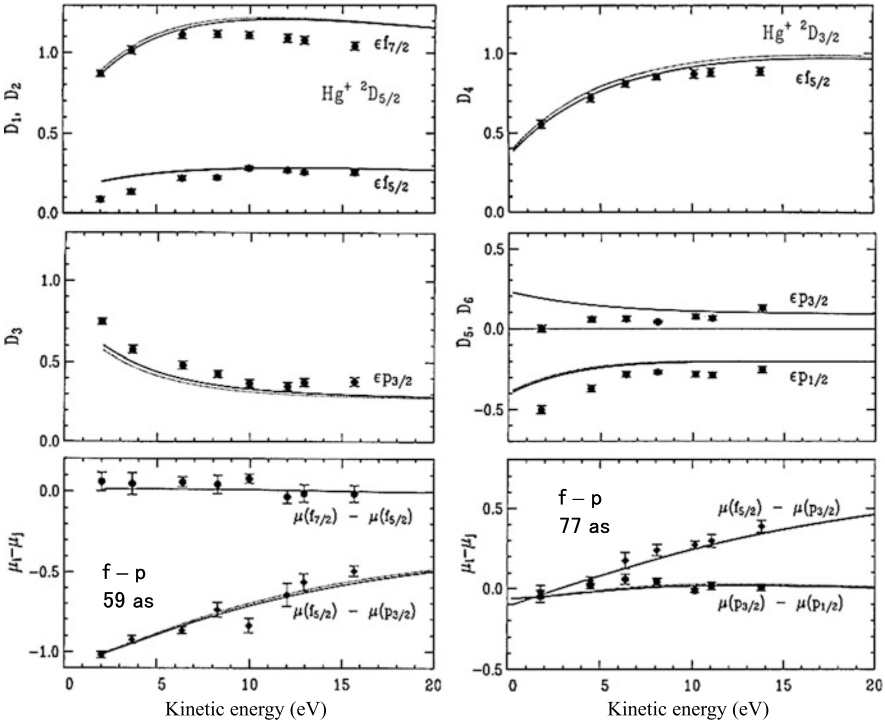

**Fig. 13.13** Matrix elements $D$ and phase shift differences $\mu = (\delta - \sigma)/\pi$ in units of $\pi$, without Coulomb phases $\sigma$, for f and p photoelectrons leaving the mercury atom back in the $5d^2D_{5/2}$ (*left part*) and $5d^2D_{3/2}$ (*right part*) final ionic state, experiment (error bars) and theory (adapted from Ref. [45]), as a function of the photoelectron kinetic energy. *The numbers* denote the corresponding time delays given by the slopes of the phase shift curves

of the photoelectrons is low and the two bands show a strong hybridization. It is obvious from Figs. 13.11, 13.12, 13.13 and 13.14 that the slope of the phase shifts and thus the time delays in photoemission strongly decrease with higher photoelectron energies which explains the result reported at the end of Sect. 13.2 for the higher photon energy. It is further obvious that the faster the photoelectrons are, the shorter the flights times and their differences have to be to pass a distance of an order of the size of an atom.

## 13.5 Outlook: The Combination of High Time and Energy Resolutions

All the cases of time delays in photoemission discussed so far show a strong variation with respect to the energy. Unlike free atoms and molecules, condensed matter has broad energy bands filled with electrons which show a pronounced dis-

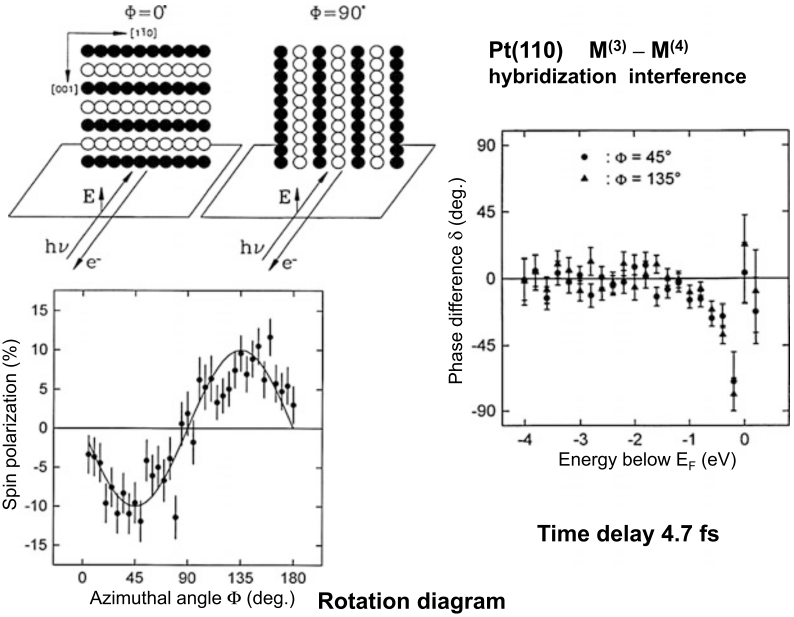

**Fig. 13.14** Dynamical spin polarization of photoemission with Pt(110) by use of linearly polarized radiation in the set up given in *the upper left part* (adapted from Ref. [44]). By use of 11.8 eV radiation, a spin polarization along the direction of ejected electrons normal to the surface has been measured as a function of the azimuthal angle $\phi$ by rotation about the surface normal (*lower part*). Evaluation of the experimental data yields the values with error bars of the phase difference for photoelectron waves according to the transition from the $\Sigma_5^3$ (M$^{(3)}$) and $\Sigma_5^4$ (M$^{(4)}$) initial bands [47]. Its slope at about 0.5 eV binding energy below the Fermi energy yields a time delay of 4.7 fs

persion. Thus attosecond-time-resolved photoemission spectroscopy in condensed matter faces its limitation in the energy-time uncertainty. The shorter the as-XUV pulse, the broader in energy its bandwidth has to be and the less the spectroscopic view is detailed to the electronic structure of the solid. Electron Spectroscopy for Chemical Analysis (ESCA) has become very important in molecular and adsorbate systems: Energy shifts in photoelectron spectra in the order of a few tenths of electron-volt indicate changes in the chemical bonds [48]. Thus it was also a scientific goal to combine ESCA with the time resolution of ultrashort photoemission studies. However, the time resolution has to stay in the fs range in order to achieve an energy resolution of less than 1 eV. Recently two types of ESCA experiments with fs-XUV pulses in photoemission of condensed matter have been performed using an apparatus very similar to that described in Fig. 13.1. Figure 13.15 describes the ESCA photoemission from iodophenylphenol molecules adsorbed on a silicon substrate [49] and shows the pump probe experiment with fs-resolution where the benzene ring is pumped by a UV pulse and the iodine atom is probed by means of the ESCA shift with respect to its 4d core level in photoemission. The selectivity of this experiment in time and energy unveils metastable molecular configurations (prefulvene, benzvalene), given in the lower part of Fig. 13.15, that appear

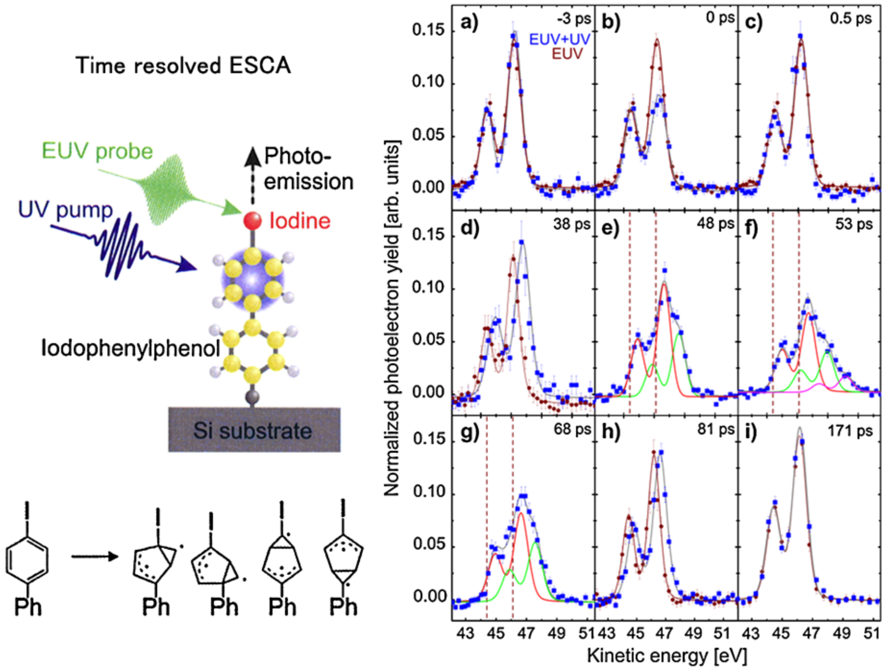

**Fig. 13.15** Time-resolved ESCA study of 30 fs pumped iodophenylphenol molecules adsorbed on silicon with photoelectron spectra for different delays (**a**)–(**g**) between the fs UV pump pulse and the fs EUV probe pulse. The pump process changes in time the structure of the benzene ring as shown in *the lower part* (adapted from Ref. [49])

about 50ps after the fs-excitation and are efficiently guarded back to the ground state.

The second case of pump probe ESCA studies, using XUV laser pulses generated by HHG in time-resolved photoemission, studied very recently the $VO_2$ insulator metal phase transition [50]. The experimental set up was again similar to Fig. 13.1 and used a 30 fs IR pump pulse to excite the HOMO electrons below the Fermi energy to the LUMO band and the XUV probe pulse to study the ESCA shifts of the V3p core levels and of the conduction bands as a function of the delay between pump and probe pulse with fs accuracy. The spectroscopic ESCA shift corresponds to the phase transition from the monoclinic insulating phase and to the tetragonal metal phase of $VO_2$ (see Fig. 13.16), as seen in the hysteresis curve in the upper part of Fig. 13.16 by thermal cooling and heating. Thus, by using ultrashort fs IR and XUV radiation, this time-resolved ESCA experiment confirmed the Mott-Hubbard nature of the band gap collapse and of the insulator-metal phase transition to be initiated by an electronic transition. These two time-resolved photoemission ESCA studies have chosen the compromise in time and energy resolution needed to perform a time-resolved spectroscopy experiment.

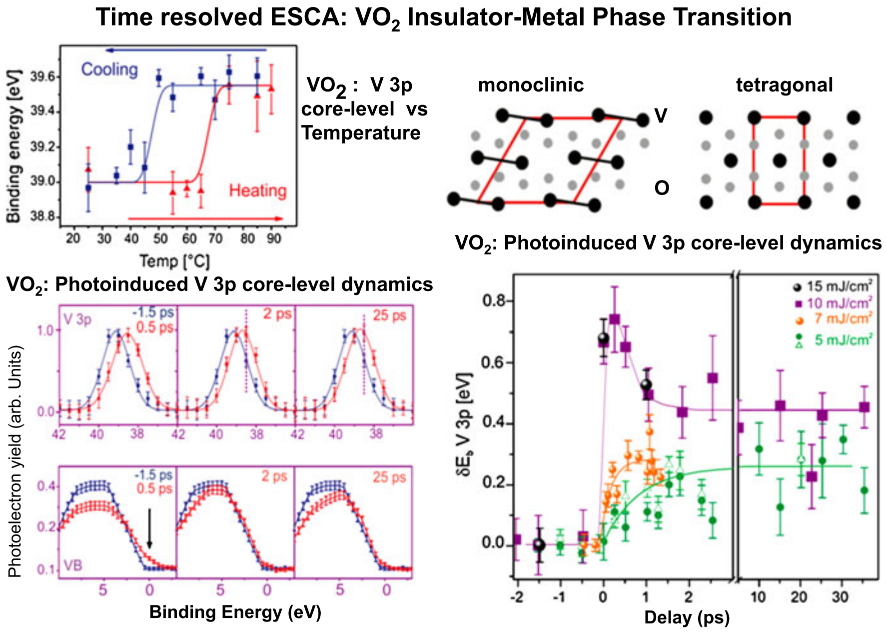

**Fig. 13.16** Time-resolved ESCA study of the $VO_2$ insulator metal phase transition (adapted from Ref. [50]). *The upper part* shows how the 3p core level photoemission binding energy shift can be used to study the phase transition from the monoclinic insulating to the tetragonal metal phase by heating and cooling the crystal (hysteresis). *The lower part* shows the fs and ps dynamics for the phase transition, pumped by 30 fs IR and probed by a EUV pulse with respect to the 3p core level photoemission

## References

1. D. Diesing, M. Merschdorf, A. Thon, W. Pfeiffer, Identification of multiphoton induced photocurrents in metal-insulator-metal junctions. Appl. Phys. B **78**, 443 (2004)
2. S. Tanuma, C.J. Powell, D.R. Penn, Calculations of electron inelastic mean free paths. II. Data for 27 elements over the 50–2000 eV range. Surf. Interface Anal. **17**, 911 (1991)
3. H.L. Dai, W. Ho, *Laser Spectroscopy and Photochemistry on Metal Surfaces* (World Scientific, Singapore, 1995)
4. M. Bauer, C. Lei, K. Read, R. Tobey, J. Gland, M.M. Murnane, H.C. Kapteyn, Direct observation of surface chemistry using ultrafast soft-x-ray pulses. Phys. Rev. Lett. **87**, 025501 (2001)
5. P.M. Echenique, R. Berndt, E.V. Chulkov, Th. Fauster, A. Goldmann, U. Höfer, Decay of electronic excitations at metal surfaces. Surf. Sci. Rep. **52**, 219 (2004) and references therein
6. X.Y. Zhu, Electronic structure and electron dynamics at molecule-metal interfaces: implications for molecule-based electronics. Surf. Sci. Rep. **56**, 1 (2004)
7. H. Zacharias, M. Wolf (guest editors), Special issue 2 on "Dynamics of electron transfer at interfaces". Appl. Phys. A **78**, 125–252 (2004)
8. M. Lisowski, P.A. Loukakos, A. Melnikov, I. Radu, L. Ungureanu, M. Wolf, U. Bovensiepen, Femtosecond electron and spin dynamics in Gd(0001) studied by time-resolved photoemission and magneto-optics. Phys. Rev. Lett. **95**, 137402 (2005)

9. V.M. Axt, T. Kuhn, Femtosecond spectroscopy in semiconductors: a key to coherences, correlations and quantum kinetics. Rep. Prog. Phys. **67**, 433 (2004)
10. R.W. Schoenlein, J.G. Fujimoto, G.L. Eesley, T.W. Capehart, Femtosecond studies of image-potential dynamics in metals. Phys. Rev. Lett. **61**, 2596 (1988)
11. U. Höfer, I.L. Shumay, Ch. Reuß, U. Thomann, W. Wallauer, Th. Fauster, Time-resolved coherent photoelectron spectroscopy of quantized electronic states on metal surfaces. Science **277**, 1480 (1997)
12. P. Siffalovic, M. Drescher, M. Spieweck, T. Wiesenthal, Y.C. Lim, R. Weidner, A. Elizarov, U. Heinzmann, Laser-based apparatus for extended ultraviolet femtosecond time-resolved photoemission spectroscopy. Rev. Sci. Instrum. **72**, 30 (2001)
13. P. Siffalovic, M. Drescher, U. Heinzmann, Femtosecond time-resolved core-level photoelectron spectroscopy tracking surface photovoltage transients on p-GaAs. Europhys. Lett. **60**, 924 (2002)
14. A. Fohlisch, P. Feulner, F. Hennies, A. Fink, D. Menzel, D. Sanchez-Portal, P.M. Echenique, W. Wurth, Direct observation of election dynamics in the attosecond domain. Nature **436**, 373 (2005)
15. L. Cavalieri, N. Müller, Th. Uphues, V.S. Yakovlev, A. Baltuska, B. Horvath, B. Schmidt, L. Blümel, R. Holzwarth, S. Hendel, M. Drescher, U. Kleineberg, P.M. Echenique, R. Kienberger, F. Krausz, U. Heinzmann, Attosecond spectroscopy in condensed matter. Nature **449**, 1029–1032 (2007) and Supplementary Material
16. M. Uiberacker, Th. Uphues, M. Schultze, A.J. Verhoef, V. Yakovlev, M.F. Kling, J. Rauschenberger, N.M. Kabachnik, H. Schröder, M. Lezius, K.L. Kompa, H.G. Müller, M.J.J. Vrakking, S. Hendel, U. Kleineberg, U. Heinzmann, M. Drescher, F. Krausz, Attosecond real-time observation of electron tunnelling and multi-electron dynamics in atoms. Nature **446**, 627 (2007)
17. P.M. Echenique, J.M. Pitarke, E.V. Chulkov, A. Rubio, Theory of inelastic lifetimes of low-energy electrons in metals. Chem. Phys. **251**, 1 (2000)
18. E. Goulielmakis, M. Uiberacker, R. Kienberger, A. Baltuska, V. Yakovlev, A. Scrinzi, Th. Westerwalbesloh, U. Kleineberg, U. Heinzmann, M. Drescher, F. Krausz, Direct measurement of light waves. Science **305**, 1267 (2004)
19. R. Kienberger, E. Goulielmakis, M. Uiberacker, A. Baltuska, V. Yakovlev, F. Bammer, A. Scrinzi, T. Westerwalbesloh, U. Kleineberg, U. Heinzmann, M. Drescher, F. Krausz, Atomic transient recorder. Nature **427**, 817 (2004)
20. M. Drescher, M. Hentschel, R. Kienberger, M. Uiberacker, V. Yakovlev, A. Scrinzi, Th. Westerwalbesloh, U. Kleineberg, U. Heinzmann, F. Krausz, Time-resolved atomic inner-shell spectroscopy. Nature **419**, 803 (2002)
21. M. Schultze, M. Fieß, N. Karpowicz, J. Gagnon, M. Korbman, M. Hofstetter, S. Neppl, A.L.Y. Komninos, Th. Mercouris, C.A. Nicolaides, R. Pazourek, S. Nagele, J. Feist, J. Burgdörfer, A.M. Azzeer, R. Ernstorfer, R. Kienberger, U. Kleineberg, E. Goulielmakis, F. Krausz, V.S. Yakovlev, Delay in photoemission. Science **328**, 1658 (2010)
22. T.M. Duc, C. Guillot, Y. Lassailly, L. Lecante, I. Jugnet, J.C. Vedrine, Direct Observation of 4f splitting between (110) surface and bulk atoms of W. Phys. Rev. Lett. **43**, 789 (1979)
23. P.M. Leu, J.D. Denlinger, E. Rotenberg, S.D. Kevan, B.P. Tonner, Y. Cheu, M.A. Van Hove, C.S. Fadley, Holographic atomic images from surface and bulk W(110) photoelectron diffraction data. Phys. Rev. B **59**, 5857 (1999)
24. Y.C. Lim, T. Westerwalbesloh, A. Aschentrup, O. Wehmeyer, G. Haindl, U. Kleineberg, U. Heinzmann, Fabrication and characterization of EUV multilayer mirrors optimized for small spectral reflection bandwidth. Appl. Phys. A **72**, 121 (2001)
25. A. Wonisch, U. Neuhäusler, N.M. Kabachnik, Th. Uphues, M. Uiberacker, V. Yakovlev, F. Krausz, M. Drescher, U. Kleineberg, U. Heinzmann, Design, fabrication and analysis of chirped multilayer mirrors for reflection of XUV attosecond pulses. Appl. Opt. **45**, 4147 (2006)
26. A. Wonisch, Th. Westerwalbesloh, W. Hachmann, N. Kabachnik, U. Kleineberg, U. Heinzmann, Aperiodic nanometer multilayer systems as optical key components for attosecond electron spectroscopy. Thin Solid Films **464–465**, 473 (2004)

27. A. Zangwill, *Physics at Surfaces* (Cambridge University Press, Cambridge, 1988)
28. U. Kleineberg, Th. Westerwalbesloh, W. Hachmann, U. Heinzmann, J. Tümmler, F. Scholze, G. Ulm, S. Müllender, Effect of substrate roughness on Mo/Si multilayer optics for EUVL produced by UHV-e-beam evaporation and ion polishing. Thin Solid Films **433**, 230 (2003)
29. H.B. Rose, A. Fanelsa, T. Kinoshita, Ch. Roth, F.U. Hillebrecht, E. Kisker, Spin-orbit induced spin polarization in W 4f photoemission. Phys. Rev. B **53**, 1630 (1996)
30. K. Starke, A.P. Kaduwela, Y. Lin, P.D. Johnson, M.H. Van Hove, C.S. Fadley, V. Chakarian, E.E. Chabran, G. Meigs, C.T. Chen, Spin polarized photoelectrons excited by circularly polarised radiation from a nonmagnetic solid. Phys. Rev. B **53**, R10544 (1996)
31. A. Cavalieri, F. Krausz, R. Ernstofer, R. Kienberger, P. Feulner, J. Earth, D. Menzel, Attosecond time-resolved spectroscopy at surfaces, in *Dynamics at Solid State Surface and Interfaces. Volume 1: Current Developments*, ed. by U. Bovensiepen, H. Petek, M. Wolf (Wiley, New York, 2010), p. 537
32. A.K. Kazansky, P.M. Echenique, One-electron model for the electronic response of metal surfaces to subfemtosecond photoexcitation. Phys. Rev. Lett. **102**, 177401 (2009)
33. J.C. Baggesen, L.B. Madsen, Theory for time-resolved measurements of laser-induced electron emission from metal surfaces. Phys. Rev. A **78**, 032903 (2008). Also in Phys. Rev. A **80**, 030901 (2009)
34. C.H. Zhang, U. Thumm, Attosecond photoelectrons spectroscopy of metal surfaces. Phys. Rev. Lett. **102**, 123601 (2009)
35. C. Lemell, B. Solleder, K. Tökesi, J. Burgdörfer, Simulation of attosecond streaking of electrons emitted from a tungsten surface. Phys. Rev. A **79**, 062901 (2009)
36. C.H. Zhang, U. Thumm, Streaking and Wigner time delays in photoemission from atoms and surfaces. Phys. Rev. A **84**, 033401 (2011)
37. E.P. Wigner, Lower limit for the energy derivative of the scattering phase shift. Phys. Rev. **98**, 145 (1955)
38. T.F. Smith, Lifetime matrix in collision theory. Phys. Rev. **118**, 349 (1960)
39. U. Heinzmann, Experimental determination of the phase differences of continuum wavefunctions describing the photoionisation process of xenon atoms. I. Measurements of the spin polarisations of photoelectrons and their comparison with theoretical results. J. Phys. B **13**, 4353 (1980)
40. U. Heinzmann, Experimental determination of the phase differences of continuum wavefunctions describing the photoionisation process at xenon atoms. II. Evaluation of the matrix elements and the phase differences and their comparison with data in the discrete spectral range in application of the multi channel quantum defect theory. J. Phys. B **13**, 4367–4381 (1980)
41. U. Heinzmann, J.H. Dil, Spin-orbit induced photoelectron spin polarization in angle resolved photoemission from both atomic condensed matter targets. J. Phys. Condens. Matter **24**, 173001 (2012)
42. B. Kessler, N. Müller, B. Schmiedeskamp, B. Vogt, U. Heinzmann, Spin resolved off-normal photoemission from xenon adsorbates in comparison with free atom photoionization. Z. Phys., D At. Mol. Clust. **17**, 11–16 (1990)
43. N. Irmer, F. Frentzen, B. Schmiedeskamp, U. Heinzmann, Spin polarized photoelectrons with unpolarized light in normal emission from Pt(110). Surf. Sci. **307–309**, 1114 (1994)
44. S.-W. Yu, R. David, N. Irmer, B. Schmiedeskamp, N. Müller, U. Heinzmann, N.A. Cherepkov, Determination of phase differences of transition matrix elements from Pt(110) by means of spin-resolved photoemission with circularly and linearly polarized radiation. Surf. Sci. **416**, 396–402 (1998)
45. F. Schäfers, Ch. Heckenkamp, M. Müller, V. Radojevic, U. Heinzmann, Hg 5d and 6s: multichannel quantum-defect analysis of experimental data. Phys. Rev. A **42**, 2603 (1990)
46. G. Leschik, R. Courths, H. Wern, S. Hüfner, H. Eckardt, J. Noffke, Band structure of platinum from angle resolved photoemission experiments. Solid State Commun. **52**, 221–225 (1984)
47. J. Noffke, Private communication. Published in N. Irmer, F. Frenzen, R. David, P. Stoppmanns, B. Schmiedeskamp, U. Heinzmann, Photon energy dependence of spin-resolved photoemis-

sion spectra in normal emission from Pt(110) by linearly polarized light. Surf. Sci. **331**, 1147 (1995)

48. K. Siegbahn, D. Hammond, H. Fellner-Feldogg, E.F. Barnett, Electron spectroscopy with monochromatized X-rays. Science **176**, 245 (1972)
49. H. Dachraoui, M. Michelswirth, P. Siffalovic, P. Bartz, C. Schäfer, B. Schnatwinkel, J. Mattay, W. Pfeiffer, M. Drescher, U. Heinzmann, Photoinduced reconfiguration cycle in a molecular adsorbate layer studied by femtosecond inner-shell photoelectron spectroscopy. Phys. Rev. Lett. **106**, 107401 (2011)
50. H. Dachraoui, N. Müller, G. Obermeier, C. Oberer, S. Horn, U. Heinzmann, Interplay between electronic correlations and coherent structural dynamics during the monoclinic insulator to rutile metal phase transition in $VO_2$. J. Phys. Condens. Matter **23**, 435402 (2011)

# Part IV
# Future Trends

# Chapter 14
# Attosecond Science Comes of Age

**Ferenc Krausz**

**Abstract** After a decade of development, attosecond science has reached a mature state. The basic tools and techniques are now established. The increase of flux and photon energies and subfemtosecond control of the fields are major technological frontiers for the near future. In this chapter we shall review the new routes for the development of the field, their applications and implications for new discoveries.

It has been about 10 years ago that the first isolated light pulses shorter than one femtosecond [1] as well as trains of such bursts [2] have been reported. They signaled the birth of metrology with attosecond resolution, allowing—for the first time—real-time observation of the fastest dynamics outside the atomic core: the motion of electrons [3] and the oscillations of light fields [4]. Along with light waveform control [5], attosecond pulses [6] sparked a revolution in the exploration and control of electronic phenomena in the microcosm. This volume provides a comprehensive overview of the first decade of attosecond science, which was dominated by developing basic tools and techniques, their validation and first applications.[1] These tools and techniques are now in place and work well, providing the basis for entering a new phase of the evolution of this new subfield of optical science.

The next decade of attosecond science will witness a further accelerating progress of attosecond sources and techniques opening entirely new research opportunities as well as a strong shift of applications from the scrutiny of simple systems (atoms and simple molecules) towards ever more complex systems such as large biological molecules, solids, surfaces and molecular systems assembled on surfaces. Advances in attosecond technologies will bring about never-before-witnessed synergies between laser- and accelerator-based light sources and applications that aim at seeking answers to grand questions of physical science, life science, and technology: Is it feasible to create compact X-ray lasers, for a number of applications in science and technology? Can initial attosecond electron motion affect changes in

---

[1] For a comprehensive review, see [7].

F. Krausz (✉)
Max Planck Institute of Quantum Optics, Hans-Kopfermann-Str. 1, 85748 Garching, Germany
e-mail: ferenc.krausz@mpq.mpg.de

L. Plaja et al. (eds.), *Attosecond Physics*, Springer Series in Optical Sciences 177,
DOI 10.1007/978-3-642-37623-8_14,

complex molecular structure and be used for affecting these changes? Is light-field-controlled attochemistry feasible? Where are the ultimate speed limits of electronics and how can we reach them? Can electronic signal processing be speeded up to light frequencies? Is the recording of snapshots with atomic resolution in space and time feasible for the direct visualization of any motion outside the atomic core, including the fastest one, the motion of electrons?

On the following pages, we shall look forward and speculate about the major routes this still very young discipline is likely to take in the next decade by addressing desirable technological advances as well as their possible implications for new discoveries and developments.

## 14.1 Frontiers in Attosecond Sources and Techniques

Few-cycle laser pulses with a controlled waveform constitute an enabling technology for the generation of isolated attosecond pulses, metrology of these tools and their applications for time-domain access to electron processes. Figure 14.1 shows a state-of-the-art apparatus for attosecond metrology and spectroscopy, the AS-2 beamline at the Max Planck Institute of Quantum Optics (photo at the top). The beamline is seeded with sub-4-fs, 750-nm-carrier-wavelength near-single-cycle laser pulses, which produce sub-100-attosecond XUV pulses in the 100-eV photon energy range. Temporal characterization of both tools is implemented with an attosecond streak camera, schematically shown in the bottom panel of Fig. 14.1. The light-field-driven streak camera records XUV-induced, laser-field-affected photoelectrons as a function of delay between the XUV and laser pulse. The resultant streaking spectrogram allows a complete retrieval of the sub-4-fs laser waveform as well as the 72-attosecond XUV pulse. Coming in perfect synchrony to each other, they allow a number of spectroscopic techniques (with the attosecond pulse serving either as a trigger or a probe pulse) to be accomplished: attosecond streaking [8, 9] and tunneling [10] spectroscopy using the XUV pulse as a trigger and the controlled laser field as a probe, or attosecond photoelectron or absorption spectroscopy of strong-field processes with the XUV pulse in the role of the probe [11].

In spite of tremendous progress, the toolbox of attosecond technology is still limited to attosecond pulses with moderate (typically sub-nanojoule) energy and photon energies in the extreme ultraviolet (typically in the range of 100 eV or below). These limitations currently prevent attosecond pulses from being simultaneously used for both triggering and interrogation as well as from probing dynamics of strongly-bound electrons deep inside atoms and molecules, respectively. There is a strong demand for increased photon flux and energy of attosecond pulses and growing efforts to meet these demands.

The most promising route to meeting both demands is offered by X-ray free electron lasers [12–14]. They provide both unparalleled flux and photon energies up to the hard-X-ray regime. FELs in the soft and hard X-ray regime have been reported to generate pulses down to the 10-fs regime [15]. They even offer the potential for

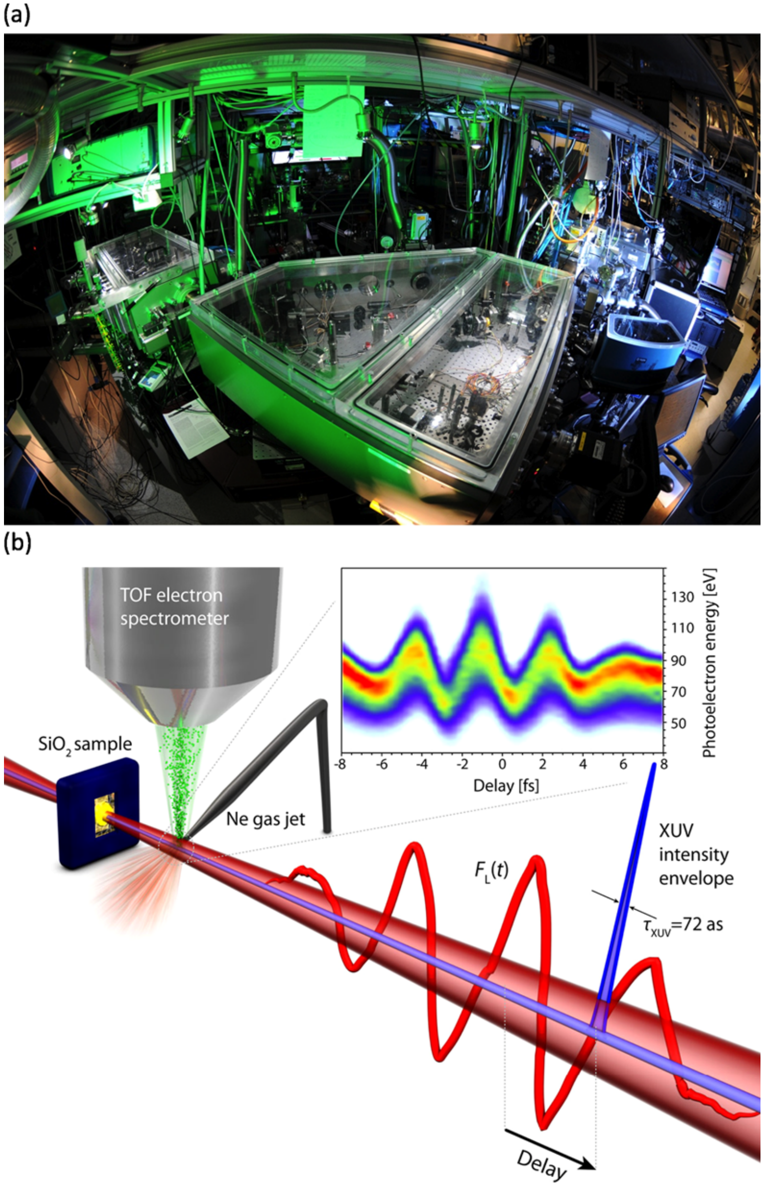

**Fig. 14.1** Second-generation attosecond beamline AS-2 at the Max Planck Institute of Quantum Optics (**a**) uses sub-4-fs waveform-controlled laser pulses and sub-100-attosecond XUV pulses for the time-resolved investigation of ultrafast electron processes (**b**). The tools are temporally characterized by attosecond streaking (see attosecond streaking spectrogram recorded) and subsequently used for pump-probe spectroscopy, e.g. for the scrutiny of strong-field-induced electron processes in dielectrics, by means of attosecond XUV absorption spectroscopy. Courtesy of Thorsten Naeser (Panel (**a**)) and Martin Schultze (Panel (**b**))

sub-femtosecond and attosecond pulses. Motivated by exciting applications, several promising concepts have been devised [16, 17] and ever more extensive theoretical as well as experimental research is under way to exploit this potential.

Laser-based techniques also afford promise for significant advances in scaling flux and photon energy of attosecond pulses, even though they are unlikely to ever be able to compete with FELs in terms of these parameters. High-order harmonic generation in gases, which is currently the standard technique for attosecond pulse generation, may be scaled to higher flux by using more powerful driver pulses with peak powers in the multi-terawatt regime [18]. With the use of a few-cycle driver source [19] or gating techniques [20], this approach affords promise for microjoule-energy, multi-gigawatt-peak-power attosecond XUV pulses. On the other hand, longer-wavelength driver fields can result in kiloelectronvolt photon energies from the atomic HHG process [21], but the process suffers from lower conversion efficiency and it is therefore an open question whether atomic HHG will be able to deliver kiloelectronvolt attosecond pulses with photon flux levels allowing a wide range of applications.

Relativistic interactions appear to be inherently more suited for scaling the flux and photon energy of attosecond pulses. Lasers can drive such interactions in several ways. In underdense plasmas they can accelerate electron bunches to superrelativistic energies that last only a few femtoseconds [22, 23]. These multi-MeV, few-femtosecond, multi-kA-peak-current electron bunches can generate ultrashort X-ray pulses [24], which may be shortened into the sub-femtosecond regime [16, 17]. In overdense plasmas created on the surface of solids, high-order harmonic generation driven by multi-terawatt laser pulses is predicted to be another promising route to increase the photon flux of laser-driven attosecond pulses by orders of magnitude and their photon energies beyond the 1-keV frontier [25]. Figure 14.2 depicts the photon energies and conversion efficiencies predicted to be achievable in the generation of isolated pulses driven by few-cycle relativistic fields. Experiments have meanwhile corroborated the viability of the approach [26–28].

Summing up, there is a number of promising routes to developing novel sources of attosecond pulses that offer the potential of outperforming current first-generation attosecond sources in terms of flux and energy coverage. The techniques range from strong-field to relativistic interactions and will rely on the advancement of the underlying laser driver and accelerator technology and synergies between them. The development of these next-generation attosecond sources will constitute one of the main research foci in the second decade of attosecond science.

## 14.2 From Scrutiny Towards Control

The force the electric field of ultrashort laser pulses exerts on electrons can rival and even far exceed the forces responsible for binding them in the valence shell of atoms and molecules. Hence, if controlled, this force lends itself for steering the motion of electrons in and around atomic systems. The first step towards controlling

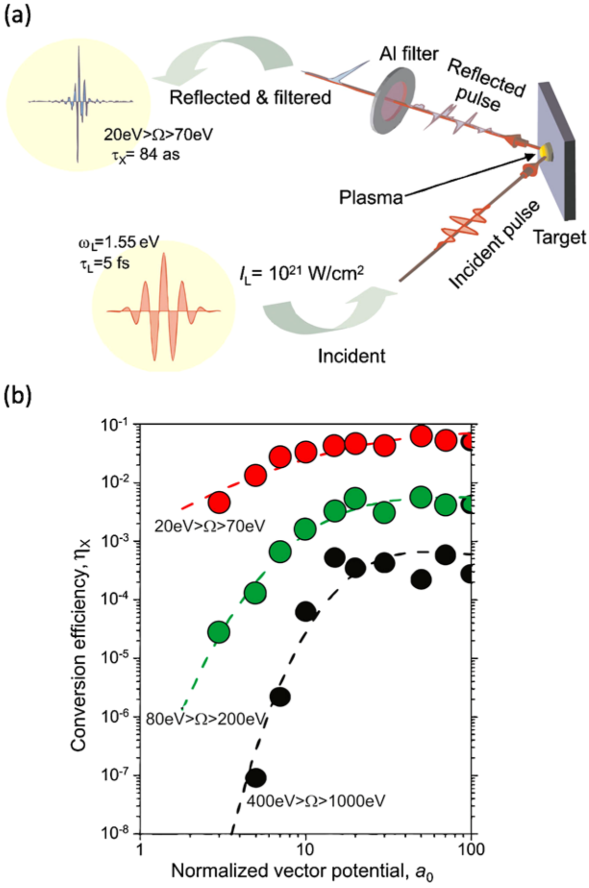

**Fig. 14.2** (**a**) High-order harmonic generation on a solid surface exposed to ultrashort laser pulses at relativistic intensities. In the case of a few-cycle excitation, the reflected coherent light, if bandpass filtered, is predicted to deliver isolated bursts of attosecond XUV light. (**b**) Conversion efficiency versus peak laser intensity for different XUV spectral ranges (from [7]). Courtesy of G. Tsakiris

the electric force of light has been the stabilization of the carrier-envelope phase of few-cycle laser pulses [5]. Control of this parameter, in addition to the pulse envelope and chirp, allowed control of the sub-cycle, i.e. sub-femtosecond evolution of the instantaneous electric field of visible/infrared light, making the electric force of light available for atomic-scale electron steering. A first manifestation of this new type of quantum control has been the controlled reproducible generation of isolated attosecond XUV pulses [6] as well as the time-resolved measurement of these pulses [6] and the waveform of few-cycle laser light [4].

Versatile control of the atomic-scale motion of electrons calls for the sub-femtosecond temporal evolution of the controlling force, i.e. the light waveform, to be varied with a much greater degree of flexibility than provided by the adjustment of the carrier-envelope phase in few-cycle laser pulses. The demanded larger flexibility requires substantially more bandwidth and control parameters. The required bandwidth can be readily obtained by self-phase modulation of femtosecond pulses in a gas-filled hollow-core fiber, the resultant supercontinuum can span a band extending over far more than an octave, e.g. from the deep ultraviolet to the near infrared [29]. It is more demanding to provide the control knobs for sub-cycle sculpting of the waveform, in other words: light waveform synthesis.

To this end, the frequency spectrum of the continuum must be subdivided into several bands of comparable width and the resultant coherent infrared, visible, and ultraviolet light wavepackets need to be superimposed on each other with variable relative phases and amplitudes. These phases and amplitudes are the control knobs for the sub-cycle shaping of light waveforms, see Fig. 14.3(a). The more bandwidth and the more spectral channels we have, the larger the variety of optical waveforms with a distinctly different evolution on an attosecond scale that can be synthesized.

Optical waveform synthesis was first demonstrated by using chirped multilayer dielectric mirrors for implementing the above mentioned concept [30]. In the first implementation, dichroic chirped mirrors separated a coherent white-light supercontinuum (stretching from wavelengths longer than 1000 nm in the near infrared to those shorter than 400 nm in the ultraviolet) into three spectral channels of comparable bandwidth. This prototypical 1.5-octave, 3-channel device allows optical waveform synthesis by independent manipulation of the resultant near-infrared, visible, and ultraviolet wavepacket, each less than 10 fs in duration. Merely delaying them with respect to each other gives rise to a variety of output waveforms, as illustrated in Fig. 14.3(b). Already its first application demonstrated the power of the new technology. Super-octave light waveform synthesis provided near-single cycle waveforms with a (full-width-of-intensity-half-maximum, FWHM) duration of approximately 2 femtoseconds, and permitted with them the confinement of the strong-field ionization to a single half-cycle, i.e. a less than 1 femtosecond accurate quantitative determination of its rate selectively from different quantum states for the first time [30]. Furthermore, this unprecedented temporal confinement of strong-field ionization permits the creation of valence electron wavepackets with nearly perfect coherence in an atomic ensemble [30].

The first prototypical system has recently been supplemented with a deep ultraviolet channel to result in a 2-octave, 4-channel synthesizer [31]. This progress now offers the potential for synthesizing intense sub-cycle transients with a duration of less than 1 femtosecond and an unprecedented variety of few-cycle light transients with tailored sub-cycle field evolution. The former, along with synchronized isolated attosecond XUV pulses, will open the door for attosecond-pump/attosecond-probe-type spectroscopy and extending nonlinear optics into a previously inaccessible regime of single-cycle and sub-cycle interactions. The latter, on the other hand, will provide a means of steering and manipulating electrons on their natural time scale of their motion within attoseconds.

Possible implications of these emerging capabilities are numerous and far reaching. For example, confinement of intense optical radiation to half wave cycle will allow multiple ionization within less than 1 femtosecond and create highly correlated electron dynamics. Tailored multi-octave waveforms, on the other hand, may open new avenues to quantum control of molecular dynamics and allow to explore routes

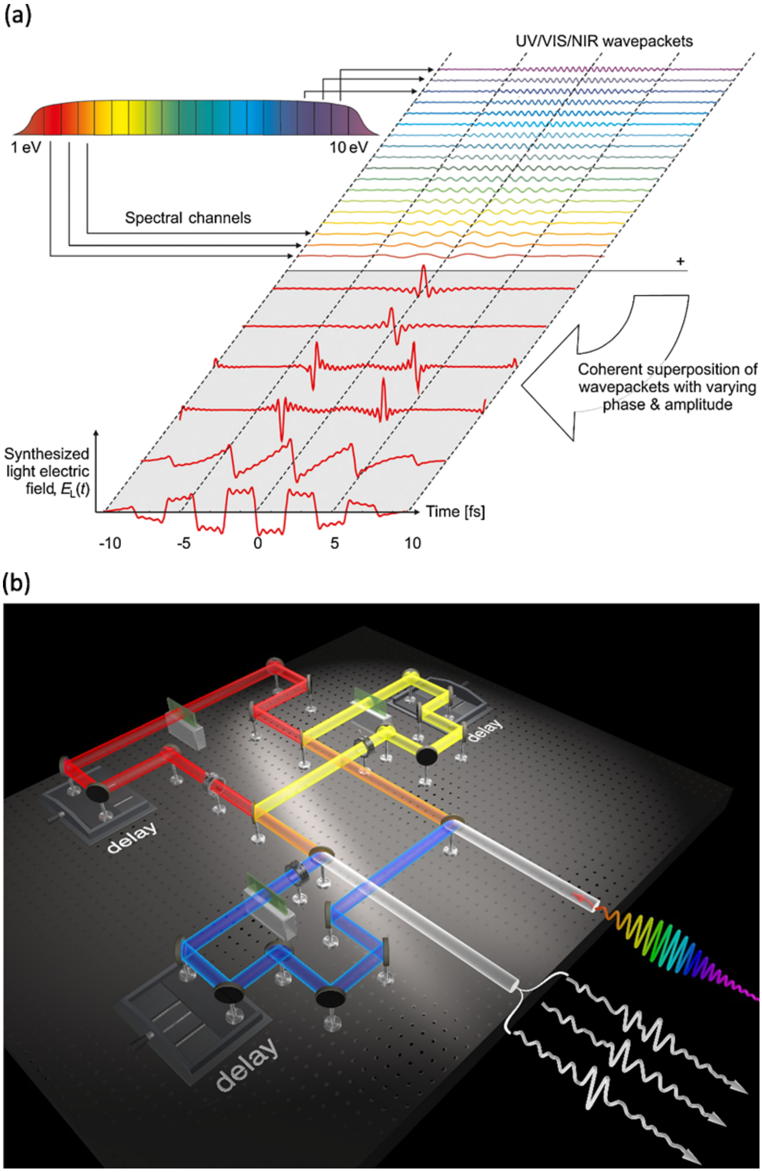

**Fig. 14.3** (**a**) Principle of optical waveform synthesis (from [7]). (**b**) Prototypical 3-channel, 1.5-octave light wave synthesizer, as reported in Ref. [30]

to speeding up solid-state electronics. Unprecedented insight into electron correlations and advancing molecular control and semiconductor electronics are only a few arguments motivating research into light field synthesis and their applications. These efforts are likely to become another major sub-field of attosecond science in the years to come.

## 14.3 Electrons in Atoms and Molecules

Time-resolved atomic- and molecular science have several terrae incognitae that can and hopefully will be explored by attosecond spectroscopy.

Inner-shell dynamics in atoms constitute such a field. The widths of isolated X-ray photoelectron and absorption spectral lines do provide a hint of the rapidity of inner-shell processes following excitation by the impact of X-ray photons or massive high-energy particles. However, in many cases, when the excited atomic state can be reached via competing quantum mechanical channels, lineshapes are complex and incapable of providing reliable information about the temporal evolution of the underlying processes. Frequency- (or energy-) domain spectroscopy also fail to do so if the dynamics under scrutiny take place under the influence of strong laser fields, which can only be applied for brief time intervals, insufficient for acquiring spectral information by conventional (time-integral) spectroscopies. In all these cases, direct temporal access with sub-femtosecond or attosecond resolution is required.

This can be provided by an attosecond X-ray pulse that is either synchronized to a strong few-cycle optical field with a controlled waveform, or is so intense, that—after being splitted—it can serve both as a pump and a probe pulse. Laser-based techniques, once providing attosecond pulses at high enough typically kiloelectronvolt photon energies, will most likely have to rely on the first approach, whereas XFELs, once providing attosecond pulses, will ideally lend themselves for the latter approach. The first method is based on the—relatively weak—attosecond X-ray pulse creating an inner-shell vacancy which is followed by the emission of a photoelectron and/or secondary (Auger) electron(s). The temporal evolution of these emissions provides information about the creation and annihilation of the inner-shell excitation (vacancy) and can be measured by the attosecond streaking implemented with the synchronized, waveform-controlled few-cycle laser field.

Once intense attosecond X-ray pulses become available in XFELs, they will open the door for the second method using the replica of the same X-ray pulse as a probe. This offers the advantage that (i) the time-resolved interrogation does not rely on free electrons bound-bound transitions, and their concomitant relaxation processes can also be accessed. Moreover, attosecond X-ray-pump/X-ray-probe spectroscopy is not restricted to photoelectrons as a physical measurable during the pump-probe exposure, but can also incorporate the measurement of transmitted X-ray probe photons often providing complementary information. Consequently, attosecond X-ray-pump/X-ray-probe spectroscopy appears to be the most versatile approach to accessing inner-shell excitation and relaxation dynamics in atoms. Attosecond XFEL pulses therefore afford promise for providing unprecedented insight into inner-shell processes, which may lead to new or improved schemes for X-ray lasers based on atomic transitions.

A terra incognita of molecular science is the coupling of electronic and nuclear motion in molecules, with particular interest in complex biological systems, and the role of this coupling for the course of conformational changes and reactions. Moreover, another very exciting question is whether initial electronic dynamics, unfolding on a sub-femtosecond to few-femtosecond time scale, can affect or even predetermine the course the subsequent evolution of nuclear coordinates and related structural changes takes, following the electronic excitation on a multi-femtosecond time scale.

The technology of synthesized multi-octave light waveforms [30, 31] offers exciting prospects for seeking answers to these questions. The UV/deep-UV portions of the broadband continua lend themselves for exciting valence electrons from the highest occupied molecular orbital to several unoccupied orbitals on a sub-fs-scale, thereby launching a coherent broadband valence electron wavepacket in the molecule. The subsequent electron wavepacket dynamics unfolding within one to several femtoseconds and the question of how this initial dynamics influence changes in molecular structure occurring on longer time scales as well as the role of electron-nuclear couplings, can be directly interrogated by a time-delayed attosecond XUV pulse via photoelectron or absorption spectroscopy. Moreover, extending waveform synthesis to wavelengths of several micrometers in the mid infrared will allow the synthesis of electric forces that is variable all the way from electronic (sub-femtosecond) to molecular (multi-femtosecond) time scales. Such a force may allow the controlled modification of a complex (bio)molecule via direct light-field steering of valence electron motion in a similar way as a simple waveform control allowed controlled dissociation of a simple (diatomic) molecule in a prototypical experiment, see Fig. 14.4 [32].

Time-resolving inner-shell processes in atoms and electron-nuclear dynamics in (ever more complex) molecules will be another major frontier of attosecond science with great potential returns for physical and life sciences.

## 14.4 Electrons in Condensed Matter

Condensed-matter physics is, to an overwhelming extent, the physics of electrons in (quasi-) periodic potentials. Whereas the static electronic structure of condensed matter, especially of solids, has been thoroughly studied by both laser and synchrotron-based techniques, a wide range of electron dynamics in solids have been elusive because their rapidity has exceeded the resolution of the fastest time-resolved metrologies available until recently. Charge screening in metals, hot electron dynamics, collective motion and coherence phenomena in semiconductors, strong-field processes in dielectrics, charge transfer in nanostructures and molecular assemblies on surfaces are a few of many examples. Attosecond technology now offers a route to accessing these and other condensed-matter phenomena in real time.

Transport and charge screening phenomena can be studied by attosecond streaking spectroscopy [8, 33] with the attosecond XUV pulse as a trigger and the controlled NIR field as a probe. Population dynamics, collective motion and coherent phenomena can be scrutinized by attosecond photoelectron spectroscopy, with the few-fs laser pulse or its low-order harmonics as a pump and the attosecond XUV pulse as a probe. Both approaches rely on ultrahigh vacuum conditions to avoid sur-

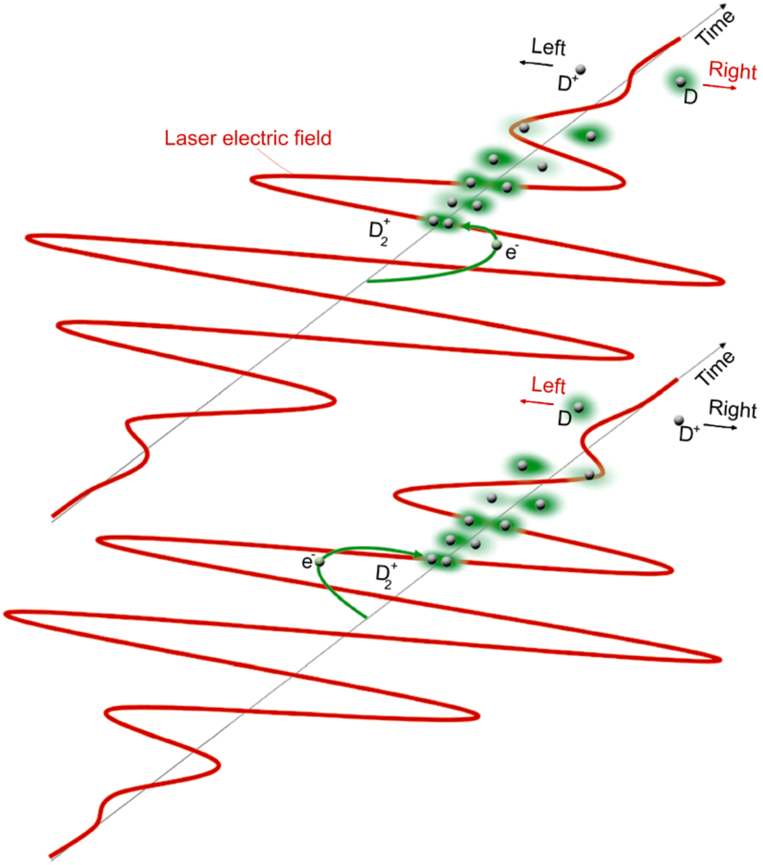

**Fig. 14.4** Controlling electron motion and localization during dissociation of a diatomic molecule with the controlled electric field of light, as reported in Ref. [32] (from [7])

face contaminations preventing photoelectrons from escaping, see Fig. 14.5. Strong-field processes in dielectric can be studied by attosecond absorption spectroscopy using XUV and UV-VUV probes. Although first proof-of-concept experiments have been demonstrated, attosecond condensed-matter spectroscopy is in its infancy. Efforts in a number of laboratories all over the world will be required to bring this new field to fruition. The tremendous discovery potential provides motivation for the endeavor.

In terms of control, synthesized few-cycle light also offers new routes to control electric current at unprecedented switching speed. Recent experiments have demonstrated that strong electric fields of few-cycle visible-near-infrared light can turn a dielectric into a highly-polarizable, i.e. a conducting state reversibly on a few-femtosecond time scale [34] and induce and direct current between metal electrodes at optical frequencies [35]. The experiments indicate a promising route to speeding up electron-based signal processing and solid-state metrology to light frequencies.

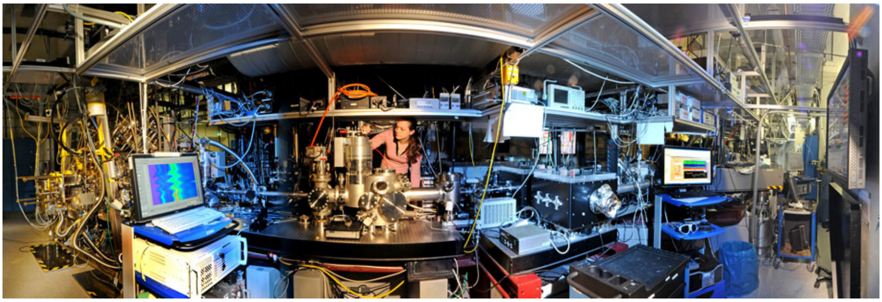

**Fig. 14.5** The world's first ultrahigh-vacuum attosecond metrology and spectroscopy apparatus, the AS-3 beamline at the Max Planck Institute of Quantum Optics. Courtesy of Thorsten Naeser

*Dielectric electronics* affords promise to become another dynamically evolving field of attosecond science.

## 14.5 Space-Time (4D) Imaging with Atomic Resolution

During the first decade of attosecond science, proof-of-principle experiments have provided time-domain access to dynamic changes in the population of stationary quantum states [3] and to the temporal evolution of quantum wavepackets [11]. No explicit information about changes of the probability distribution of the electrons' position has been acquired. For complex systems, this can be unambiguously provided only by microscopy or diffraction, provided that they can be furnished with sub-femtosecond or attosecond temporal resolution.

Let us start addressing such possibilities in microscopy. The availability of light pulses with characteristics controlled on a sub-femtosecond scale offers several natural ways of furnishing well-established microscopic techniques with attosecond resolution. In photo-emission electron microscopy (PEEM) the continuous-wave UV/XUV light source must simply be replaced with one emitting this radiation in the form of attosecond bursts [36]. In scanning tunnelling microscopy (STM), on the other hand, electron emission from the nanometer-sized tip may be confined to several hundred attoseconds by launching electrons with a cosine-shaped few-cycle light pulse via optical field ionization [37]. In this way, several-nanometer (PEEM) and angstrom (STM) resolution in space can be combined with attosecond resolution in time. Both techniques call for illumination at moderate pulse peak powers and high repetition rates, preferably $\ll 1$ kHz, in order to reconcile the requirement of the emission of less than one electron per light pulse (on average) with good statistics. This calls for the development of waveform-controlled few-cycle sources at sub-MHz repetition rates and attosecond XUV sources driven by them.

In order to extend diffraction imaging from the three spatial dimensions to the fourth, the temporal dimension, the electron or X-ray beam used for mapping the electron density in molecules or crystals must be replaced with a short pulse. The high (multi-keV) particle energy reconciles the apparently conflicting requirements

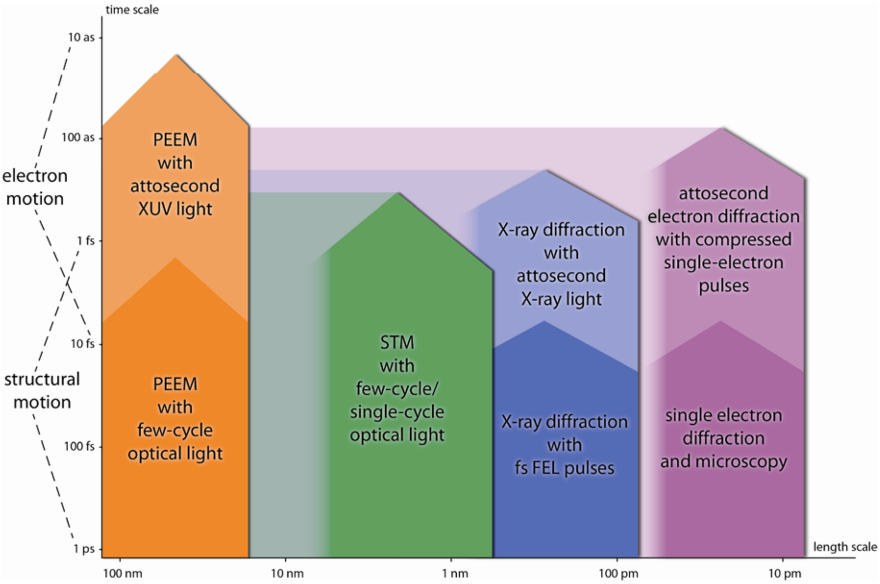

**Fig. 14.6** Routes to accessing motions (structural as well as electronic) outside the atomic core. Courtesy of P. Baum

of narrow relative energy distribution ($\leq 1$ %) required by the relatively large-size ($>$ 10 nm) of complex systems to be imaged with the ultrashort pulse duration demanded by molecular ($<$ 1000 fs) and electronic ($<$ 1 fs) time scales. The ultrashort electron [38] or X-ray [39] pulse allows recording of snapshots of the dynamic evolution of the electron density distribution following excitation by a short pump pulse. Dynamic changes in the electron distribution may occur due to (i) the motion of the nuclei: the electron cloud virtually instantly adjusts to this motion, or (ii) electronic excitation.

The former process evolves on a multi-femtosecond time scale, see Fig. 14.6, and reflects atomic rearrangement in molecules or solids. It has already been imaged with sub-picosecond time resolution [40]. Electronic rearrangements may unfold within attoseconds (Fig. 14.6). Attosecond photon pulses in the hard-X-ray regime (several kiloelectronvolt or more) may become available in the foreseeable future in X-ray FELs [16, 17] and, on the longer run, possibly from compact, laser-driven laboratory sources. Single-electron pulses accelerated to near relativistic (typically 10–100 keV) energies in static electric fields [41, 42] may reach durations below 10 femtosecond, whereas their acceleration by rapidly-varying (microwave or optical) fields affords promise for sub-femtosecond and attosecond electron pulses [43]. These single-electron wavepackets meanwhile reach coherence lengths of several ten nanometers, rendering them suitable for imaging transient states of large, biological specimens [44], see Fig. 14.7. These advances will open the way to 4D imaging of both femtosecond structural dynamics and attosecond electron density variations with atomic space-time resolution.

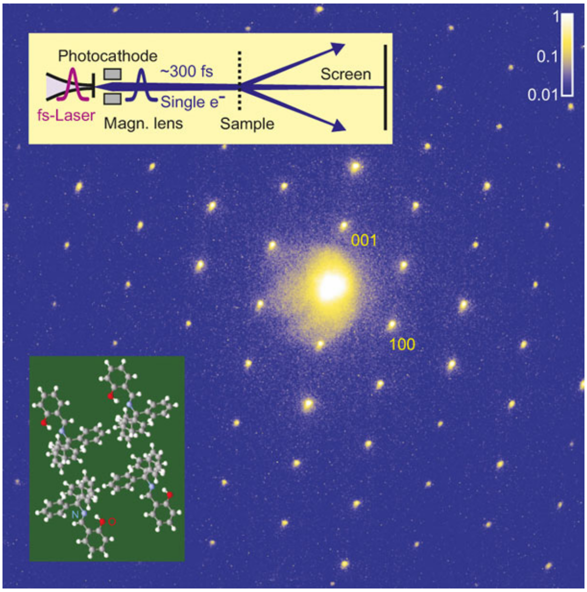

**Fig. 14.7** Single electrons offer the potential for directly imaging dynamic changes of electronic charge distribution in atomic systems. They can thereby record snapshots of extremely short-lived transient states of atomic or molecular structures during their transformations, on the longer run possibly even of electronic charge densities in motion. The figure shows a diffraction snapshot of a molecular switch undergoing photochemical isomerization on a sub-100-fs time scale [44]

## 14.6 Expected Impacts

The next decade of attosecond science will bring about unprecedented cooperation and synergies between laser-based and accelerator-based light sources. Attosecond electron and photon pulses from laser-matter interactions and accelerator-based devices will ideally supplement each other in providing real-time access to the motion of electrons on atomic and sub-atomic scales. Access means both capturing and steering motions with—potentially—attosecond precision. The microscopic motion of electrons plays a key role in advancing the technology of compact X-ray sources, or pushing electronics and magnetic storage to ever smaller dimensions and ever higher speeds, in triggering chemical reactions, in biological signal transduction and the damage and repair mechanisms of DNA, in the undesirable and desired radiation-induced damage to biological matter in cancer diagnostics and therapy, respectively. Consequently, attosecond science affords promise for having an impact on physical and life sciences as well as technology.

## References

1. M. Hentschel et al., Nature **414**, 509 (2001)
2. P.M. Paul et al., Science **292**, 1689 (2001)
3. M. Drescher et al., Nature **419**, 803 (2002)
4. E. Goulielmakis et al., Science **305**, 1267 (2004)
5. A. Baltuska et al., Nature **421**, 611 (2003)
6. R. Kienberger et al., Nature **427**, 817 (2004)
7. F. Krausz, M. Ivanov, Attosecond physics. Rev. Mod. Phys. **81**, 163 (2009)

8. A. Cavalieri et al., Nature **449**, 1029 (2007)
9. M. Schultze et al., Science **328**, 1658 (2010)
10. M. Uiberacker et al., Nature **446**, 627 (2007)
11. E. Goulielmakis et al., Nature **466**, 739 (2010)
12. P. Emma et al., Nat. Photonics **4**, 641 (2010)
13. J.N. Galayda et al., J. Opt. Soc. Am. B **27**, 106 (2010)
14. D. Pile et al., Nat. Photonics **5**, 456 (2011)
15. S. Düsterer et al., New J. Phys. **13**, 093024 (2011)
16. A.A. Zholents, W.M. Fawley, Phys. Rev. Lett. **92**, 224801 (2004)
17. E.L. Saldin, E.A. Schneidmiller, M.V. Yurkov, Opt. Commun. **239**, 161 (2004)
18. G. Sansone, L. Poletto, M. Nisoli, Nat. Photonics **5**, 655 (2011)
19. D. Herrmann et al., Opt. Lett. **34**, 2459 (2009)
20. P. Tzallas et al., Nat. Phys. **3**, 846 (2007)
21. V.S. Yakovlev, M. Ivanov, F. Krausz, Opt. Express **15**, 15351 (2007)
22. O. Lundh et al., Nat. Phys. **7**, 219 (2011)
23. A. Buck et al., Nat. Phys. **7**, 543 (2011)
24. M. Fuchs et al., Nat. Phys. **5**, 826 (2009)
25. G. Tsakiris et al., New J. Phys. **8**, 19 (2006)
26. B. Dromey et al., Nat. Phys. **2**, 456 (2006)
27. B. Dromey et al., Phys. Rev. Lett. **99**, 085001 (2007)
28. Y. Nomura et al., Nat. Phys. **5**, 124 (2009)
29. E. Goulielmakis et al., Opt. Lett. **33**, 1407 (2008)
30. A. Wirth et al., Science **334**, 195 (2011)
31. M. Hassan, E. Goulielmakis, Unpublished
32. M.F. Kling et al., Science **312**, 246 (2006)
33. S. Neppl et al., Phys. Rev. Lett. **109**, 087401 (2012)
34. M. Schultze et al., Nature **493**, 11720 (2013)
35. A. Schiffrin et al., Nature **493**, 11567 (2013)
36. M. Stockman et al., Nat. Photonics **1**, 539 (2007)
37. M. Krüger, M. Schenk, P. Hommelhoff, Nature **475**, 78 (2011)
38. H.-C. Shao, A.F. Starace, Phys. Rev. Lett. **105**, 263201 (2010)
39. G. Dixit, O. Vendrell, R. Santra, Proc. Natl. Acad. Sci. USA **109**, 11636 (2012)
40. M. Chergui, A.H. Zewail, Chem. Phys. Chem. **10**, 28 (2009)
41. A.H. Zewail, Science **328**, 187 (2010)
42. M. Aidelsburger et al., Proc. Natl. Acad. Sci. USA **107**, 19714 (2010)
43. E. Fill et al., New J. Phys. **8**, 272 (2006)
44. F.O. Kirchner et al., New J. Phys. **15**, 063021 (2013)

# Index

L. Plaja et al. (eds.), *Attosecond Physics*, Springer Series in Optical Sciences 177,
DOI 10.1007/978-3-642-37623-8,